Mutational analysis of the *P. falciparum* ARO protein, functional analysis of its predicted binding partner AIP and identification of AIP interacting proteins

-DISSERTATION-

with the aim of achieving a doctoral degree at the
Faculty of Mathematics, Informatics and Natural Sciences
Department of Biology
University of Hamburg

submitted by
Michael Geiger
Balingen

Oktober 2020

Dissertationsgutachter:	Prof. Dr. Tim-Wolf Gilberger
	Dr. Tobias Spielmann
Datum der Disputation:	18.12.2020

Eidesstattliche Versicherung

Hiermit erkläre ich eidesstattlich, dass ich die vorliegende Dissertationsschrift mit dem Titel „Mutational analysis of the *P. falciparum* ARO protein, functional analysis of its predicted binding partner AIP and identification of AIP interacting proteins“ selbst verfasst und keine anderen als die angegebenen Quellen und Hilfsmittel benutzt habe.

Dresden, den 20.10.2020

Michael Geiger

Declaration on oath

I hereby declare, on oath, that I have written the present dissertation entitled “Mutational analysis of the *P. falciparum* ARO protein, functional analysis of its predicted binding partner AIP and identification of AIP interacting proteins” on my own and have not used other than the acknowledged resources and aids.

Dresden, 20.10.2020

Michael Geiger

Language certificate

I am a native speaker, have read the present PhD thesis and hereby confirm that it complies with the rules of the English language.

Indianapolis, 20.10.2020

Alex Arnold

ZUSAMMENFASSUNG

Trotz erheblicher Erfolge in der Malariabekämpfung in den letzten 20 Jahren, ist sie noch immer eine der verheerendsten Infektionskrankheiten, welche Millionen Menschen weltweit betrifft. Die schwerste Form dieser Krankheit wird durch *Plasmodium falciparum* verursacht. Dieser Parasit kann, im sogenannten Merozoiten-Stadium, in Erythrocyten eindringen und sich in ihnen vermehren. Das damit einhergehende exponentielle Wachstum ist verantwortlich für alle klinischen Symptome der Malaria.

Die Wirtszellinvasion wird durch eine komplexe Invasionsmaschinerie des Parasiten koordiniert. Spezialisierte sekretorische Organellen (Mikroneme, Rhoptrien und dichte Granula) entleeren ihren Proteininhalt, um in einer kontrollierten Kaskade molekularer Interaktionen den Eintritt in den Erythrocyten zu ermöglichen. Die paarigen, kegelförmigen Rhoptrien sind am apikalen Pol des Parasiten lokalisiert. Die zugrundeliegenden molekularen Prozesse, welche die Rhoptrienbiogenese am apikalen Pol des Merozoiten und deren sekretorische Aktivität ermöglichen, sind gegenwärtig nur teilweise verstanden.

Für ein, für die phylogenetische Gruppe der Apikomplexa, zu welcher auch die Spezies *P. falciparum* und *Toxoplasma gondii* gehören, spezifisches Protein names ARO (Armadillo repeats only) konnte gezeigt werden, dass es mit Hilfe von Lipidankern mit der cytosolischen Seite der Rhoptrienmembran interagiert und dort eine essentielle Funktion für die intrazelluläre Positionierung der Rhoptrien ausübt. Weiterführende Arbeiten mit dem ARO-Homolog in *T. gondii* identifizierten interagierende Proteine, darunter die Adenylatcyclase β (ACβ), Myosin F (MyoF) und ein ARO interagierendes Protein, welches AIP genannt wurde. Dessen Homolog im Malariaparasiten war bislang unerforscht und eine detaillierte Information zur Tertiärstruktur von ARO war nicht vorhanden.

In der vorliegenden Arbeit wurde ein AIP-Homolog mittels der BLAST-Homologie-Suche in *P. falciparum* identifiziert und das Gen so modifiziert, dass sowohl dessen Lokalisation als auch eine funktionelle Analyse des Genproduktes möglich war. Nachfolgende Fluoreszenzmikroskopie-Kolokalisationsstudien zeigten, dass AIP an den Rhoptrienhals lokalisiert. Die quantitative Auswertung der Kolokalisationstudien zeigte eine nur teilweise Überlappung mit ARO, welches selbst eine ausgeprägte Lokalisation am Rhoptrienbauch aufwies. Die funktionelle Analyse wurde durch die „knock-sideways“-Methode realisiert, welche eine konditionelle Mislokalisierung von AIP ermöglichte. Es konnte gezeigt werden, dass eine Depletion von AIP vom Rhoptrienhals zu einem Defekt der Invasion von Erythrozyten führt. Um potentielle Interaktionspartner von AIP zu ermitteln, wurde die Methode der entfernungsabhängigen Biotinylierung, gefolgt von Massenspektrometrie, gewählt. Dieses ermöglichte die Erstellung einer Kandidatenliste, die unter anderem auch ACβ beinhaltete.

In einer Kollaboration mit dem Junop Labor (Western University, Kanada) wurde die Kristallstruktur von ARO ermittelt. Die strukturellen Informationen erlaubten eine detailliertere Untersuchung der ARO-AIP-Interaktion. Verschiedene Aminosäuren der vermutlichen Protein-Protein-Interaktionsdomäne wurden mutiert und deren Auswirkungen auf die Interaktion von ARO und AIP wurden quantifiziert. Es konnte gezeigt werden, dass Mutationen innerhalb dieser ARO-Domäne zu einer Fehllokalisation von AIP führen.

SUMMARY

Despite tremendous efforts, malaria is still one of the most devastating diseases affecting millions of humans worldwide. The most severe form of the disease is caused by *Plasmodium falciparum*. One stage of this protozoan parasite, termed merozoite, infects red blood cells, where the parasite multiplies exponentially. This multiplication step is responsible for all clinical symptoms.

The infection of an erythrocyte is coordinated by the complex invasion machinery of the parasite. Specialized secretory organelles (micronemes, rhoptries and dense granules) discharge their protein content to establish an orchestrated cascade of molecular interactions to mediate host cell entry. The dual club-shaped rhoptries are located at the apical pole (apex) of the parasite. The underlying molecular processes governing rhoptry biogenesis at the apex and its activity during secretion are not well understood.

An Apicomplexa-specific protein named ARO (Armadillo repeats only) has been identified in *P. falciparum* and in its close relative *Toxoplasma gondii*. It has been shown that ARO, which localizes to the cytosolic side of the rhoptries via lipid anchor modification, is essential to orient the nascent rhoptries at the apex. No crystal structure was available that would allow for a more detailed functional analysis. Research on *T. gondii* has shown that ARO interacts with ARO interacting protein (AIP), adenylate cyclase β (ACβ) and myosin F (MyoF), but no information was available on any ARO interacting proteins in the malaria parasite.

In this work, an AIP homologue was identified in *P. falciparum* using a BLAST homology search. Subsequent co-localization studies, using fluorescence microscopy, localized fluorescent reporter-tagged versions of AIP to the rhoptry neck. Quantitative analysis of co-localization data demonstrated only a partial overlap with ARO, which showed a pronounced rhoptry bulb localization. Flow cytometry and Giemsa smear analysis were performed to assess the phenotypic effect upon the depletion of AIP from the rhoptry neck using the conditional knock-sideways approach. The mislocalization of AIP caused a defect in the invasion of erythrocytes by merozoites. To assess AIP interaction partners, the proximity-dependent biotinylation approach followed by mass spectrometry was used. Several candidates could be identified, including ACβ, which was previously implicated in AIP interaction in *T. gondii*.

In a collaborative approach with the Junop laboratory (Western University, Canada), the crystal structure of *Pf*ARO was solved. This structural information was used to probe ARO-AIP interaction. Distinct amino acids were mutated at the putative protein-protein interaction face, and the consequences for ARO-AIP interaction were quantified. It could be shown that mutations within this ARO domain lead to mislocalized AIP.

TABLE OF CONTENTS

LIST OF FIGURES

LIST OF TABLES

ABBREVIATIONS

%	*percent*
Å	*Ångström*
aa	*amino acid, amino acids*
AmBic	*ammonium bicarbonate*
Acα	*adenylate cyclase α*
ACβ	*adenylate cyclase β*
ACN	*acetonitrile*
ACT	*artemisinin combination therapy*
AFR	*African Region*
AIP	*ARO interacting protein*
AMA1	*apical membrane antigen 1*
AMP	*adenosine monophosphate*
An.	*Anopheles*
APS	*ammonium persulfate*
AP1	*adaptor protein complex 1*
AP2-G	*Apatella2-G*
ARM	*armadillo*
ARO	*armadillo repeats-only*
as	*antisense*
AS	*alternative splicing*
ATc	*anhydrotetracycline*
ATSB	*attractive toxic sugar bait*
AQ13	*aminochinoline 13*
BiFC	*bimolecular fluorescence complementation*
BioID	*(proximity-dependent) biotin identification*
bp	*base pairs*
BRET	*bioluminescent resonance energy transfer*
BSA	*albumin bovine fraction V*
BSD	*Blasticidin S*
BSG	*basigin*
c	*conditional*
°C	*degree Celsius*
C1	*compound 1*
C2	*compound 2*
CCR	*conserved core region*
cDNA	*complementary DNA*
CDPK	*calcium-dependent protein kinase*
CD	*cluster of differentiation*
CERLI1	*cytosolic exposed leaflet interacting protein 1*
CHMI	*controlled human malaria infection*
CIP	*calf intestinal phosphatase*
CLEM	*correlated fluorescence electron microscopy*
CLMS	*cross-linking mass spectrometry*
CM	*cerebral malaria*
CRISPR	*clustered regularly interspaced short palindromic repeats*
CR1	*complement receptor 1*
CSA	*chondroitin sulfate-A*
CSP	*circumsporozoite protein*
CyRPA	*cysteine-rich protective antigen*
DAPI	*4',6-diamidino-2-phenylindole*
DDT	*dichlorodiphenyltrichloroethane*
DHA	*dihydroartemisinin*
DHE	*dihydroethidium*
DHFR	*dihydrofolate reductase*
DHFS-FPGS	*dihydrofolate synthase/folylpolyglutamate synthase*
DHODH	*dihydroorotate dehydrogenase*
dH_2O	*distilled water*
DIQ-BioID	*dimerization induced quantitative BioID*
DMSO	*dimethyl sulfoxide*
DNA	*deoxyribonucleic acid*
dNTP	*deoxynucleosidtriphosphate*
DPBS	*Dulbecco's phosphate buffered saline*
Drp	*dynamin-related protein*
DTT	*1,4,-dithiothreitol*
EBA	*erythrocyte binding antigen*
EBL	*erythrocyte binding like protein*
ECL	*enhanced chemoluminescence*
E. coli	*Escherichia coli*
EDV	*electron-dense vesicles*
EEF	*exo-erythrocytic form*
e.g.	*exempli gratia*
EGTA	*ethylene glycol-tetraacetic acid*
EM	*erythrocyte membrane, electron microscopy*
EMBL	*European Molecular Biology Laboratory*
EMP1	*erythrocyte membrane protein 1*
EMR	*Eastern Mediterranean Region*
ER	*endoplasmic reticulum*
EtBr	*ethidium bromide*
ET	*electron tomography*
et al.	*et alii*
FC	*flow cytometry, fold change*
FKBP	*FK506 binding protein*
FRB	*FKBP rapamycin binding domain*
FRET	*Förster resonance energy transfer*
fwd	*forward*
g	*grams, g-force*
GAS	*genetically attenuated sporozoites*
gDNA	*genomic DNA*

GDV1	*gametocyte development 1*
GFP	*green fluorescent protein*
GMP	*good manufacturing practice*
GPA	*glycophorin A*
GPI	*glycosylphosphatidylinositol*
GST	*glutathione S-transferase*
G6PD	*glucose-6-phosphate-dehydrogenase*
h	*hour, hours*
HEPES	*4-(2-Hydroxyethyl)-1-piperazineethane-sulfonic acid*
Ho33342	*Hoechst 33342*
HP1	*heterochromatin protein 1*
hpi	*hours post infection*
HR	*homologous region*
HRP	*horseradish peroxidase*
HSP	*heat shock protein*
HSPG	*heparan sulfate proteoglycan*
i.a.	*inter alia*
ICAM	*intercellular adhesion molecule*
ICR	*inner core region*
IDR	*intrinsically disordered region*
IFA	*immunofluorescence assay*
IMC	*inner membrane complex*
IP	*Immunoprecipitation, interaction partner*
ITN	*insecticide-treated (mosquito) nets*
IRS	*indoor residual spraying*
iRBC	*infected red blood cell*
kb	*kilo base*
kDa	*kilo Dalton*
KS	*knock-sideways, knock sideways*
l	*liter*
LB	*lysogeny broth*
LLIN	*long-lasting insecticidal net*
LNVP	*liquid nitrogen vapor phase*
LS	*liver stage*
LSM	*larval source management*
m	*milli*
M	*molar*
µ	*micro*
MACS	*magnetic-activated cell sorting*
MC	*Maurer's cleft*
MFS	*malaria freezing solution*
min	*minute, minutes*
MOPS	*3-(N-morpholino) propanesulfonic acid*
MS	*mass spectrometry*
MSC	*Mander's split coefficient*
MSP	*major surface protein*
MTS	*malaria thawing solution*
MyoA	*myosin A*
MyoF	*myosin F*
n	*nano*
NA	*not assessed*
NEB	*New England Biolabs*
Neo	*neomycin phosphotransferase II*
NLS	*nuclear localization signal*
NMT	*N-myristoyl transferase*
NPP	*new permeability pathway*
ns	*not significant*
OD	*optical density*
P	*p-value*
PAGE	*polyacrylamide gel electrophoresis*
PAT	*palmitoyl acyl transferase*
PBS	*phosphate buffered saline*
PCC	*Pearson correlation coefficient*
PCR	*polymerase chain reaction*
pH	*potentia hydrogenii*
PH	*pleckstrin homology-like*
PIC	*protease inhibitor cocktail*
PKC	*protein kinase C*
PMSF	*phenylmethylsulfonylfluoride*
POI	*protein of interest*
PPI	*protein-protein interaction*
PPM	*parasite plasma membrane*
PTM	*post translational modification*
PV	*parasitophorous vacuole*
PVM	*parasitophorus vacuole membrane*
Rab	*Ras-related in brain (protein)*
RALP1	*rhoptry-associated, leucine zipper-like protein 1*
rap	*rapalog*
RAS	*radiation-attenuated sporozoites*
RBC	*red blood cell*
RBCM	*red blood cell membrane*
rev	*reverse*
RFP	*red fluorescent protein*
Rh	*reticulocyte-binding protein homolog*
RIPA	*radioimmunoprecipitation assay*
Ripr	*Rh5 interacting protein*
RMSD	*root-mean-square deviation*
RNA	*ribonucleic acid*
RON	*rhoptry neck protein*
RPMI	*Roswell Park Memorial Institute*
RT	*room temperature*
RTS,S	*recombinant circumsporozoite protein vaccine*

s	*second,seconds*
SDS	*sodium dodecyl sulfate*
SEAR	*South-East Asia Region*
SLI	*selection linked integration*
SP	*signal peptide*
spp.	*species pluralis*
SR	*scavenger receptor*
STED	*stimulated emission depletion*
std	*(molecular) size standard*
TAE	*Tris-acetate-EDTA*
TBD	*transmission-blocking drug*
TBV	*transmission-blocking vaccine*
TE	*Tris-EDTA*
TEAB	*triethylammonium bicarbonate buffer*
TEMED	*N, N, N, N-Tetramethylethylenediamine*
TFA	*trifluoroacetic acid*
TGN	*trans-Golgi network*
TLR	*toll-like receptor*
TM	*template modelling*
TMD	*transmembrane domain*
TNF	*tumor necrosis factor*
TriFC	*tripartite fluorescence complementation*
TVN	*tubovesicular network*
U	*units*
V	*volt*
var	*variable*
VLP	*virus-like particle*
VPS	*vacuolar protein sorting*
WHO	*World Health Organization*
wt	*wild-type*
XA	*xanthurenic acid*
YFP	*yellow fluorescent protein*

Abbreviations - Amino acids

Ala	A	*alanine*	Leu	L	*leucine*
Arg	R	*arginine*	Lys	K	*lysine*
Asn	N	*asparagine*	Met	M	*methionine*
Asp	D	*aspartic acid*	Phe	F	*phenylalanine*
Cys	C	*cysteine*	Pro	P	*proline*
Gln	Q	*glutamine*	Ser	S	*serine*
Glu	E	*glutamic acid*	Thr	T	*threonine*
Gly	G	*glycine*	Trp	W	*tryptophan*
His	H	*hstidine*	Tyr	Y	*tyrosine*
Ile	I	*isoleucine*	Val	V	*valine*

Abbreviations- Nucleic acids

A	*adenine*
G	*guanine*
C	*cytosine*
T	*thymine*

CHAPTER 1 INTRODUCTION

1.1 Malaria

Almost 5,000 years ago, a disease with symptoms of (what we today know as) malaria was described, and ancient cultures believed for a long time that this disease was caused by miasmata (ancient Greek for pollution, defilement) that are mists or vapours consisting of poisonous matter. Malaria was called "marsh fevers", "intermittent fevers", "quartan fevers" or "tertian fevers" for more than 1,500 years before finally the term "malaria" (Italian: *mala aria*, bad air) was used. This term was introduced into England in the 18th century. It was known at that time that black deposits can be found in the organs of patients that died from malaria. In 1846 Heinrich Meckel diagnosed a dead malaria patient and found brown pigmented particles within capillaries of the brain and spleen. Although he did not associate these particles with malaria, he concluded that it was a blood product. Erroneously he assumed that this pigment was melatonin. Later, Rudolf Virchow concluded that the pigment was haematin crystals (or hemozoin, see 1.2.1.3) [Cox, 2010; Hempelman & Krafts, 2013].

In 1880 the causative agent of malaria was finally discovered by Charles L. A. Laveran. Examining the blood of patients suffering from malaria of different intensity, Laveran found that a common element was the presence of pigmented granules in the blood of all patients, which was in accordance with Meckel. Laveran observed pigmented spherical bodies undergoing exflagellation that moved quickly. It turned out later that he observed male gametocytes (see 1.2.1.4) as well as all erythrocytic stages (see 1.2.1.3) of a protozoan parasite that he named *Oscillaria malariae,* which was later named *Plasmodium* [Cox, 2010; Hempelman & Krafts, 2013].

By feeding female *Anopheles* mosquitoes with blood from a malaria patient, Ronald Ross discovered in 1897 pigmented bodies in the stomach wall of the mosquitoes. Knowing that mosquitoes are not able to produce haemozoin, he concluded that the pigment must have been related to malaria [Hempelman & Krafts, 2013].

1.1.1 Epidemiology and transmission

Although the number of cases per 1,000 population was reduced from 71 to 57 between the year 2010 and 2018, more than three billion people are currently at risk of being infected with malaria, with an estimated 228 million cases and 405,000 deaths (≈ 0.2 %) in 2018. The most vulnerable group affected by malaria are children under the age of five. In 2018, about 272,000 children died of malaria, which accounts for 67 % of all malaria deaths worldwide. Most malaria cases (93 %) are reported in the African Region (AFR) (213 million cases), followed by 3.4 % of cases in the South-East Asia Region (SEAR) and 2.1 % in the Eastern Mediterranean region (EMR) [WHO, 2019]. *P. falciparum*, the most prevalent malaria parasite, accounts for 99.7 % of estimated cases in the AFR, 50 % in the SEAR and 71 % in the EMR. *P. vivax* accounts for 3.3 % of global malaria cases and is the predominant malaria parasite in the Americas region accounting for 75 % of malaria cases [WHO, 2019].

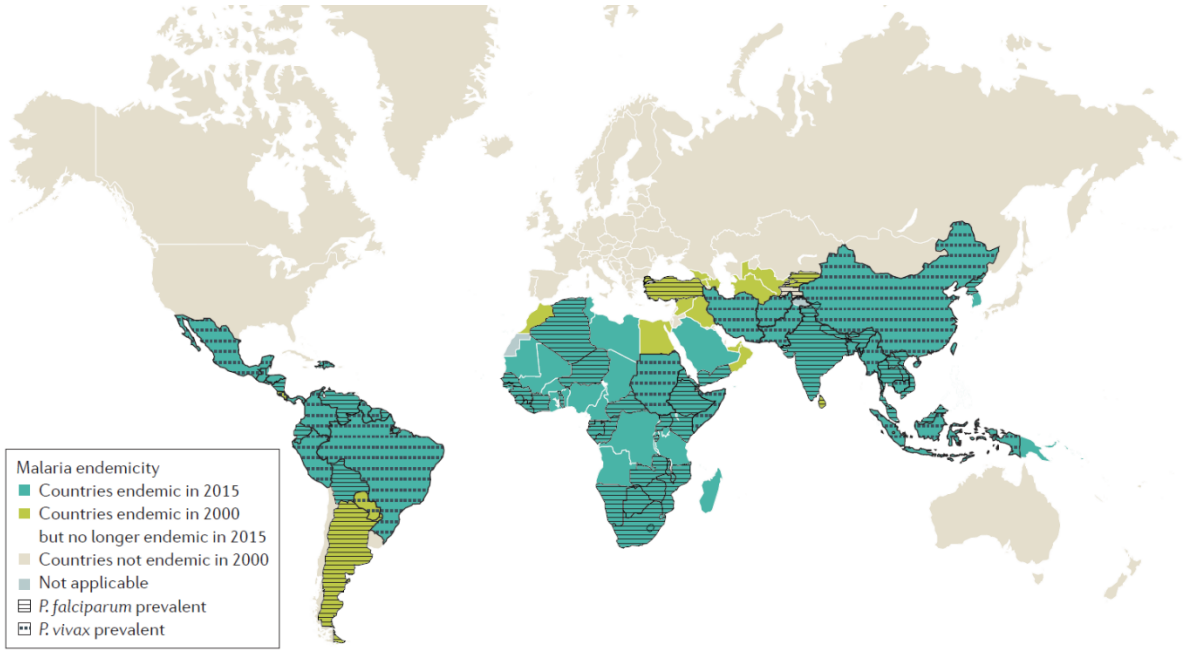

Fig. 1.1 | Map of malaria-endemic regions. *P. falciparum* is found in hot tropical areas, as its gametocytes require 10 to 18 days at a temperature of > 21 °C to mate and mature into infectious sporozoites. *P. falciparum* is temperature-sensitive, as sporozoite maturation is slowed down at lower temperatures. If the mosquito dies before sporozoite maturation is completed, the parasites perish. *P. vivax* sporogony can take place at 16 °C, while this parasite propagates at subtropical regions too. (Adopted from [Phillips *et al.*, 2017].)

The transmission of malaria is restricted to tropical and subtropical regions that support development of the sexual stage of the parasite (Fig. 1.1) and depends on female *Anopheles* mosquitoes as vector. About 70 *Anopheles* mosquito species are competent vectors to transmit human malaria. Globally, 41 species are dominant vector species. The dominant vector species in the AFR are *An. gambiae*, *An. arabiensis*, *An. merus* and *An. melas*, which all belong to the *An. gambiae* Giles species complex. *An. funestus* is another important vector which is co-dominant with the *An. gambiae* complex species [Hay *et al.*, 2010; Sinka *et al.*, 2010, 2012]. The high transmission rates in sub-Saharan Africa are probably due to preferential indoor feed behaviour and anthroposophily of *An. gambiae* complex species [Tirados *et al.*, 2006].

To become infectious to other individuals, the parasite developed a complex life cycle within the mosquito and its vertebrate host (see 1.2.1). Within the mosquito, parasite progression through the different maturation and proliferation stages depends on the ambient temperature and life span of the mosquito. If the temperature falls below 18 °C, the transmission becomes much less likely, and at temperatures below 16 °C parasite development ceases completely [Mitzmain, 1917; Noden *et al.*, 1995; Sachs & Malaney 2002; Waite & Suh *et al.*, 2019]. Transmission is further reduced as many mosquitoes stop biting activity at low temperatures [Paaijmans *et al.*, 2013].

Malaria parasite transmission intensity varies geographically in endemic countries since it is affected by temperature, humidity, and available surface water. Arid environments with low ambient humidity affect egg and adult vector survival negatively. The successful transmission of parasites depends on the ability of the adult vector to survive long enough to ensure a minimum population abundance. It is therefore dependent on the resistance of mosquitoes to arid conditions, which is species-specific [Gray & Bradley, 2005; Guerra *et al.* 2008].

1.1.2 Apicomplexa

The large phylum of Apicomplexa comprises alveolates with a parasitic lifestyle. Alveolates are defined by flattened vesicles (alveoli) underneath the plasma membrane. Most Alveolates fall into one of the following groups: ciliates (*i.a. Paramecium*), dinoflagellates, chromerids (*Chromera* and *Vitrella*), colpodellids and the obligate parasitic apicomplexans (*i.a. Toxoplasma*, *Plasmodium*) [Cavalier-Smith, 1993; Templeton & Pain, 2016].

More than 6,000 apicomplexan species are known to date and it is expected that about 1.2 million species exist [Adl *et al.*, 2007]. Apicomplexa evolved from a photosynthetically active flagellate ancestor, and most apicomplexans contain an apicoplast, a modified, non-photosynthetic plastid [Botté & Yamaryo-Botté, 2018; Salomaki & Kolisko, 2019]. However, the name Apicomplexa derived from the two Latin words *apex* (top) and *complexus* (enfold/enclose) which refers to a set of organelles located at the apical pole of the parasite, the apex, which is a unifying morphological feature of this phylum. Apical complex organelles are microtubules, polar rings, and secretory organelles (rhoptries, micronemes and dense granules), which will be explained in another chapter (see 1.2.2.2) [Votýpka *et al.*, 2017].

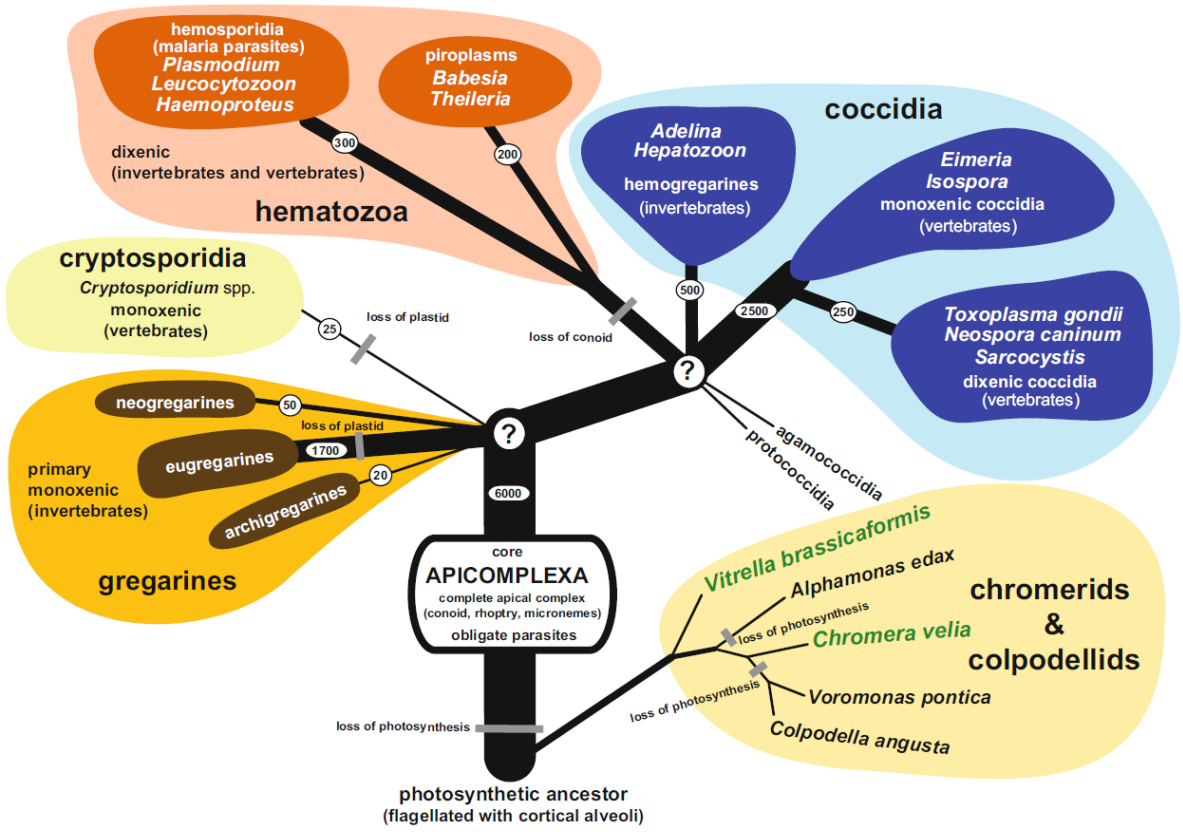

Fig. 1.2 | Hypothetical tree of life of the Apicomplexa. Relationships are derived from morphology, biology, and molecular evolutionary studies. Question marks denote uncertainty of key radiation events. Branch thickness and circles indicate the relative number of existing species. (Adopted from [Votypka *et al.*, 2017].)

The Apicomplexa phylum can be subdivided primarily into Hematozoa, Coccidia (*i.a. Eimeria, Toxoplasma*), Gregarinasina (*i.a. Nematocystis, Gregarina*) and Cryptosporidium (*Cryptosporidium*) [Adl *et al.*, 2012]. Apicomplexans are closely related to marine and freshwater protists such as *Chromera*, *Vitrella* and *Colpodella* (Fig. 1.2). While gregarines attach extracellularly to the host cell via the apical end, the host cell envelops

cryptosporidians with flat membrane folds. A modified interface, the feeder organelle, is thereby the only contact zone between host and parasitic cell. Coccidians and hematozoans on the other hand are intracellular parasites. Hematozoans are subdivided into *Piroplasmida* (*i.a*. *Babesia*, *Theileria*) and *Haemosporidia* (*i.a. Plasmodium*). Genera of the latter are marked by merogony/schizogony (see 1.2.1.3) in intermediate vertebrate hosts and sporogony (see 1.2.1) in blood-feeding dipteran vectors [Votýpka *et al.*, 2017].

1.1.2.1 Human infecting Plasmodium species

Approximately 250 *Plasmodium* species parasitize mammals, birds and reptiles, and presumably all primate malaria causing species are transmitted only by *Anopheles* mosquitoes. It is reported that more than thirty *Plasmodium* species infect non-human primates [Ramasamy, 2014; Sharp *et al.*, 2020], but only six *Plasmodium* species are recognized to cause malaria in humans: *Plasmodium falciparum, P. vivax, P. ovale wallickeri, P. ovale curtisi, P. malariae* and *P. knowlesi* [Milner, 2018] (Fig. 1.3).

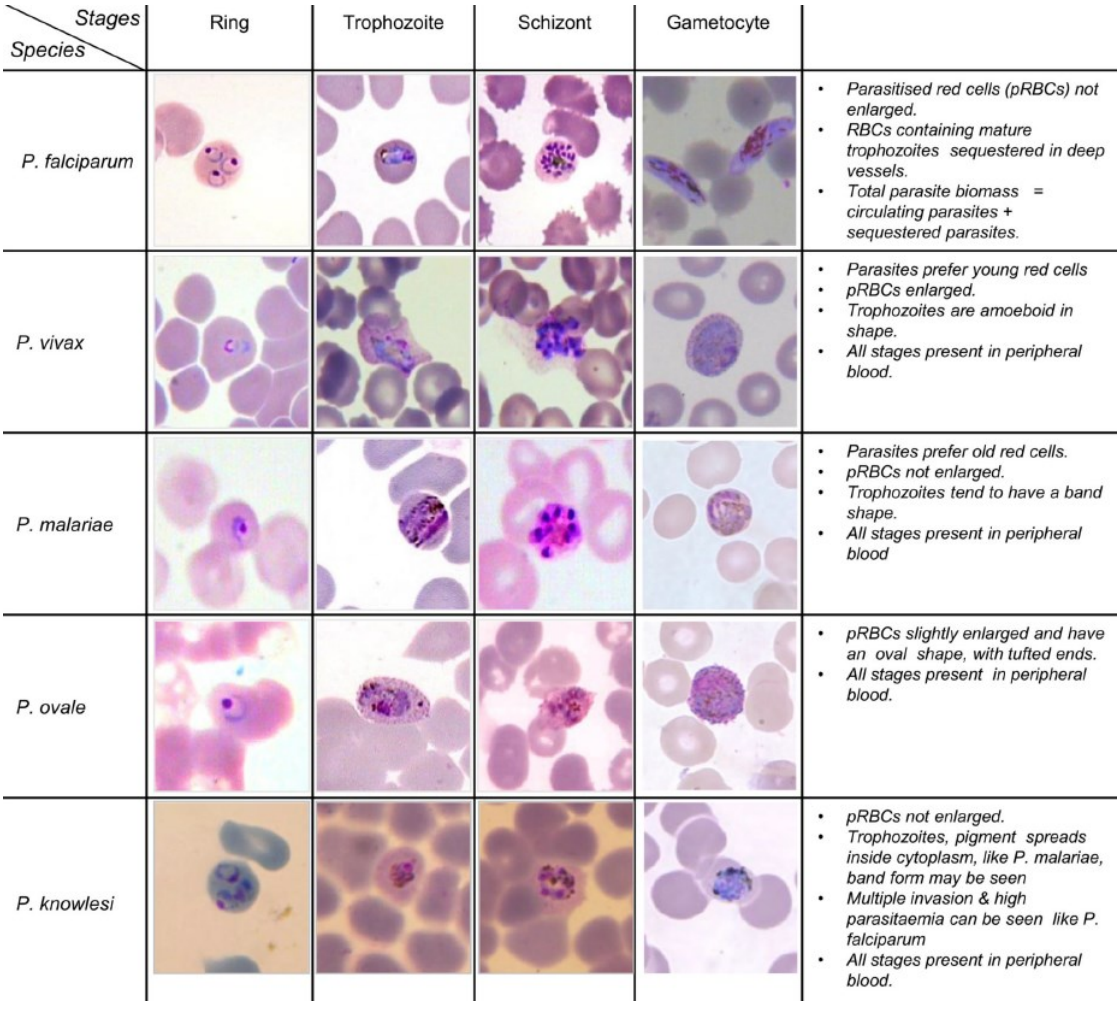

Fig. 1.3 | Giemsa-stained blood smears of five different human infecting *Plasmodium* species. Species-specific characteristics are shown at the right. *P. ovale* denotes the species *P. ovale wallickeri and P. ovale curtisi.* (Adopted from [Poostchi *et al.*, 2018].)

P. falciparum, responsible for the most casualties, causes the most severe form of human malaria. Unlike any other human-infecting *Plasmodium* species, *P. falciparum* has the ability to bind at epithelial cells in blood vessels and

capillaries during the erythrocytic stage (see 1.1.3). This leads to the sequestering of parasites in organs like the liver, spleen and brain, which contributes to the high virulence of this species [Greenwood *et al.*, 2008]. *Plasmodium falciparum* was formerly considered to be strictly restricted to humans, but it is able to infect bonobos, chimpanzees and gorillas. Those apes are therefore likely to be reservoirs for this malaria-causing agent [Prugnolle & Durand *et al.*, 2010]. The minimum temperature for *P. falciparum* survival is 18 °C, whereas the maximum temperature is 40 °C. The optimum range for its development is between 25 °C and 30 °C [Rossati *et al.*, 2016]. Fevers and chills occur every third day (tertian fever) in *P. falciparum* malaria [Garcia *et al.*, 2001].

P. vivax is the second major cause of human malaria and is the most geographically widespread malaria parasite outside of Africa. The sexual cycle (sporogony) of *P. vivax* within the vector can be accomplished at lower temperatures (as low as 16 °C) than those required for *P. falciparum,* explaining its broader distribution. Hence, *P. vivax* malaria occurs outside tropical and subtropical areas [Chu & White, 2016; Greenwood *et al*. 2008]. *P. vivax* adapted to humans by host switching from Asian macaques [Mu *et al.*, 2005]. *P. vivax* malaria prevalence is common in tropical areas outside Africa, as Africans lack the Duffy blood group antigen, a necessary receptor for *P. vivax* [Howes *et al.*, 2011; Miller *et al.*, 1976]. However, the requirement of the Duffy antigen was questioned when *P. vivax* malaria was also observed in Duffy negative Malagasy people [Ménard *et al.* 2010]. *P. vivax* preferentially invades reticulocytes, which are immature red blood cells (RBC) representing 1-2 % of circulating RBCs [Moreno-Pérez *et al*., 2013]. *P. vivax* forms liver stages (hypnozoites) that can lie dormant for weeks, months and even years. Hypnozoites are responsible for malaria relapse [Chu & White, 2016] and the hypnozoite reservoir is the cause for delays in diagnosis and ineffective treatment, contributing to the morbidity and mortality of *P. vivax* malaria [Baird, 2013]. Because of its tendency to relapse after the clearing of the primary infection, it is more difficult to control *P. vivax* than *P. falciparum*. How relapse is triggered is still not understood in detail, but it is assumed that hypnozoites are activated by external stimuli, such as malaria or other infectious diseases, which cause febrile illness [Shanks & White, 2013; White, 2011]. Fevers and chills occur every two days in *P. vivax* malaria [Garcia *et al.*, 2001].

The fact that *P. ovale* shares similarities with *P. vivax* makes it difficult to distinguish both species by examination of Giemsa-stained peripheral blood smears. Like *P. vivax*, *P. ovale* infects reticulocytes, causing malaria characterized by tertian fever [Collins & Jeffery, 2005], and as far as we know, humans are the only natural hosts of *P. ovale* [Rossati *et al.*, 2016]. Of the human infecting *Plasmodium* species, only *P. vivax* and *P. ovale* form hypnozoites [Chu & White, 2016]. *P. ovale* was described as one species at first, but sequence analysis did show that *P. ovale curtisi* and *P. ovale wallikeri* are actually two species, since they do not show sexual recombination [Sutherland *et al*., 2010].

P. malariae can persist for decades as an asymptomatic blood stage infection without forming hypnozoites. The erythrocytic life cycle (72 h) is considerably longer compared to the other human infecting *Plasmodium* species, and the number of merozoites that are produced with every schizont rupture is lower. Therefore, the overall parasitemias are lower in human hosts compared to hosts infected with other malaria types [Collins & Jeffrey, 2007; Greenwood *et al*. 2008]. *P. malariae* causes the mildest but also the most persistent form of malaria and is

associated with nephrotic syndrome. Manifestation of *P. malariae* infection is common in children but not adults [Bartoloni & Zammarachi, 2012]. Fevers and chills occur every four days in *P. malaria* malaria [Garcia *et al.*, 2001].

P. knowlesi, which has the shortest erythrocytic cycle (24 h) of all human malaria parasites, is a simian parasite infecting macaque monkeys but was recognized as an important cause of human disease. However, there is no evidence that this parasite is transmitted from human to human like any of the aforementioned species. Instead, it is zoonotic in Malaysia and other areas of Southeast Asia [Ahmed & Cox-Singh, 2015; Singh & Daneshvar, 2013]. Due to morphological similarities between *P. knowlesi* and *P. malariae* during late blood stages (see Fig. 1.3), *P. knowlesi* infection is often misdiagnosed as *P. malariae* infection [Singh *et al.*, 2004]. *P. knowlesi* malaria has a clinical profile that is similar to *P. falciparum* and *P. vivax* infections [Daneshwar *et al.* 2009].

1.1.3 Pathophysiology of *P. falciparum*

In most cases of parasite transmission, a female anopheline mosquito transmits the parasite, but this blood-borne transmission can also occur through blood transfusions, organ transplantation or needle-sharing among drug addicts. Congenital and accidental nosocomial transmission might be possible as well [Bartoloni & Zammarachi, 2012; Verra & Angheben *et al.*, 2018]. Mosquito-borne transmission requires sporozoites that are injected into subcutaneous capillaries. Within about 45 minutes after the injection, sporozoites migrate to hepatocytes, where they multiply by asexual reproduction to a schizont that contains thousands of merozoites (see 1.2.1.2). Upon rupture of schizonts, the merozoites are released into the bloodstream. The hepatic schizogony lasts on average between 5.5 days for *P. falciparum* and 15 days for the slowest replicating human-infecting species *P. malariae* [Hoffman *et al.*, 2011]. Since only a few hepatocytes are infected, the hepatic schizogony is asymptomatic. Released merozoites then invade RBCs and undergo asexual erythrocytic schizogony to multiply and release new merozoites (see 1.2.1.3). The rupture of schizonts releases malaria parasites as well as erythrocytic material into the bloodstream, which induces the pathophysiological processes of malaria. Cytokine cascade activation is triggered and is responsible for many of the symptoms [Bartoloni & Zammarachi, 2012].

In individuals that have not encountered Plasmodium before, the median pre-patent period (time of injection of sporozoites to detection of merozoites in the blood) ranges between five to ten days. The incubation period is defined as the time from infection to the onset of symptoms. The duration of the incubation period depends of different factors such as: a) the vector species, b) the mode of parasite transmission, c) the immune status of the host, d) chemoprophylactic use of antimalarial drugs and e) the number of parasites that were transmitted [Bartoloni & Zammarachi, 2012; Trampuz *et al.* 2003]. The incubation period of malaria varies between different *Plasmodium* species. *P. falciparum* and *P. vivax* malaria normally show an incubation period of about two weeks, whereas onset of symptoms in *P. malariae* malaria occurs after forty days or more [Bartoloni & Zammarachi, 2012]. Since the adaptive immune system has the ability to cope with malaria-causing agents to some extent, most infections worldwide are clinically silent. Infection with *P. falciparum* results in an uncomplicated febrile disease in which peaks of parasitemia are accompanied by episodes of fever. The infection is controlled and finally eliminated by the host's immune defences. However, in non-immune individuals, infections become clinically more obvious, partially severe, and life-threatening. While *P. falciparum* causes almost all severe and live

threatening complications, *P. vivax, P. ovale spp*. and *P. malariae* rarely lead to such severe effects [Schofield & Grau, 2005; Miller *et al*. 2013]

Children and travellers from non-endemic areas are at high risk of suffering severe complications, as they have not been previously exposed to malaria. Severe complications are anaemia, renal failure, bleeding, pulmonary oedema, and cerebral malaria (CM). The most common metabolic complications of severe malaria are acidosis and hypoglycaemia. Any single complication can progress rapidly and lead to death within hours or days and in many patients several complications occur at the same time, contributing synergistically to the life-threatening effect of this disease [Tizifa *et al.*, 2018; Trampuz *et al.*, 2003].

The first symptoms of malaria are the same for all malaria species. Symptoms are nonspecific and resemble a flu-like syndrome (headache, chills, nausea), whereas the hallmark of all types of malaria is fever, which is induced by fever-inducing agents called pyrogens that signal to the thermoregulatory regions of the hypothalamus to induce a rise in body temperature. The fever is caused by the release of parasite antigens (toxins) upon destruction of parasitized RBCs during schizogony, in a process called hemolysis. Malaria hemozoin and glycosyl-phosphatidylinositol (GPI) are two toxins that can be recognized by toll-like receptors (TLRs), which are expressed on the surface of macrophages. Recognition of malarial GPI by macrophage TLR2 induces cytokine TNF-α production leading to a fever-inducing signalling cascade [Oakley *et al*., 2011].

In case of progression to fatal CM, the mortality ranges between 15-20 %. The molecular mechanisms for CM are not fully understood, but there is evidence that the binding of parasitized RBCs to the endothelium (cytoadherence) and to other RBCs (sequestration) causes blocking of blood vessels that leads to a reduction in blood flow causing inflammation [Seydel *et al*., 2015; Wassmer *et al*., 2015]. The binding of infected red blood cells (iRBCs) to the endothelium is a unique feature of *P. falciparum* that is due to the modification of RBC membrane (RBCM) by the parasite. Adherence to the endothelium of more progressed stages is the reason why only ring stages can be found in circulating blood. The adherence is mediated by protuberances (so-called knobs, see 1.2.1.3) that are in contact with endothelial cells, preventing the parasitized cell from clearance and destruction in the spleen. Various endothelial cells in organs like the brain, kidney, liver, lung, placenta, and subcutaneous tissues express variable host cell receptors. *P. falciparum* erythrocyte membrane protein 1 family (*Pf*EMP1), which is located at the knob surface, mediates the adherence to the various receptors and sequestering of iRBCs to the endothelium [Miller *et al*. 2013; Milner, 2018; White *et al*., 2014].

1.1.4 Malaria control strategies

In 2018, 49 countries reported fewer than 10,000 indigenous cases and 27 countries reported fewer than 100 indigenous malaria cases. This shows that malaria eradication is within reach, but despite the progress made in malaria reduction, eradication of malaria still remains a challenging task [WHO, 2019].

1.1.4.1 Vector control

Vector control comprises measures that aim at limiting the ability of a vector to transmit a disease in endemic areas. Transmission depends on the capacity of a local vector to transmit malaria, which depends on *i.a*. population size, biting habits and longevity to favour the period of sporogony. Those parameters are affected by climate conditions, local ecology as well as the behaviour of humans and vectors. The objective of vector control is the reduction of the vectoral capacity below a critical threshold that is needed to maintain malaria transmission [Smith Gueye *et al.*, 2016]. Approximately US$ 2.7 billion was globally invested by governments of endemic countries and their international partners to control and eradicate malaria in 2018. The most used prevention methods are insecticide-treated mosquito nets (ITNs) and indoor residual spraying (IRS) with insecticides [WHO, 2019]. The most important interventions targeting vector transmission in Africa are ITNs and IRS that have reduced the prevalence of *P. falciparum* by 68 % and 13 %, respectively, between 2000 and 2015 [Bhatt *et al*., 2015].

The discovery of the insecticidal properties of dichlorodiphenyltrichloroethane (DDT) in 1939 provided a powerful new tool for interrupting transmission. DDT was used in areal spraying campaigns as well as for IRS during the malaria eradication programme from 1957 to 1969, which did not include tropical Africa [Enayati & Hemingway, 2010]. However, vector resistance to DDT, which is conferred by over-expression of glutathione S-transferases (GSTs) [Prapanthadara *et al.*, 1995], occurred less than two years after the introduction of DDT and is now common. Interestingly, in some high transmission areas where DDT was used for several decades, mosquitoes remain sensitive towards DDT [Tizifa *et al*., 2018]. Nowadays DDT is banned by some countries because of its environmental hazards but still used in others to battle malaria, and DDT is still recommended by the WHO for indoor spraying under specific conditions [Enayati & Hemingway, 2010].

ITNs include nets treated with insecticides that are active up to 12 months and long-lasting insecticidal nets (LLINs) with insecticides lasting for up to three years. The use of ITNs treated with pyrethroid insecticides, the only licensed insecticide class that is approved for use on ITNs, is simpler than IRS. [Enayati & Hemingway, 2010; Coleman *et al.*, 2017]. However, cytochrome P450-mediated resistance to pyrethroid insecticides in *Anopheles* mosquito vectors is widespread throughout southern Africa [Weedall *et al.*, 2019]. A review examining data sets from 1955 to 2016 from 71 malaria-endemic countries detected a global rise in insecticide resistance. Resistance resulted in the reduced efficacy of ITNs as well as IRS [Strode *et al.*, 2014].

One of the oldest tools to fight malaria is larval source management (LSM) as a means to control potential breeding sites of mosquitoes. LSM comprises methods such as habitat modification (surface water drainage, land reclamation and filling), biological control (introduction of *e.g.* predatory fish) and larviciding (application of

biological/chemical insecticides to water bodies), which is the most commonly used LSM [Fillinger & Lindsay, 2011].

Access to sugar sources (such as fruits or nectar) strongly affects vector potential [Gu *et al.*, 2011]. Sugar feeding with an attractive toxic sugar bait (ATSB) is a cheap and simple approach to kill female and male mosquitoes that seek essential sugar sources. The ATSB method uses fruit or flower scent as attractant, a sugar solution as feeding stimulant, and an oral toxin, which is usually spinosad or boric acid. ATSB has the potential to reduce vector capacity, dramatically resulting in transmission levels near zero [Beier *et al.*, 2012; Müller *et al.*, 2010].

Swarm sprays are another method to reduce vector competence. This method makes use of the stable location of *Anopheles* mating swarms (mostly consisting of males) [Manoukis *et al.*, 2009]. In a field trial in Burkina Faso, 300 swarms were identified and sprayed with aerosols containing a mixture of carbamate and pyrethroid with the result that the mass killing of swarming males led to an 80 % decrease in population size [Sawadogo *et al.*, 2017]. This study demonstrated that targeting primarily male rather than female mosquitoes drastically reduces the mosquito population.

A promising tool to eradicate malaria is the gene-drive system. Gene-drive enables transgene inheritance to the offspring with a higher probability than the natural 50 %. Recently, the CRISPR/Cas9 gene-drive was applied to alter differentiation of the *An. gambiae* sex ratio. Within few generations, female mosquitoes showed complete sterility [Hammond *et al.*, 2016; Kyrou *et al.*, 2018]. Although this method is highly efficient, it is vigorously debated whether transgenic organisms should be released into nature in order to eradicate a species [Collins, 2018].

1.1.4.2 Antimalarial drugs

Joannes Lancisius, the physician of three popes, suggested the use of Peruvian (*Cinchona*) tree bark powder. Crude extracts from this bark for the treatment of malaria have been used since the early 16th century. Francesco Torti showed in 1756 that only intermittent fevers, characteristic of malaria, could be cured with extracts of Peruvian bark that, as it was later discovered, contain quinine, which became the standard drug for curing malaria after its chemical synthesis became feasible [Hempelmann & Krafts 2013]. During the Indochina Wars, the Chinese Communist Party assigned more than 600 scientists to research for new antimalarial drugs. In 1970, in the course of this programme, the Chinese scientist, and later Nobel prize laureate, Tu Youyou extracted “qinghaosu” from the annual mugwort (*Artemisia annua*) that has been used in Chinese herbal medicine for over 2,000 years [Burns, 2008]. The isolated compound was later named artemisinin and is the basis for today’s artemisinin combination therapies (ACTs), which are currently the recommended treatment for malaria [Miller *et al.*, 2013].

In ACTs, artemisinin, or a derivative (*e.g.* dihydroartemisinin, artesunate) is combined with a partner drug, such as amodiaquine, mefloquine or piperaquine. As the partner drugs have a longer half-life in the bloodstream, they are supposed to inhibit the development of resistance to the artemisinins. The artimisinins are highly potent and reduce parasitemia fast but have a short half-life. The long-lasting but less potent partner drug is needed to kill the remaining parasites [Fairhurst *et al.*, 2012; Miller *et al.*, 2013]. The first ACT to conform with international GMP

standards was artemether-lumefantrine. Artemether-lumefantrine, DHA-piperaquine, artesunate-amodiaquine, artesunate-mefloquine and artesunate-sulfadoxine-pyrimethamine are currently the most widely used combinations [Premji, 2009]. Based on recent reviews [Ashley & Phyo, 2018; Phillips et al., 2017; Wadi *et al.*, 2019; Wicht *et al.*, 2020], Fig. 1.4 shows common antimalarials drugs and some in development or under investigation as well as their site of action within the malaria parasite [Greenwood *et al.*, 2008].

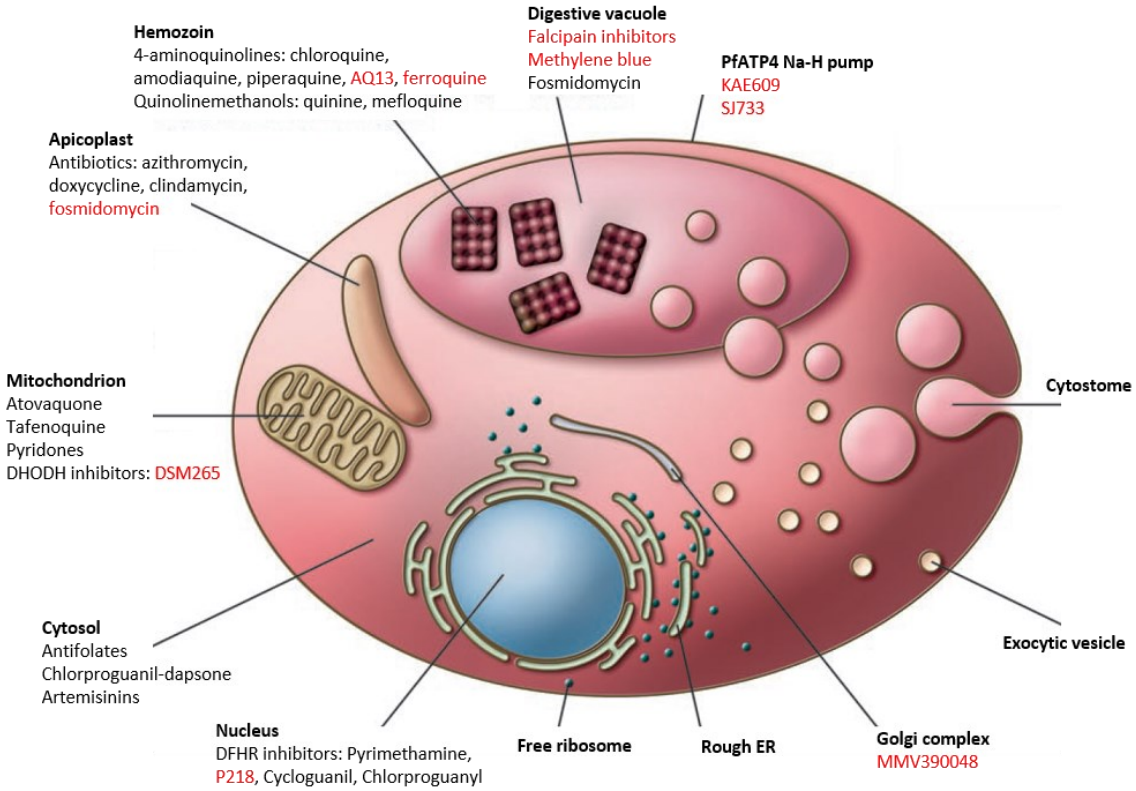

Fig. 1.4 | Antimalarial drugs and their site of action in the parasite. Antimalarial drugs mediate their effects by disrupting metabolic pathways in different subcellular organelles or the cytosol. The 4-aminoquinolines concentrate inside the acidic digestive vacuole (food vacuole) where they interfere with heme to hemozoin detoxification (see 1.2.1.3). Falcipain inhibitors interfere with hemoglobin degradation. Methylene blue inhibits glutathione reductase. Fosmidomycin disrupts digestive vacuole integrity and inhibits isoprenoid synthesis in the chloroplast-like apicoplast. Antibiotics inhibit translation in the apicoplast, resulting in a delayed death of progeny. Atovaquone and DSM625 interfere with the mitochondrial electron transport chain. MMV390048 dysregulates intracellular signalling and trafficking. Antifolates disrupt *de novo* biosynthesis of folate within the cytosol. The endoperoxide artemisinin and its derivatives cause oxidative degradation of membrane phospholipids and down-regulation of antioxidant genes. DHFR inhibitors impede nucleic acid metabolism. Compounds in red are still in development. (Modified from [Greenwood *et al.*, 2008].)

In five countries in Southeast Asia, parasite resistance to ACT has occurred, and the spread of resistance to the Indian subcontinent or to Africa could have very severe consequences [Hemingway *et al.*, 2016]. Although complete non-response to artemisinin treatment is not described to date, resistance of *P. falciparum* to artemisinin has increased steadily since 2008, which may have been due to artesunate monotherapy or to falsified or substandard drugs. Resistance to artemisinin results clinically in a delayed clearance of parasites [Ashley & Phyo, 2018]. Molecular markers conferring resistance to artemisinin derivatives were reported for the kelch gene on chromosome 13 of the parasite [Ariey *et al.*, 2014]. In Cambodia, where resistance occurred, the situation is

serious, as ACT treatment using DHA-piperaquine reverted to artesunate-mefloquine, which was replaced by DHA-piperaquine in 2008 because of the emergence of resistance [Ashley & Phyo, 2018]. Small numbers of parasites resistant to artemisinin were found in India and the Americas [Chenet *et al.*, 2016; Mishra *et al.*, 2016], whereas in Africa resistance is not established [Ménard *et al.*, 2016] although *in vitro* resistance was recently reported [Uwimana & Legrand *et al.*, 2020]. Emerging drug resistance requires the identification of new compounds for the treatment of malaria. Triple ACTs comprising standard ACT together with another antimalarial drug are currently being evaluated [Ashley & Phyo, 2018].

In order to interrupt transmission of the parasite, transmission-blocking drugs (TBDs) that interfere with gametocyte development (see 1.2.1.4) are crucial. Gametocytes are an attractive although "altruistic" drug target, as their number within the bloodstream is significantly lower than the number of merozoites, forming a bottleneck stage within the life cycle [Smith *et al.*, 2014], but play no role in the clinical manifestation. TBDs are considered as altruistic, as these drugs do not reduce the number of clinically important merozoites in the patient but inhibit transmission of gametocytes to the vector and thus other humans.
Primaquine is the only TBD with gametocytocidal activity against mature gametocytes that is also recommended by the WHO to be used with ACT. Furthermore, primaquine is the only drug available for preventing recurrent attacks (relapses) of *P. vivax* and *P. ovale*. However, due to its hemolytic toxicity in patients with a deficiency of glucose-6-phosphate-dehydrogenase (G6PD), it is not widely used [Baird, 2013; Wadi *et al.*, 2019].

1.1.4.3 Vaccine development

Malaria vaccine development began with studies in mice using irradiated sporozoites [Nussenzweig *et al.*, 1967]. Fifty years later there is still no licenced vaccine available, which reflects the technical difficulties to create a vaccine against this complex eukaryotic parasite. RTS/S (Mosquirix) is currently the most extensively tested vaccine against *P. falciparum* malaria [Draper *et al.*, 2018]. RTS/S induces immune responses against *P. falciparum* circumsporozoite protein (*Pf*CSP), which covers the surface of infecting sporozoites (see 1.2.1.2). This vaccine was designed as a virus-like particle (VLP) comprising parts of a central repeat region and the C-terminal domain of *Pf*CSP fused to hepatitis B virus surface antigen. RTS/S was formulated with the AS01 adjuvant system from GlaxoSmithKline (to boost high antibody concentrations) and was shown to protect partially against malaria in clinical trials. The major limitation of RTS/S is the low level of antibodies only a few years after the vaccination. [Draper *et al.*, 2018; Leach *et al.*, 2011; RTS, 2015]. Although efficient to 35.9 % in the first year after vaccination, the efficacy of RTS/S dropped to 2.5 % in the fourth year, showing that the protection is of limited durability [Olotu *et al.*, 2016].

The vaccination with the highest efficacy to date makes use of immunization with radiation-attenuated sporozoites (RAS), which has been the first whole sporozoite vaccine tested in rodents and humans. RAS arrest in liver-stage development at random points, conferring protection in humans [Draper *et al.*, 2018]. Irradiation of sporozoites causes DNA damage but infectivity is preserved. The DNA damage blocks parasite replication after the hepatocyte is infected. This causes the parasite to die and the presentation of parasite antigens to the immune system [Vaughan & Kappe, 2017a]. The *P. falciparum* sporozoite vaccine (*Pf*SPZ Vaccine) had to be applied intravenously

to induce potent immunity in humans challenged with controlled human malaria infection (CHMI) [Mordmüller *et al.*, 2017; Seder & Chang *et al.*, 2013]. *Pf*SPZ has to be cryopreserved in liquid nitrogen to guarantee its effectiveness, a major complication for vaccination in settings with limited infrastructure. Nevertheless, unlike refrigerated vaccines, the liquid nitrogen vapor phase (LNVP) storage of *Pf*SPZ in containers is independent of electricity and therefore available in areas with insufficient electrical infrastructure [Richie *et al.* 2015].
Genetically attenuated sporozoites (GAS) are an alternative for the sporozoite challenge model. GAS contain genetic deletions that arrest parasite development during hepatocyte infection. Complete attenuation was observed with a *P. falciparum* early liver stage-arresting triple knockout GAP (*Pf*GAP3KO) that showed complete attenuation after the infection of hepatocytes. No breakthrough blood stage infection could be observed in a humanized mouse model [Mikolajczak *et al.*, 2014]. In a recent study, *Pf*GAP3KO was administered to human subjects through the bites of mosquitoes infected with *Pf*GAP3KO. No subject showed blood stage parasites and the subjects developed inhibitory antibodies to sporozoites [Kublin & Mikolajczak *et al.*, 2017]. Further clinical trials are being conducted to test the safety and efficacy of *Pf*GAP3KO formulas against homologous and heterologous CHMI [Vaughan & Kappe, 2017a].

Blood stage vaccines induce immune responses that limit parasite replication after liver exit. Most blood stage vaccines target proteins that are expressed on the surface of merozoites, while some of them focus on parasite proteins expressed on the surface of iRBCs. However, clinical phase II studies led to disappointing results [Frimpong *et al.*, 2018]. Except for the MSP3 vaccine that conferred short-term protection [Sirima *et al.*, 2011], no other blood stage antigen vaccine was able to confer potent immunity against malaria illness [Laurens, 2018].

Transmission-blocking vaccines (TBVs) exploit functional immunity against sexual stage proteins to decrease transmission [Frimpong *et al.*, 2018]. TBV candidate antigens for *P. falciparum* include the pre-fertilization proteins Pfs48/45 and Pfs230. These proteins are expressed on the surface of gametocyte stages. The post-fertilization proteins Pfs25 and Pfs28 expressed in zygotes and ookinetes are also TBV candidates [Laurens, 2018].

1.2 Biology of Plasmodium falciparum

1.2.1 Life cycle

Plasmodium spp. undergo a complex life cycle where sporogony in the *Anopheles* mosquito alternates with merogony in the vertebrate host. Depending on the stage, the formation of unique zoite forms allows for the invasion of different cell types in which the parasite resides. Upon mosquito blood feeding, *Plasmodium* sporozoites migrate via the bloodstream to the liver, where they infect hepatocytes to multiply exponentially ("liver stage"). The liver schizont ruptures and merozoites are released into the bloodstream where they infect RBCs ("blood stage") to multiply again. Some parasites develop into gametocytes ("sexual stage") that are taken up by a mosquito during blood feeding, completing the cycle as male and female gametes give rise to sporozoites (Fig. 1.5).

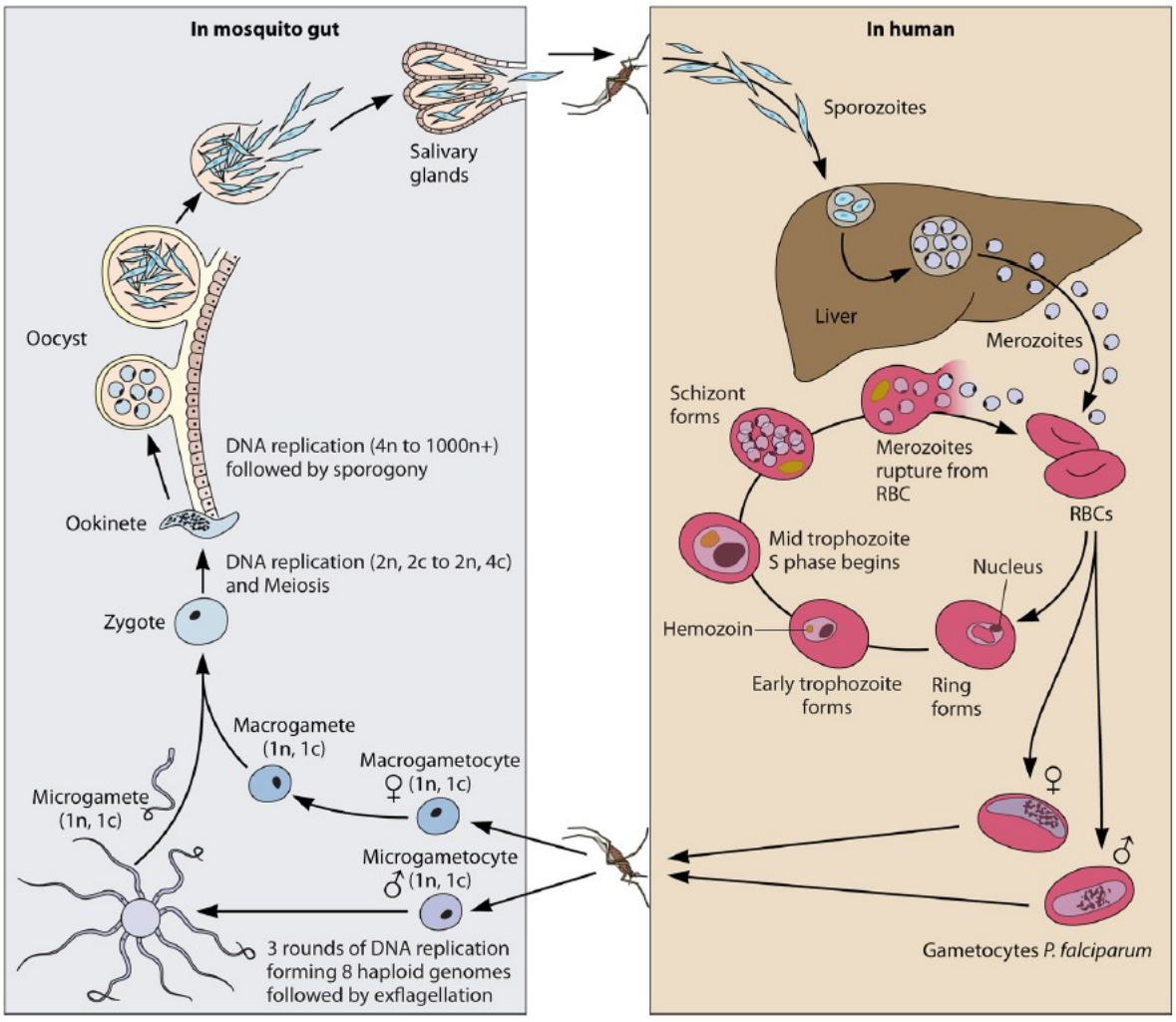

Fig. 1.5 | Life cycle of *Plasmodium falciparum* in the human body and the anopheline mosquito. The cycle begins with the injection of motile sporozoites into the human dermis by a female *Anopheles* mosquito. The sporozoites migrate to the liver to invade hepatocytes and multiply. After about a week, the liver schizont (merosome) releases thousands of merozoites into the bloodstream. Merozoites invade red blood cells and begin the asexual cycle. Some parasites develop into gametocytes that are taken up by a feeding mosquito in which they reproduce sexually by forming an ookinete and oocyst to finally give rise to thousands of sporozoites that migrate to the mosquito's salivary glands. (Adopted from [Lee *et al.*, 2014].)

1.2.1.1 Mosquito stage

Within 10-15 minutes of being taken up by a mosquito, gametocytes (see 1.2.1.4) differentiate into gametes in the mosquito midgut lumen in a process called gametogenesis. Activation of gametogenesis is promoted by the mosquito-derived tryptophan metabolite xanthurenic acid (XA) [Billker *et al.*, 1998; Garcia *et al.*, 1998] and a fall in temperature of > 5 °C [Roller & Desser, 1973; Sinden & Croll, 1975]. An additional signal reported to induce gametogenesis is an increase in pH from 7.4 to 8 [Sinden, 1983]. Whereas the female gametocyte forms a rounded female gamete, the male gametocyte undergoes three mitotic divisions that increase DNA content from haploid (1n) to octoploid (8n), producing eight motile (haploid) microgametes in a process named exflagellation [Sinden, 2015]. Male and female gametes egress from their host erythrocytes via the rupture of the parasitophorous plasma membrane (PVM) prior to the opening of the erythrocyte membrane (EM) [Guttery *et al.*, 2015].

Motile microgametes encounter female macrogametes and merge to produce diploid zygotes. The zygotes then develop into motile ookinetes that penetrate the mosquito midgut wall to differentiate into immotile oocysts. The oocyst differentiates into a sporoblast in which thousands of sporozoites are created by mitotic division that are then released into the hemocoel and migrate through the hemolymph into the mosquito's salivary glands. Sporozoites accumulate in the salivary cavities and are injected into the host as the biting mosquito ejects saliva with a small fraction of gland-residing sporozoites during blood feeding [Guttery *et al.*, 2015].

1.2.1.2 Liver stage

Sporozoites are 10-15 µm long and ≈ 1 µm in diameter and use gliding motility (≈ 1-2 µm/s) to penetrate the epithelial cell membrane during a bite of a blood-feeding mosquito. Sporozoites use *i.a.* an actin-myosin motor for substrate-dependent gliding as well as flexing, twisting, and turning motions to traverse epidermal cells and reach the bloodstream [Kappe *et al.*, 2004]. After a mosquito bite, it takes about two hours for a sporozoite to reach the hepatic capillary network (sinusoid) cavity through hepatic arteries [Sinnis & Coppi, 2007], where they attach to endothelial cells before invading a hepatocyte. Sporozoites either enter a hepatocyte through the space of discontinuous endothelial cells, or actively migrate through endothelial cells, or traverse through phagocytic Kupffer cells by rupturing their plasma membranes [Ishino *et al.*, 2004; Meis *et al.*, 1983; Pradel & Frevert, 2001]. Sporozoites express on their surface CSP, which conveys interaction to its receptor, heparan sulfate proteoglycan (HSPG) [Frevert *et al.*, 1993], located at the surface of hepatocytes. CSP-HSPG interaction signals to the parasite to actively invade the hepatocyte [Coppi *et al.*, 2007]. However, sporozoites migrate through multiple hepatocytes until they finally invade and settle in one [Vaughan & Kappe, 2017b]. Sporozoite migration to the sinusoid and hepatocyte infection is summarized in Fig. 1.6. Sporozoites that are injected into the dermis are in "migratory mode" and upon interaction with hepatocytes they convert to "invasive mode". One signal for this switch is the recognition of HSPG, which activates calcium-dependent protein kinase 6 (CDPK6) [Coppi *et al.*, 2007]. Other hepatocyte surface molecules required for infection are cluster of differentiation (CD81) and scavenger receptor B1 (SR-B1), which are recognized by the sporozoite in order to initiate the formation of a parasitophorous vacuole (PV) [Rodrigues, Hannus & Prudencio *et al.*, 2008]. Following hepatocyte infection, the *P. falciparum* sporozoite transforms into an exo-erythrocytic form (EEF), also called liver stage (LS), to give rise to up to 90,000 merozoites per hepatocyte [Vaughan *et al.*, 2012]. The merozoites are released into the bloodstream through the budding of merozoite-filled vesicles called merosomes [Sturm & Amino *et al.*, 2006].

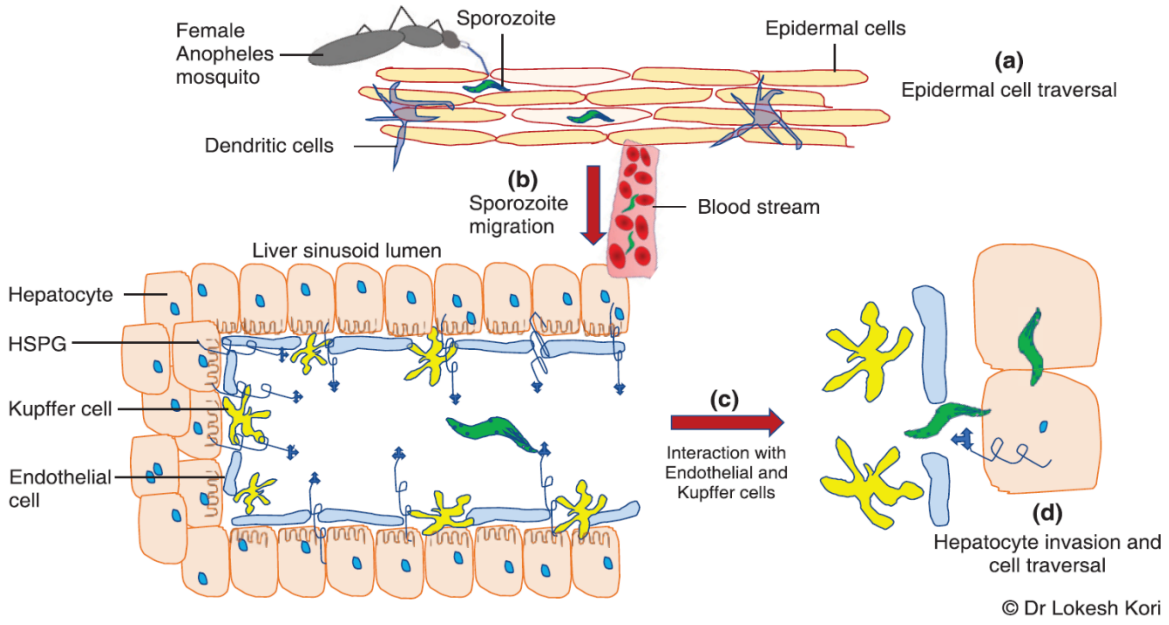

Fig. 1.6 | Schematic representation of pre-erythrocytic stages of a malaria sporozoite. (**a**) Entry of the sporozoite into dermal tissue followed by traversal to enter the bloodstream. (**b**) A sporozoite enters the liver sinusoid lumen by gliding motility out of the blood vessel. (**c**) The sporozoite escapes the endothelial and Kupffer cells to (**d**) invade hepatocytes and traverse among neighbouring hepatocytes. (Adopted from [Kori *et al.*, 2018].)

1.2.1.3 Blood stage

Following the invasion of an erythrocyte (see 1.2.2.3), the ring-stage parasite (enclosed by a PVM) resides in this terminally differentiated blood cell which lacks all organelles, including a nucleus and all endomembrane systems. To multiply within the erythrocyte, the parasite remodels its host cell to accommodate its needs, such as nutrition acquisition and cytoadherence. *P. falciparum* establishes various unusual biological processes to develop within this special host cell [Tilley *et al.*, 2011]. For instance, the parasite ingests small amounts of its host cell's cytoplasm using endocytic structures called cystostomes, which allows the parasite to metabolize hemoglobin. Hemoglobin digestion is processed in a specialized organelle known as the food vacuole [Abu Bakar *et al.*, 2010; Goldberg, 2005]. This allows the parasite to use hemoglobin-derived amino acids for protein synthesis. The toxic hematin, a by-product of hemoglobin digestion, is polymerized into a crystalline form called hemozoin, which is also known as malaria pigment [Pagola *et al.*, 2000]. Another feature of erythrocyte remodelling by the parasite is the establishment of a new permeability pathway (NPP) by inserting parasite-coded transporters into the membrane of the erythrocyte, which increases the permeability of the RBCM to allow for the importation of nutrients and the exportation of waste products [Alkhalil *et al.*, 2004; Gero & Wood, 1991; Staines *et al.*, 2000].

The asexual blood stage is cyclic and involves the differentiation of the invading merozoite into three morphologically distinct forms/stages: the ring, trophozoite and schizont stages [Boddey & Cowman, 2013]. The parasite undergoes three or four rounds of DNA synthesis, mitosis and nuclear division to produce a multi-nucleated syncytial schizont, and the last nuclei division is synchronized, which results in a schizont containing between 16 and 32 haploid merozoites (Fig. 1.7) [Gerald *et al.*, 2011].

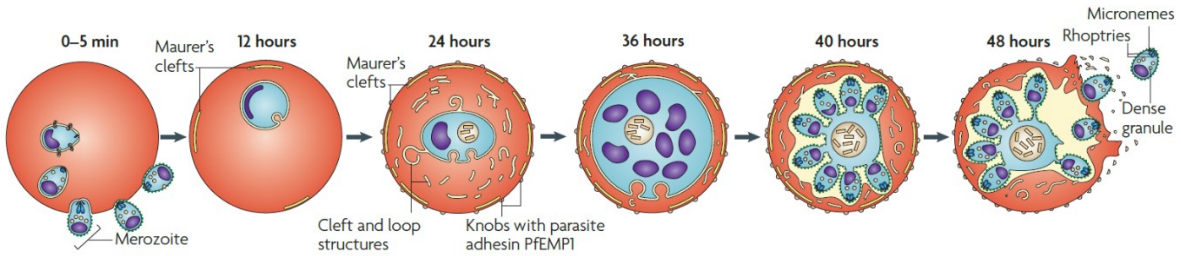

Fig. 1.7 | Different stages of *Plasmodium falciparum* development in human erythrocytes. A merozoite attaches and invades an RBC and develops within a parasitophorous vacuole (PV) through the ring (0-24 hpi), trophozoite (24-36 hpi) and schizont stages (40-48 hpi). In immature-stage parasites at > 24 hpi, Maurer's clefts and knobs occur. At about 48 hpi, the schizont ruptures to release 16-32 merozoites. (Adopted from [Maier *et al.*,2009].)

The rapid growth and proliferation of the intraerythrocytic parasite is supported by the catabolism of glucose as carbon and as an energy source via glycolysis [Salcedo-Sora *et al.*, 2014]. It has been shown that the metabolically active trophozoite stage that follows the initial ring stage consumes about six times more glucose than ring stage parasites [Shivapurkar *et al.*, 2018].

Successful exploitation of the intra-erythrocytic niche by the parasite requires the establishment of an exomembrane system within the host cell cytoplasm to allow for remodelling and the communication of the parasite with its extracellular environment. This is achieved by exporting about 400 proteins (*i.a.* kinases, lipases, adhesins, proteases and chaperone-like proteins) outside the parasite and across the PVM to various locations within the iRBC [Tilley *et al.*, 2011]. This depends upon the establishment of a protein trafficking network to sort and move exported proteins to their specific locations within the infected erythrocytes. One of the key features of this network are Maurer's clefts (MCs), flattened membranous vesicles that bud from the PV in a dynamic process during early ring-stage development (Fig. 1.7) [Grüring *et al.*, 2011]. These structures migrate to and are tethered to the underside of the erythrocyte membrane. Other membranous structures are electron-dense vesicles (EDV) and J-dots, which traffic proteins from MCs to the RBCM. MC tethering is important to traffic luminal MC proteins to the underside and the surface of the RBCM [Boddey & Cowman, 2013]. During the early blood-stage development, most of the PVM lies in close proximity to the parasite plasma membrane (PPM). During parasite maturation, the PV increases in size and complexity as it develops large membranous loops that extend far into the RBC cytoplasm. This structure is the so-called tubulovesicular network (TVN) (Fig. 1.8) and it is thought that the TVN transiently associates with the RBC surface to import nutrients from the blood plasma [Matz *et al.*, 2020].

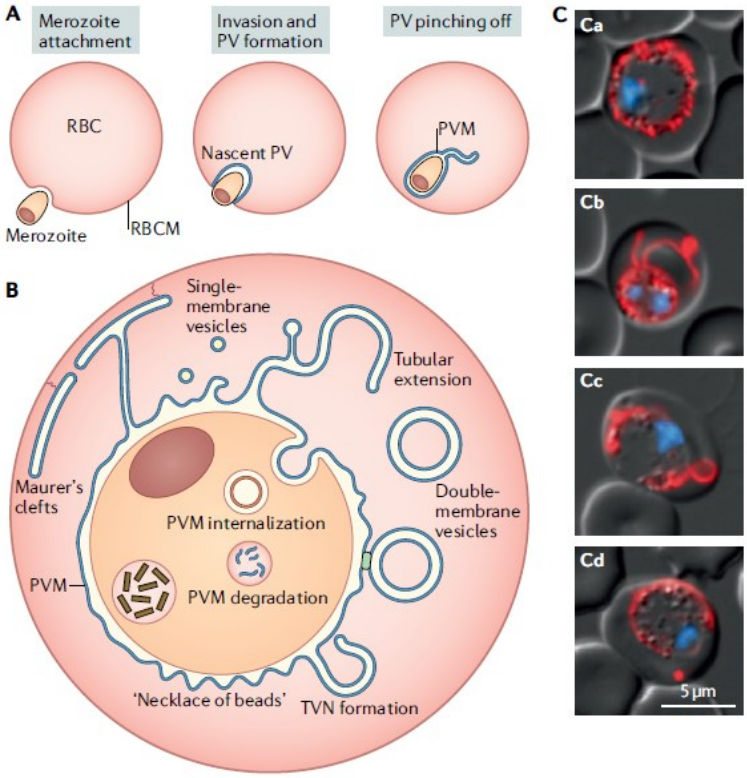

Fig. 1.8 | The parasitophorous vacuole of the malaria parasite. (**A**) The invading merozoite (see 1.2.2.1 and 1.2.2.3) induces an invagination of the RBC membrane (RBCM), resulting in the formation of a parasitophorous vacuole membrane (PVM) enclosing the parasitophorous vacuole (PV). (**B**) The PV forms a continuous space around the parasite. Membrane whorls emanate from the PVM to envelop RBC cytoplasm, forming the tubulovesicular network (TVN) and double-membrane vesicles. Maurer's clefts bud off from the PVM and become tethered to the underside of the RBCM. Host cell cytoplasm is endocytosed by PVM internalization, leading to the formation of intra-parasitic lysosomes that degrade hemoglobin, causing polymerization of hemozoin within the digestive vacuole. (**Ca - Cd**) Morphology of the PV in maturing parasites. A fluorescent reporter tagged TVN protein is indicated in red. The nucleus is indicated in blue. (Adopted from [Matz *et al.*,2020].)

The particular virulence of *P. falciparum* is due to its ability to sequester within capillaries to avoid clearance within the spleen (see 1.1.3) as the parasite exports adhesins via MCs to the iRBC surface. Infected RBCs adhere to the epithelium of blood vessels and are thereby not filtered out by macrophages that recognize and remove RBCs with compromised deformability or different antigenicity in the spleen [Tilley *et al.*, 2011]. One of the best studied adhesins is the *P. falciparum* EMP1, which is encoded by the *var* multi-gene family [Baruch *et al.*, 1995]. Approximately 60 *var* (variable) genes that are expressed mutually exclusively are present per parasite and each iRBC expresses a single *Pf*EMP1 variant on its surface [Scherf *et al.*, 2008]. *Pf*EMP1 proteins are transported via MCs to the iRBC surface where they cluster in knobs. The purpose of those electron-dense knobs is to present *Pf*EMP1 in a conformation that allows for tight adhesion of the iRBC to the blood vessel endothelium. This is achieved by the binding of the extracellular domain of *Pf*EMP1 to molecules (ICAM-1, CD31, CD36, CSA, glycosaminoglycans) presented on the surface of endothelial cells [Rowe *et al.*, 2009]. The monoallelic expression and switching of *var* genes allows the parasite to vary the antigens presented on the iRBC surface and to evade host immune responses, since the *Pf*EMP1 family proteins are targets of the acquired immune response [Boddey & Cowman, 2013].

1.2.1.4 Sexual development

It is widely believed that the commitment to sexual development occurs shortly before schizogony as all merozoites in a schizont form either a gametocyte or an asexual parasite. Also, all merozoites in a schizont undergo either male or female gametocytogenesis [Josling *et al.*, 2018].

The development of gametocytes requires several important cellular processes such as reversible protein phosphorylation and translational repression. Male gametocytogenesis is regulated by reversible protein phosphorylation, whereas translational repression is a prominent feature during female gametocytogenesis [Guttery *et al.*, 2015]. The sexual commitment of *P. falciparum* is a consequence of the activation of Apatella2-G (*Pf*AP2-G), the transcriptional master regulator of gametocytogenesis [Kafsack *et al.*, 2014; Sinha & Hughes *et al.*, 2014]. Transcription of the *ap2-g* gene is epigenetically controlled by heterochromatin protein 1 (HP1) [Brancucci *et al.*, 2014] and gametocyte development 1 (GDV1) [Filarsky *et al.*, 2018]. The interplay of those key regulators during a transcriptional cascade leads to the development of male and female gametocytes in the erythrocytic cycle. During the erythrocytic cycle only a subpopulation of parasites undergoes sexual development to finally form oocysts in the mosquito midgut (Fig. 1.9). The level of gametocytes that are produced during the erythrocytic cycle varies between clonal parasite lines, which suggests the involvement of both genetic and epigenetic factors [Josling *et al.*, 2018].

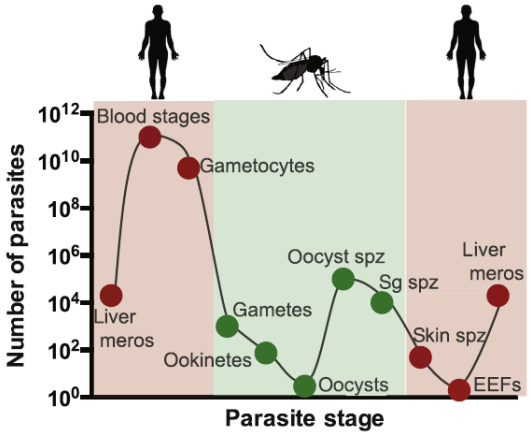

Fig. 1.9 | Estimated parasite numbers during the different life cycle stages. The numbers of different parasite life cycle stages vary significantly between the human host and anopheline vector. Sg spz, salivary gland sporozoites; meros, merozoites; EEF, extra-erythrocytic form. (Adopted from [Graumans *et al.*, 2020].)

The sexual stages of most Plasmodium species develop within two days [Sinden, 1982], but *P. falciparum* gametocytes mature within 10-12 days. This long differentiation process can be morphologically discriminated into five stages (I to V). Molecular and cellular rearrangements during the stages transform the gametocyte into a banana-shaped or falciform stage V gametocyte (Fig. 1.10) [Henry *et al.*, 2019; Josling & Llinas, 2015]. *P. falciparum* stage II – IV gametocytes have been identified as sequestering in the bone marrow and spleen, whereas stage I and V gametocytes are found in the peripheral blood [Tibúrcio *et al.*, 2015].

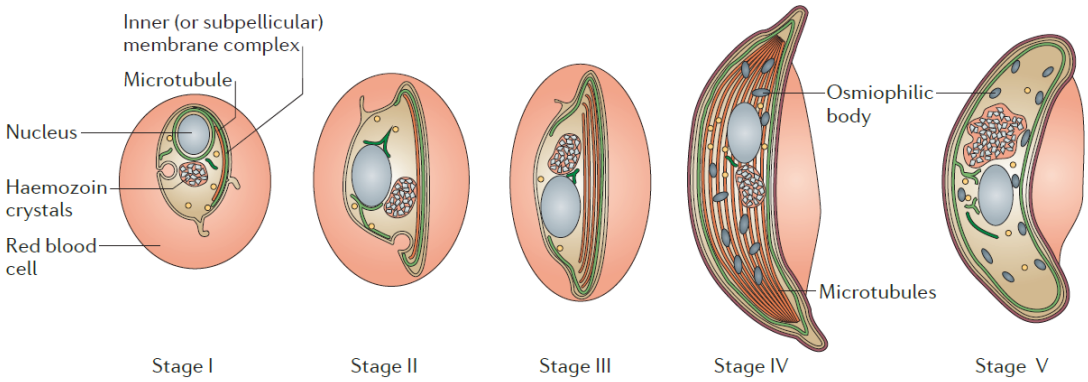

Fig. 1.10 | Schematics of the five stages of gametocyte development in *Plasmodium falciparum*. Gametocytogenesis occurs over 10-12 days. Stage I gametocytes are not distinguishable from an asexual trophozoite but begin to elongate to become D-shaped as the subpellicular microtubules begin to form. In stage III, the gametocytes elongate further with rounding ends. Stage IV gametocytes elongate even further but have pointed ends. Female gametocytes have osmiophilic bodies. The characteristic crescent shape of gametocytes is obvious in stage V. Female gametocytes are more curved and thicker than male gametocytes. (Adopted from [Josling & Llinas, 2015].)

1.2.2 Cellular biology

1.2.2.1 Merozoites

A merozoite is the invasive form of *Plasmodium spp*. and the smallest cell during the *Plasmodium* life cycle and, with a size of ≈ 1-2 µm, it is also one of the smallest known eukaryotic cells [Bannister *et al.*, 1986]. The merozoite contains the conventional organelle repertoire of eukaryotic cells, including an additional four membrane-encased DNA containing apicoplast, which is a remnant of a former plastid (Fig. 1.11) [Cowman *et al.*, 2012].

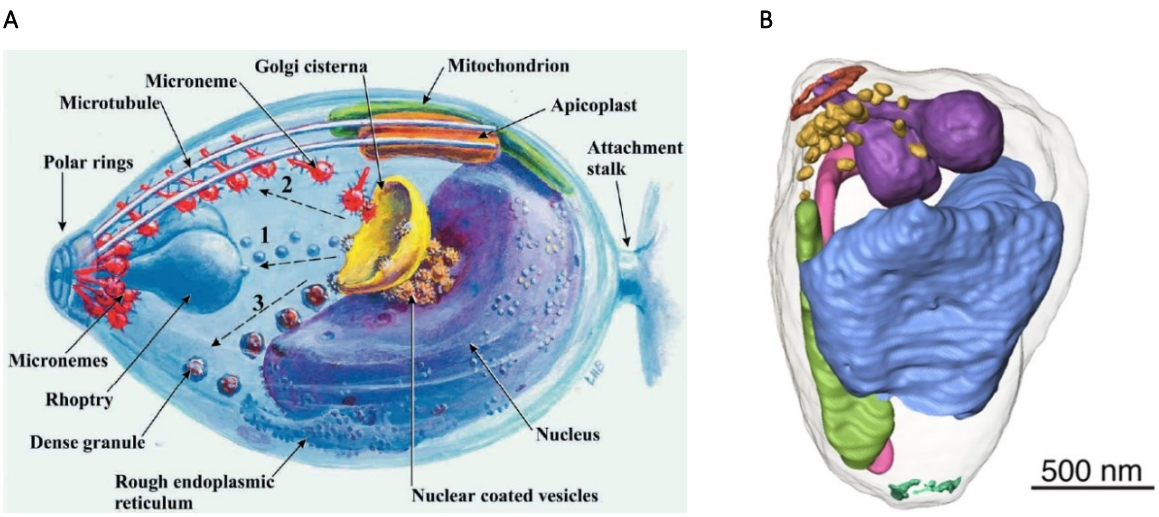

Fig. 1.11 | The *Plasmodium falciparum* merozoite. (**A**) Schematic of a *P. falciparum* merozoite with organelles and trafficking routes of secretory organelles. The three major trafficking routes are numbered from 1 to 3. Route 1 (rhoptry-directed vesicles) and route 3 (dense granules) are independent of microtubules, while route 2 represents the targeting of micronemes to the apical pole via subpellicular microtubules. (Adopted from [Bannister *et al.*, 2003].) (**B**) A merozoite rendered image from EM data. Red, apical ring; yellow, small electron-dense apical organelles; purple, rhoptries; magenta, mitochondrium; green, apicoplast; blue, nucleus; dark green basal complex. (Adopted from [Rudlaff *et al.*, 2020].)

Underlying the plasma membrane is a membranous network, named the inner membrane complex (IMC), that is derived from the secretory pathway. A group of IMC-located proteins form components of the so-called glideosome, a motor complex that allows the merozoite to enter the erythrocyte (see 1.2.2.3) [Kono *et al.*, 2013].

1.2.2.2 Apical complex organelles

The apical complex, a unique feature of Apicomplexans, comprises secretory organelles such as rhoptries (see 1.2.2.4), micronemes and exonemes, which are associated with parasite egress [Yeoh & Donnell *et al.*, 2007]. Secretory organelles, emanating from the secretory pathways, discharge effector proteins that have crucial roles during invasion [Kats *et al.*, 2008]. Merozoites and sporozoites possess all the secretory organelles, whereas ookinetes lack rhoptries as well as additional exocytic organelles termed dense granules (see below) [Lal *et al.*, 2009].

A merozoite contains up to 40 micronemes which resemble log-necked bottles and are translocated via subpellicular microtubules from the Golgi apparatus to the apical pole of the parasite, where the subpellicular microtubules radiate out from the apical polar rings (Fig. 1.11A) [Bannister *et al.*, 2003]. The content of micronemes is secreted into the rhoptry neck and onto the merozoite apex to coordinate the initial attachment of the merozoite to the RBC [Riglar *et al.*, 2011]. Proteins found in the micronemes of merozoites are adhesins, including the erythrocyte binding antigen (EBA) family (*i.a.* EBA-175) or apical membrane antigen 1 (AMA1) [Lal *et al.*, 2009].

Dense granules are spherical organelles with a similar size as micronemes. However, dense granules are situated non-apically and their discharge takes place after the merozoite enters the RBC [Bannister *et al.*, 2003]. The matrix of dense granules is uniformly electron-dense (hence the name), which is due to their high protein content. Once invasion is completed, dense granule secretion occurs in the subapical, lateral regions of the parasite. Proteins secreted by dense granules cover the PVM to facilitate traffic between the parasite and its host cell [Kats *et al.*, 2006; De Souza, 2006].

1.2.2.3 Process of erythrocyte invasion

Once released by the rupture of merosomes (see 1.2.1.2), the merozoites rapidly invade RBCs in a fast, dynamic, and multi-step process. The pre-invasion step that takes about 10 seconds is characterised by a dramatic deformation of the target erythrocyte to which the merozoite is attached. Internalization of the merozoite takes place within 20-60 seconds. After internalization, a period of echinocytosis occurs, which takes between 5-10 minutes before the erythrocyte returns to its biconcave shape (Fig. 1.12) [Dvorak *et al.*, 1975; Gilson & Crabb, 2009; Treeck *et al.*, 2009; Yahata *et al.*, 2012]. Little is known about the molecular details of the pre-invasion step. Merozoite surface protein 1 (MSP1) is the predominant merozoite surface protein that is anchored to the merozoite surface via a GPI linker [Holder, 1994]. MSP1 forms a complex with a number of peripheral proteins on the merozoite surface is required for invasion [Cowman *et al.*, 2017]. MSP1 acts as a platform on the merozoite surface for at least three large complexes with different peripheral proteins that bind to erythrocytes [Lin *et al.*, 2016], and it has been implicated in binding directly to both band 3 and glycophorin A on the erythrocyte surface

[Baldwin *et al.*, 2015; Goel *et al.*, 2003]. However, merozoites that lack MSP1 are still able to invade erythrocytes, suggesting that MSP1 is not essential for invasion [Das *et al.*, 2015]. It is suspected that MSP1 is instead involved in displaying proteins on the surface of merozoites to evade host responses [Cowman *et al.*, 2016].

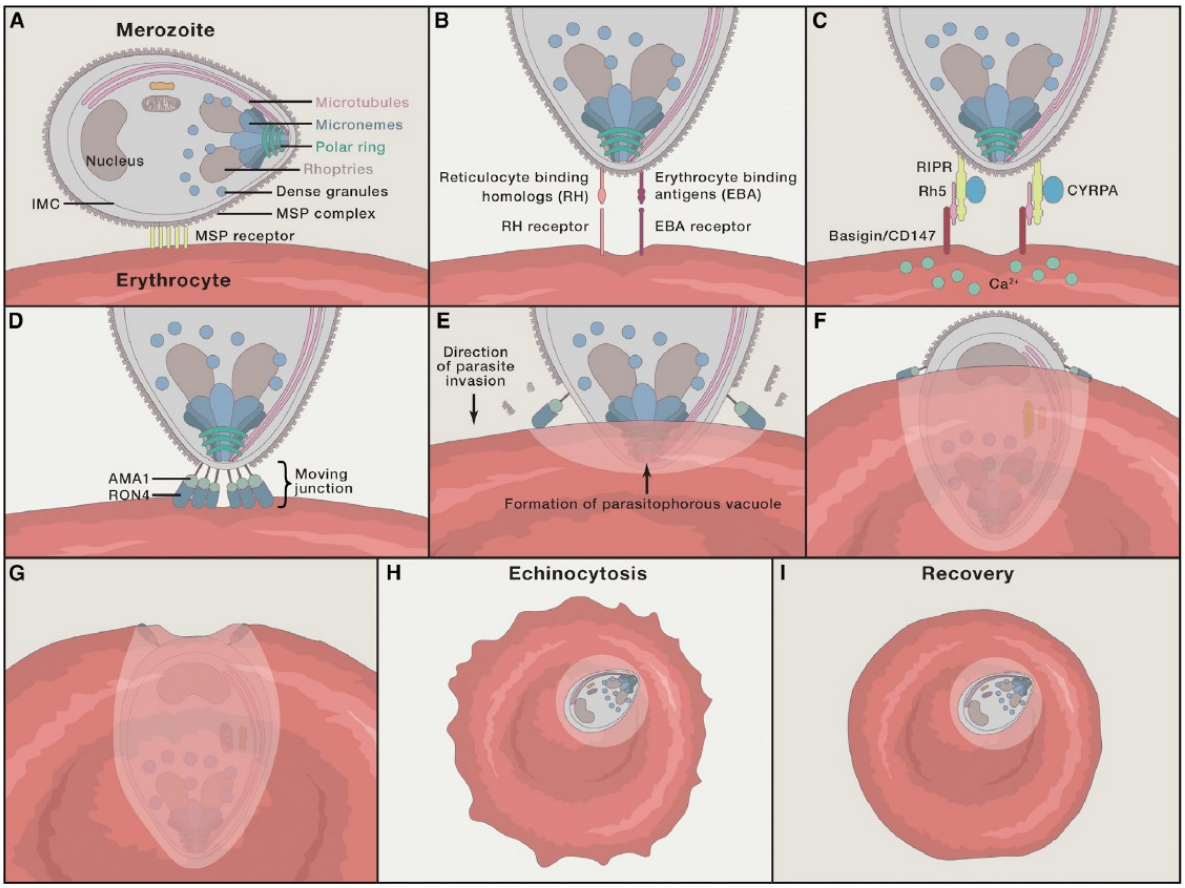

Fig. 1.12 | Merozoite invasion of erythrocytes. (**A**) Initial contact between the merozoite and the RBC is mediated by low-affinity interactions. Those interactions occur between merozoite surface proteins and RBC surface receptors. The merozoite reorients to bring its apex perpendicular to the red RBC membrane (RBCM) so that (**B**) specific receptor-ligand interactions mediated by EBA and *Pf*Rh family members occur, which initiate downstream invasion events involving the binding of the (**C**) *Pf*Rh5 complex to the RBCM located basigin (BSG) receptor. This causes a Ca^{2+}-flux in the RBC, and microneme secretion is initiated to (**D**) deposit the RON complex into the RBCM and establish the moving junction. (**E - G**) By an actin-myosin motor driven movement, the merozoite is propelled into the RBC, forming a parasitophorous vacuole by discharging rhoptry contents that contribute to the formation of the parasitophorous vacuole membrane (PVM) that surrounds the merozoite. (**H**) After sealing the PVM and RBCM, echinocytosis occurs, which is due to the loss of water from the RBC cytosol, which is followed by the (**I**) recovery of RBC homeostasis. (Adopted from [Cowman *et al.*, 2016].)

The pre-invasion involves robust interaction between the merozoite and the erythrocyte, which results in a parasite actomyosin motor-driven deformation of the host cell. This step involves two families of type 1 membrane proteins that are discharged from micronemes (see 1.2.2.2) and rhoptries (see 1.2.2.4) during invasion: the erythrocyte binding-like proteins (EBLs) and *P. falciparum* reticulocyte-binding protein homologues (*Pf*Rhs). These proteins bind to specific receptors on the erythrocyte surface (*i.a.* glycophorin A (GPA) and complement receptor 1 (CR1)) to mediate the reorientation of the merozoite by positioning its apical end toward the erythrocyte membrane [Cowman *et al.*, 2016]. Although the function of EBA and *Pf*Rh proteins shows redundancy, their overall function is essential in *P. falciparum* [Tham *et al.*, 2012]. EBA and *Pf*Rh ligands are involved in the activation of

subsequent steps during invasion and mediate the attachment of the merozoite to the erythrocyte surface through interaction with several known and unknown ligands on the RBC surface [Weiss, Gilson & Taechalertpaisarn *et al.*, 2015].

After egress from the host cell, merozoites are exposed to low-potassium ion concentrations in the blood plasma. This leads to a rise in cytosolic calcium (Ca^{2+}) levels in the parasite which in turn triggers the release of EBA-175 from micronemes. The binding of EBA-175 to GPA triggers the release of rhoptry proteins to the surface of merozoites [Singh & Chitnis, 2012]. Similarly, *Pf*Rh1 is linked to Ca^{2+} signalling in the merozoite [Gao *et al.*, 2013] and the phosphorylation of the cytoplasmic tail of *Pf*Rh4 by CDPK2 is required for invasion through *Pf*Rh4-CR1 interaction [Tham *et al.*, 2015]. Another *Pf*Rh protein with a distinct function in invasion is the essential protein *Pf*Rh5 [Crosnier & Bustamante *et al.*, 2011]. *Pf*Rh5 forms a ternary complex with the parasite Ripr (Rh5 interacting protein) and CyRPA (cysteine-rich protective antigen) to interact with basigin (BSG) on the erythrocyte surface (Fig. 1.13) [Volz, Yap & Sisquella *et al.*, 2016].

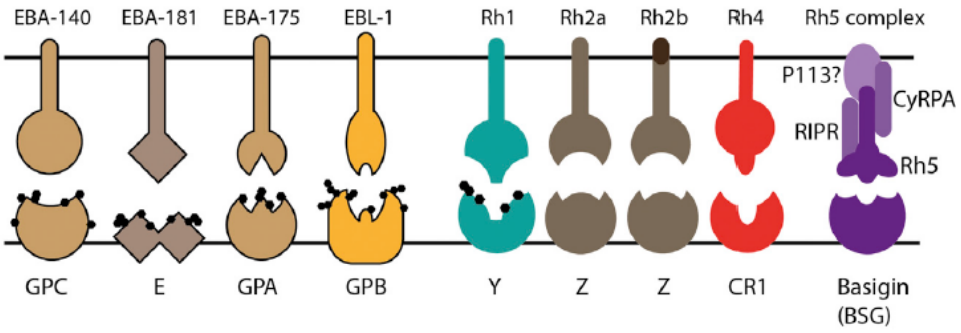

Fig. 1.13 | Parasite ligand-receptor interactions. Schematic of merozoite surface ligands and erythrocyte receptor interactions involved in merozoite invasion. (Adopted from [Cowman *et al.*, 2017].)

The ternary complex is associated with the RBCM to execute the next step in invasion, the formation of a moving junction. The merozoite moves, driven by an actomyosin motor, through the junction. As the junction moves to the posterior end of the merozoite, it is also referred to as the moving junction (Fig. 1.12). At its core, the moving junction is composed of the proteins AMA1 and RON2 [Alexander *et al.*, 2005; Besteiro & Michelin *et al.*, 2009; Riglar *et al.*, 2011; Tonkin & Roques *et al.*, 2011]. AMA1 is secreted by micronemes independently of EBA-175 [Healer *et al.*, 2002] and found on the surface of merozoites where it binds to RON2, which is part of a larger RON complex. RON2 is a rhoptry neck protein and is one of the first proteins that are injected into the erythrocyte membrane to serve as a receptor for AMA1, which is a mechanism used by apicomplexan parasites to insert their own ligand-receptor pair in order to invade their host cells. During invasion, the merozoite surface protein coat is shed at the moving junction by a serine protease, also referred as sheddase [Cowman *et al.*, 2017].

The current model of actomyosin-driven movement of the merozoite into the erythrocyte postulates that the glideosome links merozoite surface ligands such as EBA-175, *Pf*Rhs and AMA1 directly or indirectly to the IMC via a transmembrane domain (TMD). Entry into the erythrocyte is powered by an actin-myosin contractile system that uses the force of myosin A (MyoA) as a gliding motor to pull filamentous actin. This transmits force into a

movement of the surface ligands from the apex to the posterior end of the merozoite. As the ligands are connected to receptors on the erythrocyte surface, the merozoite propels itself into the erythrocyte (Fig. 1.14) [Cowman *et al.*, 2016; Koch & Baum, 2016].

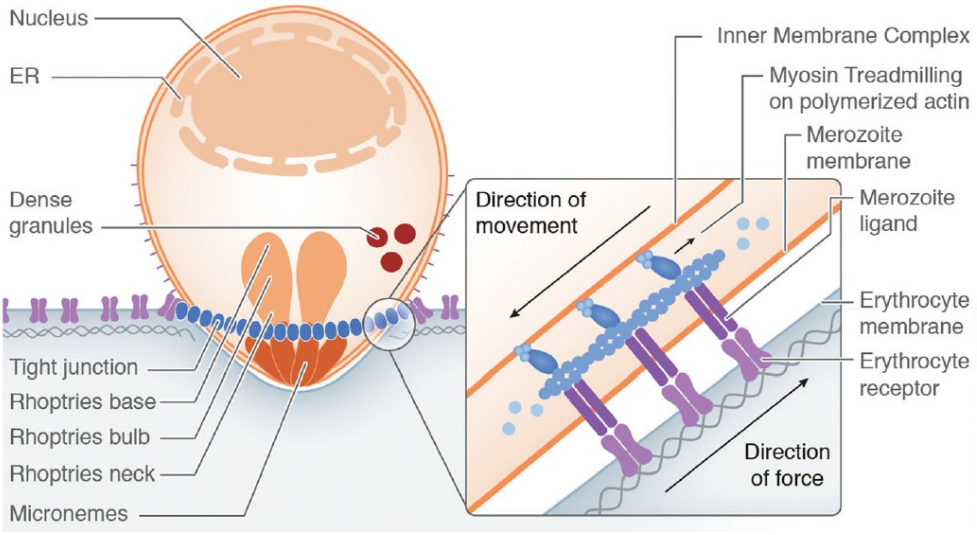

Fig. 1.14 | Schematic model of actin-myosin motor-mediated merozoite invasion. The current model of apicomplexan cell entry is explained by an actin-myosin motor complex. Myosin treadmilling occurs on polymerized actin filaments that are connected to the surface ligands which causes the ingress of the parasite. ER, endoplasmic reticulum. (Adopted from [Koch & Baum, 2016].)

1.2.2.4 Rhoptries

Rhoptries are the most prominent of the secretory organelles and are synthesized *de novo* during schizogony through the intra-erythrocytic parasite development, but they are also present in sporozoites. These pear-shaped, membrane-bound organelles are an unique feature of Apicomplexans and can be morphologically separated into an apical duct (the rhoptry neck) and a larger region (the rhoptry bulb) [Counihan & Kalanon *et al.*, 2013]. The overall size of rhoptries is about 650 nm in length and 300 nm at the base (bulb). Each region contains a different set of proteins that are secreted sequentially [Bannister *et al.*, 2000]. To date, more than thirty rhoptry neck and bulb proteins have been identified in *P. falciparum* [Haase *et al.*, 2008; Kats *et al.*, 2006; Wickramarachchi & Devi *et al.*, 2008]. The molecular details of i) the rhoptry biogenesis, ii) how proteins traffic through the secretory pathway, specifically to the rhoptries (and for instance not to the micronemes) and iii) rhoptry protein segregation within the rhoptry (bulb *vs* neck) are sparse [Counihan & Kalanon *et al.*, 2013].

All luminal rhoptry proteins display an N-terminal signal peptide (SP), which allows their trafficking through the conventional eukaryotic secretory pathway via the ER and Golgi [Deponte *et al.*, 2012]. Rhoptries are formed by the fusion of endosome-like vesicles derived from the Golgi. These vesicles deliver proteins to the rhoptries in a process that appears to depend on the adaptor protein complex AP-1 [Kaderi Kibria & Rawat *et al.*, 2015]. Studies in *P. falciparum* as well as in *T. gondii* [Agop-Nersesian *et al.*, 2009; Bradley *et al.*, 2005] have localized the small GTPase Rab11A to the rhoptry membrane. Two other GTPases, Rab5A and Rab5C, as well as dynamin-related proteins (Drps), have also been shown to be important regulators of vesicular traffic of the rhoptries (and micronemes) [Breinich *et al.*, 2009; Kremer *et al.*, 2013].

As the rhoptry matures, the rhoptry neck and rhoptry bulb are sub-compartmentalized [Bannister *et al.*, 2000]. Luminal rhoptry proteins are heterologous and include soluble proteins, transmembrane proteins, and GPI-anchored proteins. They are involved in invasion as well as the formation of the PVM [Kats *et al.*, 2006, 2008] and nutrient uptake [Counihan *et al.*, 2017]. Formation of the junction likely triggers the discharge of the rhoptry bulb to release the proteins and lipids required for the formation of the PV and PVM [Riglar *et al.*, 2011].

1.2.2.5 The rhoptry surface proteins ARO, CERLI1 and AIP

In addition to signal peptide containing rhoptry proteins, three other proteins, *Pf*ARO, *Pf*CERLI1 (*Pf*RASP2) and *Pf*AIP [Cabrera *et al.*, 2012; Liffner *et al.*, 2019; Mueller *et al.*, 2013, 2016; Suarez *et al.*, 2019] are associated with the rhoptry membrane. These proteins lack a signal peptide and are located at the cytosolic face of this organelle. *Pf*CERLI1 (*Pf*RASP2) localizes to the rhoptry bulb membrane and its knockdown disrupts merozoite invasion as the secretion of key rhoptry antigens, such as RON4 and Rh4 that coordinate merozoite invasion, is inhibited [Liffner *et al.*, 2019; Suarez *et al.*, 2019]. *Tg*RASP2 - The *T. gondii* rhoptry apical surface protein 2 (a homologue of *Pf*CERLI2) binds specifically to charged lipids such as phosphatidic acid (PA) and phosphatidylinositol 4,5-bisphosphate ($PI(4,5)P_2$). The binding is presumably mediated by a calcium lipid-binding-like domain (C2) and a pleckstrin homology-like (PH) domain. It has been suggested that *Tg*RASP2 binds to PA and $PI(4,5)P_2$, which are concentrated at the apex of the PPM, to facilitate the close apposition of the rhoptry towards the PPM. Subsequently, the recruitment of hypothetical membrane fusion machinery proteins, such as SNARE proteins, could be initiated [Suarez *et al.*, 2019].

*Pf*ARO - the *P. falciparum* Armadillo (ARM) repeats only protein has been identified in the *P. falciparum* genome and localized to the rhoptries [Hu *et al.*, 2010]. Consecutive work has shown that *Pf*ARO membrane attachment is accomplished by co- and post-translational modification (PTM) with the fatty acids myristate and palmitate. These modifications are catalyzed by N-myristoyl transferase (NMT) and palmitoyl acyl transferase (PAT) [Cabrera *et al.*, 2012]. In *T. gondii*, the knockdown of the rhoptry membrane-localized PAT *Tg*DHHC7 causes the dispersion of rhoptries in the cytosol, resulting in a disruption of invasion [Beck *et al.*, 2013].

Recombinant expression and its subsequent purification allowed for the structural determination of *Pf*ARO (PDB accession: 5EWP). The structure of *Pf*ARO (residue 32-274) was solved by single-wavelength anomalous dispersion phasing (using a selenomethionine-derivatized protein) to a resolution of 1.8 Å [Geiger & Brown *et al.*, 2020]. The *Pf*ARO32-274 monomer (Fig. 1.15) comprises five ARM-like repeats, each containing three α-helices. Although the first ARM repeat (Fig. 1.15A, purple) is similar to the other four ARM repeats in terms of fold, it differs in the relative positioning of its first helix and is therefore a somewhat atypical or 'degenerate' ARM repeat. Similar to what is observed in other ARM-containing proteins such as β-Catenin (PDB accession: 2I22), helices from adjacent ARM repeats of *Pf*ARO stack in a head-to-tail fashion, resulting in an elongated right-handed superhelix. As shown in Fig. 1.15B, *Pf*ARO exhibits an overall shape that resembles a kidney bean with the concave surface formed by the last helix from each ARM repeat.

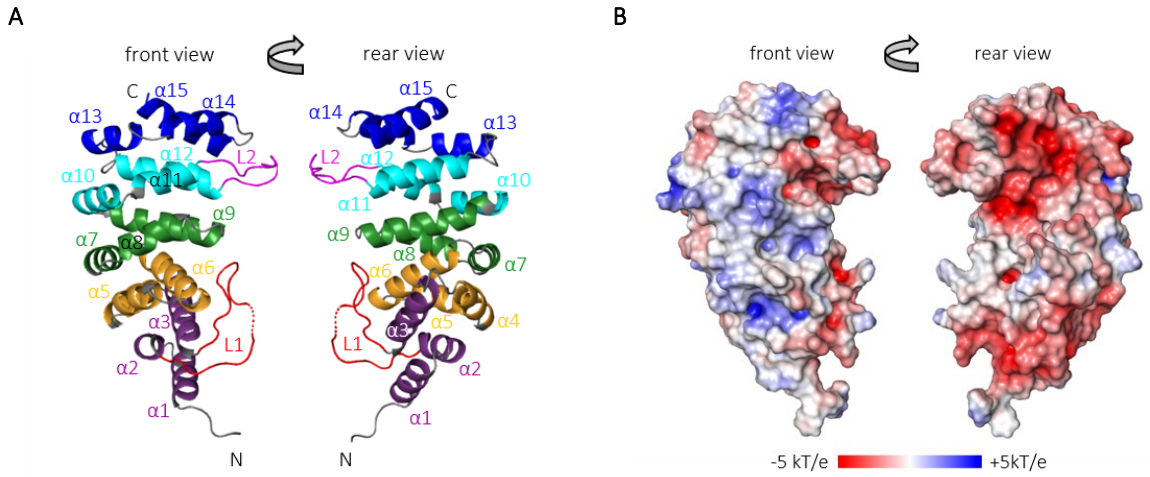

Fig. 1.15 | Structure of *Pf*ARO protein. (**A**) Front and rear view of *Pf*ARO (PDB: 5EWP) structure. Each ARM-like domain is colored separately (ARM1, purple; ARM2, gold; ARM3, green; ARM4, cyan; ARM5, blue). Individual alpha (α) helices are labeled in sequential order starting with α1. N and C indicate residues L_{32} and T_{274}, respectively. Surface exposed loop1 (S_{60} to T_{80}) and loop2 (E_{203} to L_{214}) are indicated by L1 (red) and L2 (magenta), respectively. (**B**) Surface electrostatic map of *Pf*ARO. Front and rear views of *Pf*ARO are presented. The front view (left) is oriented identically to the left structure shown in (A). The rear view is oriented identically to the right structure shown in (A). The electrostatic surface potential scale is from 5 kT/e (red) to +5 kT/e (blue). Light grey indicates neutral electrostatic potential.

Similar to ARM repeat proteins such as importin α7 (PDB accession: 4UAD, 6N88), the concave surface of *Pf*ARO has been suggested to potentially function as an interaction surface for *Pf*ARO binding partners [Geiger & Brown *et al.*, 2020]. In addition to its distinct shape, the surface has a significant negative charge (Fig. 1.15B) that might help mediate interaction. The electrostatic surface potential of *Pf*ARO is not evenly distributed. While the front side (Fig. 1.15B, left) of *Pf*ARO is slightly positive, the opposing rear side is almost entirely covered with a negative charge, suggesting that the rear side may be well suited for interaction with a positively charged protein or helps to orient *Pf*ARO relative to a positively charged surface.

Perhaps the most notable feature of the *Pf*ARO structure is the presence of two loops inserted between α2- α3 of ARM1 and α11- α12 of ARM4 (Fig. 1.15A). Both loops protrude from the same surface. However, loop1 (residue 60-80) is considerably larger than loop2 (residue 203-214) and contains a surprisingly large number of highly conserved residues (S1, Appendix). In fact, loop1 and the adjacent helix α3 represent the most highly conserved region of *Pf*ARO (Fig. 1.15A). Residues from the apex of loop1 (residues 71-78) extend toward α3, forming a continuous surface of highly conserved residues between these elements in 3-dimensional space. As such, this region is expected to be important for *Pf*ARO function by mediating interaction with binding partners.

It has been shown that the *T. gondii* homologue *Tg*ARO is necessary for the correct positioning of rhoptries to the apical pole and that its depletion recapitulates the phenotype of dispersed rhoptries observed for *Tg*DHHC7 knockdown [Beck *et al.*, 2013; Mueller *et al.*, 2013]. It has been further shown that *Tg*ARO interacts with the motor protein myosin F (*Tg*MyoF) and ARO interacting protein (*Tg*AIP), which recruits the key regulator enzyme adenylate cyclase β (*Tg*ACβ) to a rhoptry neck sub-compartment [Mueller *et al.*, 2013, 2016]. *Tg*ACβ is unstable upon *Tg*AIP knockout and no longer recruited to this sub-compartment, but *Tg*ARO's location is unchanged [Mueller *et al.*, 2016]. Through the depletion of different ARM repeats of *Tg*ARO, the authors demonstrated that

each ARM repeat is necessary for rhoptry positioning to the parasite apex (Fig. 1.16). Interestingly, *Tg*AIP knockdown did not result in a disruption in invasion and no defect in parasite proliferation is reported. Furthermore, *Pf*ARO was able to functionally complement *Tg*ARO [Mueller *et al.*, 2013, 2016]. This might point towards a conserved mode of rhoptry biogenesis and discharge across the Apicomplexa phylum.

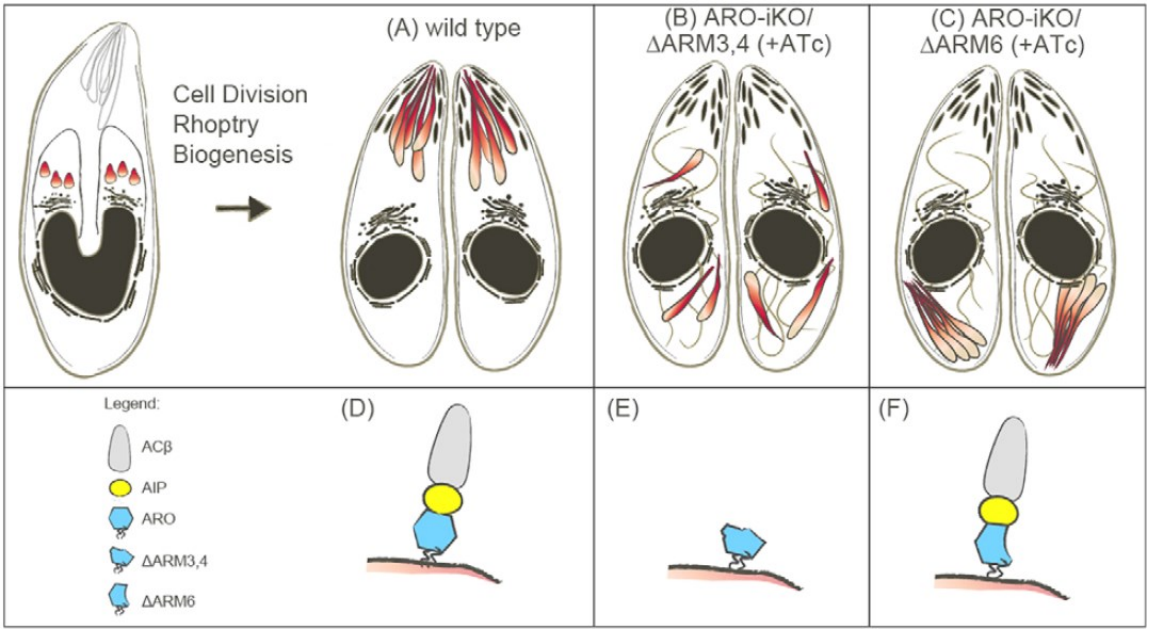

Fig. 1.16 | Summarized model visualizing the effect of *Tg*ARO mutations and *Tg*AIP knockdown on rhoptry positioning. The upper box shows the parasite during endodyogeny with nascent rhoptries (red) in the forming daughter cells. Ultrastructural changes on rhoptry positioning are shown for *Tg*ARO mutant lines (A-C) that allow anhydrotetracycline (ATc) induced knockout of endogenous *Tg*ARO (ARO-iKO) while stably expressing mutated versions of *Tg*ARO. (**A**) Parasites expressing wild-type *Tg*ARO (**B**) Parasites expressing mutated versions of *Tg*ARO where ARM repeats 3 and 4 were deleted (ΔARM3,4). (**C**) Parasites expressing a mutated version of *Tg*ARO where ARM repeat 6 was deleted (ΔARM6). In situation A, rhoptries are located at the apical end. In situation B, rhoptries are randomly dispersed throughout the cytosol. In situation C, rhoptries are dispersed but bundled together. The lower box shows (from D-F) schematics of the interactions between wild-type *Tg*ARO or its mutants with *Tg*AIP and *Tg*ACβ. (Adopted from [Mueller *et al.*, 2016].)

1.3 Aims of this thesis

Despite intensive research over the past years, rhoptry morphogenesis is still largely elusive. This work aims to i) identify and locate a homologue of *Tg*AIP in the related species *P. falciparum* as well as to functionally analyze this protein using a conditional functional inactivation method, ii) use emerging structural information of the *Pf*ARO protein - that allows a mutational approach to determine *Pf*ARO/*Pf*AIP interaction, and iii) use proximity-based biotinylation to identify *Pf*AIP interacting proteins.

CHAPTER 2 MATERIALS & METHODS

2.1 Materials

2.1.0 Technical devices

Device	Specifications	Brand/Distributor
Agarose gel chamber	Wide Mini-Sub© Cell GT basic	Bio-Rad, München
Analytical Balance	870 572	Kern & Sohn, Balingen
Blot device Cooling unit Electrode assembly Foam pads Gel holder cassettes	Mini-PROTEAN Tetra Cell System	Bio-Rad, München
Centrifuge	Megafuge 1.0R J2-HS Ultracentrifuge Rotor JA-12 Avanti J-26S XP Rotor JA-14	Heraeus, Hannover Beckmann Coulter, Krefeld Beckmann Coulter, Krefeld
Table Centrifuge	Eppendorf 5415D	Eppendorf, Hamburg
Casting stand Casting plates Casting frames 12-well combs	Mini Protean	Bio-Rad, München
Cell-Separator	VarioMACS™	Miltenyi Biotech, Bergisch Gladbach
Electrophoresis chamber	Mini Protean 67s	Bio-Rad, München
Electroporator	Nucleofector II AAD-1001N	Amaxa Biosystems, Germany
Flow cytometer	LSR II NovoCyte®	BD Instruments, USA ACEA Biosciences Inc.
Ice machine	EF 156 easy fit	Scotsmann, Vernon Hills, USA
Imaging system	ChemiDoc XRS+ imaging system Odyssey© Fc imaging system	Bio-Rad, Müchen LI-COR Biosciences
Incubator	Heratherm IGS400 Innova 40 Max Q4000 Thermo function line	Thermo Fisher Scientific New Brunswick Scientific Barnstead, Iowa/USA Heraeus, Hannover
Fluorescence microscope	Axio Imager M1	Zeiss, Jena
Light microscope	Axio Lab A1	Zeiss, Jena
Magnetic stirrer	RSM-10HP	PHOENIX Instrument
Digital microscope camera	Orca C4742-95	Hamamatsu Photonics K.K. Systems, Japan
Microwave	Micro 750W	Whirlpool, China
Laboratory scale	Atilon	Acculab Sartorius, Göttingen
PCR cycler	C1000 Touch™ Thermo Cycler Mastercycler EP gradient	Bio-Rad, Munich Eppendorf, Hamburg
Photometer	BioPhotometer plus	Eppendorf, Hamburg
pH-meter	SevenEasy	Mettler-Toledo, Gießen
Pipettes	1-10/200/1000 µl	Gilson, Middleton, USA
Pipettor	Matrix CellMate II Pipetboy acu	Thermo Fisher Scientific IBS, USA
Power supply	Consort EV231	Merck, Darmstadt

	PowerPac basic	Bio-Rad, Munich
Roller mixer	SRT 6D	Stuart
Spectrophotometer	NanoDrop 2000c	Thermo Fisher Scientific
Safety cabinet	Steril Gard III Advance Safe 2020	Baker, Stanford USA Thermo Fisher Scientific
Thermoblock	Thermomixer F1.5	Eppendorf, Hamburg
Ultrapure water purification system	Milli Q	Millipore
UV transilluminator	PHERO-lum 289	Biotec Fischer, Reiskirchen
Vacuum pump	BVC Control	Vacuubrand, Deutschland
Vortexer	Vortex-Genie 2	Scientific Industries, USA
Waterbath	1083	GFL, Burgwedel

2.1.1 Chemicals

Reagent	Brand/Distributor
Acetic acid ($C_2H_4O_2$)	Roth, Karlsruhe
Acrylamide/Bisacrylamide solution (40 %)	Roth, Karlsruhe
Agar LB (Lennox)	Roth, Karlsruhe
Agarose	Invitrogen, USA
AlbumaxII	Gibco, Life Technologies, USA
Albumin bovine fraction V (BSA)	Biomol, Hamburg
Ammonium persulfate (APS)	Applichem, Darmstadt
Ampicillin	Roche, Mannheim
Bacto™ yeast extract Bacto™ Peptone	BD, USA
Biotin	Sigma-Aldrich, Steinheim
Blasticidin S (BSD)	Invitrogen, USA
Bromophenol blue	Roth, Karlsruhe
Calcium chloride ($CaCl_2$)	Sigma-Aldrich, Steinheim
Clarity™ Western ECL Substrate	Bio-Rad
Coomassie Brilliant Blue G-250	Merck, Darmstadt
Cut Smart® reaction buffer	NEB, Ipswich, USA
Dako Fluorescence mounting medium	DAKO, Hamburg
4',6-diamidino-2-phenylindole (DAPI)	Roche, Mannheim
Dihydroethidium (DHE)	Cayman, Ann Arbor, USA
Deoxynucleotides (dNTPs)	Thermo Fisher Scientific, Lithuania
Dihydroethidium (DHE)	Cayman Chemical, Michigan, USA
Dimethyl sulfoxide (DMSO)	Sigma-Aldrich, USA
Dipotassium phosphate (K_2HPO_4)	Merck, Darmstadt
Disodium phosphate (Na_2HPO_4)	Roth, Karlsruhe
1,4,-dithiothreitol (DTT)	Biomol, Hamburg
Dulbecco's phosphate buffered saline (DPBS)	PAN, Biotech, Aidenbach
Ethanol	Roth, Karlsruhe
Ethidium bromide (EtBr)	Sigma-Aldrich, Steinheim
Ethylene glycol-tetraacetic acid (EGTA)	Biomol, Hamburg
FIREPol® reaction buffer	Solis BioDyne, Estonia
Formaldehyde 10%, methanol free, ultra-pure	Polysciences, Hirschberg
G418 disulfate salt (Neomycin)	Sigma-Aldrich, Steinheim
Gentamicin	Ratiopharm, Ulm
Giemsa's azure, eosin, methylene blue solution D-Glucose Glycerol	Merck, Darmstadt
Glutardialdehyde (25 %)	Roth, Karlsruhe

Glycine	Biomol, Hamburg
4-(2-Hydroxyethyl)-1-piperazineethane-sulfonic acid (HEPES)	Roche, Mannheim
Hoechst 33342 (Ho33342)	Chemodex, Switzerland
Hydrochloric acid (HCl)	Merck, Darmstadt
Hypoxanthine	Sigma-Aldrich, Steinheim
Isopropanol	Roth, Karlsruhe
Magnesium chloride ($MgCl_2$)	Merck, Darmstadt
Methanol (MeOH)	Roth, Karlsruhe
3-(N-morpholino)propanesulfonic acid (MOPS)	Sigma-Aldrich, Steinheim
Milk powder	Roth, Karlsruhe
Percoll	GE Healthcare, Sweden
Phenylmethylsulfonylfluoride (PMSF)	Sigma-Aldrich, Steinheim
Phusion® HF reaction buffer	NEB, Ipswich, USA
Potassium chloride (KCl) Potassium dihydrogen phosphate (KH_2PO_4)	Merck, Darmstadt
Protease inhibitor cocktail ("Complete Mini") (PIC)	Roche, Mannheim
Rapalog (A/C Heterodimerizer AP21967)	Clontech, Mountain View, USA
Rubidium chloride (RbCl)	Sigma-Aldrich, Steinheim
RPMI (Roswell Park Memorial Institute)-Medium	Applichem, Darmstadt
Saponin	Sigma-Aldrich, Steinheim
Sodium acetate ($C_2H_3NaO_2$)	Merck, Darmstadt
Sodium bicarbonate ($NaHCO_3$)	Sigma-Aldrich, Steinheim
Sodium chloride (NaCl)	Gerbu, Gaiberg
Sodium dodecyl sulfate (SDS)	Applichem, Darmstadt
Sodium dihydrogen phosphate (NaH_2PO_4)	Roth, Karlsruhe
Sodium hydroxide (NaOH)	Merck, Darmstadt
Sorbitol	Sigma-Aldrich, Steinheim
SYBR® Green	Sigma-Aldrich, Steinheim
N, N, N, N-Tetramethylethylenediamine (TEMED)	Merck, Darmstadt
Triethylammonium bicarbonate buffer (TEAB)	Sigma-Aldrich
Tris base	Roth, Karlsruhe
Tris-EDTA (TE)	Invitrogen, Karlsruhe
Triton X-100	Biomol, Hamburg
TWEEN-20	Merck, Darmstadt
T4 DNA ligase reaction buffer	NEB, Ipswich, USA
Water for molecular biology (Ampuwa)	Fresenius Kabi, Bad Homburg
WR99210 (WR)	Jacobus Pharmaceuticals, Washington, USA
Yeast extract	Becton Dickinson, Heidelberg

2.1.2 Labware & disposables

Labware and disposables	Specifications	Brand/Distributor
Conical Falcon™ tubes Cryotubes Culture bottles	15 ml, 50 ml 1.6 ml 50 ml	Sarstedt, Nümbrecht
DAKO Pen		DAKO, Hamburg
Disposable pipette tips	1-10/20-200/100-1000 µl	Sarstedt, Nümbrecht
Filter, round	150 mm	Macherey-Nagel, Düren
Filter tips	1-10/20-200/100-1000 µl	Sarstedt, Nümbrecht
Flow cytometry tubes	75x12 mm	Sarstedt, Nümbrecht
Glass cover slips	24x65 mm 0.13-0.16 mm thickness	R. Langenbrinck, Emmendingen

Glass slides		Engelbrecht, Edermünde
Gloves, latex		Kimtech Science EcoShield™
Gloves, purple, nitrile		Kimtech Science
Leukosilk tape		BSN medical GmbH
Low protein binding tubes	1.5 ml	Thermo Fisher Scientific
MACS cell separation column		Miltenyi Biotech
Nitrocellulose blotting membrane Protran®	Amersham 0.45 µm	GE Healthcare, Deutschland
One way cannula		Braun, Melsungen
Parafilm		Bemis, USA
Pasteur pipette		Brand, Wertheim
Pierce™ Spin Columns - Snap Cap		Thermo Fisher Scientific
PCR Reaction tubes Petri dishes Plastic pipettes	Multiply-µmStrip Pro 8-Strip 15x60mm, 14x90 mm 5/10/25 ml	Sarstedt, Nümbrecht
Reaction tubes	1.5 ml/2 ml	Sarstedt, Nümbrecht Eppendorf, Hamburg
Scalpel	Braun, Tuttlingen	
Sterile filter	0.22 µm	Sarstedt, Nümbrecht
Transfection cuvettes	0.2 cm	Bio-Rad, München
Whatman™ chromatography paper	3 MM Chr	GE Healthcare

2.1.3 Kits

Designation	Manufacturer/Distributor
NucleoSpin© Plasmid Kit	Macherey-Nagel, Düren
NucleoSpin© Gel and PCR cleanup	Macherey-Nagel, Düren
QIAamp© DNA Mini Kit	Qiagen, Hilden
QIAGEN© Plasmid Midi Kit	Qiagen, Hilden
Western Blot ECL-Clarity™ Detection Kit	Bio-Rad, USA

2.1.4 DNA- and protein-ladders

Designation	Manufacturer/Distributor
GeneRuler™ 1 kb DNA Ladder	Thermo Fisher Scientific, Schwerte
PageRuler™ prestained protein ladder	Thermo Fisher Scientific, Schwerte
PageRuler™ (Plus) prestained protein ladder	Thermo Fisher Scientific, Schwerte

2.1.5 Media, buffers and solutions

2.1.5.1 Solutions and buffers for bacterial culture

10x LB medium stock solution	10 % NaCl 5 % peptone 10 % yeast extract in dH_2O autoclaved
1x LB medium working solution	1:10 dilution of 10x LB medium stock solution in autoclaved dH_2O
LB Agar plate solution	1.5 % Agar-Agar 10 % NaCl 5 % peptone 10 % yeast extract in dH_2O autoclaved
Ampicillin stock solution	100 mg/ml in 70 % ethanol
Glycerol stabilate solution	50 % (v/v) glycerol in 1x LB working solution

Buffers for competent *E. coli* cells

TFBI buffer	30 mM acetic acid 50 nM $MnCl_2$ 100 mM RbCl 10 mM $CaCl_2$ 15 % (v/v) glycerol pH 5.8 (with 0.2 M Acetic acid) ad 500 ml dH_2O

TFBII buffer	10 mM MOPS 75 mM $CaCl_2$ 10 mM RbCl 15 % (v/v) glycerol pH 7.0 (with NaOH) ad 500 ml dH_2O

2.1.5.2 Solutions and buffers for DNA precipitation and analyses

Agarose gel	0.5 - 2 % Agarose in 1x TAE buffer
Ethanol	100 %, 70 % in dH_20
Sodium acetate	3 M, pH 5.2
Tris-EDTA (TE) buffer	10 mM Tris-HCl, pH 8.0 1 mM EDTA in dH_20 autoclaved
50x TAE (Tris-acetate) buffer	2 M Tris base 1 M Acetic acid 50 mM EDTA pH 8.5 in dH_20 autoclaved
1x TAE buffer	1:50 dilution of 50x TAE buffer in dH_2O
6x Loading buffer	40 % Glycerol (v/v) 2.5 % (w/v) Xylene cyanol 2.5 % (w/v) Bromophenol blue in dH_2O

2.1.5.3 Solutions and buffers for parasite culture and cell biology experiments

P. falciparum in vitro culture

RPMI complete medium	1.587 % (w/v) RPMI 1640 12 mM $NaHCO_3$ 6 mM D-Glucose 0.5 % (v/v) Albumax II 0.2 mM Hypoxanthine 0.4 mM Gentamicin pH 7.2 in dH_2O sterile filtered
10 % Giemsa solution	10 ml Giemsa's azure, eosin, methylene blue solution 90 ml dH_2O
Synchronization solution	5 % (w/v) D-Sorbitol in dH_2O sterile filtered
Amaxa transfection buffer	90 mM $NaPO_4$ 5 mM KCl 0.15 mM $CaCl_2$ 50 mM HEPES pH 7.3 in dH_2O sterile filtered
Malaria freezing solution (MFS)	4.2 % D-sorbitol 0.9 % NaCl 28 % Glycerol in dH_2O sterile filtered
Malaria thawing solution (MTS)	3.5 % NaCl in dH_2O, sterile filtered
WR99210 stock solution	20 mM WR99210 in DMSO

WR99210 working solution	1:1,000 dilution of WR99210 stock solution in RPMI complete medium, sterile filtered
Blasticidin S (BSD) working solution	5 mg/ml BSD in RPMI complete medium, sterile filtered
DHE stock solution (10x)	5 mg DHE in 1 ml DMSO
DHE working solution (1x)	1:10 dilution of DHE stock solution in dH_2O
Ho33342 stock solution (10x)	4.5 mg Ho33342, in 1 ml DMSO
Ho33342 working solution (1x)	1:10 dilution of Ho33342 stock solution in dH_2O
Flow cytometry stop solution	0.5 µl Glutaraldehyde (25 %) in 40 ml RPMI complete medium
G418 working solution	50 mg/ml in RPMI complete medium sterile filtered
Rapalog (AP21967) stock solution	500 µM AP21967 in ethanol
Rapalog working solution	1:20 dilution of rapalog stock solution in RPMI complete medium sterile filtered
Human red blood cells	sterile concentrate, blood group 0+ Blood bank Universitätsklinikum Eppendorf (UKE), Hamburg

Solutions for cell biology and biochemical assays

Parasite lysis buffer	4 % SDS 0.5 % Triton X-100 0.5x PBS in dH_2O

Percoll stock solution	90 % (v/v) Percoll 10 % (v/v) 10x PBS
60 % Percoll solution	6.7 ml Percoll stock solution 3.3 ml RPMI complete medium 0.8 g Sorbitol sterile filtered
Saponin lysis buffer	Saponin 0.03 % (w/v) in DPBS
RIPA buffer	10 mM Tris/HCl pH 7.5 150 mM NaCl 0.1 % SDS 1 % Triton X-100 1 mM PMSF 2x Protease inhibitor cocktail in dH_2O
Dilution buffer	10 mM Tris/HCl pH 7.5 150 mM NaCl 1 mM PMSF 2x Protease inhibitor cocktail in dH_2O

2.1.5.4 Solutions and buffers for protein analyses

SDS-Page and Western blot

10x Running buffer stock solution	250 mM Tris base 1.92 M Glycine 1 % (w/v) SDS in dH_2O
1x Running buffer working solution	1:10 dilution of 10x Running buffer stock solution in dH_2O
Ammonium persulfate	10 % (w/v) in dH_2O

Separating gel buffer	1.5 M Tris-HCl, pH 8.8 in dH_2O
Stacking gel buffer	1 M Tris-HCl, pH 6.8 in dH_2O
Stacking gel (for two gels, 5 % acrylamide)	0.75 ml stacking gel buffer 4.35 ml dH_2O 750 µl acrylamide (40 %) 60 µl SDS (10 %) 60 µl APS (10 %) 6 µl TEMED
Separating gel (for two gels, 12% acrylamide)	2.5 ml running gel buffer 4.2 ml dH_2O 3 ml acrylamide (40 %) 100 µl SDS (10 %) 100 µl APS (10 %) 4 µl TEMED
6x SDS sample buffer	375 mM Tris-HCl pH 6.8 12 % (w/v) SDS 60 % (v/v) Glycerol 0.6 M DTT 0.06 % (w/v) Bromophenol blue
Coomassie de-staining solution	50 ml H_2O 40 ml methanol 10 ml acetic acid
10x Western blot transfer buffer stock solution	250 mM Tris-Base 1.92 M glycerol 0.1 % (w/v) SDS in dH_2O
1x Western blot transfer buffer working solution	10 % dilution of 10x Western blot transfer buffer stock solution 20 % Methanol in dH_2O
Blocking solution	5 % (w/v) milk powder in 1xPBS

Washing buffer (PBS-Tween)	1xPBS 0.05 % Tween-20

2.1.6 Bacterial and Plasmodium strains

P. falciparum strain 3D7	clone of NF54 isolated from an airport malaria patient, near Schiphol Airport, Amsterdam, Netherlands
Bacterial strain *E. coli* XL-10 Gold	Tetr Δ(mcrA)183 Δ(mcrCB-hsdSMR-mrr)173 endA1 supE44 thi-1 recA1 gyrA96 relA1 lac Hte [F' proAB lacIqZΔM15 Tn10 (Tetr) Amy Camr]

2.1.7 DNA-polymerases and enzymes

DNA-Polymerase	Concentration (units/µl)	Manufacturer/Distributor
FirePol® DNA Polymerase	5	Solis BioDyne, Estonia
Phusion® High-Fidelity DNA Polymerase	2	NEB, Ipswich, USA

Ligase	Concentration (units/µl)	Manufacturer/Distributor
T4 DNA-Ligase	400	NEB, Ipswich, USA

Phosphatase	Concentration (units/µl)	Manufacturer/Distributor
Alkaline Phosphatase, Calf Intestinal (CIP)	5	NEB, Ipswich, USA

Restriction enzyme (cut site)	Concentration (units/µl)	Manufacturer/Distributor
AvrII (C'CTAGG)	5	NEB, Ipswich, USA
BamHI-HF® (G'GATCC)	20	NEB, Ipswich, USA
EcoRI-HF® (G'AATTC)	20	NEB, Ipswich, USA
EcoRV-HF® (GAT'ATC)	20	NEB, Ipswich, USA
KpnI-HF® (G'GTACC)	20	NEB, Ipswich, USA
MluI-HF® (A'CGCGT)	20	NEB, Ipswich, USA
NotI-HF® (GC'GGCCGC)	20	NEB, Ipswich, USA
SalI-HF® (G'TCGAC)	20	NEB, Ipswich, USA

Protease		Manufacturer/Distributor
Trypsin		Roche, Mannheim

2.1.8 Antibodies

		Dilution/Application	Source
Primary antibodies	Aldolase (rabbit)	1:2,000 for Western blot	Mesén-Ramírez *et al.*, 2016
	anti-GFP (mouse)	1:1,000 for Western blot	Roche, Mannheim
	anti-mCherry (rat)	1:1,000 for Western blot	Chromotek, München
	anti-RALP1 (rabbit)	1:500 for IFA	Haase *et al.*, 2008
Secondary antibodies	anti-mouse-HRP (rabbit)[1)]	1:3,000 for Western blot	Dianova, Hamburg
	anti-rabbit Alexa Fluor®594 (goat) [2)]	1:2,000 for IFA	Invitrogen
	anti-rat-HRP (goat)[1)]	1:3,000 for Western blot	Dianova, Hamburg
	IRDye®800CW streptavidin[2)]	1:1,000 for Western blot	LI-COR Biosciences
	anti-rat IRDye®800CW (goat)[2)]	1:5,000 for Western blot	LI-COR Biosciences
	anti-mouse IRDye®680RD (goat)[2)]	1:5,000 for Western blot	LI-COR Biosciences
	anti-rabbit IRDye®800CW (goat)[2)]	1:10,000 for Western blot	LI-COR Biosciences
	Streptavidin-HRP[1)]	1:1,000 for Western blot	Thermo Fisher Scientific
Antibody coupled beads	GFP-TRAP	IP	Chromotek, München
	RFP-TRAP	IP	Chromotek, München
	Streptavidin-Sepharose	BioID pulldown	GE Healthcare life sciences

[1)] used in combination with the ChemiDoc XRS+ imaging system (see 2.2.5.4)

[2)] used in combination with the Odyssey© Fc imaging system (see 2.2.5.4)

2.1.9 Oligonucleotides

Oligonucleotide (ordered from Sigma-Aldrich)	**Sequence** (restriction site written in lower case characters, mutations written in bold characters)
*Pf*AIP_fwd_pARL_forced_NotI	GGCgcggccgcTAACTTTTTTGATTTGGAAGAAGGC
*Pf*AIP_rev_pARL_AvrII	GGCcctaggTCTTAACATATCTTGATTAACAC
*Pf*AIP_check_integration_fwd	GGTAATGTCTTACACAAAGAATAATATTTTAC
GFP_as_272	CCTTCGGGCATGGCACTC
*Pf*ARO_wt_fwd_KpnI	GCGCggtaccATGGGAAATAATTGCTGTGC
*Pf*ARO_rev_AvrII	GCGCcctaggATCCGTTAGTCTCAATAAGAGAACATTG
*Pf*AIP_fwd_MluI	GCGCacgcgtATGGATAAATTAATAAAAGAAAATATTAATG
*Pf*AIP_rev_SalI	GCGCgtcgacTCTTAACATATCTTGATTAACACTAAC
*Pf*ARO_mut1_PCRprod1_rev	GGGGTCAGCAGC**A**C**T**AGGAT**C**CATTCTATCTTC
*Pf*ARO_mut1_PCRprod2_fwd	GAAGATAGAATG**G**ATCCT**A**G**T**GCTGCTGACCCC
*Pf*ARO_mut2_PCRprod1_rev	CTAAAATTGCCAATT**C**AGTTGCGGA**ATC**TGCACCAATAG
*Pf*ARO_mut2_PCRprod2_fwd	CTATTGGTGCA**GAT**TCCGCAACT**G**AATTGGCAATTTTAG
*Pf*ARO_mut3_PCRprod1_rev	GATAATGCACCAAT**TGC**TTT**ACC**GTCAGCAGCCCAAG
*Pf*ARO_mut3_PCRprod2_fwd	CTTGGGCTGCTGAC**GGT**AAA**GCA**ATTGGTGCATTATC
*Pf*ARO_mut4_PCRprod1_rev	GATAAAGCAACAACAGCAGCATGTACT**TG**AT**T**TAATTCGTGTG
*Pf*ARO_mut4_PCRprod2_fwd	CACACGAATTA**A**AT**CA**AGTACATGCTGCTGTTGTTGCTTTATC
*Pf*ARO_mut5_PCRprod1_rev	GAGTTGCGGATAATGCACCAATAGTTTCGCATGTTGAAGAACATAAGTTTAC
*Pf*ARO_mut5_PCRprod2_fwd	GTAAACTTATGTTCTTCAACATGCGAAACTATTGGTGCATTATCCGCAACTC
*Pf*ARO_mut6_PCRprod1_rev	CATTGTCAACGGATAA**ATC**TGATAAAGCAACAACAGCAGC
*Pf*ARO_mut6_PCRprod2_fwd	GCTGCTGTTGTTGCTTTATCA**GAT**TTATCCGTTGACAATG
FKBP39rev (sequencing)	TTGACCTCTTTTTGGAAATGTACG
pA_as (sequencing)	CAGTTATAAATACAATCAATTGG

2.2 Methods

2.2.0 Cloning strategies

For the generation of the transgenic cell line *Pf*AIP-2xFKBP-GFP (AIP_{endo}), the 3'end of the gene (634 bp) was PCR amplified (see 2.2.3.1) from *P. falciparum* strain 3D7 genomic DNA (gDNA) and cloned into the pSLI-2xFKBP-GFP vector [Birnbaum & Flemming *et al.*, 2017] in frame with 2xfkbp-gfp using Not/AvrII restriction sites. For co-localization studies, the AIP_{endo} cell line was transfected with an over-expression vector expressing *Pf*ARO-mCherry under the control of the late stage specific *ama*-1 promoter using a BSD resistance cassette for selection [Cabrera *et al.*, 2012]. To generate the *Pf*ARO-mCherry vector, the *Pfaro* gene was amplified from cDNA using the primer combination *Pf*ARO_wt_fwd_KpnI/*Pf*ARO_rev_AvrII and cloned into the vector backbone using KpnI/AvrII restriction sites. For the generation of the conditional *Pf*AIP knock-sideways (KS) cell line (AIP_{condKS}), the AIP_{endo} cell line was transfected with a mislocalizer plasmid 2xNLS-FRB-mCherry (mislocalizer) [Birnbaum & Flemming *et al.*, 2017]. For the generation of transgenic parasites overexpressing *Pf*ARO-GFP variants in conjunction with *Pf*AIP-mCherry, full length coding sequences were obtained using either cDNA library (*Pf*AIP) or plasmid (*Pf*ARO) DNA. *Pfaip* was PCR amplified using primer combination *Pf*AIP_fwd_MluI/*Pf*AIP_rev_SalI and cloned into a skip vector that enables bicistronic expression under the control of the late stage specific ama1 promoter [Kono *et al.*, 2016] using MluI/SalI restriction sites. *Pf*ARO variants were PCR amplified using overlap PCR [Ho *et al.*, 1989]. Firstly, PCR1 product was amplified using the forward primer *Pf*ARO_wt_fwd_KpnI and the reverse primer containing the mutation (see 2.1.9). Secondly, PCR2 product was amplified using the forward primer containing the mutation and the reverse primer *Pf*ARO_rev_AvrII. In a third amplification step, full length *Pfaro* variants were generated using primer combination *Pf*ARO_wt_fwd_KpnI/*Pf*ARO_rev_AvrII and template combination PCR1 product/PCR2 product. The *Pf*ARO variants were cloned into the skip vector using the KpnI/AvrII restriction sites.

2.2.1 Sterilisation

All media, buffers, solutions, glass materials and pipette tips were autoclaved at 121 °C and 1.5 bar vapour pressure for 20 min. Heat-unstable solutions were sterilized by filtration, using sterile filters with a pore size of 0.22 µm.

2.2.2 Microbiological methods

2.2.2.1 Production of chemo-competent *E. coli*

To increase the plasmid uptake of *E. coli,* the rubidium chloride method was applied to decrease bacterial cell wall stability [Hanahan, 1983]. 20 ml of LB medium was inoculated with the *E. coli* XL-10 Gold strain from a glycerol stock and incubated overnight at 37 °C with vigorous shaking. 10 ml of this culture was then transferred to a 1 liter Erlenmeyer flask with 200 ml LB-medium and incubated at 37 °C with vigorous shaking until an optical density (OD) of 0.5-0.6 was obtained. After harvesting the bacteria by centrifugation at 2,400 x g at 4 °C, the pellet was resuspended in a 60 ml TFBI buffer and incubated on ice for 10 min. After another centrifugation step (2,400 x g at 4 °C), the pellet was suspended in an 8 ml TFBII buffer and aliquoted (100 µl) into 1.5 ml reaction tubes and stored at -80 °C until further use.

2.2.2.2 Transformation of chemo-competent *E. coli*

For transformation, an aliquot with chemo-competent *E. coli* (100 µl) was thawed on ice and plasmid DNA (10 µl of a ligation (see 2.2.3.4) or 0.2 µl of a sequenced plasmid) was added before the mix was incubated on ice for 30 min. After a heat-shock of 42 °C for 45 seconds, the mix was immediately placed on ice for 2 min. 20-100 µl of the bacteria suspension was then plated on LB-agar plates containing ampicillin [100 µg/ml]. The plates were incubated at 37 °C overnight and stored at 4 °C until further use.

2.2.2.3 Overnight culture of *E. coli* for subsequent plasmid DNA preparation

For plasmid mini preparations, an LB-Amp medium volume of 1.8 ml in a 2 ml reaction tube was inoculated with a bacterial colony from an agar plate or glycerol stock and incubated overnight at 37 °C with vigorous shaking. For plasmid midi preparations, a LB-Amp medium volume of 200 ml was inoculated in an Erlenmeyer flask and incubated overnight at 37 °C with vigorous shaking.

2.2.2.4 Freezing of *E. coli*

For long term storage of *E. coli* cells, a 500 µl overnight culture was mixed with 500 µl of glycerol in a 1.5 ml reaction tube and stored at -80 °C.

2.2.3 Molecular biological methods

2.2.3.1 Polymerase chain reaction (PCR)

Two different DNA polymerases were used for the amplification of a DNA template. For preparative PCRs, Phusion polymerase with a proofreading function was used. For diagnostic PCRs, FirePol polymerase was used. The oligonucleotides used are listed in 2.1.9. Typical PCR-reactions were prepared as follows:

Preparative PCR	µl
5x Phusion buffer	10
dNTPs [2 mM]	5
Primer fwd [50 µM]	0.5
Primer rev [50 µM]	0.5
Phusion® High-Fidelity DNA Polymerase (2 U/µl)	0.5
Template [100 ng/µl]	1
dH_2O	32.5

Diagnostic PCR	µl
10x FIREPol buffer	1
dNTPs [2 mM]	1
Primer fwd [50 µM]	0.4
Primer rev [50 µM]	0.4
FirePol® DNA Polymerase (5 U/µl)	0.1
Template/colony	0.2
dH_2O	5.9
$MgCl_2$ [25 mM]	1

Phase		Temperature	Time
Denaturation		95 °C	4 min
25-30 cycles	Denaturation	95 °C	30 s
	Primer annealing	48-70 °C	30 s
	Elongation	64-72 °C	X min
Storage (optional)		4 °C	∞

(X) depends on the expected size of the PCR-product and was usually 1 min per 1,000 base pairs (bp).

2.2.3.2 PCR-product purification

To purify PCR-products and digested vector DNA for subsequent ligation, the NucleoSpin Gel and PCR Clean-up kit were used, according to the manufacturer's protocol. PCR products and vector DNA were eluted with a 15-30 µl AE elution buffer.

2.2.3.3 DNA restriction digest

Preparative digests of PCR products and vectors were performed using different DNA restriction enzymes to create sticky ends for the cloning of plasmids. Analytical digests were performed of mini and midi DNA preparations to exclude recombination and to confirm the correct insertion of PCR products into the plasmid. The incubation time for preparative digests was 2-3 h, and for analytical digests it was 30-60 min, each at 37 °C. Analytical digests were performed using at least five different enzymes, resulting in a distinct vector-specific band pattern of fragmented DNA within the agarose gel. Typical digest-reactions were prepared as follows:

Preparative digest	µl
10x Cut Smart Buffer	2
Restriction enzyme A [20 U/µl]	0.2
Restriction enzyme B [20 U/µl]	0.2
Vector/insert [100 ng/µl]	4
dH_2O	13.6

Analytical digest	µl
10x Cut Smart Buffer	2
Restriction enzyme A [20 U/µl]	0.2
Restriction enzyme B [20 U/µl]	0.2
Restriction enzyme C [20 U/µl]	0.2
Restriction enzyme D [20 U/µl]	0.2
Restriction enzyme E [20 U/µl]	0.2
Vector [100 ng/µl]	4
dH_2O	13

After a preparative digest of a vector, 0.5 µl of CIP phosphatase was added to the reaction and incubated for 30 min at 37 °C in order to dephosphorylate the 5' ends of digested vector DNA.

2.2.3.4 DNA fragment ligation

Digested PCR products and vectors were ligated using the T4 ligase. The ligation mix was incubated for 30-60 min at room temperature (RT) and heat-inactivated by incubation at 65 °C for 20 min. Afterwards the ligation-reaction was used for the transformation of chemo-competent *E. coli* cells. Needed volumes of the cut vector and the insert were calculated depending on their length. Generally, a vector/insert ratio of 1:3 was used. Given a vector length of 10,000 bp and an insert size of 1,000 bp, a ligation-reaction was prepared as follows:

Ligation	µl
10x T4 ligase buffer	1
Vector [100 ng/µl]	0.5
Insert [100 ng/µl]	0.15
T4 ligase (400 U/µl)	0.5
dH_2O	7.85

2.2.3.5 Agarose gel electrophoresis

For agarose gel electrophoresis, usually 1 % agarose gels were used in this study. The agarose was mixed with a 1x TAE buffer and dissolved by boiling using the microwave. Ethidium bromide was added to a final concentration of 1 µg/ml. The solution was transferred into a gel tray and combs were placed to create pockets to allow for the loading of DNA samples. After the solidification of the gel the tray was transferred to the electrophoresis chamber, which was filled with 1x TAE. The DNA samples were prepared by adding of a 6x DNA loading buffer in a 1:6 ratio and loaded into the pockets. Electrophoresis was performed at a voltage of 150 V for 15-25 min. The size of the DNA fragments was analyzed under UV light by comparison to a DNA ladder using the ChemiDoc XRS+ imaging system. Vectors subjected to preparative digests (see 2.2.3.3) were separated using a 0.5 % gel.

2.2.3.6 Colony PCR-screen

After the overnight incubation of agar plates containing transformed *E. coli* colonies, single colonies were analyzed to determine if they contained the desired vector and the new insert. For this, diagnostic PCR (see 2.2.3.1) was performed. Sterile pipette tips were used to transfer single colonies into the PCR reaction volume. Primers that bind within the new insert and the vector were selected. The resulting PCR products were analyzed using agarose gel electrophoresis.

2.2.3.7 Plasmid preparation

Plasmids were either purified with the Nucleo Spin Plasmid Kit for small-scale purification (1.8 ml of overnight culture, Mini) or with the QIAGEN© Plasmid Midi Kit for the isolation of plasmids (Midi) used for *P. falciparum* transfection (see 2.2.6.6), according to the manufacturers' protocols. Plasmids from Minis were eluted with a 20-30 µl TE buffer. Plasmids isolated with the Midi Kit were usually eluted with a 200 µl TE buffer.

2.2.3.8 Determination of DNA concentration

DNA concentration was determined using the Thermo Fisher Scientific NanoDrop 2000c spectrophotometer to measure the absorbance at 260 nm. The purity of the DNA is determined by the quotient of the absorption of DNA at 260 nm and of proteins at 280 nm (260/280 nm). The optimum 260/280 value for pure DNA is considered about 1.8. A value < 1.8 indicates contamination with proteins, while a value > 1.8 indicates contamination with RNA.

2.2.3.9 Sequencing of plasmid DNA

After the analytical digest, the insert was sequenced to confirm that it does not contain mutations introduced during the preparative PCR (see 2.2.3.1) amplification process. For the sequencing-reaction in a 1.5 ml reaction tube, a final vector concentration of 80 ng/µl in a volume of 15 µl was desired. The final sequencing primer concentration was adjusted to 10 µM. The sequencing was performed by Seqlab, Göttingen. A typical sequencing reaction was prepared as follows:

Sequencing	µl
Vector [100 ng/µl]	12
Primer fwd/rev [50 µM]	3

2.2.4.0 Plasmid DNA precipitation for transfection

For DNA precipitation, 50 µg of purified plasmid DNA (Midi-isolated, see 2.2.3.7) was mixed with a 0.1 volume of sodium acetate and three volumes of 100 % ethanol in a 1.5 reaction tube and left at RT for 20 min. During gentle mixing, a cloudy DNA precipitate becomes visible. The solution was centrifuged at 16,000 x g for 15 min. After removing the supernatant, the DNA pellet was washed with 500 µl of 70 % ethanol. Following a subsequent centrifugation step, the supernatant was removed, and the pellet was air-dried under sterile culture conditions. The opaque DNA pellet was resuspended in 10 µl of sterile TE buffer and subjected to transfection (see 2.2.6.6).

2.2.4.1 Isolation of genomic DNA from *P. falciparum*

After saponin lysis of parasites (see 2.2.6.7), gDNA was isolated using the QIAamp© DNA Mini Kit according to manufacturer's protocol. DNA was eluted in a 50-100 µl TE buffer.

2.2.5 Biochemical methods

2.2.5.1 Discontinuous SDS-Polyacrylamide gel electrophoresis (SDS-PAGE)

To separate proteins by size, the SDS-PAGE was performed with 10-12 % SDS gels. A 6x SDS sample buffer was added to the parasite suspension (see 2.2.6.7) in a 1:6 ratio and the sample was heat-denatured at 85-95°C for 5 min with vigorous shaking. Afterwards the samples and protein ladder were loaded into the gel pockets. Depending on the size of the gel pocket, 10-20 µl of sample was loaded. The separation was carried out at 150-200 V for 60-90 min.

2.2.5.2 Coomassie Brilliant Blue staining

To detect proteins in a polyacrylamide gel, the gel was stained after separation with a Coomassie solution for 30 min with gentle shaking. Afterwards the gel was de-stained with warm Coomassie de-staining solution until the background staining was low and the blue protein bands were visible.

2.2.5.3 Western blotting

Proteins separated by SDS-PAGE were blotted from SDS gel on a nitrocellulose membrane using the wet transfer method. The polyacrylamide gel and the nitrocellulose membrane were first soaked for 10 min in a 1x Western blot transfer buffer. The gel was layered on the nitrocellulose membrane. One sponge and three Whatman filter papers, soaked in a 1x Western blot transfer buffer, were put below the nitrocellulose membrane and on top of the polyacrylamide gel. The sandwich was then placed into a cassette. The cassette was placed into the Biorad tank blotting chamber so that the nitrocellulose membrane was oriented toward the anode (+). The chamber was

filled with a 1x transfer buffer and the transfer was carried out by applying a voltage of 100 V for 60-90 min at 4 °C. Alternatively, the transfer was performed overnight by applying 15 V at 4 °C.

2.2.5.4 Immunodetection of proteins

After the transfer of proteins onto a nitrocellulose membrane, proteins can be visualized by immunodetection. First, the nitrocellulose membrane was blocked in a blocking solution for 1 hour at RT in order to block nonspecific antibody binding. Afterwards the membrane was incubated with the primary antibody (see 2.1.8), which was diluted in a 5 ml washing buffer for 1-2 hours at RT or overnight at 4 °C. After five washing steps (5 min each) with a 5 ml washing buffer, the secondary antibody, also diluted in a 5 ml washing buffer, was applied for 1 hour at RT. After five more washing steps (5 min each), the membrane was either prepared for detection using the ChemiDoc XRS+ or the Odyssey© Fc imaging system.

Using the ChemiDoc XRS+ imaging system

For HRP-coupled secondary antibodies, the ChemiDoc XRS+ imaging system was used. The washed nitrocellulose membrane was transferred to a 50 ml Falcon tube and 5 ml of enhanced chemiluminescence (ECL) substrate (ECL-Clarity™ Detection Kit) was applied to the nitrocellulose membrane for 5 min under rolling conditions. Then the membrane was transferred between two transparent foils and subsequently used for imaging. The HRP catalyzes the conversion of the substrate (*i.e.* oxidation of luminol) to a chemiluminescence signal, which was detected by the ChemiDoc XRS+ imaging system. The time of detection was dependent on the signal intensity and varied between 1-45 min.

Using the Odyssey© Fc imaging system

For LI-COR secondary antibodies, the Odyssey© Fc imaging system was used. No ECL substrate is necessary, as the LI-COR secondary antibodies (see 2.1.8) used are coupled with a fluorophore. The nitrocellulose membrane was attached with tape at its edges to a tray and the signal was detected by the Odyssey© Fc imaging system. The time of detection was dependent on the signal intensity and varied between 1-45 min.

2.2.5.5 Pulldown of biotinylated proteins and mass spec analysis (BioID)

Parasites from a 100 ml culture were harvested (see 2.2.6.8) and washed twice with DPBS (centrifugation at 10,000 x g for 5 min at 4 °C). Pellets were lysed in a 2 ml RIPA buffer on ice and three freeze-thaw cycles at -80 °C were performed for better lysis. The sample was centrifuged twice at 25,000 x g for 30 min at 4 °C and the supernatant was stored at -80 °C.

To purify the biotinylated proteins, streptavidin-sepharose beads (equilibrated in 50 mM Tris-HCl, pH 7.5) were added to the parasite lysate and incubated overnight at 4 °C by overhead rotation. Beads were washed twice in a lysis buffer, once in dH_2O, twice in Tris-HCl (pH 7.5), and three times in a 100 mM triethylammonium bicarbonate buffer (TEAB, pH 7.5). The washed beads were resuspended in a 200 µl of ammonium bicarbonate (AmBic, pH 8.3) and on-bead trypsin digestion was performed with 1 µg of trypsin for 16 h at 37 °C followed by a second trypsin digest with 0.5 µg for 2 h at 37 °C. To separate the beads from the supernatant (AmBic fraction), the sample was centrifuged at 2,000 x g for 5 min at RT and resuspended in 2x150 µl of AmBic (pH 8.3). The suspension was

transferred to a Pierce™ spin column placed in a low protein binding tube and AmBic fraction was collected. Left-over biotinylated peptides, bound to beads via interaction with streptavidin, were eluted from the beads by 2 x 150 µl of 80 % acetonitrile (ACN) and 20 % trifluoroacetic acid (TFA) solution. The suspension was collected in a separate low protein binding tube to collect the supernatant (ACN/TFA fraction). A SpeedVac centrifuge was used to dry the AmBic and ACN/TFA fractions. Dried peptides were sent to the Proteomics Core Facility at the EMBL Heidelberg. TMT labelling, desalting, mass spectrometry, and data analysis were performed by Dominik Helm, Frank Stein, and Mandy Rettel (Proteomics Core Facility, EMBL, Heidelberg). The purification of biotinylated proteins using streptavidin-sepharose beads and the preparation of AmBic and ACN/TFA fractions was performed by Samuel Pazicky (EMBL, Hamburg).

2.2.5.6 Co-Immunoprecipitation (Co-IP)

All steps were performed on ice if not stated otherwise. Parasites from a 50 ml culture were harvested (see 2.2.6.7). The purified parasites were washed twice with DPBS (centrifugation at 10,000 x g for 5 min at 4 °C) and lysed by resuspension in a 250 µl RIPA buffer. For better protein extraction, the lysate was frozen and resuspended three times at -80 °C. Afterwards the lysate was centrifuged twice at 16,000 x g at 4 °C for 10 min. The supernatant was diluted with a 750 µl dilution buffer and 100 µl of diluted supernatant (input fraction) was prepared for Western blot analysis (see 2.2.5.1). 20 µl of GFP-TRAP or RFP-TRAP agarose beads (equilibrated in a 500 µl dilution buffer) were transferred to the diluted supernatant/input fraction and incubated overnight at 4 °C with gentle overhead rotation. After centrifugation at 2,500 x g for 20 min at 4 °C, 100 µl of supernatant (post-input fraction) was prepared for Western blot analysis. The beads were washed three times with a dilution buffer (centrifugation steps at 2,500 x g for 20 min at 4 °C). From each washing, a supernatant volume of 100 µl (washing 1-3 fraction) was prepared for Western blot analysis. The agarose bead pellet was resuspended in a 100 µl 2x SDS sample buffer and prepared for subsequent Western blot analysis (eluate fraction).

2.2.6 *P. falciparum* cell biological methods

2.2.6.1 *P. falciparum* in vitro culture

The parasites were cultivated in petri dishes at a haematocrit of 2-5 % in an RPMI complete medium at 37 °C. The dishes were kept in a gas-tight chamber in which the atmosphere was adjusted to high carbon dioxide and low oxygen levels: 5 % CO_2, 1 % O_2, 94 % N_2. Depending on the experiments, the parasitemia was adjusted to 0.1-5 % by dilution and the medium was generally changed every second day. In parasite cultures with higher parasitemia, the medium was changed every day. Transfectants were selected using WR99210 in a 4 nM concentration. Integration of the pSLI construct (see 2.2.0) was selected with G418 at a final concentration of 6 nM, initially added to a 10 % parasitemia culture [Birnbaum & Flemming *et al.*, 2017]. Parasites expressing *Pf*ARO-mCherry or NLS-FRB-mCherry were selected using BSD in a 4 µg/ml concentration. Parasites expressing mCherry-FRB-BirA* were selected with BSD in a 2 µg/ml concentration.

2.2.6.2 *P. falciparum* cryo-stabilates

For the long-term storage of *P. falciparum*, ring stage parasite cultures were pelleted by centrifugation at 1.800 x g for 3 min. The medium was aspirated, and the pellet was resuspended in 1 ml MFS and transferred into a cryotube. Storage was carried out at -80 °C or in liquid nitrogen at -196 °C. To thaw the cryo-stabilates, the cryotube was put in a 37 °C water bath for 1-2 min. The suspension was transferred to a 1.5 ml reaction tube and centrifuged at 1,800 x g for 3 min. After removing the supernatant, the pellet was resuspended in 1 ml MTS. After another centrifugation step, the pellet was washed in a 1 ml RPMI complete medium and transferred to a petri dish containing a fresh RPMI complete medium and a hematocrit of 5 % for continuous cell culture. The selection drug was added 24 h later.

2.2.6.3 Giemsa staining of blood smears

Parasitemia was monitored by Giemsa staining of thin blood smears. For this, 0.2-1.0 µl of parasite culture was transferred to a glass slide and smeared using a second glass slide, resulting in a thin smear of blood. The smear was fixated to the slide by incubation in methanol for 30 seconds and was subsequently stained with a Giemsa staining solution for 5-10 min. After incubation, the staining solution was rinsed off with water and the smear was analyzed by an optical light microscope (Axio Lab A1).

2.2.6.4 Parasite sorbitol synchronization

To obtain tightly synchronized parasites, ring stage parasites were treated twice 6 hours apart with 5 % D-sorbitol. D-sorbitol is taken up by metabolically active parasites (trophozoites and schizonts), but not ring stages. A high intracellular D-sorbitol concentration allows for the hypotonic lysis of cells after the removal of sorbitol and resuspension in an RPMI complete medium. To synchronize a parasite culture, the culture was transferred into a 15 ml Falcon tube and spun down at 1,800 x g for 3 min. The supernatant was discarded, and the pellet was resuspended in a pre-warmed (37 °C) 5 % D-sorbitol solution. After incubation for 10 min at 37 °C, the Falcon tube was centrifuged at 1,800 x g for 3 min. The pellet was washed with a pre-warmed RPMI complete medium and transferred to a petri dish containing a fresh RPMI complete medium and a hematocrit of 2-5 % for continuous cell culture.

2.2.6.5 Purification of *P. falciparum* schizonts

To isolate schizonts stage parasite for transfection, parasites were harvested by overlaying 4 ml of 60 % Percoll solution with 8 ml of parasite suspension in a 15 ml Falcon tube. If the culture volume was higher, the volume was reduced by repeated centrifugation at 1,800 x g for 3 min. The 15 ml Falcon was centrifuged for 6 min without using a brake at 2,500 x g. The resulting schizont layer was transferred to a new 15 ml Falcon tube and washed two times with a pre-warmed RPMI complete medium. The schizont pellet was transferred to a 1.5 ml reaction tube.

2.2.6.6 Transfection of *P. falciparum* schizonts using the Amaxa system

50 µg of plasmid DNA was precipitated (see 2.2.4.0). The DNA pellet dissolved in a 10 µl TE-buffer was supplemented with 90 µl of Amaxa transfection buffer. The 100 µl DNA-transfection solution was used to resuspend the schizont pellet (see 2.2.6.5). The suspension was transferred to an electroporation cuvette and electroporation was performed using the Nucleofector II AAD-1001N (program U-033). Immediately after electroporation, the parasites were transferred to a 1.5 ml reaction tube containing 500 µl of packed RBCs and an equal amount of RPMI complete medium. The tube was incubated at 37 °C with vigorous shaking for 30-60 min. Afterwards the parasites were transferred to a petri dish containing 5 ml of an RPMI complete medium. After 12-16 hours the medium was changed, and the selection drug was added. During the following 5 days, the medium was changed every 24 hours.

2.2.6.7 Isolation of parasites by (restricted) saponin lysis

Parasites can be isolated from RBC by lysing in low concentrations of saponin. Saponin lyses the RBC and the PVM, but not the PPM. 5-10 ml of parasite culture was harvested (centrifugation at 1,800 x g for 3 min) and the supernatant was discarded. The pellet was resuspended in a 10 x pellet volume of ice-cold saponin lysis buffer and incubated on ice for 5-20 min on ice. The mixture was transferred into a 2 ml reaction tube and centrifuged for 5 min at 2,000 x g at 4 °C. The pellet was washed three times with DPBS (supplemented with 1 mM PMSF and 2x PIC) on ice until no hemoglobin was visible in the supernatant anymore. The supernatant was aspirated until 100 µl were left in the tube, which was used to resuspend the lysed pellet. The resuspended pellet was either stored at -20 °C until further use or SDS-PAGE (see 2.2.5.1) was performed.

2.2.6.8 Isolation of parasites by magnetic-activated cell sorting (MACS)

In order to obtain schizonts for the extraction of biotinylated proteins (see 2.2.5.5), 100 ml of parasite culture was pelleted by centrifugation for 5 min at 2,000 x g). The pellet was resuspended in approximately 20 ml of RPMI complete medium. A MACS cell separation column containing ferromagnetic fibers was placed into the VarioMACS magnetic stand and equilibrated with a 50 ml RPMI complete medium. Afterwards the parasite suspension was added to the column and allowed to flow slowly through it. Due to the high amount of hemozoin, trophozoites and schizonts are captured by the ferromagnetic fibers. The column was washed with a 50 ml RPMI complete medium to remove all unbound cells. Then, the column was removed from the magnetic stand and bound parasites were eluted with a 25 ml RPMI complete medium. The parasite suspension, now enriched in schizonts (due to D-sorbitol synchronization), was centrifuged for 5 min at 2,000 x g. Afterwards the parasites were subjected to saponin lysis to remove RMC material (see 2.2.6.7). The resulting pellet was used for the pull-down of biotinylated proteins (see 2.2.5.5).

2.2.6.9 Biotin labelling of parasite proteins for BioID

The culture of transgenic AIP_{bioID} parasites expressing the *Pf*AIP-2xFKBP-GFP and mCherry-FRB-BirA* construct was expanded to 210 ml and synchronized multiple times with D-sorbitol in the course of expansion to maintain a tightly synchronized culture. When parasitemia reached 20-30 %, the medium was changed twice a day. At 38 hpi, biotin was added to a final concentration of 50 µM and the 210 ml culture was subsequently divided into two

identical 100 ml cultures. A rapalog working solution was added to one culture for a final concentration of 250 nM. To increase the level of biotinylated proteins proximal to biotin ligase BirA* [Roux *et al.*, 2012], cultures were left at RT. When parasites reached the late schizont stage, the apical location of mCherry coupled BirA* ligase was confirmed by wide-field fluorescence microscopy (see 2.2.8.1). Parasites were then isolated by MACS (see 2.2.6.8) to enrich for schizonts.

2.2.7.0 Assessment of parasite growth and stage quantification by flow cytometry (FC)

Using the LSRII flow cytometer

Tightly sorbitol-synchronized parasites were adjusted to 1 % parasitemia at 30 hpi before the culture was split evenly into two dishes. To one dish, rapalog working solution was added in a final concentration of 250 nM, whereas the other served as an untreated control. Parasitemia was measured after 24 h via FC using a previously established protocol [Malleret *et al.*, 2011] with minor modifications: PBS was substituted by an RPMI complete medium. For staining, a volume of 80 µl of RPMI complete medium was added to a 1.5 ml reaction tube, followed by the addition of 1 µl of Ho33342 working solution and 1 µl of DHE working solution. The parasite culture to be analyzed was thoroughly resuspended and 20 µl of the culture was transferred into a flow cytometry tube. 82 µl of the RPMI dye mix were added to the flow cytometry tube and the suspension was mixed by shaking the tube. The mix was incubated for 20 min in the dark. Afterwards 400 µl of flow cytometry stop solution was added. Then the parasitemia was measured using the LSRII flow cytometer, using the gating as described [Malleret *et al.*, 2011].

Using the NovoCyte® flow cytometer

The procedure was as described above, except parasitemia was adjusted to 0.2 %. 20 µl of resuspended parasite culture was transferred to a 1.5 ml reaction tube. 80 µl of RPMI containing SYBR® Green and DHE was then added to obtain the final concentrations of 0.25x and 5 mg/ml, respectively. Samples were incubated for 20 min in the dark. Parasitemia was determined using a NovoCyte® cytometer. For every sample, 100,000 events were recorded.

2.2.7.1 Assessment of parasite growth and stage quantification by Giemsa smear analysis

For parasite stage quantification, tightly sorbitol-synchronized parasites were split at 30 hpi evenly into two dishes, with one dish left untreated and the other treated with rapalog at a final concentration of 250 nM. The number of trophozoites, schizonts and rings was assessed at 30 hpi and after re-invasion at 6 hpi by methanol-fixed, Giemsa-stained, thin blood smears (see 2.2.6.3) either in the presence or the absence of rapalog. For each time point, a series of 30 images were taken, and the number of RBCs, schizonts, and rings was determined manually for each image. Approximately 6,000 cells were analyzed for each culture. Then the percentage of schizonts and rings within each biological replicate was determined.

2.2.8 Microscopy

Giemsa-stained smears were analyzed by an optical light microscope.

2.2.8.1 Wide-field fluorescence microscopy

Wide-field fluorescence microscopy images were taken with a Zeiss Axio Imager M1 equipped with a Hamamatsu Orca C4742-95 camera and the Zeiss Axiovision software (version 4.7). A 100×/1.4–numerical aperture oil objective was used. Nuclei were stained with DAPI. The images were processed in ImageJ. For sample preparation, a volume of 500 µl of a parasite culture was transferred into a 1.5 ml reaction tube and incubated with DAPI (final concentration: 1 µg/ml) for 10 min. The tube was centrifuged at 1,800 x g for 1 min and the supernatant was exchanged by a 1 x pellet volume of fresh RPMI complete medium. The pellet and supernatant were resuspended and 4-5 µl were transferred to a glass slide, covered with a cover slip, and imaged immediately.

2.2.8.2 Immunofluorescence assay (IFA)

A thin blood smear was incubated in ice-cold 100 % methanol for 30 min and dried on air afterwards. Subsequently, a region of interest (appr. 0.5 x 0.5 cm^2) was marked with a DAKO pen and rehydrated with 1x PBS (containing 5 % BSA) for 5 min. The PBS was removed, and all further steps were performed in a humid chamber. The marked area was incubated with the primary anti-RALP1 antibody (see 2.1.8) diluted in 1x PBS/3 % BSA for 2 h at RT. After incubation, the primary antibody solution was washed three times with 1x PBS/3 % BSA (5 min incubation per wash step), and subsequently incubated with the secondary antibody anti-rabbit Alexa Fluor®594 (see 2.1.8) in 1x PBS/3 % BSA in the dark for 1 hour. Afterwards, the secondary antibody solution was washed off three times with 1x PBS/3 % BSA (5 min incubation per wash step). The third wash step was performed with 1x PBS supplemented with DAPI (1:1,000) and a fourth wash step using 1x PBS was performed. One drop of DAKO mounting medium was added and the slide was covered with a cover slip and sealed with nail polish. The IFA was imaged by fluorescence microscopy a few hours later after the mounting medium had dried.

2.3 Software, bioinformatic tools and databases

2.3.1 Computer software

Software	Manufacturer/Source (last access: 15.10.2020)
APBS V1.5 plugin for PyMol	https://sourceforge.net/projects/apbs/files/apbs/apbs-1.5/
Axio Vision 40 V4.7.0.0	Zeiss
Citavi V6	Swiss Academic Software
FACS Diva V6.1.3	BD Bioscience
ImageJ	https://imagej.net/Welcome
JACoP plugin for ImageJ	https://imagejdocu.tudor.lu/doku.php?id=plugin:analysis:jacop_2.0:just_another_colocalization_plugin:start#download
Windows 10 Home	Microsoft Corporation
Microsoft Office 365	Microsoft Corporation
NanoDrop 2000 V1.6	Thermo Fisher Scientific
NovoExpress	Agilent
Prism V6	GraphPad Software
PyMol V2.1.1	Schrödinger

Serial Cloner V2.6.1	SerialBasics

2.3.2 Bioinformatic tools and databases

Bioinformatical tool	Source (last access: 15.10.2020)
BLAST, blastp suite	https://blast.ncbi.nlm.nih.gov/Blast.cgi
CD-Search	https://www.ncbi.nlm.nih.gov/Structure/cdd/wrpsb.cgi
COACH	https://zhanglab.ccmb.med.umich.edu/COACH/
CSS-Palm	http://csspalm.biocuckoo.org/online.php
DEPTH	http://cospi.iiserpune.ac.in/depth
EMBOSS Needle	https://www.ebi.ac.uk/Tools/psa/emboss_needle/
Exon-Intron Graphic Maker	http://wormweb.org/exonintron
HHpred	https://toolkit.tuebingen.mpg.de/tools/hhpred
iPBA	https://www.dsimb.inserm.fr/dsimb_tools/ipba/
InterPro	https://www.ebi.ac.uk/interpro/
I-TASSER	https://zhanglab.ccmb.med.umich.edu/I-TASSER/
LALIGN	https://www.ebi.ac.uk/Tools/psa/lalign/
MobiDB	https://mobidb.bio.unipd.it/
MotifScan	https://myhits.sib.swiss/cgi-bin/motif_scan
Myristoylator	https://web.expasy.org/myristoylator/
NEBioCalculator	http://nebiocalculator.neb.com/#!/dsdnaamt
PDB	https://www.rcsb.org/
PepCalc	https://pepcalc.com/
PfamScan	https://www.ebi.ac.uk/Tools/pfa/pfamscan/
Phyre^2 V2.0	http://www.sbg.bio.ic.ac.uk/~phyre2/html/page.cgi?id=index
PlasmoDB	https://plasmodb.org/plasmo/app
PubMed	https://pubmed.ncbi.nlm.nih.gov/
PRALINE	https://www.ibi.vu.nl/programs/pralinewww/
PredGPI	http://gpcr.biocomp.unibo.it/predgpi/pred.htm
QUARK	https://zhanglab.ccmb.med.umich.edu/QUARK/
RADAR	https://www.ebi.ac.uk/Tools/pfa/radar/
Reverse complement	http://reverse-complement.com/
Robetta	https://robetta.bakerlab.org/
TargetP-2.0 Server	http://www.cbs.dtu.dk/services/TargetP/
TMHMM Server V2.0	http://www.cbs.dtu.dk/services/TMHMM-2.0/
TMpred	https://embnet.vital-it.ch/software/TMPRED_form.html
ToxoDB	https://toxodb.org/toxo/app
Translate	https://web.expasy.org/translate/
UniProt	https://www.uniprot.org/blast/

2.4 Statistical analysis

All statistical analysis was performed using GraphPad Prism 6 software. Flow cytometry and *Pf*ARO/*Pf*AIP co-localization data were tested for normal distribution with the D'Agostino Pearson test. Statistical significances were determined with unpaired, two-tailed t-test.

CHAPTER 3 RESULTS

3.1 Identification of *Tg*ARO interacting protein homologue in *P. falciparum*

It was shown that *Tg*ARO (Gene ID: TGME49_261440) interacts at the rhoptry with *Tg*AIP (Gene ID: TGME49_309190), which could be localized to a distinct rhoptry neck sub-compartment separating the rhoptry bulb from the rhoptry neck [Mueller *et al.*, 2013, 2016] (see 1.2.2.5). This part describes the identification of a *Tg*AIP homologue in *P. falciparum* and its functional characterization.

3.1.1 Putative *Pf*AIP is significantly smaller than *Tg*AIP and exhibits a positively charged conserved core region

For the identification of AIP homologues in other species, in particular *P. falciparum*, a BLASTp [Altschul *et al.*, 1990] search analysis with the protein sequence of *Tg*AIP as query sequence against the nr database [NCBI Resource Coordinators, 2018] was performed. Hits were retrieved exclusively for species of the Apicomplexa phylum and the chromerid *Vitrella brassicaformis*. Putative AIP homologues with the highest similarity in length and amino acid sequence to *Tg*AIP were found in *Hammondia. hammondi* (Gene ID: HHA_309190, query cover: 99 %, identity: 91.5 %. *H. hammondi* is a cat parasite), *Neospora caninum* (Gene ID: BN1204_053620 query cover: 99 %, identity: 69.1 %. *N. caninum* is a dog parasite) and *Besnoita besnoiti* (Gene ID: BESB_070610 query cover: 99 %, identity: 52.7 %. *B. besnoiti* is a cattle parasite). The protein length of putative AIP homologues from *Plasmodium spp*. with about 400 aa were about half the size of *Tg*AIP (822 aa) (Fig. 3.1A). Homology to a gene (GeneID: Vbra_13064) of *V. brassicaformis*, a free-living, photosynthetic marine algae, was also identified. The sequence of the corresponding uncharacterized protein has a length of 1,704 aa which is considerably longer than the *Tg*AIP sequence. The alignment (query cover: 19 %, identity: 31.3 %) occurred at the C-terminal region of Vbra_13064.

A putative AIP homologue (hereafter named *Pf*AIP) could be identified in the *P. falciparum* genome. The *Pfaip* gene (Gene ID: PF3D7_1136700) is located on chromosome 11 and comprises 2,017 bp subdivided into seven exons. Its transcription is upregulated in late blood stage parasites [Bozdech *et al.*, 2003; Llinás *et al.*, 2006]. The coding sequence of the *Pfaip* gene consists of 1,266 bp and the deducted amino acid sequence comprises 421 aa. The predicted molecular weight of *Pf*AIP is 49 kDa, which is considerably less than *Tg*AIP with a length of 822 aa and a predicted molecular weight of 89 kDa.

Two splice variants of *Pf*AIP are annotated at PlasmoDB: PF3D7_1136700.1 (7 exons) and PF3D7_1136700.2 (6 exons), whereas splicing exon 3 (resulting peptide sequence: S_{101}IDNFPFKSYGHVPSISDKIK$_{121}$) results in the shortening of the exon 3 sequence to a single arginine in splice variant PF3D7_1136700.2 (Fig. 3.1B).

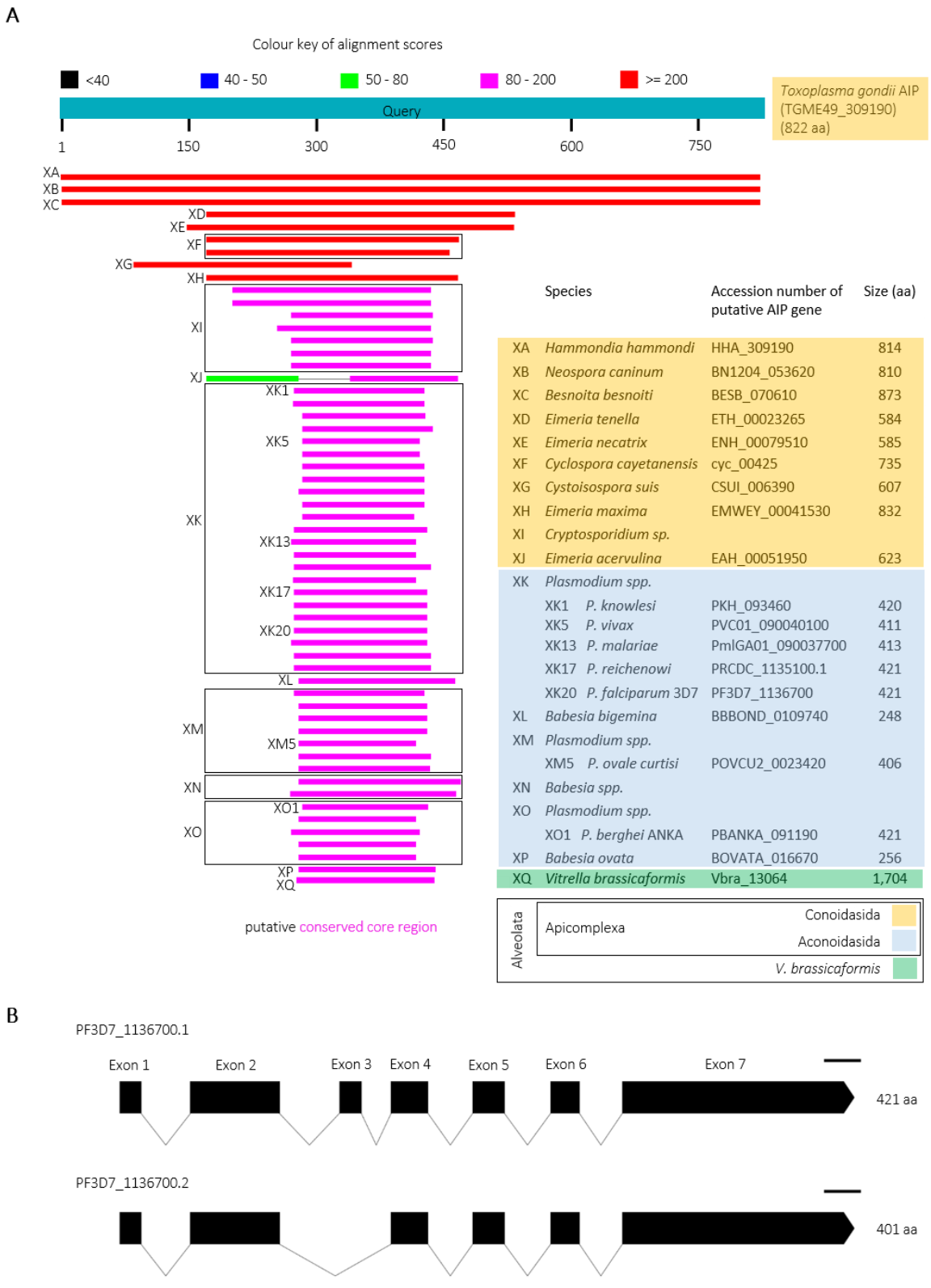

Fig. 3.1 | *Tg*ARO interacting protein (*Tg*AIP) sequence homology analysis identified putative AIP predominantly in Apicomplexa. (**A**) Using the amino acid sequence of *Tg*AIP (Gene ID: TGME49_309190) as query, an NCBI BLASTp search analysis against the nr database was performed. Only hits with an alignment score of ≥ 80 are shown. Color key reflects alignment scores of *Tg*AIP with retrieved putative AIP proteins from several alveolate species of the Apicomplexa phylum and the chromerid *V. brassicaformis*. Retrieved hits are named XA - XQ and refer to the alveolate species listed. The size of the retrieved proteins is denoted in amino acids (aa). Alignment suggests a putative conserved core region (magenta). (**B**) Schematic shows two isoforms of the AIP homologue in *P. falciparum*. Isoform PF3D7_1136700.1 contains exon 3, which is spliced out in isoform PF3D7_1136700.2.

Black scale bars indicate a length of 100 nucleotides (nt). The length of the deducted amino acid sequence is depicted on the right.

To assess possible repetitive protein sequences in *Tg*AIP and *Pf*AIP, both proteins were examined for internal repeats using RADAR [Madeira *et al.*, 2019]. RADAR analysis of the *Tg*AIP protein did not suggest internal repeats as the reason for its considerably larger size compared to *Pf*AIP (data not shown). Phosphoproteomic data displayed at PlasmoDB (www.PlasmoDB.org) showed that *Pf*AIP is phosphorylated at residues S_{76}, Y_{91}, T_{92}, S_{101}, S_{115}, S_{371} and T_{374} (data not shown). Apart from phosphorylation, no other PTM is reported or could be predicted using online prediction tools PredGPI (GPI-anchor), CSS-Palm (palmitoylation) and Myristoylator (myristoylation). No functional domains could be identified using available online prediction tools such as HHpred, InterPro, MotifScan, PfamScan, TMpred, TargetP and the TMHMM prediction server.

The onset of *Pfaro* transcription appears to lag behind *Pfaip* transcription by about two hours (S2A, Appendix). Transcript levels of asexual and sexual life stages [López-Barragán *et al.*, 2011] retrieved from PlasmoDB showed a higher transcription level for *Pfaro* in late trophozoite and schizont stages, whereas the transcript level of *Pfaip* is highest in ookinetes [López-Barragán *et al.*, 2011] and oocysts [Zanghì *et al.*, 2018] (S2B, Appendix). *Pfaip* and *Pfaro* genes are listed in the invadome subnetwork [Hu *et al.*, 2010].

BLAST search analysis (see Fig. 3.1A) suggested that putative AIP proteins of different Apicomplexa parasites share a conserved core region (CCR). A PRALINE multiple sequence alignment [Simossis & Heringa, 2005] was performed for AIP homologues of different Apicomplexa species to isolate the CCR (S3A, Appendix). Using LALIGN [Madeira *et al.*, 2019], a CCR was identified for *Pf*AIP spanning residue K_{82} to E_{260} (length: 179 aa) and for *Tg*AIP spanning residue K_{239} to E_{416} (length: 178 aa) (S3B, Appendix). EMBOSS Needle alignment [Madeira *et al.*, 2019] of *Pf*AIP and *Tg*AIP CCRs revealed a 29.4 % identity and 54.5 % similarity, whereas the alignment of full length *Tg*AIP and *Pf*AIP showed only a 10.1 % identity and 21.2 % similarity (S3B, Appendix). The phosphorylation-sites (S_{76}, Y_{91}, T_{92}, S_{101}, S_{115}, S_{371} and T_{374}) are located at the beginning of the CCR and within the C-terminus of *Pf*AIP. Interestingly, phospho-proteomic data displayed at ToxoDB [www.ToxoDB.org] shows excessive phosphorylation after the CCR of *Tg*AIP within its C-terminus at residues S_{562}, S_{564}, S_{567}, T_{568}, T_{585}, S_{645}, S_{677}, S_{679}, S_{694}, S_{716}, T_{726}, S_{731}, S_{741}, S_{742}, Y_{747}, T_{801}, T_{805} and T_{810}.

Intrinsically disordered regions (IDR) lack a unique 3D structure because of an insufficient amount of hydrophobic amino acids to mediate folding. IDRs increase conformational heterogeneity, allowing the protein to exhibit various conformations. Also, IDRs contain linear peptide motifs that mediate protein-protein interaction (PPI) [Babu, 2016; Deiana *et al.*, 2019]. MobiDB [Piovesan & Tabaro *et al.*, 2018] was used to determine the IDRs of *Tg*AIP and *Pf*AIP. For *Pf*AIP, no IDRs were determined. The disorder content of full length *Tg*AIP was calculated to 62.4 %, whereas for the CCR of *Tg*AIP, no IDRs were predicted (data not shown).

BLASTp analysis also retrieved a protein from *V. brassicaformis* (Gene ID: Vbra_13064) (see Fig. 3.1A). Sequence alignment occurred within a short region on Vbra_13064 at its C-terminus. CD-search analysis

[Marchler-Bauer & Bryant, 2004] was performed to identify conserved sequence motifs of Vbra_13064 and showed that part of its C-terminal region, where the BLASTp alignment occurred, is predicted as a putative PH domain (E-value: 5.52^{-03}) spanning 52 aa between position T_{1605} and K_{1656} (data not shown). Using LALIGN, an inner core region (ICR) of *Tg*AIP and *Pf*AIP with highest similarity to *Vb*AIP's putative PH domain was determined (S3B, Appendix). The ICR of *Tg*AIP spans residue G_{329} to K_{382} (length: 54 aa). The ICR of *Pf*AIP spans residue K_{170} to S_{225} (length: 56 aa). To assess the level of conservation between *Vb*AIP's putative PH domain to the ICRs of *Tg*AIP and *Pf*AIP, EMBOSS Needle alignment was performed. Aligning *Vb*AIP's putative PH domain to *Tg*AIP's ICR showed a 31.5 % identity and 55.6 % similarity, whereas aligning *Vb*AIP's putative PH domain to *Pf*AIP's ICR showed a 30.4 % identity and 42.9 % similarity (S3C, Appendix). PH domains accommodate binding sites for phosphorylated inositol head groups, polyproline helices, and phosphotyrosine peptides and mediate membrane anchoring to phospholipids and versatile protein-protein interactions [Scheffzek & Welti, 2012].

Assuming that the CCR (see S3A, Appendix) might be implicated in binding to other proteins by surface charge, the CCR net charge was determined using PepCalc [Lear & Cobb, 2016]. The net charge of *Pf*AIP's CCR (residue K_{82} to E_{260}) was determined to 13.2 at pH 7. The total number of negatively and positively charged residues was determined by ExPASY ProtParam [Gasteiger *et al.*, 2005]. *Pf*AIP's CCR contains 18 negatively charged residues (Asp + Glu) and 31 positively charged residues (Arg + Lys). Arg and Lys contribute to 17.3 % of the amino acid composition. The net charge of *Tg*AIP's CCR (residue K_{239} to E_{416}) was determined to -5 at pH 7. *Tg*AIP's CCR contains 31 negatively charged residues (Asp + Glu) and 26 positively charged residues (Arg + Lys). Asp and Glu contribute to 17.4 % to the amino acid composition. The net charges of full length *Pf*AIP and *Tg*AIP were determined to 11.3 and 1.7, respectively. The net charges of the *Vb*AIP putative PH domain, the *Pf*AIP ICR and the *Tg*AIP ICR were determined to -2, -1 and 0, respectively (data not shown).

3.1.2 Structure prediction of *P. falciparum* AIP

A structure of the *Pf*AIP protein is not reported. In order to obtain structural insights into the *Pf*AIP structure, this project aimed to recombinantly express the *Pf*AIP protein for structural analysis. For this, *Pf*AIP was cloned in a pET-28a vector and transformed into BL21 cells. Different concentrations of IPTG for induction as well as incubation temperature and incubation time did not result in detectable His6x-*Pf*AIP (predicted MW: 53.6 kDa) as judged by a missing band of appropriate size in Coomassie-stained gels (data not shown). As a control, an induction of His6x-*Pf*ARO [Geiger & Brown *et al.*, 2020] expression was performed, which led to a detectable band in Coomassie-stained gel (data not shown). *Pf*AIP expression from the pET-28a vector in BL21 cells was insufficient for further approaches.

Hence, different web servers for protein structure prediction were applied to model *Pf*AIP structure. First, the fast protein fold recognition server PHYRE2 [Kelley *et al.*, 2015] was used to predict the *Pf*AIP structure using the extensive mode for prediction. Out of 421 residues, 324 were modelled *ab initio* (data not shown). *Pf*AIP residues K_{172} - E_{216} were aligned with a confidence score of 61.2 to the PH domain of human protein kinase C (PDB accession: 2COA). Due to a low overall confidence in the model as well as obtaining different models for each run, the PHYRE2 determined models were rejected. Additionally, COACH [Yang *et al.*, 2013a, 2013b], Robetta [Raman, Vernon,

Thompson & Tyka *et al.*, 2009; Song & DiMaio *et al.*, 2013] and I-TASSER [Roy *et al.*, 2012; Yang & Zhang, 2015; Zhang, 2009] were used to predict the structure of *Pf*AIP.

Prediction by COACH, a meta-server for structural and protein-ligand binding sites prediction, did not suggest a known structural motif for *Pf*AIP, as indicated by low C-score of 0.03. The predicted structural model (Z-score: 5.84) was declared a "hard target for structure modelling" by COACH and therefore rejected. The structure prediction service Robetta predicted a domain of *Pf*AIP, spanning residues K_{153}-V_{296}, with a confidence score of 0.45, which was aligned to different alignment clusters. The highest ranked alignment cluster was the kindlin-1 PH domain (PDB accession: 4BBK) from *Mus musculus* (data not shown).

The top hit *Pf*AIP model, predicted by I-TASSER, showed a C-score of -1.65, an estimated template modelling (TM)-score of 0.51 ± 0.15 and an estimated root-mean-square deviation (RMSD) of atomic positions of 10.8 ± 4.6 Å. This model was matched by I-TASSER to all structures in the PDB library [Berman *et al.*, 2000]. The top hit of identified structural analogues was the recently published structure of SspE (PDB accession: 6JIV) [Xiong *et al.*, 2020]. I-TASSER alignment of the *Pf*AIP model with SspE resulted in a TM-score of 0.958 and a RMSD of 1.67. The sequence identity in the structurally aligned region was 0.074, whereas the alignment coverage was 0.993. Superposition of the 6JIV query structure and the predicted *Pf*AIP model shows the level of structural similarity (S4, Appendix). The predicted *Pf*AIP structure can be divided into two domains that are connected by a linker separating the N-terminal domain, containing most of the CCR (spanning residue K_{82} - E_{260}), from the C-terminal domain. The electrostatic surface potential, calculated by APBS [Baker *et al.*, 2001], showed patches of positive and negative charges within the N-terminal domain. Another model (data not shown) with a C-score of -1.65 (no information about TMD and RMSD) was predicted. Since I-TASSER did not align this model to putative structural analogues as it did for the first model, the iPBA web server [Gelly *et al.*, 2011] was used to identify structural analogues within the SCOP (structural classification of proteins) databank [Andreeva *et al.*, 2014, 2020]. With a low structural alignment score of 1.6 (SCOP sequence identity cut-off: 70 %), structural similarity to NADH-dependent butanol dehydrogenase A (SCOP identifier: 1vlja) and interferon-inducible GTPase (SCOP identifier: 1tq4a) was identified. In an attempt to model the structure of *Pf*AIP's CCR, the QUARK web server [Xu & Zhang, 2012, 2013] was used. QUARK predicted five different structures which were analyzed by the iPBA web server (using the same cut-off value). A structural alignment score higher than 2.5 was calculated for none of the five predicted structures, hence all models were rejected.

To allow for statements about the relative position of individual amino acids on the surface of the protein obtained from I-TASSER's calculation, DEPTH, a web server for computing the depth of amino acids [Tan *et al.*, 2011, 2013] for a given protein structure was used. DEPTH calculation suggested that *Pf*AIP phosphorylation-sites (Y_{91}, T_{92}, S_{101}, S_{115}, S_{371} and T_{374}) are located at or near the surface of the protein, whereupon residue S_{76} was declared as a buried amino acid since it is located at a depth of about 10, as calculated by DEPTH (S4, Appendix).

The data presented here suggests the presence of a *Tg*AIP homologue in *P. falciparum* (*Pf*AIP) with considerably smaller size that exhibits a positively charged conserved core region. The *Pfaip* gene is transcribed in two splice isoforms. Apart from phosphorylation, no other post-translational modifications are annotated or predicted for *Pf*AIP. Its highest expression occurs in oocyst and ookinetes, which is different to *Pf*ARO expression.

3.2 Endogenous tagging and localization of *P. falciparum* AIP

Since *Pf*AIP exhibits a significantly smaller size than *Tg*AIP and shares a low overall identity and similarity (see 3.1.1), another function or localization besides its *T. gondii* homologue seemed conceivable. To assess the spatio-temporal localization of *Pf*AIP and its function in asexual blood stage parasites, a transgenic knock-in line with a 2xFKBP-GFP tagged *Pf*AIP was created by using the selected linked integration (SLI) approach [Birnbaum & Flemming *et al.*, 2017].

3.2.1 *Pf*AIP tolerates tagging with 2xFKBP-GFP

To achieve tagging of *Pf*AIP with 2xFKBP-GFP, the last 634 nucleotides of the *Pfaip* gene were PCR amplified and used as targeting region to enable the insertion of SLI plasmid by homologous recombination to create line AIP_{endo} (Fig. 3.2A). After appropriate drug selection (see 2.2.6.1), diagnostic PCR on isolated AIP_{endo} gDNA indicated correct integration of the SLI plasmid (Fig. 3.2B). The expression of *Pf*AIP-2xFKBP-GFP in late schizont stage parasites was confirmed by Western blot (WB) analysis using a GFP-specific antibody. A protein band was detected at appr. 110 kDa (calculated MW of *Pf*AIP-2xFKBP-GFP is 106 kDa) in AIP_{endo} parasites but not in parental 3D7 parasites (Fig. 3.2C). Additionally, a faint band at appr. 70 kDa was also detected for AIP_{endo} parasites, possibly indicating a N-terminal degraded/processed form of *Pf*AIP-2xFKBP-GFP.

3.2.2 *Pf*AIP localizes to rhoptry neck of merozoites

Localization of *Pf*AIP-2xFKBP-GFP was examined by wide-field fluorescence microscopy of unfixed AIP_{endo} parasites. In late schizonts as well as in free merozoites, *Pf*AIP-2xFKBP-GFP is localized to the parasite apex (Fig. 3.2D). To allow for comparative analysis of *Pf*AIP and *Pf*ARO localization, AIP_{endo} parasites were transfected with a vector for ectopic over-expression of *Pf*ARO-mCherry controlled by the late schizont-specific Ama1 promoter. *Pf*AIP-2xFKBP-GFP and *Pf*ARO-mCherry signals are distinct with a partial overlap putatively at the rhoptry neck (Fig. 3.2E). To further confirm the rhoptry neck localization of *Pf*AIP-2xFKBP-GFP, an indirect immunofluorescence assay (IFA) using an antibody against the C-terminal region of the rhoptry neck marker RALP1 [Haase *et al.*, 2008; Ito *et al.*, 2013] was performed. The IFA labelling pattern showed a higher degree of *Pf*AIP-2xFKBP-GFP and RALP1-C signal overlap (Fig. 3.2F).

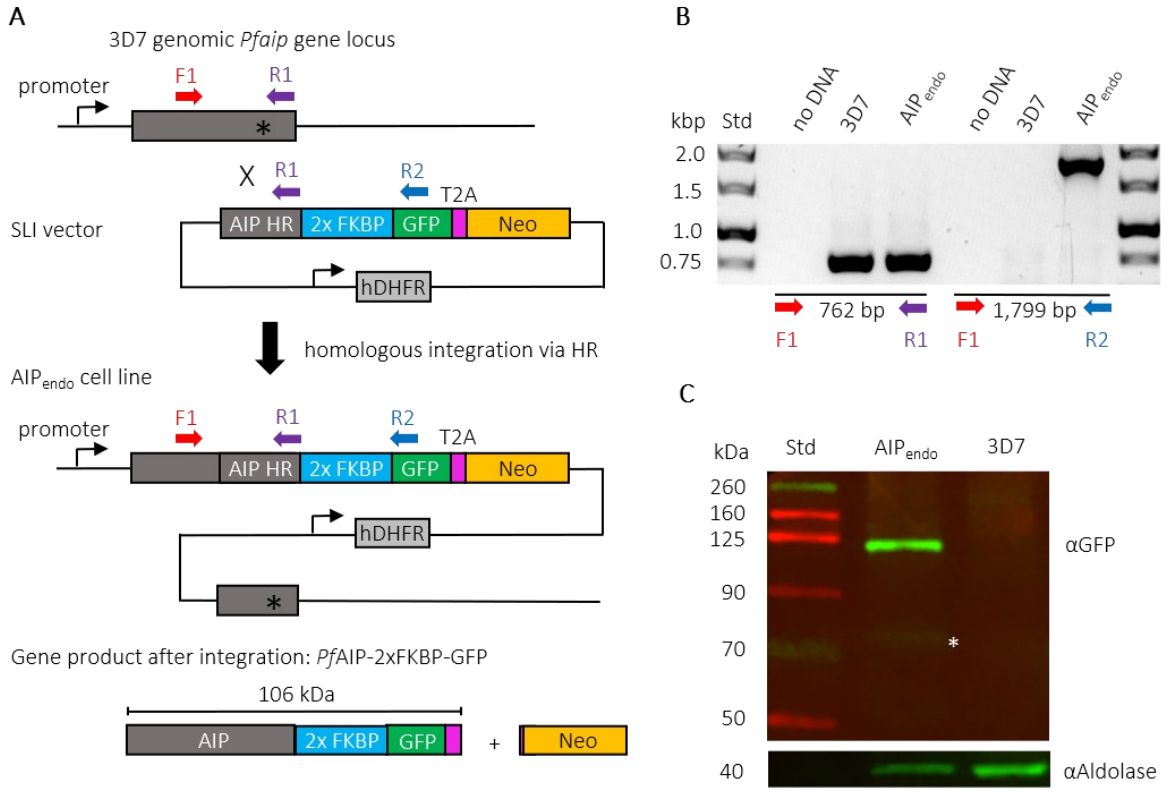
A
3D7 genomic Pfaip gene locus
promoter
F1
R1
X
R2
T2A
SLI vector
AIP HR
2x FKBP
GFP
Neo
hDHFR
homologous integration via HR
AIP endo cell line
Gene product after integration: PfAIP-2xFKBP-GFP
106 kDa
AIP
B
kbp
Std
no DNA
3D7
AIP endo
2.0
1.5
1.0
0.75
762 bp
1,799 bp
C
kDa
260
160
125
90
70
50
40
αGFP
αAldolase

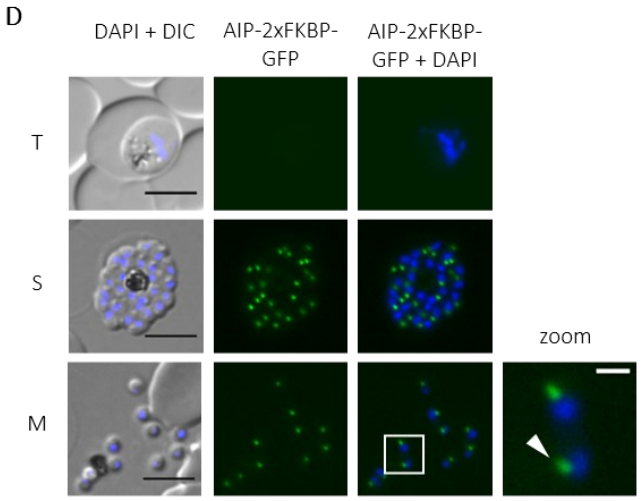
D
DAPI + DIC
AIP-2xFKBP-GFP
AIP-2xFKBP-GFP + DAPI
T
S
M
zoom

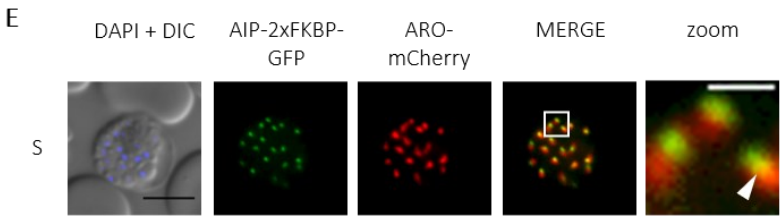
E
DAPI + DIC
AIP-2xFKBP-GFP
ARO-mCherry
MERGE
zoom
S

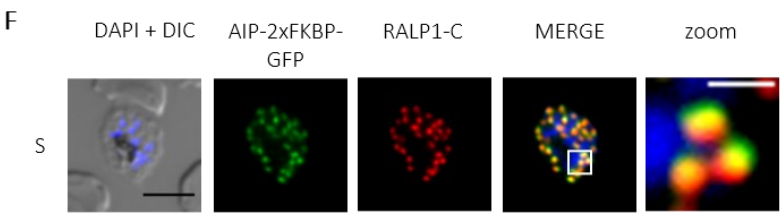
F
DAPI + DIC
AIP-2xFKBP-GFP
RALP1-C
MERGE
zoom
S

Fig. 3.2 | Endogenous *Pf*AIP can be fused with 2xFKBP-GFP and localizes to the rhoptry neck of merozoites. (**A**) Schematic representation of the most important building blocks of the pSLI-*Pf*AIP-2xFKBP-GFP vector used for homologous integration in the genomic *Pfaip* locus of the parental 3D7 wild-type cell line. Homologous recombination is indicated by "X". Integration results in tagging of the *Pfaip* gene with 2x*fkbp-gfp*, generating the cell line AIP_{endo}. The resulting gene product after integration is *Pf*AIP-2xFKBP-GFP with a calculated MW of 106 kDa and neomycin phosphotransferase II. Gray, *Pfaip* gene and homologous region (HR); turquoise, 2xFKBP; green, GFP; magenta, T2A skip peptide; orange, gene coding for neomycin phosphotransferase II conferring resistance to the selection marker neomycin used for positive selection of integrants; light gray, gene coding for hDHFR conferring resistance to the selection marker WR99210 used for positive selection of the pSLI-*Pf*AIP-2xFKBP-GFP vector; black asterisk, 3'end of the endogenous *Pfaip* gene. Arrows indicate the positions of primers used for diagnostic PCR in (B). F1, forward primer 1 binding upstream HR; R1, reverse primer 1 binding at the 3'end of HR; R2, reverse primer 2 binding within the GFP coding region. (**B**) Diagnostic PCR analysis of the rendered *Pf*AIP locus from the isolated genomic DNA (gDNA) of AIP_{endo} parasites using primers F1, R1 and R2. Primer combinations show expected sizes of PCR products in base pairs (bp). PCR analysis was performed for AIP_{endo} and 3D7 parasites as well as control without gDNA (no DNA). Std, molecular size standard; kbp, kilo base pairs. (**C**) Western blot (WB) analysis on the lysate of AIP_{endo} and 3D7 late schizont stage parasites. WB analysis was performed using a GFP-specific antibody (αGFP) and detected a band of approximately 110 kDa only for AIP_{endo} but not parental 3D7 parasites. White asterisk marks a faint band at appr. 70 kDa for AIP_{endo} parasites that could be attributed to protein processing/degradation. An aldolase-specific antibody (αAldolase) was used as loading control. (**D**) Images of wide-field fluorescence microscopy of unfixed AIP_{endo} parasites show localization of *Pf*AIP-2xFKBP-GFP (green signal) at the apical pole (white arrowhead) in developing merozoites (M) within schizonts (S) and merozoites released from ruptured schizonts. Zoom is indicated by the white square. (**E**) Wide-field fluorescence microscopy images of unfixed AIP_{endo} parasites, co-transfected with *Pf*ARO-mCherry over-expression vector. Co-localization shows some marginal overlap (white arrowhead) of *Pf*AIP-2xFKBP-GFP (green signal) and *Pf*ARO-mCherry (red signal) at the rhoptry neck. (**F**) IFA was performed with methanol-fixed AIP_{endo} schizont stage parasites that were probed with the rhoptry neck marker antibody anti-RALP1-C (αRALP1-C). For the detection of *Pf*AIP-2xFKBP-GFP, no antibody was used. The representative image of an IFA-subjected schizont shows strong co-localization of *Pf*AIP-2xFKBP-GFP (green signal) and αRALP1-C (red signal) at the rhoptry neck. Zoom is indicated by the white square. (D-F): DAPI (blue signal) was used to stain nuclei. T, trophozoite; S, schizont; M, merozoites; DIC, differential interference contrast; black scale bars, 5 µm; white scale bars, 1 µm.

Additionally, parental 3D7 parasites were transfected with a bicistronic vector for AMA1 promoter-controlled expression of *Pf*ARO-GFP and *Pf*AIP-mCherry separated by a self-cleaving skip peptide [Kono *et al*., 2016; Straimer *et al*. 2012; Szymczak *et al*., 2004] (Skip vector cell line, see also 3.4.1) and examined by wide-field fluorescence microscopy. Again, similar to the first approach, *Pf*ARO-GFP and *Pf*AIP-mCherry signals are distinct with a partial overlap putatively at the rhoptry neck (Fig. 3.3A). To verify the full-length bi-cistronic expression of *Pf*ARO-GFP(-T2A) skip peptide, predicted MW: 59.6 kDa), skip vector cell line schizont parasites were used for WB analysis using a GFP-specific antibody. WB analysis revealed two bands: one strong band matching the expected size at appr. 65 kDa and a weaker band at appr. 55 kDa (Fig. 3.3B). Milder denaturation conditions (< 85°C) did not have an influence on the occurrence or intensity of the second band (data not shown). WB on lysate from late schizont stage AIP_{endo} parasites transfected with a vector coding for *Pf*ARO-mCherry (predicted MW: 57.9 kDa) using an mCherry-specific antibody detected, again, a strong band at appr. 65 kDa and a weaker band at appr. 55 kDa, irrespective of denaturing conditions (data not shown).

To quantify the level of co-localization of *Pf*AIP and *Pf*ARO, a Pearson's correlation analysis was performed. Parasites expressing *Pf*ARO-GFP and *Pf*AIP-mCherry from the bicistronic vector and AIP_{endo} parasites co-transfected with the *Pf*ARO-mCherry over-expression vector showed the same Pearson's correlation coefficient

(PCC) of 0.7, indicating a partial overlap of *Pf*AIP and *Pf*ARO. The PCC of IFA-subjected AIP_{endo} schizonts showed almost complete co-localization of *Pf*AIP and RALP1-C as indicated by a PCC of 0.9 (Fig. 3.3C).

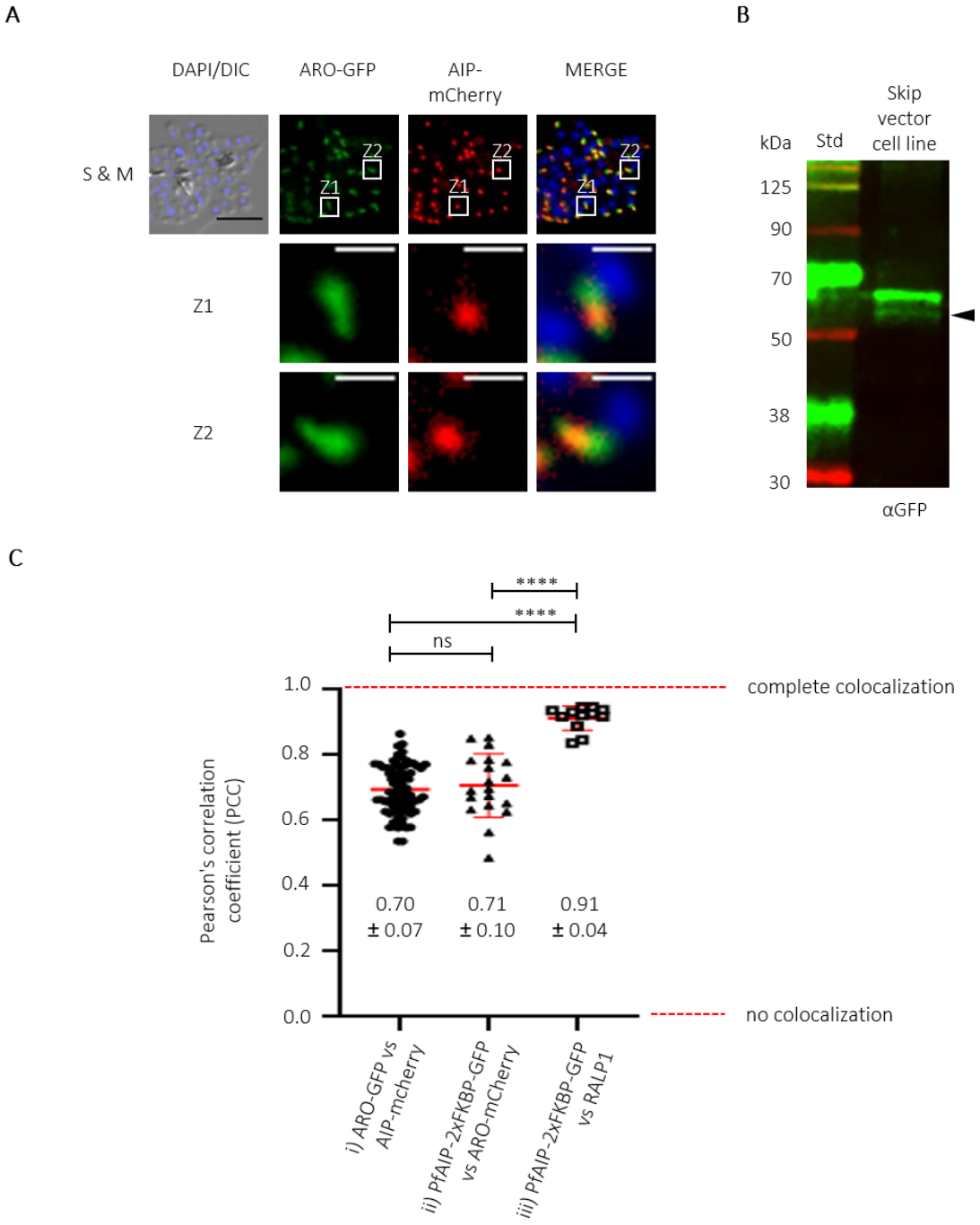

Fig. 3.3 | *Pf*ARO and *Pf*AIP show partial co-localization at the rhoptry neck. (**A**) Wide-field fluorescence microscopy images of unfixed skip vector cell line parasites expressing *Pf*ARO-GFP (green signal) and *Pf*AIP-mCherry (red signal) show partial co-localization of both signals. *Pf*ARO-GFP and *Pf*AIP-mCherry were expressed under the control of the late schizont stage Ama1 promoter from a bicistronic vector. Zoom Z1 and zoom Z2 are indicated by white squares. DAPI (blue signal) was used to stain nuclei. S, schizonts; M, merozoites; DIC, differential interference contrast; black scale bar, 5 µm; white scale bars, 1 µm. (**B**) Western blot (WB) on lysate from late schizont stage skip vector cell line parasites using a GFP-specific antibody (αGFP) detects a strong protein band at appr. 65 kDa and a weaker protein band (black arrowhead) at appr. 55 kDa, irrespective of denaturing conditions. (**C**) Partial co-localization of *Pf*ARO and *Pf*AIP at the rhoptry neck is demonstrated by Pearson's correlation coefficient (PCC) values. Each symbol of the scatter plot represents the PCC value of an individual schizont. PCC values were determined from schizont images of: i) parasites expressing *Pf*ARO-GFP and *Pf*AIP-mCherry from a bicistronic expression vector (*Pf*ARO-GFP *vs* *Pf*AIP-mCherry), ii) AIP_{endo} parasites

transfected with a vector coding for the rhoptry marker *Pf*ARO-mCherry (*Pf*AIP-2xFKBP-GFP *vs* *Pf*ARO-mCherry) (see Fig. 3.2E) and iii) AIP_{endo} parasites fixed with methanol and subjected to IFA using RALP1-C-specific antibody (*Pf*AIP-2xFKBP-GFP *vs* RALP1-C) (see Fig. 3.2F). The number (n) of analyzed cells are as follows: i) n = 79; ii) n = 19; iii) n = 12. PCC values were tested positive for normal distribution by the D'Agostino & Pearson test. Values shown below the symbols are the mean PCC values ± standard deviation. A two-tailed unpaired t-test was performed to compare the PCC values of i), ii) and iii). Values that are significantly different are indicated by asterisks. ****, P < 0.0001; ns, not significant. Error bars show standard deviation.

3.3 Functional analysis of *Pf*AIP

It has been shown that *Tg*AIP is a prerequisite for the stabilization of *Tg*ACβ and its targeting to the rhoptry neck, but, apart from that, the exact function of *Tg*AIP is unclear [Mueller *et al.*, 2016]. The same study does not report a growth perturbation in *Tg*AIP knockout parasites. Additionally, the *aip* gene was successfully knocked out in *T. gondii* [Sidik & Huet *et al.*, 2016], indicating that *Tg*AIP is not essential for *T. gondii* proliferation. In a saturation mutagenesis of *P. falciparum* NF54 wild-type parasites, 2,680 genes were identified as essential for *in vitro* asexual blood-stage growth [Zhang *et al.*, 2018]. The mutagenesis index score (MIS) and the mutant fitness score (MFS) for those genes are displayed at PlasmoDB. The parental line used for this thesis was the 3D7 line that was derived from NF54 isolate by limiting dilution [Walliker *et al.*, 1987]. Zhang *et al*. determined the MIS and MFS of *Pfaip* to 0.19 and -3.3, respectively. PhenoPlasm [Sanderson & Rayner, 2017], a database of phenotypes for malaria parasite genes, displayed *Pfaip* as a gene that is refractory to disruption. The gene was therefore considered as essential and indispensable for parasite proliferation. Hence, a targeted gene disruption (TGD) of the *Pfaip* gene using *e.g.* the SLI-TGD approach [Birnbaum & Flemming *et al.*, 2017] was not attempted and a conditional system was adapted to deplete *Pf*AIP from the rhoptry.

Since *Tg*AIP and *Pf*AIP differ significantly in size (89.3 kDa versus 49.1 kDa, respectively) (see section 3.1.1), it was assumed that they may differ in function as well. To provide functional data a conditional knock-sideways (KS) strategy [Geda *et al.*, 2008; Haruki *et al.*, 2008; Papanikou & Day, *et al.*, 2015; Patury *et al.*, 2009; Robinson *et al.*, 2010; Xu *et al.*, 2010] that was recently adapted for functional characterization of proteins in *P. falciparum* [Birnbaum & Flemming *et al.*, 2017] was applied.

As described above, *Pf*AIP is devoid of acylation or myristoylation motifs, a signal peptide and transmembrane domains and therefore is a suitable candidate for inducible mislocalization. A vector for strong constitutive HSP86 promoter-controlled expression of a 3xNLS-FRB-mCherry (hereafter named mislocalizer) containing a nuclear localized FRB domain [Birnbaum & Flemming *et al.*, 2017] was transfected to the AIP_{endo} line. The nuclear localization of the mislocalizer is mediated by three stretches of a nuclear localization signal (NLS) [Kalderon *et al.*, 1984]. The resulting line was named AIP_{condKS} (referring to *Pf*AIP conditional knock-sideways).

3.3.1 Knock-sideways of *Pf*AIP reduces number of newly formed rings per ruptured schizont

The addition of rapalog allowed the depletion of *Pf*AIP-2xFKBP-GFP from the rhoptry neck of AIP_{condKS} schizont parasites. The signal for *Pf*AIP-2xFKBP-GFP could barely be detected within the nucleus, indicating that it is either degraded or its expression is too weak to enable its localization in the nucleus. In some cases, a residual signal for *Pf*AIP-2xFKBP-GFP at the rhoptry neck could be observed (Fig. 3.4A). To quantify the expression of the mislocalizer

in the transgenic population, ≈ 300 AIP_{condKS} parasites of schizont stage were investigated via fluorescence microscopy, and all of them showed a strong nuclear FRB-mCherry signal (data not shown). Transcriptomic data (see S2A, Appendix) of erythrocytic expression time series [Bozdech *et al.*, 2003; Llinás *et al.*, 2006] displayed at PlasmoDB suggested that an appropriate timepoint to start the *Pf*AIP KS is at 30 hpi, given that transcription is increasing.

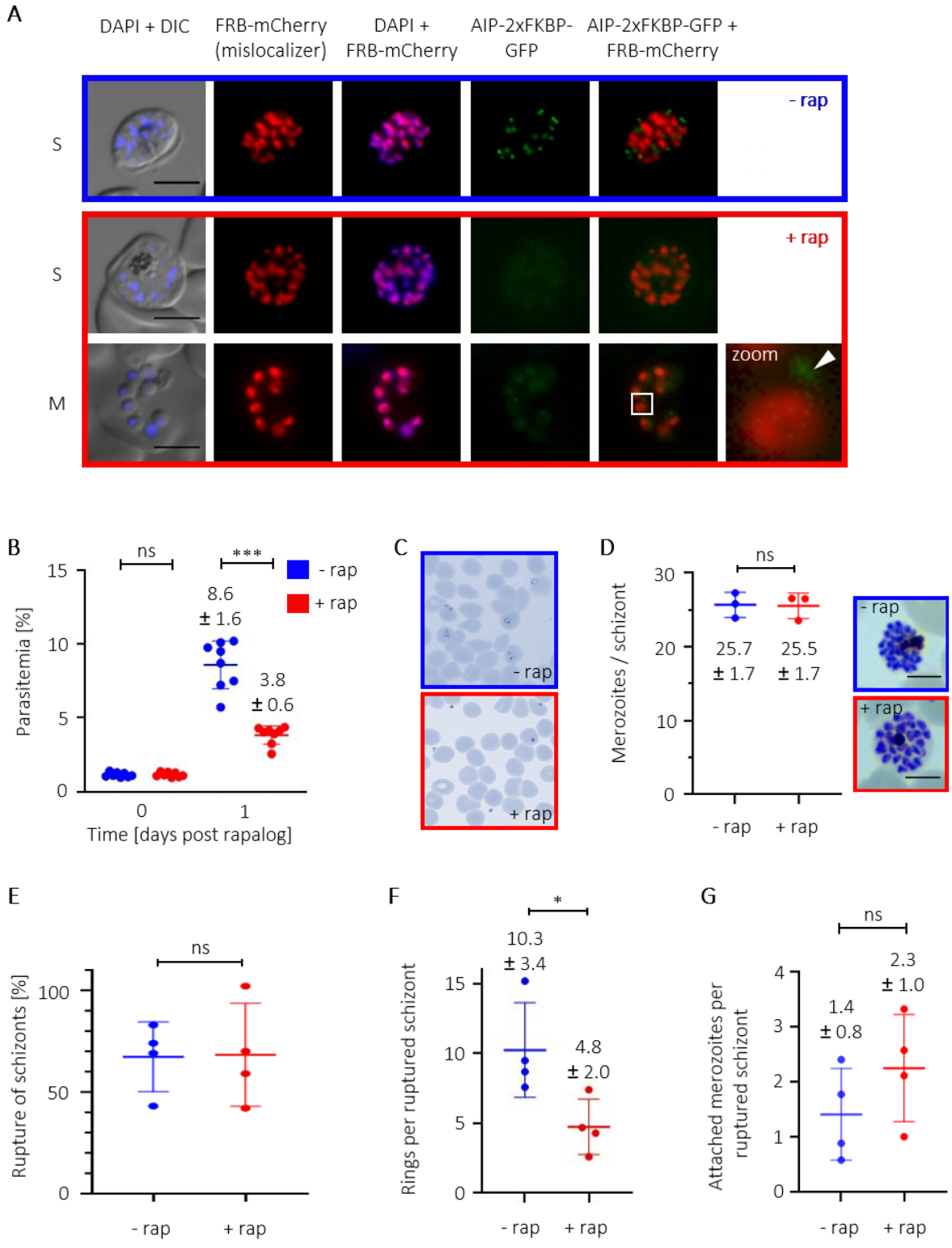

Fig. 3.4 | Conditional depletion of *Pf*AIP from the rhoptry neck leads to reduced parasitemia. (**A**) Wide-field fluorescence microscopy images of unfixed AIP_{condKS} parasites show rapalog-induced depletion of *Pf*AIP-2xFKBP-GFP (green signal) from the rhoptry neck of AIP_{condKS} parasites. Mislocalizer (red signal) co-localizes with DAPI (blue signal). Some rapalog treated merozoites show a residual green signal at the rhoptry neck (white arrowhead). 5x zoom is indicated by the white square. DAPI was used to stain nuclei. DIC, differential interference contrast; black scale bars, 5 µm; S, schizont; M, merozoites; rap, rapalog. (**B**) Phenotypic characterization of conditional *Pf*AIP-2xFKBP-GFP depletion from the rhoptry neck. Depletion of *Pf*AIP-2xFKBP-GFP from the rhoptry neck was induced by adding rapalog at 30 hours post infection on day 0. Depletion of *Pf*AIP-2xFKBP-GFP leads to a 2.2-fold reduction in parasitemia on day 1 post rapalog treatment. Each symbol of the scatter plot represents an independent experiment performed in duplicates. (**C**) Giemsa-stained thin blood smears were taken from parasite cultures (rapalog-treated and control) before FC analysis. (**D**) The number of merozoites per schizont was determined by Giemsa-stained thin blood smears taken prior to rupture. Representative images of rapalog negative (-rap) and rapalog positive (+rap) schizonts are shown on the right. Ten to twelve schizonts per condition (+/- rap) were analyzed in biological triplicates. Scale bars, 5 µm. (**E**) Egress (percentage of ruptured schizonts), (**F**) Invasion (rings per ruptured schizont) and (**G**) RBC-attached merozoites per ruptured schizont was determined from Giemsa-stained thin blood smears for each condition (+/- rap). Depletion of *Pf*AIP-2xFKBP-GFP leads to a 2.2-fold reduction in rings per ruptured schizont on day 1 post rapalog treatment. (E-G) Each symbol of the scatter plot represents an independent experiment. Approximately 6,000 cells were analyzed from Giemsa-stained thin blood smears for each experiment and condition (+/- rap). (B & D-G): Statistical significances were determined by a two-tailed unpaired t-test and are indicated by asterisks. *, $P < 0.05$; ***, $P < 0.001$; ns, not significant. Values shown below or above the symbols are the mean values ± standard deviation. Error bars show the standard deviation.

Quantification of infected erythrocytes was performed using flow cytometry (FC) analysis at a starting parasitemia of 1 %. Rapalog induced mislocalization of *Pf*AIP-2xFKBP-GFP from the rhoptry led to a 55.3 % (2.2-fold) reduction in parasitemia in the following cycle relative to untreated control (Fig. 3.4B). Giemsa-stained blood smears mirror this finding and show that in the following cycle ring stages were hardly detectable in rapalog treated parasites but were abundant in the control parasites (Fig. 3.4C). To test if the decrease in parasitemia was due to a reduced number of merozoites, the number of segmented merozoites inside mature AIP_{condKS} schizonts was counted from Giemsa-stained slides of rapalog treated and control parasites. No reduction or aberrant morphology was observed with an average of 26 merozoites per schizont (Fig. 3.4D), an expected number compared to 16-32 merozoites reported in the literature [Cowman *et al.*, 2016]. Also, the parasite egress (the percentage of ruptured schizonts) was not altered by rapalog induced *Pf*AIP mislocalization (Fig. 3.4E). However, the number of newly formed rings per ruptured schizont was significantly reduced by 53.4 % (2.2-fold) (Fig. 3.4F), indicating that invasion is compromised. Experiments to analyze this invasion phenotype, such as counting the number of RBC-attached merozoites per ruptured schizont (Fig. 3.4G) or the number of free, unattached merozoites, did not result in significant differences (data not shown).

For further investigation, additional growth assays were performed with AIP_{condKS} parasites with a starting parasitemia of 0.1 % on day 0 to allow for FC analysis of their growth over two replication cycles. Fig. 3.5A exemplarily shows the setting of gates to determine parasitemia and the proportion of rings, trophozoites and schizonts. Again, rapalog-induced mislocalization of *Pf*AIP-2xFKBP-GFP led to a 36.1 % (1.6-fold) reduction in parasitemia for AIP_{condKS} parasites after one cycle, whereas the parasitemia of 3D7 parasites was unaffected by rapalog (Fig. 3.5B). Parasite egress of AIP_{condKS} and 3D7 parasites was not affected (Fig. 3.5C), but the number of rings per ruptured schizont was significantly reduced by 36.7 % (1.6-fold) for AIP_{condKS} but not for parental 3D7 parasites (Fig. 3.5D). Egress and the number of rings per ruptured schizont obtained from Giemsa smear (see

Fig. 3.4E + F) and FC analysis (see Fig. 3.5C + D) was compared. No significant difference was determined for egress (Fig. 3.5E) or for the number of rings per ruptured schizont (Fig. 3.5F).

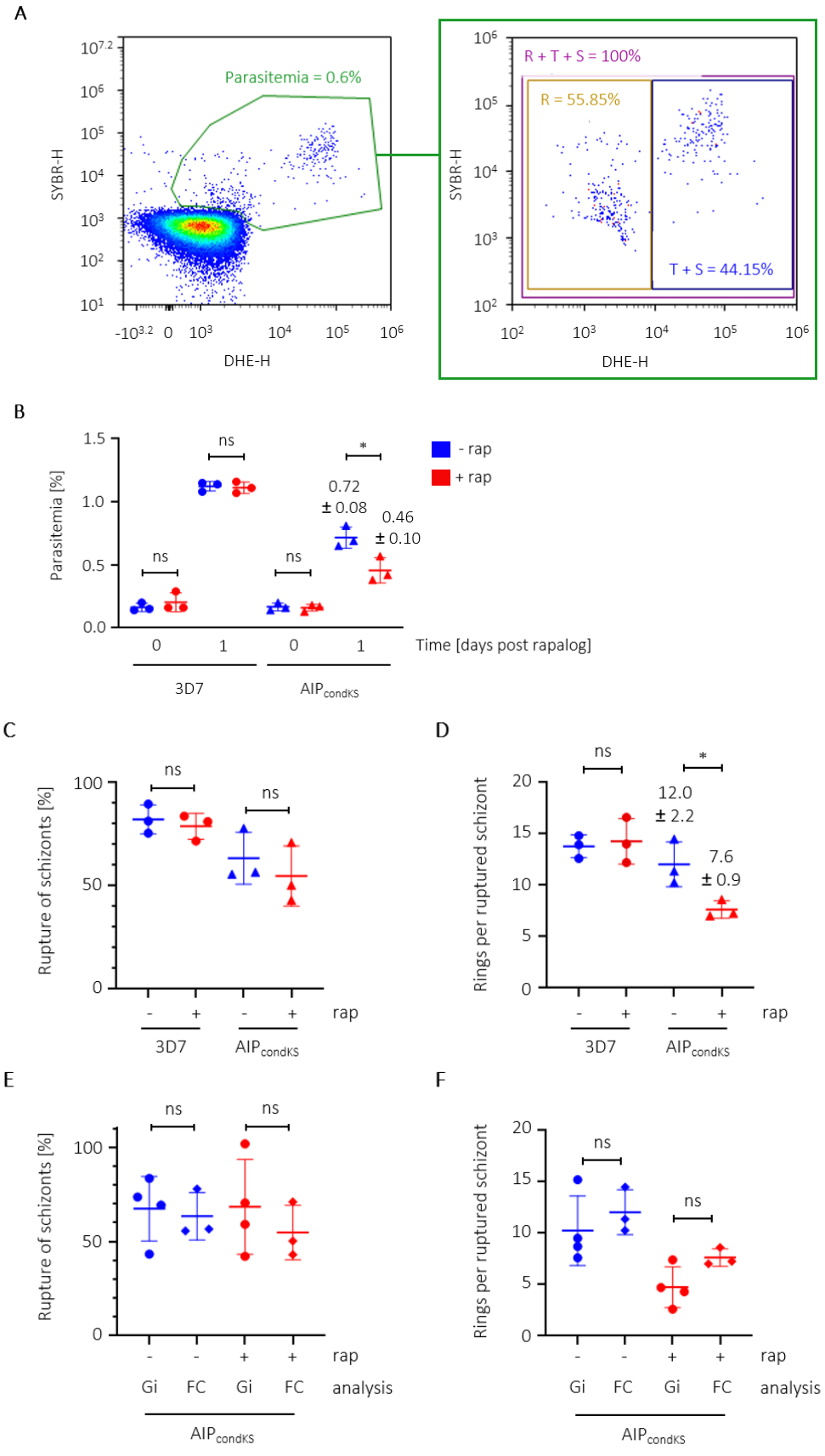

Fig. 3.5 | Knock-sideways of *Pf*AIP leads to a decrease in parasitemia due to impaired invasion. (**A**) A representative FC dot plot shows gate setting for the determination of parasitemia and the distribution of rings and later stages (trophozoites and schizonts) from singlets for 3D7 and AIP_{condKS} parasites. Signal intensities of the DNA staining chemicals SYBR green I (SYBR) and DHE are shown on the x- and y-axes, respectively. R, rings; T, trophozoites; S, schizonts. (**B**) Parasitemia was determined as in Fig. 3.4B, except parasitemia on day 0 was adjusted to 0.1 %. Rapalog induced mislocalization of *Pf*AIP-2xFKBP-GFP leads to a 1.6-fold reduction in parasitemia for AIP_{condKS} parasites. (**C**) Egress (percentage of ruptured schizonts) and (**D**) Invasion (rings per ruptured schizont) was calculated from the stage distribution determined by FC analysis. Rapalog-induced depletion of *Pf*AIP-2xFKBP-GFP from the rhoptry neck leads to a 1.6-fold reduction in rings per ruptured schizont after the reinvasion cycle on day 1 post rapalog treatment. (**E**) and (**F**) show a comparison of data obtained from Giemsa-stained thin blood smears (Gi) (see Fig. 3.4E-F) and FC analysis. (B-D) Each symbol of the scatter plot represents an independent experiment performed in duplicates. (B-F): Statistical significances were determined by a two-tailed, unpaired t-test and are indicated by asterisks. *, $P < 0.05$; ns, not significant. Values shown above the symbols are the mean values ± standard deviation. Error bars show the standard deviation. Rap, rapalog.

The invasion rate was determined by dividing the number of merozoites (26 merozoites, see Fig. 3.4D) by the number of rings per ruptured schizont. The mean invasion rate, calculated from data obtained from Giemsa smear (see Fig. 3.4F) and FC analysis (see Fig. 3.5D) of control AIP_{condKS} parasites, is 39.4 ± 13.1 % and 46.3 ± 8.4 %, respectively. It was assumed that the number of 26 merozoites per schizont was the same for parental 3D7 parasites, which resulted in a mean invasion rate of 53.0 ± 4.3 % for control and 54.9 ± 8.5 % for rapalog treated parasites, calculated from FC analysis (data not shown). The invasion rate of parental 3D7 and AIP_{condKS} parasites did not differ significantly ($P = 0.284$, data not shown).

The data presented here indicates that *Pf*AIP-2xFKBP-GFP localizes to the rhoptry neck sub-compartment and that the depletion of *Pf*AIP-2xFKBP-GFP from this rhoptry sub-compartment by KS interferes with the invasion of RBCs by merozoites.

3.4 Functional analysis of *Pf*AIP/*Pf*ARO interaction

Previous data revealed that each armadillo (ARM) repeat of *Tg*ARO is indispensable for rhoptry positioning at the parasite apex [Mueller *et al.*, 2016], and it was suggested that *Tg*ARO likely interacts directly or indirectly with *Tg*AIP [Mueller *et al.*, 2013, 2016] (see 1.2.2.5). Small angle X-ray scattering (SAXS) and *ab initio* modelling indicated a monomeric structure of *Tg*ARO with a highly negatively charged groove [Mueller *et al.*, 2016]. However, some differences between the *Tg*ARO model obtained by SAXS and the structural model of *Pf*ARO (PDB accession: 5EWP) obtained by X-ray diffraction [Geiger & Brown *et al.*, 2020] are present. For this part of the thesis, different mutations that are likely to interfere with *Pf*AIP interaction were designed based on the crystal structure of *Pf*ARO. Subsequently, these *Pf*ARO variants were cloned and expressed in the parasite to test whether putative *Pf*ARO/*Pf*AIP interaction, indirect or direct, can be averted.

3.4.1 Mutations of *Pf*ARO cause cytosolic distribution of *Pf*AIP

*Pf*ARO (Gene ID: PF3D7_0414900) protein contains two surface exposed loops (see Fig. 1.15A). It was hypothesized that the first loop (loop 1, residue 60-80), which is highly conserved between *Tg*ARO and *Pf*ARO (see S1, Appendix), is an obvious location for an interaction surface [Geiger & Brown *et al.*, 2020]. If bound to a partner protein, loop 1 probably opens up to expose residues from within loop 1 as well as on the core surface of *Pf*ARO

to contact its interaction partner. Loop 2, on the other hand, is not conserved between *Tg*ARO and *Pf*ARO (see S1, Appendix). Phospho-proteomic data displayed at PlasmoDB and ToxoDB show eight phosphorylation-sites for *Pf*ARO and just two phosphorylation-sites for *Tg*ARO, while S_{33} and S_{59} (≙ S_{61} in *T. gondii*) are phosphorylated in both proteins (see S1, Appendix).

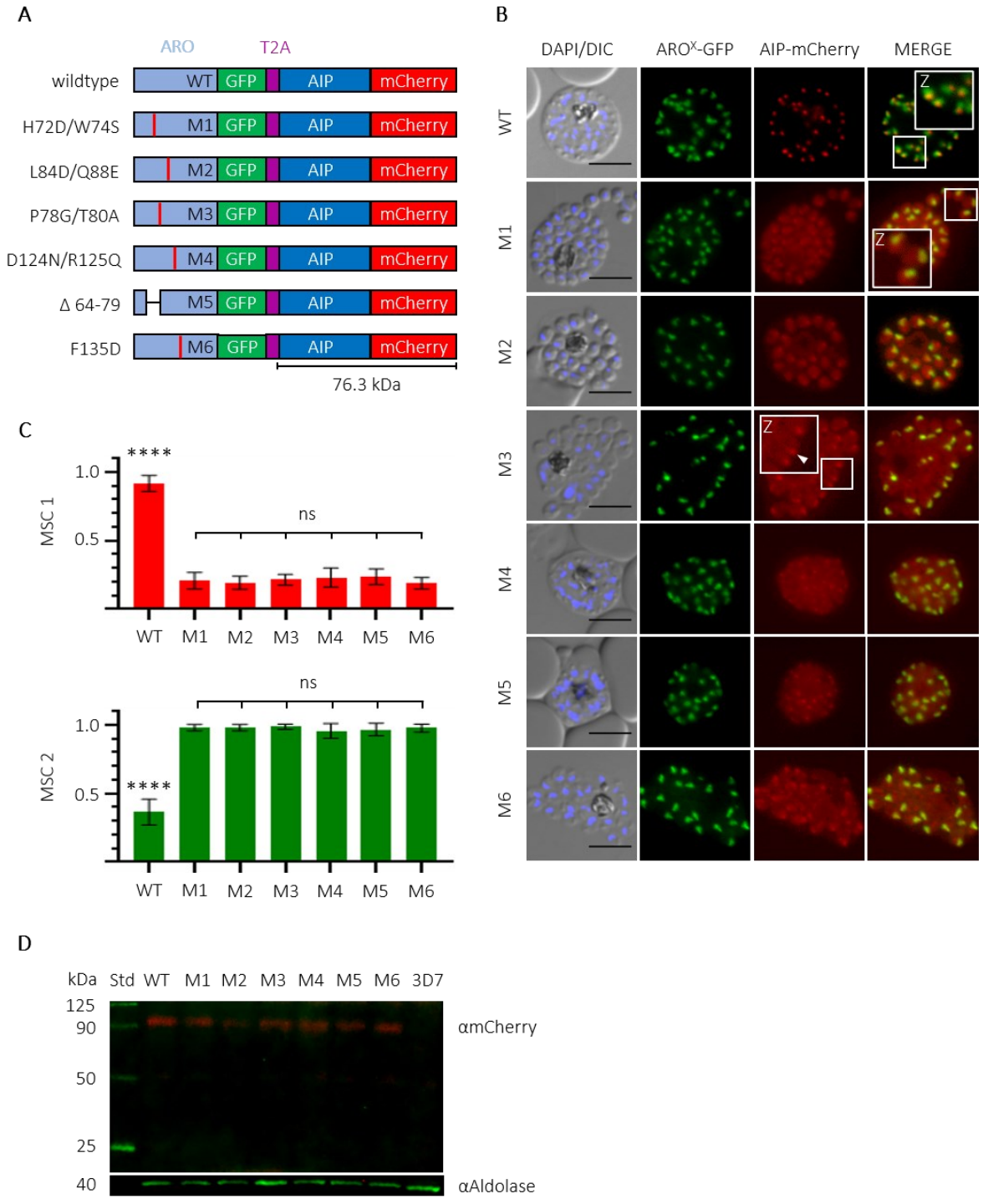

Fig. 3.6 | Mutations in putative *Pf*ARO interaction domain cause cytosolic distribution of *Pf*AIP. (**A**) Schematic representation of the most important building blocks of the bicistronic construct for the episomal expression of *Pf*ARO-GFP and its putative interaction partner *Pf*AIP-mCherry. Amino acid substitutions introduced in *Pf*ARO mutants 1-6 are shown on the left, and the resulting mutations are indicated by M1 (mutation 1) to M6 (mutation 6). The unaltered wild-type *Pf*ARO protein coding sequence is indicated by WT. *Pf*ARO-GFP and

*Pf*AIP-mCherry cassette are separated by a T2A skip peptide. Expression is under the control of late schizont stage AMA1 promoter. Light blue, *Pf*ARO coding region; green, GFP; magenta, T2A skip peptide; dark blue, *Pf*AIP coding region; red, mCherry. The predicted MW of *Pf*AIP-mCherry is shown below. (**B**) Representative wide-field fluorescence images of late stage parasites expressing either wild-type or mutant *Pf*ARO-GFP (green signal) and *Pf*AIP-mCherry (red signal). The expression of mutant *Pf*ARO-GFP converts the *Pf*AIP-mCherry distribution from apical to cytosolic. The white arrowhead indicates residual *Pf*AIP-mCherry signal at the rhoptry neck. Insets: 3x zoom, indicated by Z. The "X" in ARO^{X}-GFP denotes different *Pf*ARO versions. Zoom (Z) is indicated by the white square. DAPI was used to stain nuclei. DIC, differential interference contrast; black scale bars, 5 µm. (**C**) Cytosolic distribution of the *Pf*AIP-mCherry signal was quantified using Manders split coefficient 1 (MSC1) and Manders split coefficient 2 (MSC2). MSC1 (red) reflects the fraction of *Pf*AIP-mCherry signal overlapping with WT or the mutant *Pf*ARO-GFP signal. MSC2 (green) reflects the fraction of WT or the mutant *Pf*ARO-GFP signal overlapping with the *Pf*AIP-mCherry signal. MSC1 and MSC2 were determined from 30 schizonts for each condition (*Pf*ARO wild-type and mutant 1-6). MSC values were tested positive for normal distribution by the D'Agostino & Pearson test. MSC values were compared by a two-tailed, unpaired t-test. Statistical significances are indicated by asterisks. ****, $P < 0.0001$. (**D**) Western blot (WB) analysis of late schizont stage parasite lysates from wild-type and mutant *Pf*ARO-GFP expressing parasites to test for possible *Pf*AIP-mCherry (calculated MW: 76 kDa) degradation. WB analysis was performed using mCherry-specific antibody (αmCherry). A protein band at appr. 95 kDa was detected for *Pf*AIP-mCherry expressing parasites. As control, parental 3D7 parasite lysate and aldolase-specific antibody (αAldolase) were used. WT, wild-type *Pf*ARO; M1-M6, *Pf*ARO mutant 1-6. Std, molecular size standard.

Different mutants of *Pf*ARO protein were created, fused to GFP and expressed using a bicistronic over-expression vector (= skip vector, see 3.2.2). The following mutations were introduced into the *Pf*ARO protein. *Pf*ARO mutation 1 (ARO$_{M1}$): H72D/W74S; *Pf*ARO mutation 2 (ARO$_{M2}$): L84D/Q88E; *Pf*ARO mutation 3 (ARO$_{M3}$): P78G/T80A; *Pf*ARO mutation 4 (ARO$_{M4}$): D124N/R125Q; *Pf*ARO mutation 5 (ARO$_{M5}$): Δ64-79 (deletion of loop 1) and *Pf*ARO mutation 6 (ARO$_{M6}$): F135D (Fig. 3.6A). Parasites expressing *Pf*ARO wild-type (*Pf*ARO$_{WT}$) showed a similar rhoptry localization for *Pf*ARO$_{WT}$-GFP and *Pf*AIP-mCherry signal as described in Fig. 3.2E and Fig. 3.3A. All other *Pf*ARO variants caused a cytosolic distribution of *Pf*AIP-mCherry signal (Fig. 3.6B). Some residual *Pf*AIP-mCherry signal was often detectable at the rhoptry neck, which is most likely due to the interaction with endogenous *Pf*ARO protein.

The cytosolic distribution of *Pf*AIP-mCherry was quantified by the Manders split coefficient (MSC). MSC1 reflects the fraction of *Pf*AIP-mCherry signal overlapping with the *Pf*ARO-GFP signal. For *Pf*ARO^{WT}-GFP, almost all *Pf*AIP-mCherry signal overlapped with the *Pf*ARO$_{WT}$-GFP signal, leading to a high MSC1. All *Pf*ARO mutants, however, showed a low MSC1 because most of the cytosolic *Pf*AIP-mCherry signal did not overlap with the *Pf*ARO-GFP signal located at the rhoptry neck (Fig. 3.6C). MSC2 reflects the fraction of the *Pf*ARO-GFP signal overlapping with the *Pf*AIP-mCherry signal. A low MSC2 was calculated for *Pf*ARO$_{WT}$-GFP since only a small proportion of the *Pf*ARO$_{WT}$-GFP signal overlapped with the *Pf*AIP-mCherry signal at the rhoptry neck. For all ARO mutants, a high MSC2 was calculated because most *Pf*ARO-GFP was overlapped by the cytosolic *Pf*AIP-mCherry signal (Fig. 3.6C).

When *Tg*AIP was depleted, *Tg*ACβ became undetectable, indicating that *Tg*AIP is necessary for *Tg*ACβ stabilization [Mueller *et al.*, 2016]. The *Pf*AIP-2xFKBP-GFP signal was detectable only at background level when mislocalized (see Fig. 3.4A). To exclude the possibility of degradation or the processing of *Pf*AIP-mCherry leading to cytosolic mCherry, WB analysis of parasite lysate using an mCherry-specific antibody was performed. A single band at appr. 95 kDa was detected for all wild-type and mutant *Pf*ARO expressing parasites (Fig. 3.6D), indicating that no free mCherry moiety caused the observed cytosolic signal.

3.4.2 *Pf*ARO-GFP/*Pf*AIP-mCherry interaction could not be verified by co-IP

It has been shown that *Tg*AIP (together with *Tg*ACβ and *Tg*MyoF) can be pulled-down by *Tg*ARO-GFPTy in co-immunoprecipitation (co-IP) experiments [Mueller *et al.*, 2013]. To test whether this interaction can be verified for *P. falciparum* in the context of wild-type *Pf*ARO-GFP/*Pf*AIP-mCherry expressing parasites and to verify the ablated interaction caused by *Pf*ARO mutations, a pull-down assay using GFP-Trap® was performed. It was expected that mutant versions of *Pf*ARO-GFP would be unable to pull down *Pf*AIP-mCherry, given that these proteins are indeed interaction partners like their *T. gondii* homologues. However, co-IPs using GFP-Trap® and RFP-Trap® followed by WB analysis did not suggest an interaction of wild-type *Pf*ARO-GFP and *Pf*AIP-mCherry (data not shown.)

3.4.3 An ARO homologue in *V. brassicaformis*

Since Vbra_13064 was retrieved by BLASTp analysis using *Tg*AIP as the query (see 3.1.1), additional BLASTp analysis against the *V. brassicaformis* genome was performed using the *Tg*ARO protein sequence (Gene ID: TGME49_261440) as the query sequence. A single hit (Gene ID: VBRA_4126, length: 291 aa) was retrieved (BLASTp E-value: $5e^{-73}$), suggesting the presence of an ARO protein homologue (*Vb*ARO) in *V. brassicaformis*. CD-search analysis retrieved two Armadillo (ARM) repeats located at residues K_{109} to S_{141} and N_{147} to V_{185} of *Vb*ARO, which correspond well with the ARM2 and ARM3 repeats of *Pf*ARO (S5, Appendix). PRALINE multiple sequence and NEEDLE alignment determined a high level of conservation between *Vb*ARO, *Tg*ARO and *Pf*ARO (S5, Appendix). The N-terminal palmitoylation motif as well as the positively charged residues R_9, K_{14} and K_{16}, which are important for the rhoptry membrane attachment of *Pf*ARO [Cabrera *et al.*, 2012], are highly conserved between *Vb*ARO, *Tg*ARO and *Pf*ARO (S5, Appendix). However, *Tg*ARO and *Pf*ARO exhibit R_9, K_{14} and K_{16}, whereas the *Vb*ARO protein exhibits K_9, R_{14} and R_{16}. The sequence that forms loop1 in *Pf*ARO is also highly conserved between *Vb*ARO, *Tg*ARO and *Pf*ARO, whereas *Pf*ARO loop2 is not. A calcium-dependent phosphorylation at *Tg*ARO residue S_{33} was detected, which suggests the response of *Tg*ARO to calcium signalling [Nebl *et al.*, 2011]. Further, S_{33} is conserved between *Tg*ARO, *Pf*ARO and *Vb*ARO. Lysine acetylation of *Pf*ARO residues K_{26} and K_{168} has been determined [Cobbold *et al.*, 2016] and residue K_{26} of *Pf*ARO and *Vb*ARO is conserved (S5, Appendix).

3.5 Identification of *Pf*AIP interaction partners using 2C-BioID (DIQ-BioID)

It has been shown via co-IP that *Tg*AIP, *Tg*MyoF and *Tg*ACβ are interaction partners of *Tg*ARO [Mueller *et al.*, 2013]. As described in section 3.4.2, co-IP using *Pf*ARO-GFP and *Pf*AIP-mCherry did not indicate a stable interaction of *Pf*ARO and *Pf*AIP. In order to identify potential interaction partners of *Pf*AIP in the malaria parasite, the two component BioID approach (2C-BioID) [Chojnowski *et al.*, 2018] was used. This method was recently applied for *P. falciparum* and was termed DIQ-BioID [Birnbaum & Scharf *et al.*, 2020]. It has been shown that this method leads to a minimized pool of false positive candidates. Birnbaum *et al.* fused a promiscuous biotin ligase BirA* [Roux *et al.*, 2012] to mCherry and FRB to express this construct in a line where the protein of interest (POI), the Kelch-13 protein, was fused to 2xFKBP-GFP. Expression of the BirA* construct is controlled by the weak *sf3a2* promoter to reduce the background of unspecific biotinylated proteins. Biotinylated proteins can be affinity-purified using a streptavidin matrix and subsequently identified by mass spectrometry (MS).

3.5.1 Active biotin ligase can be localized inducibly to *Pf*AIP-2xFKBP-GFP

In order to establish the DIQ-BioID for *Pf*AIP, the parasite line AIP_{bioID} was established by transfecting the line AIP_{endo} with a vector coding for the mCherry-2xFRB-BirA* construct. The addition of rapalog induces dimerization of the FKBP/FRB domain to localize BirA* ligase to *Pf*AIP, where it biotinylates putative *Pf*AIP interaction partners in close proximity (Fig. 3.7A). WB analysis was performed on late schizont stage parasite lysate from tightly synchronized cultures, which were split into two cultures to treat one with rapalog and leave the other untreated. The GFP-specific antibody detected a band at appr. 110 kDa matching *Pf*AIP-2xFKBP-GFP with a predicted MW of 106 kDa. Using the mCherry-specific antibody, a band at appr. 80 kDa was detected, corresponding to mCherry-2xFRB-BirA* construct with a predicted MW of 78 kDa (Fig. 3.7B). The signal intensities indicate that the constructs were expressed equally in rapalog-treated and control parasites. After adding rapalog to the AIP_{bioID} line, the mCherry-2xFRB-BirA* signal overlapped with the *Pf*AIP-2xFKBP-GFP signal at the rhoptry neck, indicating the successful recruitment of mCherry-2xFRB-BirA* to *Pf*AIP-2xFKBP-GFP (Fig. 3.7C).

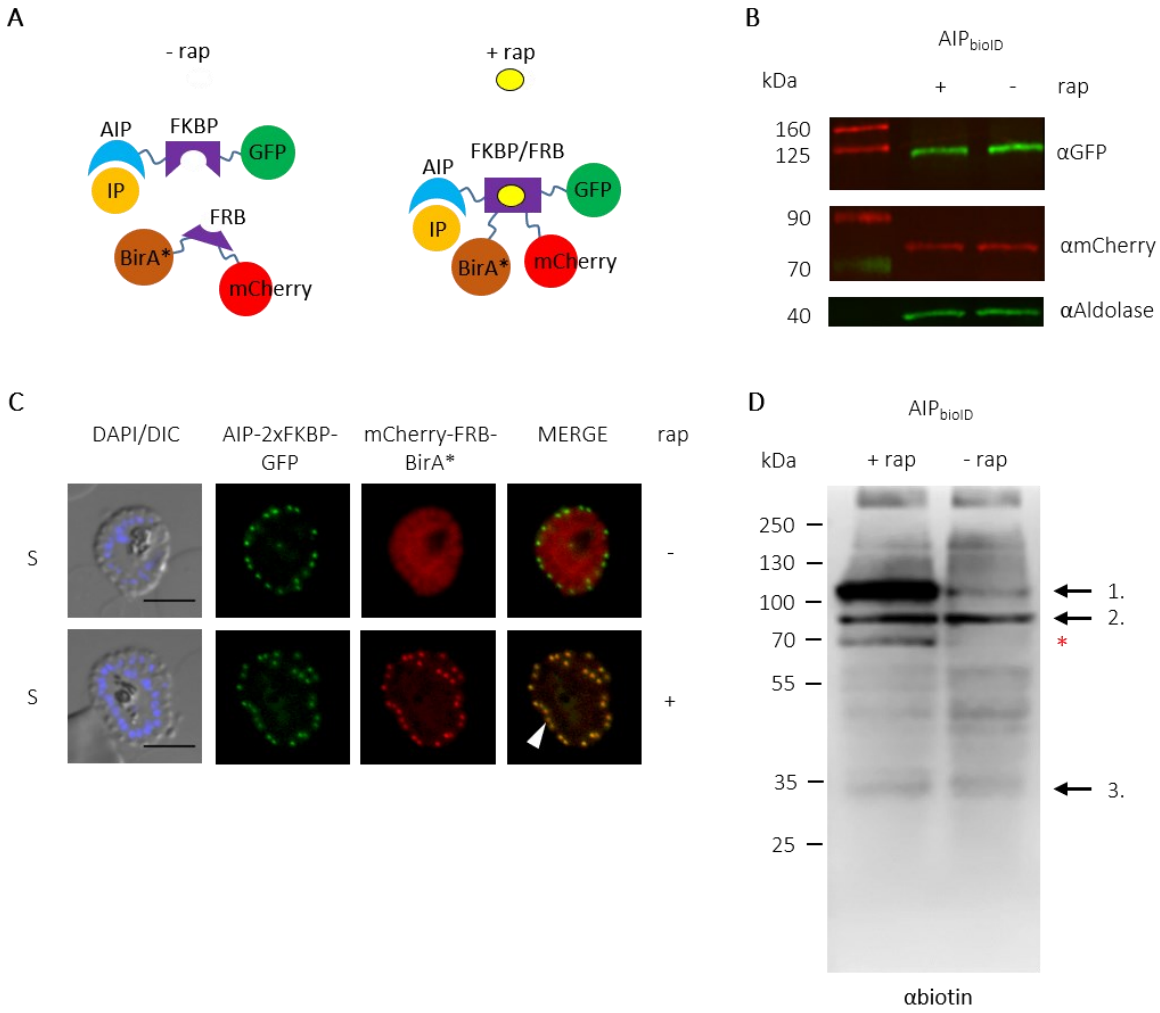

Fig. 3.7 | Rapalog-induced dimerization of FKBP-FRB localizes active biotin ligase to *Pf*AIP. (**A**) Schematic representation of rapalog-induced re-localization of cytosolic mCherry-FRB-BirA* construct to *Pf*AIP-2xFKBP-GFP in AIP_{bioID} parasites (AIP_{endo} parasites transfected with mCherry-FRB-BirA* construct). BirA* ligase biotinylates proteins proximal to *Pf*AIP-2xFKBP-GFP upon rapalog addition. Blue, *Pf*AIP; purple: FKBP/FRB domains; green, GFP; red, mCherry; brown, BirA* ligase; orange, interaction partner (IP); yellow, rapalog (rap). (**B**) Western blot (WB) analysis of AIP_{bioID} schizont stage parasites. Tightly synchronized parasites were grown to

38 hpi. The culture was split into two identical cultures and one was supplemented with rapalog (+rap) while the other served as control (-rap). At the late schizont stage, prior to rupture, parasites were harvested, and Western blot (WB) analysis was performed using GFP-specific (αGFP) and mCherry-specific (αmCherry) antibodies. WB using αGFP detects a protein band at approximately 110 kDa. The predicted size of *Pf*AIP-2xFKBP-GFP is 106 kDa. Using αmCherry, a protein band at approximately 80 kDa is detected. The predicted size of mCherry-FRB-BirA* is 78 kDa. An aldolase-specific antibody (αAldolase) was used as loading control. (**C**) Representative images from wide-field fluorescence microscopy of unfixed AIP_{bioID} parasites. The white arrowhead indicates the co-localization of mCherry-FRB-BirA* (red signal) and *Pf*AIP-2xFKBP-GFP (green signal). DAPI (blue signal) was used to stain nuclei. DIC, differential interference contrast; scale bars, 5 µm; S, schizont; rap, rapalog. (**D**) WB analysis of AIP_{bioID} schizonts to test for the biotinylation of proteins proximal to *Pf*AIP-2xFKBP-GFP. Highly synchronized parasites were grown to 38 hpi. The culture was split into two identical cultures and one was supplemented with rapalog (+rap). Both cultures were supplemented with biotin and incubated at RT until the parasites reached the late schizont stage prior to rupture. Samples were probed with a biotin-specific antibody (αbiotin). Black arrows indicate the predicted MW of the following proteins: 1. *Pf*AIP-2xFKBP-GFP, 106 kDa; 2. mCherry-FRB-BirA*, 78 kDa; 3. *Pf*ARO, 31 kDa. Red asterisk marks a protein band at appr. 70 kDa for rapalog condition.

*Pf*AIP is expressed during late schizogony [Bozdech *et al.*, 2003; Llinás *et al.*, 2006] (see S2A, Appendix) and potential interaction partners should be accessible within this window. However, for optimal labelling, *E. coli* derived BirA* requires more than 18 hours [Branon *et al.*, 2018; Rhee *et al.*, 2013]. It was therefore reasoned that the window could be too short for the efficient biotinylation of proteins proximal to *Pf*AIP within late schizonts prior to rupture. One possibility to increase the time window for efficient biotinylation is represented by the use of compounds that prevent schizont rupture. The protein kinase G (PKG) inhibitors compound 1 (C1) [Gurnett & Liberator *et al.*, 2002] and compound 2 (C2) [Donald *et al.*, 2006] or the nonspecific papain family protease inhibitor E64 [Greenbaum *et al.*, 2002] are such tools. C2 and E64 were tested in the context of the AIP_{bioID} line, and neither compound had an apparent effect on rapalog-induced recruitment of BirA* construct to *Pf*AIP-2xFKBP-GFP (data not shown). While nonetheless promising, these compounds were not used in the DIQ-BioID experiments given the possibility of drug-induced artifacts and the high cost of some of these compounds.

Instead, after reaching 38 hpi, the culture was split into a rapalog-treated and a control culture and left at room temperature (RT) until the late schizont stage prior to rupture. It was expected that parasite development is slowed down sufficiently to allow for the biotin ligase biotinylation of proteins proximal to *Pf*AIP-2xFKBP-GFP at RT. Subsequent WB analysis on lysate from saponin-isolated late schizonts using a biotin-specific antibody (see 2.1.8) showed a strongly increased signal at appr. 110 kDa compared to control (Fig. 3.7D). This matches the molecular weight of *Pf*AIP-2xFKBP-GFP (calculated MW: 106 kDa), confirming that the mCherry-FRB-BirA* construct was localized to *Pf*AIP-2xFKBP-GFP. A band at appr. 80 kDa, corresponding to the size of mCherry-2xFRB-BirA* (calculated MW: 78 kDa), was also found, suggesting that BirA* does biotinylate itself and/or the FRB-mCherry moiety independently of rapalog treatment. A band at 70 kDa was detected exclusively for rapalog-induced cells (Fig. 3.7D). This band could either indicate a potential interaction partner of *Pf*AIP or a degraded/processed form of *Pf*AIP-2xFKBP-GFP (see Fig. 3.2C).

3.5.2 Potential interaction partners of PfAIP-2xFKBP-GFP identified by DIQ-BioID

Even though increased bands are often not visible for rapalog-induced cultures, hits still occur in MS [Tobias Spielmann, personal communication, 2018]. The rapalog-induced culture and the control were harvested, and their biotinylated proteins were purified and subjected to MS. This first DIQ-BioID screen identified 72 proteins

whose biotinylated peptides were enriched in the rapalog-treated sample compared to control. Candidates and hits are compiled in Table 3.1, which lists the log2 fold changes (log2FC) of the rapalog-induced culture versus the control. Log2FC values above 1 were considered as candidates. Values equal to or above 1.3 were considered as hits. Fold changes of the two fractions are displayed. The ammonium bicarbonate (AmBic) fraction contained peptides that were cleft off from streptavidin-beads by trypsin digest and were subjected to MS. The acetonitrile/trifluoroacetic acid (ACN/TFA) fraction contained peptides that were still bound to streptavidin beads after trypsin digest and were eluted by ACN/TFA before being subjected to MS. All the listed proteins were reviewed for likely/unlikely *Pf*AIP interaction judged on subcellular localization, DNA/RNA binding capacity, secretory pathway association and metabolic function.

Table 3.1 | Hits identified by DIQ-BioID. The table shows the gene identifiers of proteins corresponding to peptides enriched by mass in the rapalog-induced culture compared to the control. A log2FC value > 1 indicates candidates. A log2FC value ≥ 1.3 indicates hits. The column on the right indicates the mutagenesis index score [Zhang *et al.*, 2018] color-coded from red (essential) to green (dispensable) for the corresponding genes. ACN, acetonitrile/trifluoroacetic acid fraction; Am, AmBic fraction; SP, signal peptide; TMD, trans-membrane domain; M, mutagenesis index score; NA, not assessed.

Gene ID	log2 FC		category		Description	SP	TMD	Size (kDa)	M
	ACN	Am							
PF3D7_0113000	2,7	1,5	hit	hit	Glutamic acid-rich protein (GARP)	yes	1	79.8	
PF3D7_0201900	0,6	1,3	no hit	hit	Erythrocyte membrane protein 3 (EMP3)	yes	1	273.7	
PF3D7_0202000	2,2	1,6	hit	hit	Knob-associated histidine-rich protein (KAHRP)	yes	0	71.3	
PF3D7_0307200	1,9	1,6	hit	hit	60S ribosomal protein L7, putative	no	0	30.5	
PF3D7_0320900	3,4	3,7	hit	hit	Histone H2A.Z	no	1	16.5	
PF3D7_0401800	1,8	2,2	hit	hit	Plasmodium exported protein (PHISTb), unknown function	no	1	60.3	
PF3D7_0402000	2,3	1,3	hit	hit	Plasmodium exported protein (PHISTa), unknown function	no	1	49.7	
PF3D7_0500800	2,1	2,5	hit	hit	Mature parasite-infected erythrocyte surface antigen (MESA)	no	0	168.3	
PF3D7_0508500	1,4	1,2	hit	cand	Guanidine nucleotide exchange factor (RCC1)	no	0	304.1	
PF3D7_0517400	2,3	2,7	hit	hit	FACT complex subunit SPT16, putative	no	0	132.7	
PF3D7_0519400	1,1	1,2	cand	cand	40S ribosomal protein S24	no	0	15.4	
PF3D7_0532400	2,0	1,6	hit	hit	Lysine-rich membrane-associated PHISTb protein	no	1	61.1	
PF3D7_0610400	3,8	3,4	hit	hit	Histone H3	no	0	15.5	
PF3D7_0612200	1,3	1,1	cand	cand	Leucine-rich repeat protein (LRR6)	no	0	220.3	
PF3D7_0617800	3,5	3,9	hit	hit	Histone H2A	no	0	14.1	
PF3D7_0617900	3,3	3,4	hit	hit	Histone H3 variant	no	0	15.4	
PF3D7_0707300	NA	1,8	NA	hit	Rhoptry-associated membrane antigen (RAMA)	yes	0	103.6	
PF3D7_0708400	2,5	3,0	hit	hit	Heat shock protein 90	no	0	86.2	
PF3D7_0710600	1,7	1,5	hit	hit	60S ribosomal protein L34	no	0	17.4	
PF3D7_0714000	3,5	3,7	hit	hit	Histone H2B variant	no	0	13.8	
PF3D7_0731600	1,2	2,1	cand	hit	Acyl-CoA synthetase (ACS5)	yes	0	93.3	
PF3D7_0802600	3,2	3,2	hit	hit	Adenylyl cyclase beta (ACβ)	no	0	269.5	
PF3D7_0814000	1,3	1,5	cand	hit	60S ribosomal protein L13-2, putative	no	0	25.4	

PF3D7_0821700	1,2	1,6	cand	hit	60S ribosomal protein L22, putative	no	0	16.4	
PF3D7_0918000	1,5	1,2	hit	cand	Glideosome-associated protein 50 (GAP50)	yes	1	44.6	
PF3D7_0923900	1,2	1,1	cand	cand	Polyadenylate (RNA)-binding protein 2, putative	no	0	23.0	
PF3D7_0930300	1,9	2,0	hit	hit	Merozoite surface protein 1 (MSP1)	yes	0	195.7	
PF3D7_1006200	0,8	1,1	no hit	cand	DNA/RNA-binding protein Alba 3	no	0	12.0	
PF3D7_1006800	2,0	2,0	hit	hit	Single-strand telomeric DNA-binding protein GBP2, putative	no	0	29.5	
PF3D7_1008000	1,1	1,3	cand	hit	Histone deacetylase 2	no	0	282.2	
PF3D7_1017500	1,1	0,0	cand	no hit	Myosin essential light chain ELC	no	0	15.7	
PF3D7_1027300	0,4	2,6	no hit	hit	Peroxiredoxin	no	0	43.9	
PF3D7_1104400	1,8	2,2	hit	hit	Thioredoxin-like mero protein	yes	1	49.3	
PF3D7_1105000	3,5	3,4	hit	hit	Histone H4	no	0	11.5	
PF3D7_1105100	3,5	4,1	hit	hit	Histone H2B	no	0	13.1	NA
PF3D7_1105400	1,6	1,5	hit	hit	40S ribosomal protein S4, putative	no	0	29.7	
PF3D7_1109900	1,8	1,9	hit	hit	60S ribosomal protein L36	no	0	12.8	
PF3D7_1121600	2,2	2,1	hit	hit	Exported protein 1	yes	1	17.3	
PF3D7_1124900	1,4	1,0	hit	cand	60S ribosomal protein L35, putative	no	0	14.8	
PF3D7_1136700	NA	3,1	NA	hit	Conserved Plasmodium protein, unknown function (AIP)	no	0	49.1	
PF3D7_1220900	2,5	2,8	hit	hit	Heterochromatin protein 1	no	0	31.0	
PF3D7_1228600	1,6	1,3	hit	hit	Merozoite surface protein 9	yes	0	86.6	
PF3D7_1232100	2,1	2,5	hit	hit	60 kDa chaperonin	yes	1	81.5	
PF3D7_1245800	2,1	2,1	hit	hit	Epsin-like protein, putative	no	0	49.7	
PF3D7_1246400	0,5	1,0	no hit	cand	Myosin A tail domain interacting protein (MTIP)	no	0	23.5	
PF3D7_1247400	2,5	2,3	hit	hit	FK506-binding protein (FKBP)-type peptidyl-prolyl isomerase (FKBP35)	no	0	34.8	
PF3D7_1323400	1,5	1,3	hit	hit	60S ribosomal protein L23	no	0	22.1	
PF3D7_1324800	2,6	3,2	hit	hit	Dihydrofolate synthase/folylpolyglutamate synthase (DHFS-FPGS)	no	0	60.1	
PF3D7_1330800	2,1	1,6	hit	hit	RNA-binding protein, putative	no	0	68.0	
PF3D7_1333700	2,6	2,8	hit	hit	Histone H3-like centromeric protein CSE4	no	0	19.6	
PF3D7_1335100	1,9	1,9	hit	hit	Merozoite surface protein 7	yes	0	41.3	
PF3D7_1338200	1,2	2,6	cand	hit	60S ribosomal protein L6, putative	no	0	25.5	
PF3D7_1342000	1,8	1,6	hit	hit	40S ribosomal protein S6	no	0	35.4	
PF3D7_1346300	1,7	1,3	hit	hit	DNA/RNA-binding protein Alba 2	no	0	25.0	
PF3D7_1347500	1,3	1,2	cand	cand	DNA/RNA-binding protein Alba 4	no	0	42.1	
PF3D7_1352500	1,4	2,1	hit	hit	Thioredoxin-related protein, putative	yes	2	24.0	
PF3D7_1358800	1,6	1,7	hit	hit	40S ribosomal protein S15	no	0	17.3	
PF3D7_1408600	1,6	1,7	hit	hit	40S ribosomal protein S8e, putative	no	0	25.1	
PF3D7_1421200	1,4	0,9	hit	no hit	40S ribosomal protein S25	no	0	11.7	
PF3D7_1424400	2,0	2,4	hit	hit	60S ribosomal protein L7-3, putative	no	0	32.7	
PF3D7_1431700	1,8	1,6	hit	hit	60S ribosomal protein L14, putative	no	0	19.3	
PF3D7_1434300	1,4	1,4	hit	hit	Hsp70/Hsp90 organizing protein	no	0	66.1	
PF3D7_1434800	1,3	2,0	cand	hit	Mitochondrial acidic protein MAM33, putative	no	0	28.9	

PF3D7_1441200	1,6	1,6	hit	hit	60S ribosomal protein L1, putative	no	0	24.8	
PF3D7_1441400	2,5	2,9	hit	hit	FACT complex subunit SSRP1, putative	no	0	58.8	
PF3D7_1450700	0,8	1,1	no hit	cand	Conserved Plasmodium protein, unknown function	no	0	72.8	
PF3D7_1456000	1,1	0,7	cand	no hit	AP2 domain transcription factor, putative	no	0	161.5	
PF3D7_1460700	1,0	1,1	no hit	cand	60S ribosomal protein L27	no	0	16.8	
PF3D7_1463900	1,5	1,3	hit	hit	EF-hand calcium-binding domain-containing protein, putative	yes	7	127.1	
PF3D7_1471100	1,1	0,8	cand	no hit	Exported protein 2	yes	0	33.4	
PF3D7_1473200	3,0	2,8	hit	hit	DnaJ protein, putative	no	0	52.5	
PF3D7_1477500	1,0	1,4	no hit	hit	Plasmodium exported protein (PHISTb), unknown function	no	1	60.5	

Contaminants/false positives (DNA/RNA binding, metabolic function, different compartment/localization)
Exported/Secretory pathway/Signal peptide (SP)
*Pf*AIP/putative *Pf*AIP interaction partner

Although retrieved only from the AmBic fraction, the *Pf*AIP protein (Gene ID: PF3D7_1136700), as expected, was one of the top candidates. Adenylyl cyclase β (*Pf*ACβ, gene ID: PF3D7_0802600), epsin-like protein (Gene ID: PF3D7_1245800), dihydrofolate synthase/folylpolyglutamate synthase (DHFS-FPGS, PF3D7_1324800), FK506-binding protein (FKBP)-type peptidyl-prolyl isomerase (FKBP35, gene ID: PF3D7_1247400), and heat shock protein 90 (HSP90, gene ID: PF3D7_0708400) were also retrieved (Table 3.1). However, *Pf*ARO (Gene ID: PF3D7_0414900) and *Pf*MyoF (Gene ID: PF3D7_1329100) could not be retrieved by this approach, suggesting some functional differences to the *Tg*AIP homologue.

The experiment was confirmed by Jan Stephan Wichers (Gilberger laboratory, BNITM), using slightly different conditions [Geiger & Brown *et al.*, 2020]: instead of incubation at RT, the cultures, which had been incubated under standard conditions, were supplied with C2 to arrest schizonts before egress. Enriched proteins included, again, *Pf*AIP and *Pf*ACβ, DHFS-FPGS, FKBP35, HSP90 but not *Pf*ARO and *Pf*MyoF. Additionally, the vacuolar protein-sorting 9 (VPS9, gene ID: PF3D7_0815800) protein was identified.

In conclusion, DIQ-BioID as well as co-IP did not suggest an interaction of *Pf*AIP with *Pf*ARO, whereas *Pf*ACβ was retrieved as a potential interaction partner of *Pf*AIP. The indicated functional relationship of *Pf*AIP and *Pf*ACβ is reflected by a similar expression profile that is shared by *Pf*DHHC7 (data not shown).

CHAPTER 4 DISCUSSION

4.1 Importance of this study

Despite extensive research, rhoptry morphogenesis, the molecular mechanisms affecting rhoptry docking to the apex, and the signalling pathways controlling rhoptry discharge are still not well understood. Although *Toxoplasma* and *Plasmodium spp*. show similarities in molecular mechanisms, regarding *e.g.* the invasion motor, there are fundamental differences. For instance, for the glideosome trimeric complex formed by *Pf*ELC (essential light chain), MLC1 and MyoA, it has been shown that, despite the topological similarity between these complexes in *T. gondii* and *P. falciparum*, the last five helices of *Pf*ELC deviate from those of *Tg*ELCs. This results in a different orientation of the C-terminal lobe of *Pf*ELC1 leading to MyoA [Pazicky *et al.*, 2019].

Previous work on *T. gondii* suggested the essential function of the armadillo repeats only (*Tg*ARO) protein for rhoptry positioning at the apical pole of the parasite [Beck *et al*., 2013; Mueller *et al.*, 2013, 2016]. *Tg*ARO was also shown to interact with ARO interacting protein (*Tg*AIP), which itself recruits adenylate cyclase β (*Tg*ACβ) [Mueller *et al.*, 2013, 2016]. Dissecting the differences in the molecular invasion machinery of *P. falciparum* will broaden the understanding of host cell invasion in both parasites and will identify the similarities and molecular differences that might reflect their ecological niche and physiological requirements.

The work presented in this thesis aimed to deliver a detailed functional analysis of AIP in *P. falciparum*. The conditional depletion of *Pf*AIP from its site of action led to an invasion deficit, demonstrating its importance in *P. falciparum*. Additionally, it was shown that *Pf*AIP localization to the rhoptry sub-compartment is disturbed by mutations in the *Pf*ARO protein. Moreover, in an attempt to identify *Pf*AIP interaction partners, *Pf*ACβ was identified as a putative interaction partner, linking it to signal transduction pathways, whereas stable interaction for *Pf*AIP and *Pf*ARO could not be shown.

4.2 Discussion of major findings

4.2.1 AIP homology

An AIP homologue of *Tg*AIP was identified in *P. falciparum* and other Apicomplexa species by BLASTp search, suggesting that AIP is largely restricted to the phylum Apicomplexa. One hit identified by BLASTp search was Vbra_13067, a gene from *Vitrella brassicaformis* [Oborník *et al*., 2012], of which only a short amino acid sequence within the C-terminus (which is predicted as PH domain) showed homology to *Tg*AIP. *V. brassicaformis* is a member of the non-parasitic, photosynthetically active chromerid phylum that is closely related to Apicomplexa, as indicated by phylogenetic analyses [Janouškovec *et al.*, 2015]. Sequencing of the nuclear genomes from *V. brassicaformis* and *Chromera velia* [Moore *et al.*, 2008; Oborník et al., 2012; Woo *et al.*, 2015], the only two known species of the chromerid phylum thus far, revealed that the genes associated with a free-living lifestyle, such as endomembrane trafficking proteins and metabolic pathway enzymes, have been lost or repurposed during adaptation to the parasitic lifestyle of Apicomplexa in adaptation to different host tropisms [Woo *et al.*, 2015].

Recently, a coral-infecting apicomplexan lineage, namely *corallicola*, that shows ultrastructural features (such as micronemes) known from apicomplexan parasites as well as similar plastid genome content, was discovered [Kwong *et al.*, 2018]. The authors reported large structures (up to 1.6 µm) that could be homologous to rhoptries, and they suggested that *corallicola* may be an evolutionary intermediate, as it shows characteristics of both its free-living (Chromerida) and parasitic (Apicomplexa) relatives. A sequenced genome of *corallicola* has not been published yet, hence it could not be assessed whether an AIP homologue is present in this lineage or whether it shows a higher level of similarity to *Pf*AIP than the Vbra_13067 putative PH domain shows to *Tg*AIP/*Pf*AIP.

BLASTp search and PRALINE alignment suggested the presence of a *Tg*ARO homologue (*Vb*ARO) in *V. brassicaformis*. An additional BLASTp search was performed against the *C. velia* genome but did not retrieve homologous sequences for *Tg*AIP or *Tg*ARO (data not shown). This may either indicate the loss of the corresponding genes in *C. velia,* after splitting from the proto-apicomplexan ancestor (the ancestor of Apicomplexa and Chromerida), or that these genes have been acquired later in *V. brassicaformis* and the apicomplexan ancestor. Since homology to *Pf*ARO was found in the dinoflagellate *Perkinsus marinus*, the cilliate *Paramecium* and even yeast [Cabrera *et al.*, 2012], the first theory seems more likely. The repurposing of evolutionarily conserved genes for different functions may have occurred for *Tg*AIP and *Pf*AIP, which vary significantly in size (89 kDa *vs* 49 kDa, respectively), which could indicate adaptation to different host tropisms by *T. gondii* and *P. falciparum*.

4.2.2 Functional characterization of *Pf*AIP

*Pf*AIP was shown to co-localize with the rhoptry neck marker *Pf*RALP1 and partially co-localize with *Pf*ARO, which is in accordance with previous data that demonstrated rhoptry neck localization for *Tg*AIP [Mueller *et al.*, 2013, 2016]. (See 4.3.4 for further discussion on this point.)

The depletion of *Pf*AIP from the rhoptry neck by KS resulted in a significant decrease in parasitemia, indicating that *Pf*AIP is important for efficient parasite proliferation. This is in accordance with a recently published genome-wide saturation mutagenesis screen performed in *P. falciparum* [Zhang *et al.*, 2018], suggesting that *Pf*AIP is refractory to disruption and therefore considered essential. In contrast, *Tg*AIP is considered non-essential as no growth perturbation is reported for the *Tg*AIP knockout line [Mueller *et al.*, 2016] and a dispensable function of *Tg*AIP is suggested by a CRISPR/Cas9 screen of the reference RH strain [Sidik & Huet *et al.*, 2016].

This might point towards functional differences of these two homologues. Alternatively, other proteins encoded in the genome of *T. gondii*, although no additional homologue could be identified (data not shown), might functionally compensate for *Tg*AIP, or *Pf*AIP might have additional functions in malaria parasites. Interestingly, a high transcription of *Pf*AIP, but not *Pf*ARO, in ookinetes [López-Barragán *et al.*, 2011] and oocysts [Zanghì *et al.*, 2018] indicates an additional role of *Pf*AIP in these stages, that yet has to be explored.

The invasion phenotype generated by the KS of *Pf*AIP is characterized by a normal development into mature schizonts and egress from the infected erythrocyte, but a decreased number of re-invaded erythrocytes (counted by rings per schizont). KS resulted in an efficient depletion of *Pf*AIP-2xFKBP-GFP from the rhoptry neck, although the expected re-distribution to the nucleus could not be visualized, most likely due to the low signal intensity (see 3.3.1). The *Pf*AIP-2xFKBP-GFP signal was clearly visible as small foci at the rhoptry neck of control parasites.

Mislocalization of *Pf*AIP-2xFKBP-GFP to the nucleus would distribute the signal to the whole nuclear area, which is considerable larger than the rhoptry neck sub-compartment [Rudlaff *et al.*, 2020], thereby extensively diluting the signal intensity, which is probably the reason for the visually undetectable *Pf*AIP-2xFKBP-GFP signal in the nucleus.

Three possibilities for the invasion phenotype are conceivable: i) attachment, ii) invasion or iii) formation of the PV is hampered. Possibility i) appears unlikely, as the number of free merozoites did not differ from the control (data not shown). Possibility iii) might be an explanation but was not assessed. For possibility ii) one might have expected to find more attached merozoites per ruptured schizont for rapalog-induced parasites, but their number did not differ significantly from the control.
For *Pf*ACβ, it was observed that the attachment of merozoites and the deformation of RBC membrane is not affected by the ablation of *Pf*ACβ, as shown by time-lapse video microscopy [Patel & Perrin *et al.*, 2019]. Giemsa smear analysis to determine the number of attached merozoites per ruptured schizont was probably unsuitable for this approach. To determine the exact phenotype of the *Pf*AIP depletion, other experiments such as FC analysis or time-lapse microscopy could be performed. (See 4.4.3 for further discussion on this point.)

4.2.3 *Pf*AIP interacting proteins

DIQ-BioID-based proximity labelling, using an inducible dimerization of a BirA* construct to *Pf*AIP, did not identify *Pf*ARO, but did identify other proteins, such as *Pf*ACβ, as putative interaction partners of *Pf*AIP. This finding agrees with previously published data, which demonstrated the co-localization and interaction of *Tg*AIP and *Tg*ACβ in *T. gondii* [Mueller *et al.*, 2013, 2016]. It is further supported by a recent study that localized *Pf*ACβ to the rhoptry neck. In this study, the DiCre-mediated loss of *Pf*ACβ produced merozoites defective in invasion (and a slight delay in egress), resulting in the absence of new ring stage parasites in the subsequent cycle [Patel & Perrin *et al.*, 2019]. In respect to the congruent invasion deficient phenotype, a functional relationship of *Pf*AIP and *Pf*ACβ seems likely.

The adenylyl cyclase beta (*Pf*ACβ), but not adenylyl cyclase alpha (*Pf*ACα), a homologue of the mammalian soluble adenylyl cyclase, is expressed in asexual blood stage malaria parasites and is responsible for the synthesis of cAMP to activate *Pf*PKA in response to external stimuli [Baker *et al.*, 2017; Salazar *et al.*, 2012]. A knockout of *Pf*ACβ led to the hypo-phosphorylation of *Pf*AIP phosphorylation-sites S_{76}, S_{101}, S_{115}, S_{371} and T_{374}, whereas a knockout of *Pf*PKA did not induce hypo-phosphorylation [Patel & Perrin *et al.*, 2019], which indicates that *Pf*AIP phosphorylation depends (indirectly) on *Pf*ACβ activity. Likewise, for *Pf*ARO protein, the phosphorylation-sites S_{25}, S_{33}, T_{35} and S_{36} were hypo-phosphorylated upon *Pf*ACβ depletion, and S_{33} was also hypo-phosphorylated when the *Pfpka* gene was excised [Patel & Perrin *et al.*, 2019]. Additionally, *Pf*ARO and *Pf*AIP have been shown to be putative substrates of *Pf*CDPK5, as the phosphorylation of *Pf*ARO S_{33} as well as *Pf*AIP S_{76} and S_{115} is dependent on *Pf*CDPK5 [Blomqvist *et al.*, 2020]. A calcium-dependent phosphorylation of S_{33} has also been shown for *Tg*ARO [Nebl *et al.*, 2011], although a specific CDPK using *Tg*ARO as a substrate has not been identified so far. *Pf*CDPK1 has been found to be a direct substrate of *Pf*PKA, suggesting that cAMP-dependent *Pf*PKA, and hence *Pf*ACβ, may affect calcium signalling through the stimulation of calcium release and the phosphorylation of CDPKs [Alam *et al.*, 2015]. The exact signalling cascade interplay that leads to the (de)activation of *Pf*AIP and *Pf*ARO through (de)phosphorylation

and eventually to proper rhoptry function has not been identified yet. To what extent S_{33} contributes to the described phenotype is unknown, but the conservation of S_{33} in *Tg*ARO, *Pf*ARO and *Vb*ARO suggests that this phosphorylation-site is likely important, as it is phosphorylated in *Tg*ARO as well as *Pf*ARO. S_{33} is also conserved in the ARO homologues of *N. caninum*, *B. besnoiti*, and *E. tenella* (data not shown). An analysis of *Pf*ARO phosphorylation-sites mutations and their effect on parasite development is not reported and should be assessed in future studies. (See 4.3.4 for further discussion on this point.)

Epsin-like protein (Gene ID: PF3D7_1245800) was also retrieved by DIQ-BioID as a putative interaction partner of *Pf*AIP. Epsins regulate clathrin coat formation by inducing curvature of the lipid bilayers and are important for endocytosis and signalling [Sen *et al.*, 2012]. The only homologue found for PF3D7_1245800 in *T. gondii* is *Tg*EpsL (Gene ID: TGME49_214180), which localizes to the trans-Golgi network (TGN) [Venugopal *et al.*, 2017]. Again, the localization of PF3D7_1245800 in *P. falciparum* is not yet reported and its putative rhoptry localization would be interesting to explore.

The essential dihydrofolate synthase/folylpolyglutamate synthase (DHFS-FPGS, gene ID: PF3D7_1324800), an unusual bifunctional enzyme [Wang *et al.*, 2010], is involved in folate biosynthesis [Salcedo *et al.*, 2001], but a localization in *P. falciparum* is not reported. In the absence of a predicted signal peptide or transmembrane domain, future studies should probe the putative *Pf*DHFS-FPGS association with the rhoptry neck membrane in late stage schizonts.

Vacuolar protein sorting (VPS) proteins are key factors in secretory organelle biogenesis [Bowers & Stevens, 2005]. *Tg*VPS9 depletion leads to the mislocalization of secretory organelle proteins and is required for the targeted transport of rhoptry proteins [Morlon-Guyot *et al.*, 2015]. The identification of *Pf*VPS9 by DIQ-BioID [Geiger & Brown *et al.*, 2020], using *Pf*AIP as bait, suggests that VPS9 may be a putative interaction partner of *Pf*AIP.

Although the DIQ-BioID approach offers a way to minimize false positive hits, other putative interaction partners with well-documented different cellular localizations were also identified, as judged by their log2FC. Non-specific background can be produced by free BirA* ligase generated through the cleavage or degradation of the fusion protein. Also, proteins that bind biotin directly are known. Furthermore, the high affinity of streptavidin to biotin aggravates elution from the matrix. This can lead to more efficient elution of proteins that are less biotinylated, which affects quantification [Trinkle-Mulcahy, 2019].

The rapamycin-sensitive immunophilin FK506-binding protein (FKBP)-type peptidyl-prolyl isomerase (*Pf*FKBP35) (Gene ID: PF3D7_1247400) as well as *Pf*HSP90 (Gene ID: PF3D7_0708400) are likely and somewhat expected false positive hits, since FKBP35 exhibits a stage-dependent nucleoplasmic shuttling and is associated with *Pf*HSP90 [Kumar *et al.*, 2005]. The addition of rapalog likely induced the dimerization of the mCherry-2xFRB-BirA* construct to *Pf*FKBP35, causing the biotinylation of *Pf*FKBP35 and *Pf*HSP90.

The protein of unknown function (Gene ID: PF3D7_1450700) is expected to be a false hit as well. PF3D7_1450700 showed a 27 % sequence identity to TGME49_082140, a splicing factor protein, as suggested by BLASTp analysis (data not shown) and is therefore not considered to be an interaction partner of *Pf*AIP.

Notably, *Pf*ARO, *Pf*AIP, *Pf*ACβ and PF3D7_1245800 (epsin-like protein) are listed as invadome subnetwork members [Hu *et al.*, 2010], whereas the likely false positive hits HSP90, FKBP35, PF3D7_1450700 but also DHFS-FPGS and *Pf*MyoF are not among the 418 genes listed in the invadome subnetwork.

4.2.4 DIQ-BioID-based proximity labelling to identify *Pf*AIP interacting proteins

Mueller *et al*. applied co-IPs to probe *Tg*ARO-interacting proteins [Mueller *et al.*, 2013]. In the experiments summarized by this thesis, it was not *Pf*ARO but *Pf*AIP that was used as bait for the identification of interacting proteins by applying a different technique: proximity-based biotinylation. With this approach, *Pf*ACβ was identified as a putative interaction partner of *Pf*AIP. Somewhat surprisingly, neither *Pf*ARO nor *Pf*MyoF were retrieved [Geiger & Brown *et al.*, 2020]. Although it appears important to reflect on the differences in the methodologies and the baits (IP with *Tg*ARO, DIQ-BioID with *Pf*AIP), this could also indicate differences in the ARO/AIP interactomes of these two parasites.

One explanation for why *Pf*ARO was not retrieved by DIQ-BioID (and also not by co-IP) could be a transient interaction of *Pf*AIP/*Pf*ARO, which was too short to allow for the efficient biotinylation of *Pf*ARO (and IP without cross-linking). Hence, the DIQ-BioID approach using *Pf*AIP should be repeated with a faster biotin ligase. Two promiscuous biotin ligase mutants, TurboID and miniTurboID have been created, which show a much greater efficiency than BioID (BirA*) [Branon *et al.*, 2018]. TurboID made it possible to map a GSK3 kinase signalling network in *A. thaliana* [Kim *et al.*, 2019], affirming the capability of TurboID to detect short transient interactions such as those during phosphorylation. By using TurboID or APEX2 (explained below), combined with tightly synchronized parasites (see 4.4.2), it may be possible to determine transient interactions down to minutes.

A recently published study demonstrates the use of split-TurboID (sTurboID) [Cho *et al.*, 2020], which could be used to dissect complex composition during transient *Pf*ARO-*Pf*AIP-interaction by fusing *Pf*ARO and *Pf*AIP to C- and N-terminal split TurboID, respectively. However, TurboID also shows signs of protein instability and persistent biotinylation in the absence of exogenous biotin as well as an increase in the labelling radius [May *et al.*, 2020]. Its practical use in *P. falciparum* still has to be ascertained.

Additionally, DIQ-BioID based interactome identification could be also extended to *Pf*ARO. During the course of this work, the cloning of a pSLI based *Pf*ARO-2xFKBP-GFP vector was arduous. Transfectants (selected with WR99210) were achieved, but the integration of the SLI vector was not attempted. However, the endogenous tagging of the *Pfaro* gene with *apex2-gfp* was successful (data not shown), demonstrating that the *Pf*ARO protein is accessible for endogenous tagging with a construct of comparable size to 2xFKBP-GFP. The DIQ-BioID approach should be repeated using *Pf*ARO as the bait to complement reciprocally the findings obtained by using *Pf*AIP as the bait.

Other methods that are suitable to identify transient *Pf*ARO/*Pf*AIP interaction partners include for instance: 1. the recently described fluorescence complementation mass spectrometry (FCMS) [Zeng *et al.*, 2017], 2. cross-linking based proteomics and 3. a different method of proximity-based biotinylation based on a peroxidase. The principles of the three methods and their potential applications in *P. falciparum* are explained below.

1. The FCMS method is based on bimolecular fluorescence complementation (BiFC, see below). Instead of the detection of a fluorescence signal, FCMS specifically isolates interaction partner pairs for mass spectrometric analyses to identify multiple interaction partners capable of interacting with a single protein within one experiment. The first step of FCMS is the establishment of a cDNA (substrate) library. The cDNA library is sub-cloned into a vector that produces the cDNA library gene products fused to an N-terminal fragment of a split-GFP. A second vector expresses the protein of interest (POI) fused to the C-terminal fragment of the split-GFP. Transient interactions of the POI and its substrate are stabilized by the irreversible association of the split-GFP fragments. Immunoprecipitation using a nanobody, which binds only to the reconstituted GFP, is followed by MS to identify protein-protein interactions of the POI and its substrates [Zeng *et al.*, 2017]. This method could be applied to identify (transient) interaction partners of *Pf*ARO and *Pf*AIP, which are not identified by the promiscuous biotin ligase approach.
It has been reported that a limitation of the FCMS approach is the use of an over-expression system, which may induce false positives [Zeng *et al.*, 2017]. But false positives could be reduced by tagging *Pf*AIP or *Pf*ARO endogenously with splitGFP using the SLI system [Birnbaum & Flemming *et al.*, 2017]. Another limitation might be that not all cDNA library gene products tolerate the N-terminal tagging with split-GFP and are therefore not detectable by the FCMS approach.

2. Cross-linking in combination with protein identification by MS is another powerful method to probe PPI. In contrast to classical co-IP, it has a superior capability to detect transient or weak interactions. The cross-linking reaction in cross-linking mass spectrometry (CLMS) uses soluble cross-linkers with a defined length (*e.g.* 11.4 Å) to add covalent bonds between proximal residues. After trypsin treatment, the digested peptides are still connected via the cross-linker. Subsequent MS analysis identifies which peptides are crosslinked and hence must be proximal residues, defining a binding interface, if derived from two different proteins. CLMS is able to identify different crosslink patterns, which can indicate conformational changes [O'Reilly & Rappsilber, 2018; Tabb, 2012]. Determining crosslink patterns by CLMS would enable statements about the PPI surfaces of *Pf*ARO, *Pf*AIP, and *Pf*ACβ even without crystallographic data.

3. Proximity-based biotinylation using APEX: The ascorbate peroxidase APEX2 (a variant of soybean ascorbate peroxidase) was developed to allow for high-resolution imaging of mitochondrial structures by EM [Martell *et al.*, 2012]. Later, the ability of APEX to oxidize and activate biotin-phenol to short lived biotin-phenoxyl radicals in the presence of H_2O_2 was used to biotinylate proximal proteins, which were subsequently identified in MS [Rhee *et al.*, 2013]. Because the biotin-phenoxyl radicals react with water molecules and other radicals, they rapidly decay while diffusing away from the active site of APEX2, creating a 'snapshot' of the local environment around the POI fused to APEX2. APEX2 generates high cytosolic background, but it is estimated that the cloud of activated biotin-phenol is restricted to the range of appr. 20 nm in living cells [Hung *et al.*, 2014; Kalocsay, 2019; Rhee *et al.*, 2013] and could be therefore superior to biotin ligase since interaction partners of *Pf*AIP that are more distant would be in range. The biotinylation of proteins proximal to the APEX2 tag depends on the dwelling time within the cloud of activated biotin-phenol radicals and its proximity to the APEX2 tag [Lobingier *et al.*, 2017]. The activity of BioID

is significantly reduced at temperatures below 37°C, but APEX2 has been shown to be active within a temperature range of RT to 37°C [Chen & Perrimon, 2017].

Recently, a split APEX2 (sAPEX2) was developed that makes use of an inactive N-terminal AP and C-terminal EX fragment, which can be fused to two proteins, respectively. Interaction of the two proteins reconstitutes active sAPEX2 [Han *et al.*, 2019]. The sAPEX2 approach could be combined with FRET or BRET (see 4.2.5), fusing *Pf*ARO and *Pf*AIP to donor and acceptor chromophores as well as to AP and EX. H_2O_2 would be added as soon as interaction is detected by a fluorescence signal. The fast proximity labelling kinetics of APEX2 (< 1 min) should enable high spatio-temporal resolution of a putative *Pf*ARO/*Pf*AIP/*Pf*ACβ/*Pf*MyoF interaction complex.

A selection marker-free parasite line could be established where AP is fused to FRB (FRB-AP) and inserted in the p230p locus via CRISPR/Cas9 [Marin-Mogollon *et al.*, 2016]. Using the SLI approach, POIs could be tagged quickly with FKBP-EX within the established FRB-AP line. The sAPEX2 would be reconstituted by the addition of rapalog. The regulation of biotinylation would be controlled by the addition of rapalog and H_2O_2. Subsequent MS would identify interaction partners analogously to the DIQ-BioID approach. The labelling radius could be increased by using linkers with extended lengths separating FRB/FKBP and AP/EX.

Protein interaction can be verified by co-IP, but many PPIs are not detected, as only high affinity interactions are measured and most transient interactions are lost, which is partially attributed to inappropriate buffer conditions [Dwane & Kiely, 2011]. Co-IP on the lysate of parasites expressing the bicistronic vector did not suggest an interaction of *Pf*ARO-GFP and *Pf*AIP-mCherry, despite the mild buffer conditions (0.1 % Triton X-100) used for lysis. Co-IP was performed with supernatant (input) fraction after lysis. Therefore, only soluble *Pf*ARO-GFP was pulled down, whereas the rhoptry membrane attached *Pf*ARO-GFP might not be eluted quantitatively by low Triton X-100 concentration. Additionally, it is conceivable that the tagging of both proteins with GFP and mCherry could have weakened the interaction. Applying bimolecular or trimolecular fluorescence complementation (BiFC, TriFC) could be suitable to determine *Pf*ARO/*Pf*AIP interaction, as BiFC and TriFC are able to capture weak or transient PPIs.

The bimolecular fluorescence complementation (BiFC) makes use of two fragments of a split fluorophore such as GFP1-10 and GFP11, which are fused to two (interacting) proteins of interest, respectively. The fragments only assemble together non-covalently when the two proteins are in close proximity, establishing fluorophore maturation [Cabantous *et al.*, 2005; Hu *et al.*, 2002]. The irreversible reconstitution of the fluorophore enables the detection of weak or transient interactions but limits the approach to monitor dynamic PPI which can be assessed by BRET (see 4.2.5). Since false positive signals can be detected, proper controls are needed. A binding partner with a mutation in the binding interface could be such a control. [Avilov & Aleksandrova, 2018; Kodama & Hu, 2012; Miller *et al.*, 2015]. Because of misfolding due to protein tagging with the GFP1-10 detector, or self-assembly background fluorescence, an improved split-GFP sensor was developed based on a tripartite association (TriFC) of short amino acids with the GFP detector [Cabantous *et al.*, 2013]. The split-GFP approach is applicable in *P. falciparum,* as demonstrated by recent publications [Garten *et al.*, 2018; Istvan *et al.*, 2019; Külzer *et al.*, 2013; Tarr & Osborne, 2015]. These publications show the use of split-GFP to determine the topology of membrane proteins and compartmentalization. No data could be found in the literature reporting the use of the split-GFP approach in *P. falciparum* to identify PPI. The BiFC/TriFC system, possibly combined with (s)TurboID or (s)APEX2,

could be used to dissect the interacting complexes of *Pf*ARO and *Pf*AIP, as shown in Fig. 4.1. A possible advantage of this system is that the background in subsequent MS should be minimal.

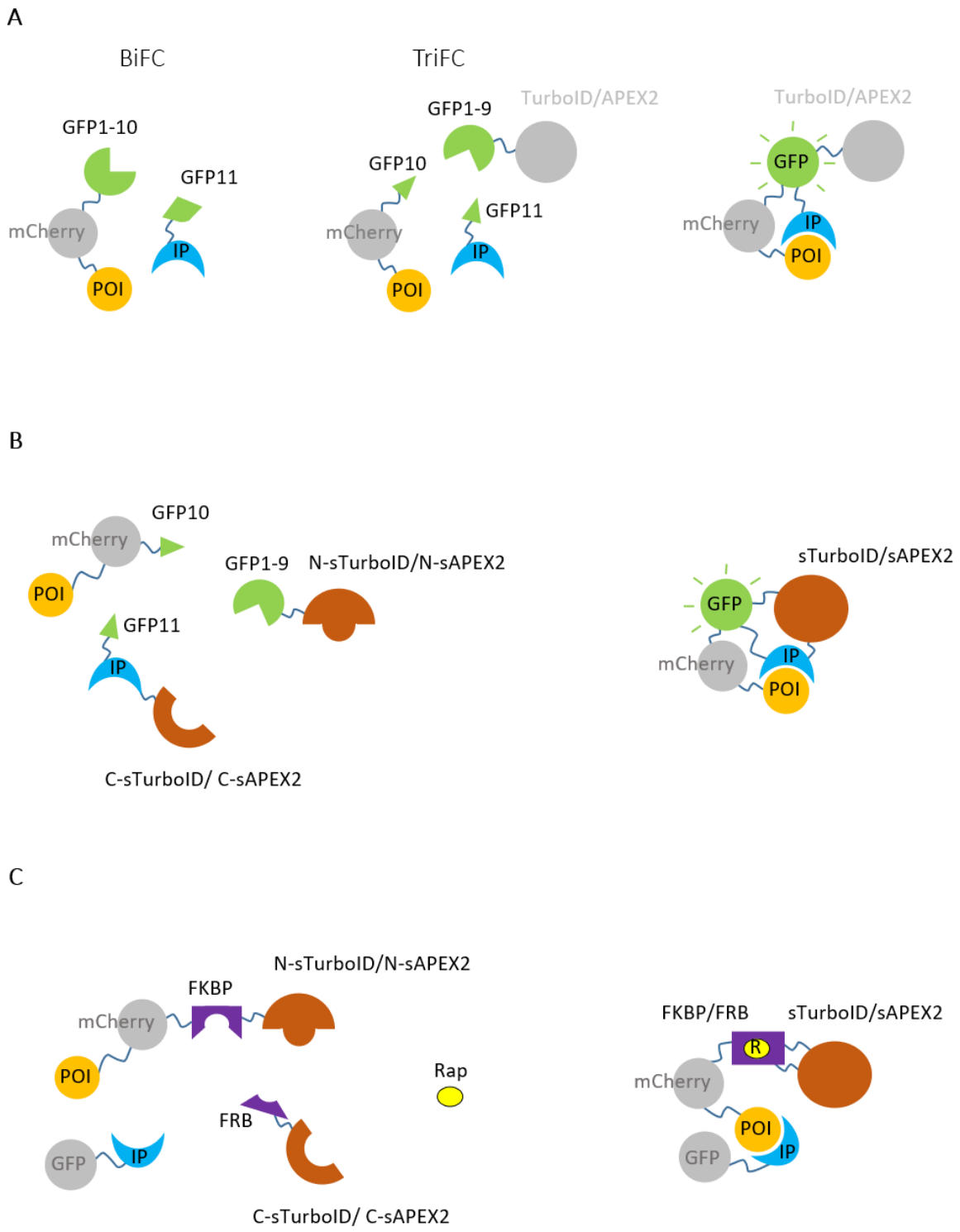

Fig. 4.1 | Use of fluorescence complementation to capture transient protein-protein interactions. (**A**) Schematic representation of bimolecular fluorescence complementation (BiFC) and trimolecular fluorescence complementation (TriFC). The GFP protein is split into fragments GFP1-10 and GFP11 for BiFC or split into fragments GFP1-9, GFP10 and GFP11 for TriFC. The interaction of POI and IP reconstitutes fluorescing GFP. TurboID and APEX2, fused to the GFP1-9 fragment, allow for the biotinylation of proximal proteins after the reconstitution of split GFP. (**B**) Same principle as in (A) but the interaction additionally reconstitutes split-

TurboID/split-APEX2 (sTurbo/sAPEX2) fragments. **C**) FKBP/FRB domain cause the reconstitution of sTurboID/sAPEX2 fragments upon rapalog addition to allow the biotinylation of proximal proteins. (A-C) Optional reporters/linkers are shown in grey. POI, protein of interest (*e.g. Pf*ARO); IP, interaction partner (*e.g. Pf*AIP); N-sTurboID, N-terminal split-TurboID fragment; N-sAPEX2, N-terminal split-APEX2 fragment; C-sTurboID, C-terminal split-TurboID fragment; C-sAPEX2, C-terminal split-APEX2 fragment; Rap/R, rapalog.

4.2.5 *Pf*ARO's mutations and its functional implication

The detailed analysis of the crystal structure of *Pf*ARO led to the identification of residues within the conserved regions of the protein, which appeared likely to be involved in PPI, or, more precisely, were predicted to be involved in *Pf*ARO-*Pf*AIP-interaction. To validate these predictions, mutant *Pf*ARO variants were over-expressed, and it was shown that mutations lead to a cytosolic distribution of over-expressed *Pf*AIP-mCherry. The results suggest either a direct or an indirect interaction of *Pf*ARO and *Pf*AIP, which is in accordance with previously published data that showed the interaction of *Tg*ARO with *Tg*AIP [Mueller *et al.*, 2013, 2016]. However, in the course of this work, co-IP experiments failed to detect *Pf*ARO-*Pf*AIP-interaction [Geiger & Brown *et al.*, 2020], nor did DIQ-BioID detect *Pf*ARO as a protein proximal to *Pf*AIP-2xFKBP-GFP, despite the partial co-localization (PCC = 0.7) of both proteins. A transient interaction during rhoptry development would be one explanation as to why *Pf*ARO mutations lead to the mislocalization of *Pf*AIP, although the interaction cannot be shown by co-IP or DIQ-BioID approaches, using late stage schizont material.

Using the bicistronic vector approach, it was not possible to assess the phenotypic effect of *Pf*ARO mutations, as the vector was transfected to the parental 3D7 line with intact *Pfaro* and *Pfaip* loci. For future studies, a complementation approach, as previously reported [Prinz *et al.*, 2016; Treeck *et al.*, 2009], in combination with the loxPint strategy [Jones *et al.*, 2016] could be applied. A parasite line could be created, which allows for the conditional DiCre-mediated knockout (see 4.4.1) of the endogenous *Pfaro* gene (resulting in parasite line cΔAROe). The parasite line cΔAROe could be transfected with vectors coding for different (recodonized) versions of *Pf*ARO-GFP mutants (resulting parasite line: cΔAROe/vARO^{mutant}). This would allow to assess if DiCre-mediated loss of endogenous *Pf*ARO (or *Pf*AIP) can be rescued by the complementation vectors.

To show if different versions of *Pf*ARO interact with *Pf*AIP, wide-field fluorescence microscopy was used. Whether interaction occurred or not was determined from the distribution of cytosolic *Pf*AIP signal. However, different approaches, such as ones which result in fluorescence signals only upon interaction, would be beneficial.

Förster resonance energy transfer (FRET) is one of the most commonly used methods to study bimolecular PPI in living cells. FRET is based on energy transfer between a (genetically encoded) donor chromophore (DC) and an acceptor chromophore (AC). The energy transfer results in DC quenching and excitation of the AC - if it is in close range to the DC. Live-cell FRET imaging provides a high spatio-temporal resolution, as quenching occurs within a 1-10 nm range [Bajar *et al.*, 2016]. FRET was used in combination with automated fluorescence lifetime imaging microscopy (FLIM) to identify binding partners [Margineanu *et al.*, 2016] and could also be applied to detect a transient interaction of *Pf*ARO/*Pf*AIP and additional interaction partners with high statistical power.

Alternatively, the bioluminescent resonance energy transfer (BRET) system can be used to detect dynamic/transient PPI. This method mostly uses the bioluminescent energy donor *Renilla* luciferase (RLuc, MW: 36 kDa). RLuc, fused to the POI, catalyzes the oxidation of coelenterazine (CLZN) to emit blue light at 482 nm. The blue light excites yellow fluorescent protein (YFP), which is fused to the putative interaction partner. Upon excitation, the YFP emits light at 530 nm. Unlike FRET, BRET does not require external excitation but the addition of cell permeant CLZN, which is used as a substrate by the RLuc. The addition of CLZN grants temporal control over the microplate reader assay to prevent inadvertent acceptor activation [Pfleger & Eidne, 2006; El Khamlichi *et al.*, 2019].

The small luciferase NanoLuc (NLuc, MW: 19.1 kDa) with a > 150-fold increased luminescence has been developed [Hall *et al.*, 2012] and recently expressed in *P. falciparum* [Azevedo *et al.*, 2014] as well as in *P. berghei* [De Niz *et al.*, 2016]. NLuc systems are used for a broad range of applications, such as NanoBRET, to study protein interaction dynamics [Machleidt *et al.*, 2015], and recent reviews highlight the applications of BRET and NanoBRET assays [Dale *et al.*, 2019; El Khamlichi *et al.*, 2019; England *et al.*, 2016].

FRET has been *i.a.* used in an *in situ* immunofluorescence approach to examine the interaction of the *Pf*RAMA protein and other rhoptry proteins [Topolska *et al.*, 2004], and a recently published work demonstrates the use of FRET live-cell imaging to explore PPI between CLAG3 and RhopH2 [Ahmad *et al.*, 2020].

Combining NanoBRET with automated detection in a microplate reader format should allow for the identification of transient interactions with high temporal resolution and statistical power. For this, *Pf*ARO and *Pf*AIP could be tagged endogenously with NLuc and YFP, creating the parasite line *Pf*ARO-NLuc/*Pf*AIP-YFP. Highly synchronized parasites (see 4.4.2) would be distributed on 96-Well microwell plates. Automated detection would be performed after adding the CLZN analogue furimazine, which is the substrate converted by NLuc. If *Pf*AIP and *Pf*ARO interact transiently, the interaction is expected to result in the excitation of YFP during the time of interaction, creating a fluorescence signal that can be detected by the microwell plate reader. NanoBRET data could be compared with stage-dependent expression data and the protein abundance to determine at which time point (hpi) *Pf*ARO and *Pf*AIP interact. Using the NanoBRET approach, it could also be assessed if and when a putative *Pf*ARO/*Pf*AIP/*Pf*ACβ complex interacts.

4.3 Discussion of additional findings

4.3.1 Conserved core region and *Pf*AIP structure prediction

Protein pairs with a sequence identity of 35 % and higher are considered to be structurally similar, whereas the structural similarity of protein pairs with a sequence identity of 20-35 % is considered as a “twilight-zone” where less than 10 % of proteins exhibit similar structures [Kinjo & Nishikawa, 2004; Rost, 2004]. Protein structure is, to a certain extent, tolerant of residue substitutions that preserve the hydropathic sequence profile [Krissinel, 2007]. As judged by the identity and similarity values of the CCRs and ICRs of *Tg*AIP, *Pf*AIP and the Vbra_13064 putative PH domain, the structural similarity of those regions seems likely.

I-TASSER was used for *Pf*AIP structure prediction, and the model with the highest C-score was superimposed on SspE (PDB accession: 6JIV) from *Streptomyces yokosukanensis*. This hydrolase is implicated in anti-phage activity

by phosphorothioation-sensing and introduces DNA nicks that impede viral DNA replication [Xiong *et al.*, 2020]. *Pf*AIP exerting such a function in the context of rhoptry development and invasion seems highly unlikely. However, proteins can show a global structural similarity and yet perform different functions. Also, proteins with the same fold and even members of a single homologous family can vary in the biochemical functions they perform [Keskin & Nussinov, 2005; Thornton *et al.*, 2000]. Whether this applies to *Pf*AIP and SspE needs to be ascertained.

The structure of *Pf*AIP or any other AIP protein is not known. This work tried to predict *Pf*AIP's structure using I-TASSER, which resulted in a low confidence model. It is not known whether *Pf*AIP has enzymatic functions or whether it is just an adaptor protein to recruit *Pf*ACβ to the rhoptry surface. Resolving *Pf*AIP structure, in particular when co-crystallized with *Pf*ARO, could possibly reveal the molecular interfaces that mediate catalytic activities.

4.3.2 Charge of the conserved core region

Charged residues are important for electrostatic PPI. The specificity of some interactions is increased by charged residues. For instance, the binding of proteins to cell membranes or to nucleic acids that exhibit a surface charge is expected to be strongly affected by electrostatic interactions, and residues important for interaction are often conserved between homologous proteins [Zhou & Pang, 2018]. The homologues *Pf*ARO and *Tg*ARO exhibit patches of strong positive and negative surface charges, which are likely important for PPI [Geiger & Brown *et al.*, 2020; Mueller *et al.*, 2016]. Additionally, *Pf*ARO was found to be acetylated at residues K_{26} and K_{168} [Cobbold *et al.*, 2016]. The acetylation of lysine side chains has diverse consequences. In histones, the acetylation of lysine compensates its positive charge and abolishes the formation of salt bridges with negatively charged DNA, and for some proteins it has been shown that lysine acetylation modulates PPI [Drazic *et al.*, 2016]. *Pf*AIP's CCR has an overall positive charge due to the content of the positively charged amino acids arginine and lysine, resulting in a calculated net charge of 13.2, whereas for *Tg*AIP a net charge of -5 was calculated. This circumstance might implicate different functions for their CCRs. The positively charged *Pf*AIP CCR may be important for interaction with a negatively charged interaction surface, such as that exposed by the *Pf*ARO protein [Geiger & Brown *et al.*, 2020].
Phosphorylations can introduce a negative charge on positively charged regions or further increase the negative charge of negatively charged regions, which affects PPI [Nishi *et al.*, 2014]. Phosphorylation, which acts as a fast process of PPI modulation, could affect *Pf*ARO-*Pf*AIP binding affinity, leading to its putative transient interaction.

4.3.3 *Pf*AIP isoforms

The *Pf*aip gene is alternatively spliced into two isoforms of *Pf*AIP that differ in length by 20 aa because of exon skipping without frameshift [Sorber *et al.*, 2011] within the first quarter of the CCR. Alternative splicing (AS) events are implicated in the stage differentiation of malaria parasites [Yeoh *et al.*, 2019a], and although many AS events in apicomplexans do not generate isoform proteins but noncoding transcripts, AS is an essential process in *P. falciparum* and other apicomplexan parasites [Yeoh *et al.*, 2019b]. Recent work on a proteomic scale identified different PPI profiles for alternatively spliced isoforms of human genes and suggested that many isoforms are functionally divergent [Yang *et al.*, 2016]. The shorter isoform of *Pf*AIP does not contain the phosphorylation-sites S_{101} and S_{115}. Considering the divergent functions of alternatively spliced isoforms and the contributions of PTM on PPI, it seems plausible that the two *Pf*AIP isoforms may have different functions, which might also be linked to

different parasite stages. However, no data currently available supports conclusions that a particular *Pf*AIP isoform is predominantly expressed in EEFs or ookinetes/oocysts. It is interesting to reflect on the fact that *Pfaip*, unlike *Pfaro*, is highly expressed in ookinetes [López-Barragán *et al.*, 2011] and also expressed in oocysts [Zanghì *et al.*, 2018].

To test if the two *Pf*AIP isoforms differ in function depending on the stage, one should first assess which isoform is expressed at what stage of development (asexual *vs* sexual stage). To determine the functions of both isoforms, a parasite line could be established that allows for the conditional depletion of *Pf*AIP by DiCre-mediated excision (see 4.4.1) of the endogenous *Pfaip* gene (resulting parasite line: cΔAIPe). Vectors would be transfected to the cΔAIPe line to assess which vector-coded *Pf*AIP isoforms (or *Pf*AIP phosphorylation-mutants) are able to compensate for the DiCre-mediated loss of *Pfaip*. Using the cΔAIPe line, one could also examine if the CCR or ICR of *Tg*AIP is able to functionally compensate for *Pf*AIP's CCR and ICR. To achieve this, a vector could be created that expresses a version of *Pf*AIP in which its CCR/ICR is replaced by CCR/ICR from *Tg*AIP or the putative PH domain of Vbra_13067.

4.3.4 Rhoptry protein sub-compartmentalization

If the *Pf*ARO protein were the only determinant for *Pf*AIP rhoptry membrane attachment, *Pf*AIP should also be distributed on the whole rhoptry surface. However, *Pf*AIP showed only a partial co-localization with *Pf*ARO, restricting it to the rhoptry neck, which implies some kind of sorting mechanism. A sub-compartmentalization of rhoptry proteins is well-established for other proteins such as RONs, RALP1 and CERLI1 (Haase *et al.*, 2008; Ito *et al.*, 2013; Liffner *et al.*, 2019; Tokunaga & Nozaki *et al.*, 2019), but how this is achieved is not known.

A differential localization is also reported for *Tg*AIP and *Tg*ACβ, which have been suggested as the first markers [Mueller *et al.*, 2016] of a morphologically defined intermediate rhoptry sub-compartment in *T. gondii* localized between the rhoptry bulb and neck [Lemgruber *et al.*, 2011]. This intermediate region is not described in *P. falciparum* yet, which could be due to the considerably smaller size of *P. falciparum* rhoptries compared to *T. gondii* rhoptries. Regarding the diffraction limit of widefield microscopy, which is about 200-250 nm in the XY dimension and 500-1,000 nm in the Z dimension [Galbraith & Galbraith, 2011; Heintzmann & Ficz, 2013], a more detailed rhoptry localization study would benefit from higher resolution techniques such as super-resolution or electron microscopy (see 4.4.5). Nevertheless, the rhoptry neck of *P. falciparum* has a length of about 250-280 nm [Hans *et al.*, 2013; Hanssen *et al.*, 2013; Rudlaff *et al.*, 2020], which allows the discrimination of a signal at the apical tip of the rhoptry neck and the bulbous region adjacent to the neck region (see Fig. 3.2E and Fig. 3.3A and [Geiger & Brown *et al.*, 2020]) by wide-field fluorescence microscopy. Correlative light EM or correlative super-resolution cryo EM would allow for the localization of *Pf*AIP and *Pf*ARO in more detail.

The sub-compartmentalization of membrane proteins is a well-known phenomenon of the plasma membrane (PM), but the extent to which lateral protein segregation contributes to specific biological functions at the PM is not clear. Recent work suggests that lateral compartmentalization provides a regulatory link between the function and turnover of PM proteins [Busto *et al.*, 2018]. It has been shown that compartmentalization leads to a reduced diffusional mobility of proteins and lipids, which in turn results *i.a.* in a reduced rate of protein dimerization within the membrane [Koldsø *et al.*, 2016].

Rhoptries show an organized structure, separated into the rhoptry neck and the rhoptry bulb (see Fig. 1.11B). It is currently not known what factors are responsible for the establishment of the rhoptry structure, but its sub-compartmentalization is a prerequisite for the ordered secretion of rhoptry protein content during invasion [Zuccala *et al.*, 2012].

As suggested in this thesis, *Pf*ARO shows a pronounced rhoptry bulb localization and partial co-localization with *Pf*AIP. Using super-resolution microscopy, it was shown that *Pf*AIP localizes in close proximity to *Pf*ARO with a minimal overlap [Geiger & Brown *et al.*, 2020].
The recruitment of *Pf*ARO to the rhoptry membrane depends solely on the first 20 aa (construct: 20ARO-GFP) that are recognised by a rhoptry specific PAT, which is most likely *Pf*DHHC7, the homologue of *Tg*DHHC7 that palmitoylates *Tg*ARO [Beck *et al.*, 2013; Cabrera *et al.*, 2012; Frénal *et al.*, 2013]. Membrane-attached proteins diffuse laterally depending on their concentration [Ramadurai *et al.*, 2009], which should be valid for acylated *Pf*ARO and 20ARO-GFP. Within an intermediate rhoptry sub-compartment, a sorting mechanism might shift a certain population of *Pf*ARO out of this intermediate region and prevent its lateral diffusion. Alternatively, *Pf*ARO might be pushed out from the intermediate region by specialized rhoptry neck proteins such as *Pf*AIP or *Pf*ACβ, probably assisted by accessory proteins.
As the knockout of *Tg*AIP and *Tg*ACβ had no reported effect on parasite proliferation [Mueller *et al.*, 2016], both proteins are unlikely to be accessory proteins mediating apical rhoptry positioning by *Tg*ARO. However, in *P. falciparum*, both homologues are essential [Geiger & Brown *et al.*, 2020; Patel & Perrin *et al.*, 2019; Zhang *et al.*, 2018], while the effect of *Pf*AIP and *Pf*ACβ depletion on rhoptry positioning was not shown on an ultrastructural level and should be assessed in future studies. (See 4.4.5 for further discussion on this point.)

It is tempting to speculate that a sorting depends on specific *Pf*ARO phosphorylation status. Phosphorylation, a universal regulative mechanism to regulate protein activity and subcellular localization, enables fast acting dynamics. The addition or removal of a phosphate group can change protein stability, structural properties and dynamics. Also, phosphorylation modulates PPI [Nishi *et al.*, 2014], and protein phosphorylation is described for many apicomplexan proteins [Doerig *et al.*, 2015]. Phospho-proteomics showed that *Pf*ARO has eight phosphorylation sites: S_{25}, T_{27}, S_{33}, T_{35}, S_{36}, S_{59}, T_{61} and T_{253} (see S1, Appendix). As mentioned in section 4.2.3, *Pf*ARO phosphorylation depends on *Pf*ACβ, *Pf*PKA and *Pf*CDPK5 activity. Hence, *Pf*ARO's function and rhoptry sub-compartment localization beeing controlled by its phosphorylation status seems plausible.
A slower migration through SDS gel is a well-known phenomenon of phosphorylated proteins. Differently phosphorylated populations of *Pf*ARO-GFP/*Pf*ARO-mCherry protein are suggested by two bands repeatedly detected at appr. 65 kDa and 55 kDa, although the possibility that the second and weaker band at 55 kDa was due to degradation cannot be completely excluded, given that other research did not identify two bands for *Pf*ARO using *Pf*ARO-specific antibodies [Cabrera *et al.*, 2012; Mitra *et al.*, 2016].

Recruitment to the rhoptry surface alone is not sufficient for proper rhoptry positioning, as indicated by a chimeric *Tg*DHHC7-*Tg*ARO construct, which localized independent of acylation to the rhoptry membrane and failed to rescue *Tg*ARO knockdown, resulting in the dispersion of rhoptries throughout the cytosol [Beck *et al.*, 2013]. The

authors assumed that more than simple localization of *Tg*ARO to the rhoptry surface is required for proper rhoptry function. The phosphorylation of ARO protein might be an important additional step for its function at the rhoptry. Interestingly, both *Tg*ARO and *Pf*ARO are phosphorylated at the conserved residues S_{33} and S_{59} (≙ S_{61} in *Tg*ARO) suggesting that those phosphorylation-sites are important for ARO function. Apart from phosphorylation, other modifications such as the lysine acetylation-sites (K_{26} and K_{168}) could be also important regulators with other effector proteins. Lysine acetylation is implicated in various cellular processes, including PPI [Drazic *et al.*, 2016].

To examine which *Pf*ARO phosphorylation-mutants interact with *Pf*AIP protein, bimolecular complementation affinity purification (BiCAP) [Croucher *et al.*, 2016] could be applied. For this method, *Pf*ARO phosphorylation-mutants and *Pf*AIP would be fused to GFP1-10 and GFP11, respectively. BiCAP of assembled GFP β-barrel conformation would be performed using the GFP-Trap© system. Alternatively, *Pf*ARO-GFP1-10 phosphorylation-mutants and *Pf*AIP-GFP11 could be tagged additionally with HA and FLAG tags to pull down the *Pf*ARO/*Pf*AIP/GFP complex. Subsequent WB analysis would reveal which *Pf*ARO phosphorylation-mutants interact with *Pf*AIP. MS analysis could be performed to confirm *Pf*ARO phosphorylation status. To test which *Pf*ARO/*Pf*AIP phosphorylation-sites are important for rhoptry sub-compartment localization, different phosphorylation-mutants could be fused to GFP and co-localized to rhoptry bulb and rhoptry neck markers to determine a phosphorylation-dependent sub-compartment localization.

4.4 Limitations of the study

Some of the methods applied in this study were probably not ideal to assess all the issues. For instance, KS of *Pf*AIP did not result in a reduction in parasitemia of more than 56 %. Also, the bicistronic vector approach used showed some technical limitations, as the vector for the over-expression of *Pf*ARO-GFP and *Pf*AIP-mCherry was integrated at the *Pfaip* locus (data not shown). In the following paragraphs, some of the methods used for this work are critically discussed and optimizations or alternative approaches are suggested.

4.4.1 Genetic manipulation and knock-sideways

After obtaining a stable transgenic AIP_{endo} line, drug selection with neomycin and WR99210 was ceased. After continuous cell culture of AIP_{condKS} parasites over several weeks without drug pressure, it was observed that the invasion phenotype became alleviated as KS caused a reduction in parasitemia of less than 30 % (data not shown). In fact, approximately one third of the parasites showed weak or no GFP signal, suggesting the presence of parasites (revertants) that reverted the integration of the SLI vector, outgrowing parasites with altered locus over time (data not shown). It was therefore necessary to keep cultures on continuous drug pressure with neomycin. When drug pressure is abolished, homologous integration of the vector can be reversed during continuous cell culture. It has been shown that a heterogenous population of revertant parasites can be produced from a clonal parent population after genomic rearrangements [Uzureau *et al.*, 2004]. To avoid the occurrence of revertants, transgenic parasite culture should be periodically tested by diagnostic PCR and kept on positive drug selection.

The mislocalization of *Pf*AIP-2xFKBP-GFP was not fully effective, as shown by some rapalog-treated schizonts that exhibited a residual GFP signal at the rhoptry neck. Furthermore, invasion was not completely inhibited in the

replication/invasion assay. This indicates that merozoites invaded with remaining rhoptry neck localized *Pf*AIP-2xFKBP-GFP (probably below the detection limit of fluorescence microscopy). It is unlikely that revertants were responsible for inefficient KS, since the parasite culture was selected with neomycin and was controlled for parasites with unaltered *Pfaip* locus. Hence, it is most likely that KS was leaky and not efficient. Another explanation could be that the KS induction by rapalog addition at 30 hpi was too late for some parasites that were ahead in development due to insufficient sorbitol synchronization (see 4.4.2). In those parasites, *Pf*AIP-2xFKBP-GFP could have been already associated within a putative interaction complex at the nascent rhoptry neck.

DiCre-mediated gene excision is a common method applied for different functional studies on *P. falciparum* genes [Collins *et al.*, 2013a; Jones *et al.*, 2016; Knuepfer *et al.*, 2017; Singh *et al.*, 2019; Tibúrcio *et al.*, 2019]. Recent work has used DiCre to excise *Pfacβ* gene from the genome to show its essentiality for invasion [Patel & Perrin *et al.*, 2019]. As the *Pfaip* gene exhibits six intron sequences, the loxPint strategy [Jones *et al.*, 2016] could be applied to enable the DiCre-mediated excision of *Pfaip*. The obtained phenotype is expected to show a higher reduction of parasitemia in the replication assay than the KS approach.
Another method to deplete parasites of *Pf*AIP is the use of the glmS ribozyme, which has been reported for *P. falciparum* [Prommana *et al.*, 2013]. Combining KS with the glmS system could improve the efficacy of *Pf*AIP depletion.

In the absence of a parasite line with endogenous-tagged *Pf*ARO, co-localization studies were performed using vectors with Ama1 promoter-controlled over-expression of *Pf*ARO-GFP or *Pf*ARO-mCherry. Therefore, it was not possible to assess the localization and protein abundance of endogenous *Pf*ARO. However, this data point is interesting, as it is not known whether *Pf*ARO protein is abundant before *Pf*AIP, which would be expected from the model suggested by Mueller and peers (see Fig. 1.16) [Mueller *et al.*, 2013]. Tagging both proteins within the same cell line would allow for the determination of protein abundance in an endogenous context.
One possible way to tag both proteins within the same cell line would be use of CRISPR/Cas9 technology, which was first applied in 2014 to alter the *P. falciparum* genome [Ghorbal *et al.*, 2014] and is now a commonly used genetic tool to study *P. falciparum* biology, as reported by more than 30 studies so far (www.pubmed.gov). CRISPR/Cas9 could be used to insert the desired genetic modification (*e.g.* fusion of 2xFKBP-GFP, mCherry) into the *P. falciparum* genome. Sequential genetic CRISPR/Cas9 editing, making use of negative selection of the donor plasmid [Marin-Mogollon *et al.*, 2016; Zhang & Gao *et al.*, 2017], would allow the tagging of *Pf*AIP and *Pf*ARO within the same parasite line.

4.4.2 Synchronization

For Giemsa smear and FC analysis as well as DIQ-BioID, parasites were synchronized twice a day with D-sorbitol. However, a tighter synchronization window may have led to a higher statistical effect in KS experiments, if schizonts with higher synchronicity release merozoites at about the same time. Given that *Pf*ARO and *Pf*AIP interact transiently, a higher synchronicity could allow for a 'snapshot' of the transient complex over time using TurboID (see 4.2.4). Furthermore, to test for the protein abundance of both proteins over time, a high synchronicity would also be beneficial. Upon examining cytograms from FC analysis, it became apparent that

rapalog may cause a lag in the development from ring to later stages, although this finding could not statistically be verified, presumably due to the insufficient synchronisation of parasites (data not shown). A higher level of synchronicity might enable the quantification of a putative rapalog-induced effect.

The sorbitol synchronization method [Lambros & Vanderberg, 1979] has a low degree of achieved synchronization, as the synchronization window (following one single sorbitol synchronization) is appr. 20 h [Kobayashi & Kato, 2016]. However, for some approaches (*e.g.* mRNA isolation from late schizont stage parasites) a much tighter synchronization window is desired, hence other synchronization methods combining sorbitol, Percoll® cushion centrifugation and magnetic-activated cell sorting (MACS) treatments [Childs *et al.*, 2013; Mata-Cantero *et al.*, 2014] could be applied. The Percoll®-sorbitol and MACS methods acquire parasite cultures with a relatively short synchronization window (appr. 8 h) but are time-consuming and expensive, which is why another, heparin-based, method was developed [Kobayashi & Kato, 2016]. A different method using concanavalin A (ConA) allows synchronization windows of 30 minutes and possibly even lower [Ranford-Cartwright *et al.*, 2010]. Generating such tight synchronization windows would enable studies of the asexual cell cycle with high temporal resolution. An easy, inexpensive, and labor-saving synchronization method has been described, which makes use of refrigerating asynchronous *P. falciparum* cultures to yield synchronous ring stage parasites [Yuan, Hao, Wu & Zhao *et al.*, 2014]. This method could be of particular use in cases where large quantities of synchronous parasites are needed.

4.4.3 Replication/invasion assay

The Giemsa smear analysis is a time-consuming procedure, and it yielded a lower statistical significance compared to the FC analysis in the KS experiments. Furthermore, Giemsa smear analysis should have been performed blinded, as observer bias and expectations can influence the study's outcome [Holman & Head *et al.*, 2015].
It was assumed that parasites depleted of *Pf*AIP are able to attach but unable to invade the RBC. Unexpectedly, the number of RBC-attached merozoites per ruptured schizont did not differ significantly, although a trend towards a higher number of RBC-attached merozoites for rapalog-induced parasites might be assumed. Performing the Giemsa smear analysis with a higher parasitemia and better synchronization could improve statistical validation. A further drawback of the Giemsa smear analysis is that only fixed time points are covered, and it is not possible to distinguish between attached or invaded merozoites. Hence, 2D time-lapse video microscopy of invading *P. falciparum* merozoites [Collins *et al.*, 2013b; Grüring *et al.*, 2011; Patel & Perrin *et al.*, 2019; Perrin *et al.*, 2018] could be performed to observe the behavior of merozoites depleted of *Pf*AIP.

The determination of egress and newly formed rings per ruptured schizont was possible with FC analysis. Hence it is superior to Giemsa smear analysis, as it is less biased and allows fast high-throughput analysis, although FC analysis is not reliable during the first timepoints as long as parasitemia is below 0.2 % [Bei *et al.*, 2010]. However, as the parasite culture was treated identically before splitting and adding rapalog, this can be neglected.

In case merozoites depleted of *Pf*AIP are unable to attach or detach after initial attachment, the determination of free merozoites by high-throughput FC analysis would be beneficial. To detect free merozoites, the forward scatter

(FSC) voltage has to be adjusted [Lehmann *et al.*, 2018]. By doing so, the populations of free merozoites of rapalog-treated and control parasites could be assessed for different time points after egress.

Indeed, the number of merozoites within schizonts has to be counted to exclude that the addition of rapalog or the depletion of the protein affects merozoite formation or schizont morphology. Counting intracellular merozoites by classical 2D microscopy is erroneous, since merozoites are not represented sufficiently in one optical plane of a schizont. An automated method for counting intracellular merozoites based on 3D microscopy has been developed [Garg *et al.*, 2015], which could be applied in future studies. To further define invasion events for *Pf*AIP depleted parasites, viable merozoites could be isolated [Boyle *et al.*, 2010] from rapalog-treated and control parasites to analyze the kinetics of invasion in more detail.

4.4.4 Controls

From previous work using KS [Birnbaum & Flemming *et al.*, 2017], it was expected that the addition of rapalog does not induce detrimental effects. However, the KS system lacks a proper control, because the effect of rapalog cannot be determined in the context of the FKBP-GFP tagged gene, as the rapalog addition causes the mislocalization of the POI, inducing the phenotype. Such a control could be realized by transfecting AIP_{endo} parasites with a mislocalizer construct bearing a non-functional FRB domain that is unable to dimerize with *Pf*AIP-2xFKBP-GFP. To ensure that both mislocalizer versions are expressed equally, the coding gene and preceding promoter could be integrated into the genome at a locus such as *p230p,* which is unimportant for blood stage development [Marin-Mogollon *et al.*, 2018], creating an integrated mislocalizer cell line that could be used for subsequent KS approaches of a POI tagged with FKBP. Alternatively, the AIP_{endo} line could be transfected individually with two mislocalizer versions (wild-type and mutant FRB). Selection with blasticidin should result in the same copy numbers of episomes, and equal protein abundance could be assessed using WB analysis.

Different FRB mutants are known to selectively interact with the FKBP domain depending on the compound used [Putyrski & Schultz, 2012]. As a control, an FRB mutant could be chosen that is unable to dimerize with FKBP upon rapalog addition. Using an FRB mutant should be considered for the DIQ-BioID approach as well to subtract false positive hits.

4.4.5 Microscopy

The depletion of functional *Tg*DHHC7 and *Tg*ARO led to the dispersion of rhoptries throughout the cytosol [Beck *et al.*, 2013; Frénal *et al.*, 2013; Mueller *et al.*, 2013, 2016]. Since it was suspected that the small size of *P. falciparum* merozoites compared to *T. gondii* tachyzoites limits the cytosolic dispersion of rhoptries, whether KS of *Pf*AIP-2xFKBP-GFP also leads to a rhoptry dispersion was not tested. The phenotype would most likely not be obvious using light microscopy. The ultrastructural effect of *Pf*ARO and *Pf*AIP depletion from rhoptries on rhoptry morphology should rather be assessed using electron microscopy (EM). To test whether *Pf*AIP is indeed localized to an intermediate rhoptry sub-compartment (see 4.3.4), immuno-EM could be performed. However, a well-known problem with immuno-EM is that the antibody needs to get through fixed samples and the fixation process of cells destroys a lot of antigenic reactivity.

In *T. gondii* rhoptries, the intermediate rhoptry sub-compartment has a length of less than 200 nm [Lemgruber *et al.*, 2011] whereas, if existing, this compartment would expectedly be significantly smaller (< 50 nm) in

P. falciparum rhoptries. It is questionable whether immuno-EM would be able to adequately pinpoint *Pf*AIP's or *Pf*ARO's sub-compartment localization. Instead, *Pf*AIP/*Pf*ARO could be tagged with a mini Singlet Oxygen Generator (miniSOG) to allow correlated fluorescence electron microscopy (CLEM) as well as electron tomography (ET) for 3D protein localization. The miniSOG is a small fluorescent protein that generates reactive oxygen species (ROS) when exposed to 488 nm. Local ROS catalyze the reaction of diaminobenzidine (DAB) to an osmiophilic polymer that can be resolved by ET or EM [Shu *et al.*, 2011]. Applying this technique on tightly synchronized parasites, a high spatio-temporal resolution of *Pf*AIP-miniSOG and *Pf*ARO-miniSOG localization could be achieved. In a recent publication, a miniSOG-FLAG tag was used to label CLAG3 in *P. falciparum*, but EM studies are not reported yet [Gupta *et al.*, 2018]. Split-miniSOG allows visualization of intracellular PPI by CLEM [Boassa *et al.*, 2019] and could be used to identify *Pf*AIP/*Pf*ARO interaction on an ultrastructural level.

Due to the diffraction limit, conventional wide-field fluorescence microscopy is limited to a spatial resolution of appr. 200-250 nm. Super-resolution imaging methods such as stimulated emission depletion (STED) can reach resolutions below the diffraction limit and are likely to become the method of choice to study subcellular structures at the nanoscale [Vicidomini *et al.*, 2018]. A recently published study describes the use of STED nanoscopy in *P. falciparum,* which allowed imaging of individual microtubules and nuclear pores [Mehnert & Guizetti *et al.*, 2019]. STED nanoscopy could be applied to examine *Pf*ARO and *Pf*AIP rhoptry localization in more detail.

4.5 Conclusion

In summary, the rhoptry neck protein *Pf*AIP was identified and functionally characterized. The presented study shows that *Pf*AIP is essential for efficient erythrocyte invasion that might be - at least in part - mediated by its interaction partner *Pf*ACβ. We also delivered, for the first time, a crystal structure of *Pf*ARO and used this structural information to probe its putative interaction with *Pf*AIP. The cytosolic distribution of *Pf*AIP, provoked by mutations within *Pf*ARO protein, suggests that interaction with *Pf*ARO is essential for rhoptry distribution. However, this interaction appears to be transient or indirect as *Pf*ACβ but not *Pf*ARO was identified using proximity-based biotinylation.

4.6 Outlook

An *Pf*ACβ-*Pf*AIP-interaction at the rhoptry links *Pf*AIP function to cyclic nucleotide signalling in order to activate downstream processes at the rhoptry surface that finally trigger rhoptry secretion. How this is achieved is currently unknown, but *Pf*AIP appears to be an important cornerstone. The elucidation of the *Pf*AIP structure will be an important step to understand this conserved apicomplexan-specific protein, which does not reveal any domain with known function.

Another important aspect is the molecular interplay between *Pf*AIP and *Pf*ARO at the rhoptry neck. They show only a partial overlap, but nevertheless, *Pf*AIP is not recruited to the rhoptry upon depletion of *Pf*ARO. It is likewise astonishing that *Pf*ARO and *Pf*AIP are located in different rhoptry sub-compartments despite their apparent interaction. Further experiments are needed to pinpoint the exact localization of both proteins during rhoptry biogenesis and elucidate when *Pf*ARO-*Pf*AIP interaction occurs.

BIBLIOGRAPHY

Abu Bakar, N.; Klonis, Nectarios; Hanssen, Eric; Chan, Cherrine; Tilley, Leann (2010). Digestive-vacuole genesis and endocytic processes in the early intraerythrocytic stages of Plasmodium falciparum. *J Cell Sci* **123**, 441–450 [DOI: 10.1242/jcs.061499].

Adl, S. M.; Leander, Brian S.; Simpson, Alastair G. B.; Archibald, John M.; Anderson, O. Roger; Bass, David *et al.* (2007). Diversity, nomenclature, and taxonomy of protists. *Syst Biol* **56**, 684–689 [DOI: 10.1080/10635150701494127].

Adl, S. M.; Simpson, Alastair G. B.; Lane, Christopher E.; Lukeš, Julius; Bass, David; Bowser, Samuel S. *et al.* (2012). The revised classification of eukaryotes. *J Eukaryot Microbiol* **59**, 429–493 [DOI: 10.1111/j.1550-7408.2012.00644.x].

Agop-Nersesian, C.; Naissant, Bernina; Ben Rached, Fathia; Rauch, Manuel; Kretzschmar, Angelika; Thiberge, Sabine *et al.* (2009). Rab11A-controlled assembly of the inner membrane complex is required for completion of apicomplexan cytokinesis. *PLoS Pathog* **5**, e1000270 [DOI: 10.1371/journal.ppat.1000270].

Ahmad, M.; Manzella-Lapeira, Javier; Saggu, Gagandeep; Ito, Daisuke; Brzostowski, Joseph A.; Desai, Sanjay A. (2020). Live-Cell FRET Reveals that Malaria Nutrient Channel Proteins CLAG3 and RhopH2 Remain Associated throughout Their Tortuous Trafficking. *mBio* **11** [DOI: 10.1128/mBio.01354-20].

Ahmed, M. A.; Cox-Singh, J. (2015). Plasmodium knowlesi - an emerging pathogen. *ISBT Sci Ser* **10**, 134–140 [DOI: 10.1111/voxs.12115].

Alam, M. M.; Solyakov, Lev; Bottrill, Andrew R.; Flueck, Christian; Siddiqui, Faiza A.; Singh, Shailja *et al.* (2015). Phosphoproteomics reveals malaria parasite Protein Kinase G as a signalling hub regulating egress and invasion. *Nat Commun* **6**, 7285 [DOI: 10.1038/ncomms8285].

Alexander, D. L.; Mital, Jeffrey; Ward, Gary E.; Bradley, Peter; Boothroyd, John C. (2005). Identification of the moving junction complex of Toxoplasma gondii: a collaboration between distinct secretory organelles. *PLoS Pathog* **1**, e17 [DOI: 10.1371/journal.ppat.0010017].

Alkhalil, A.; Cohn, Jamieson V.; Wagner, Marissa A.; Cabrera, Jennifer S.; Rajapandi, Thavamani; Desai, Sanjay A. (2004). Plasmodium falciparum likely encodes the principal anion channel on infected human erythrocytes. *Blood* **104**, 4279–4286 [DOI: 10.1182/blood-2004-05-2047].

Altschul, S. F.; Gish, Warren; Miller, Webb; Myers, Eugene W.; Lipman, David J. (1990). Basic local alignment search tool. *J Mol Biol* **215**, 403–410 [DOI: 10.1016/S0022-2836(05)80360-2].

Andreeva, A.; Howorth, Dave; Chothia, Cyrus; Kulesha, Eugene; Murzin, Alexey G. (2014). SCOP2 prototype: a new approach to protein structure mining. *Nucleic Acids Res* **42**, D310-4 [DOI: 10.1093/nar/gkt1242].

Andreeva, A.; Kulesha, Eugene; Gough, Julian; Murzin, Alexey G. (2020). The SCOP database in 2020: expanded classification of representative family and superfamily domains of known protein structures. *Nucleic Acids Res* **48**, D376-D382 [DOI: 10.1093/nar/gkz1064].

Archibald, J. M., Simpson, A. G. B. & Slamovits, C. H., eds (2017). Handbook of the protists, 2nd ed., Springer, Cham. [https://www.springer.com/de/book/9783319281476]

Ariey, F.; Witkowski, Benoit; Amaratunga, Chanaki; Beghain, Johann; Langlois, Anne-Claire; Khim, Nimol *et al.* (2014). A molecular marker of artemisinin-resistant Plasmodium falciparum malaria. *Nature* **505**, 50–55 [DOI: 10.1038/nature12876].

Ashley, E. A.; Phyo, Aung Pyae (2018). Drugs in Development for Malaria. *Drugs* **78**, 861–879 [DOI: 10.1007/s40265-018-0911-9].

Avilov, S. V.; Aleksandrova, Nataliia (2018). Fluorescence protein complementation in microscopy: applications beyond detecting bi-molecular interactions. *Methods Appl Fluoresc* **7**, 12001 [DOI: 10.1088/2050-6120/aaef01].

Azevedo, M. F.; Nie, Catherine Q.; Elsworth, Brendan; Charnaud, Sarah C.; Sanders, Paul R.; Crabb, Brendan S. *et al.* (2014). Plasmodium falciparum transfected with ultra bright NanoLuc luciferase offers high sensitivity detection for the screening of growth and cellular trafficking inhibitors. *PLoS ONE* **9**, e112571 [DOI: 10.1371/journal.pone.0112571].

Babu, M. M. (2016). The contribution of intrinsically disordered regions to protein function, cellular complexity, and human disease. *Biochem Soc Trans* **44**, 1185–1200 [DOI: 10.1042/BST20160172].

Baird, J. K. (2013). Evidence and implications of mortality associated with acute Plasmodium vivax malaria. *Clin Microbiol Rev* **26**, 36–57 [DOI: 10.1128/CMR.00074-12].

Bajar, B. T.; Wang, Emily S.; Zhang, Shu; Lin, Michael Z.; Chu, Jun (2016). A Guide to Fluorescent Protein FRET Pairs. *Sensors (Basel)* **16** [DOI: 10.3390/s16091488].

Baker, D. A.; Drought, Laura G.; Flueck, Christian; Nofal, Stephanie D.; Patel, Avnish; Penzo, Maria *et al.* (2017). Cyclic nucleotide signalling in malaria parasites. *Open biology* **7** [DOI: 10.1098/rsob.170213].

Baker, N. A.; Sept, D.; Joseph, S.; Holst, M. J.; McCammon, J. A. (2001). Electrostatics of nanosystems: application to microtubules and the ribosome. *Proc Natl Acad Sci U S A* **98**, 10037–10041 [DOI: 10.1073/pnas.181342398].

Baldwin, M. R.; Li, Xuerong; Hanada, Toshihiko; Liu, Shih-Chun; Chishti, Athar H. (2015). Merozoite surface protein 1 recognition of host glycophorin A mediates malaria parasite invasion of red blood cells. *Blood* **125**, 2704–2711 [DOI: 10.1182/blood-2014-11-611707].

Bannister, L. H.; Hopkins, J. M.; Fowler, R. E.; Krishna, S.; Mitchell, G. H. (2000). Ultrastructure of rhoptry development in Plasmodium falciparum erythrocytic schizonts. *Parasitology* **121 (Pt 3)**, 273–287 [DOI: 10.1017/s0031182099006320].

Bannister, L. H.; Hopkins, John M.; Dluzewski, Anton R.; Margos, Gabriele; Williams, Ian T.; Blackman, Michael J. *et al.* (2003). Plasmodium falciparum apical membrane antigen 1 (PfAMA-1) is translocated within micronemes along subpellicular microtubules during merozoite development. *J Cell Sci* **116**, 3825–3834 [DOI: 10.1242/jcs.00665].

Bannister, L. H.; Mitchell, G. H.; Butcher, G. A.; Dennis, E. D.; Cohen, S. (1986). Structure and development of the surface coat of erythrocytic merozoites of Plasmodium knowlesi. *Cell Tissue Res* **245**, 281–290 [DOI: 10.1007/BF00213933].

Bartoloni, A.; Zammarchi, Lorenzo (2012). Clinical aspects of uncomplicated and severe malaria. *Mediterr J Hematol Infect Dis* **4**, e2012026 [DOI: 10.4084/MJHID.2012.026].

Baruch, D. I.; Pasloske, Britten L.; Singh, Hardeep B.; Bi, Xiahui; Ma, Xin C.; Feldman, Michael *et al.* (1995). Cloning the P. falciparum gene encoding PfEMP1, a malarial variant antigen and adherence receptor on the surface of parasitized human erythrocytes. *Cell* **82**, 77–87 [DOI: 10.1016/0092-8674(95)90054-3].

Beck, J. R.; Fung, Connie; Straub, Kurtis W.; Coppens, Isabelle; Vashisht, Ajay A.; Wohlschlegel, James A. *et al.* (2013). A Toxoplasma palmitoyl acyl transferase and the palmitoylated armadillo repeat protein TgARO govern apical rhoptry tethering and reveal a critical role for the rhoptries in host cell invasion but not egress. *PLoS Pathog* **9**, e1003162 [DOI: 10.1371/journal.ppat.1003162].

Bei, A. K.; Desimone, Tiffany M.; Badiane, Aida S.; Ahouidi, Ambroise D.; Dieye, Tandakha; Ndiaye, Daouda *et al.* (2010). A flow cytometry-based assay for measuring invasion of red blood cells by Plasmodium falciparum. *Am J Hematol* **85**, 234–237 [DOI: 10.1002/ajh.21642].

Beier, J. C.; Müller, Günter C.; Gu, Weidong; Arheart, Kristopher L.; Schlein, Yosef (2012). Attractive toxic sugar bait (ATSB) methods decimate populations of Anopheles malaria vectors in arid environments regardless of the local availability of favoured sugar-source blossoms. *Malar J* **11**, 31 [DOI: 10.1186/1475-2875-11-31].

Berman, H. M.; Westbrook, J.; Feng, Z.; Gilliland, G.; Bhat, T. N.; Weissig, H. *et al.* (2000). The Protein Data Bank. *Nucleic Acids Res* **28**, 235–242 [DOI: 10.1093/nar/28.1.235].

Besteiro, S.; Michelin, Adeline; Poncet, Joël; Dubremetz, Jean-François; Lebrun, Maryse (2009). Export of a Toxoplasma gondii rhoptry neck protein complex at the host cell membrane to form the moving junction during invasion. *PLoS Pathog* **5**, e1000309 [DOI: 10.1371/journal.ppat.1000309].

Bhatt, S.; Weiss, D. J.; Cameron, E.; Bisanzio, D.; Mappin, B.; Dalrymple, U. *et al.* (2015). The effect of malaria control on Plasmodium falciparum in Africa between 2000 and 2015. *Nature* **526**, 207–211 [DOI: 10.1038/nature15535].

Billker, O.; Lindo, V.; Panico, M.; Etienne, A. E.; Paxton, T.; Dell, A. *et al.* (1998). Identification of xanthurenic acid as the putative inducer of malaria development in the mosquito. *Nature* **392**, 289–292 [DOI: 10.1038/32667].

Birnbaum, J.; Flemming, Sven; Reichard, Nick; Soares, Alexandra Blancke; Mesén-Ramírez, Paolo; Jonscher, Ernst *et al.* (**2017**). A genetic system to study Plasmodium falciparum protein function. *Nat Methods* **14**, 450–456 [DOI: 10.1038/nmeth.4223].

Birnbaum, J.; Scharf, Sarah; Schmidt, Sabine; Jonscher, Ernst; Hoeijmakers, Wieteke Anna Maria; Flemming, Sven *et al.* (**2020**). A Kelch13-defined endocytosis pathway mediates artemisinin resistance in malaria parasites. *Science* **367**, 51–59 [DOI: 10.1126/science.aax4735].

Blomqvist, K.; Helmel, Michaela; Wang, Chengqi; Absalon, Sabrina; Labunska, Tetanya; Rudlaff, Rachel M. *et al.* (**2020**). Influence of Plasmodium falciparum Calcium-Dependent Protein Kinase 5 (PfCDPK5) on the Late Schizont Stage Phosphoproteome. *mSphere* **5** [DOI: 10.1128/mSphere.00921-19].

Boassa, D.; Lemieux, Sakina P.; Lev-Ram, Varda; Hu, Junru; Xiong, Qing; Phan, Sebastien *et al.* (**2019**). Split-miniSOG for Spatially Detecting Intracellular Protein-Protein Interactions by Correlated Light and Electron Microscopy. *Cell Chem Biol* **26**, 1407-1416.e5 [DOI: 10.1016/j.chembiol.2019.07.007].

Boddey, J. A.; Cowman, Alan F. (**2013**). Plasmodium nesting: remaking the erythrocyte from the inside out. *Annu Rev Microbiol* **67**, 243–269 [DOI: 10.1146/annurev-micro-092412-155730].

Botté, C. Y.; Yamaryo-Botté, Yoshiki (**2018**). Complex Endosymbioses II: The Nonphotosynthetic Plastid of Apicomplexa Parasites (The Apicoplast) and Its Integrated Metabolism. *Methods Mol Biol* **1829**, 37–54 [DOI: 10.1007/978-1-4939-8654-5_3].

Bowers, K.; Stevens, Tom H. (**2005**). Protein transport from the late Golgi to the vacuole in the yeast Saccharomyces cerevisiae. *Biochim Biophys Acta* **1744**, 438–454. http://www.sciencedirect.com/science/article/pii/S0167488905000753 [DOI: 10.1016/j.bbamcr.2005.04.004].

Boyle, M. J.; Wilson, Danny W.; Richards, Jack S.; Riglar, David T.; Tetteh, Kevin K. A.; Conway, David J. *et al.* (**2010**). Isolation of viable Plasmodium falciparum merozoites to define erythrocyte invasion events and advance vaccine and drug development. *Proc Natl Acad Sci U S A* **107**, 14378–14383 [DOI: 10.1073/pnas.1009198107].

Bozdech, Z.; Llinás, Manuel; Pulliam, Brian Lee; Wong, Edith D.; Zhu, Jingchun; DeRisi, Joseph L. (**2003**). The transcriptome of the intraerythrocytic developmental cycle of Plasmodium falciparum. *PLoS Biol* **1**, E5 [DOI: 10.1371/journal.pbio.0000005].

Bradley, P. J.; Ward, Chris; Cheng, Stephen J.; Alexander, David L.; Coller, Susan; Coombs, Graham H. *et al.* (**2005**). Proteomic analysis of rhoptry organelles reveals many novel constituents for host-parasite interactions in Toxoplasma gondii. *J Biol Chem* **280**, 34245–34258 [DOI: 10.1074/jbc.M504158200].

Brancucci, N. M. B.; Bertschi, Nicole L.; Zhu, Lei; Niederwieser, Igor; Chin, Wai Hoe; Wampfler, Rahel *et al.* (**2014**). Heterochromatin protein 1 secures survival and transmission of malaria parasites. *Cell Host Microbe* **16**, 165–176 [DOI: 10.1016/j.chom.2014.07.004].

Branon, T. C.; Bosch, Justin A.; Sanchez, Ariana D.; Udeshi, Namrata D.; Svinkina, Tanya; Carr, Steven A. *et al.* (**2018**). Efficient proximity labeling in living cells and organisms with TurboID. *Nat Biotechnol* **36**, 880–887 [DOI: 10.1038/nbt.4201].

Breinich, M. S.; Ferguson, David J. P.; Foth, Bernardo J.; van Dooren, Giel G.; Lebrun, Maryse; Quon, Doris V. *et al.* (**2009**). A dynamin is required for the biogenesis of secretory organelles in Toxoplasma gondii. *Curr Biol* **19**, 277–286 [DOI: 10.1016/j.cub.2009.01.039].

Burns, W. R. (**2008**). East meets West: how China almost cured malaria. *Endeavour* **32**, 101–106 [DOI: 10.1016/j.endeavour.2008.07.001].

Busto, J. V.; Elting, Annegret; Haase, Daniel; Spira, Felix; Kuhlman, Julian; Schäfer-Herte, Marco *et al.* (**2018**). Lateral plasma membrane compartmentalization links protein function and turnover. *EMBO J* **37** [DOI: 10.15252/embj.201899473].

Cabantous, S.; Nguyen, Hau B.; Pedelacq, Jean-Denis; Koraïchi, Faten; Chaudhary, Anu; Ganguly, Kumkum *et al.* (**2013**). A new protein-protein interaction sensor based on tripartite split-GFP association. *Sci Rep* **3**, 2854 [DOI: 10.1038/srep02854].

Cabantous, S.; Terwilliger, Thomas C.; Waldo, Geoffrey S. (**2005**). Protein tagging and detection with engineered self-assembling fragments of green fluorescent protein. *Nat Biotechnol* **23**, 102–107 [DOI: 10.1038/nbt1044].

Cabrera, A.; Herrmann, Susann; Warszta, Dominik; Santos, Joana M.; John Peter, Arun T.; Kono, Maya *et al.* (2012). Dissection of minimal sequence requirements for rhoptry membrane targeting in the malaria parasite. *Traffic* 13, 1335–1350 [DOI: 10.1111/j.1600-0854.2012.01394.x].

Cavalier-Smith, T. (1993). Kingdom protozoa and its 18 phyla. *Microbiol Rev* 57, 953–994. [PMC372943]

Chen, C.-L.; Perrimon, Norbert (2017). Proximity-dependent labeling methods for proteomic profiling in living cells. *Wiley Interdiscip Rev Dev Biol* 6 [DOI: 10.1002/wdev.272].

Chenet, S. M.; Akinyi Okoth, Sheila; Huber, Curtis S.; Chandrabose, Javin; Lucchi, Naomi W.; Talundzic, Eldin *et al.* (2016). Independent Emergence of the Plasmodium falciparum Kelch Propeller Domain Mutant Allele C580Y in Guyana. *J Infect Dis.* 213, 1472–1475 [DOI: 10.1093/infdis/jiv752].

Childs, R. A.; Miao, Jun; Gowda, Channe; Cui, Liwang (2013). An alternative protocol for Plasmodium falciparum culture synchronization and a new method for synchrony confirmation. *Malar J* 12, 386 [DOI: 10.1186/1475-2875-12-386].

Cho, K. F.; Branon, Tess C.; Rajeev, Sanjana; Svinkina, Tanya; Udeshi, Namrata D.; Thoudam, Themis *et al.* (2020). Split-TurboID enables contact-dependent proximity labeling in cells. *Proc Natl Acad Sci U S A* 117, 12143–12154 [DOI: 10.1073/pnas.1919528117].

Chojnowski, A.; Sobota, Radoslaw M.; Ong, Peh Fern; Xie, Wei; Wong, Xianrong; Dreesen, Oliver *et al.* (2018). 2C-BioID: An Advanced Two Component BioID System for Precision Mapping of Protein Interactomes. *iScience* 10, 40–52 [DOI: 10.1016/j.isci.2018.11.023].

Chu, C. S.; White, Nicholas J. (2016). Management of relapsing Plasmodium vivax malaria. *Expert Rev Anti Infect Ther* 14, 885–900 [DOI: 10.1080/14787210.2016.1220304].

Cobbold, S. A.; Santos, Joana M.; Ochoa, Alejandro; Perlman, David H.; Llinás, Manuel (2016). Proteome-wide analysis reveals widespread lysine acetylation of major protein complexes in the malaria parasite. *Sci Rep* 6, 19722 [DOI: 10.1038/srep19722].

Coleman, M.; Hemingway, Janet; Gleave, Katherine Ann; Wiebe, Antoinette; Gething, Peter W.; Moyes, Catherine L. (2017). Developing global maps of insecticide resistance risk to improve vector control. *Malar J* 16, 86 [DOI: 10.1186/s12936-017-1733-z].

Collins, J. P. (2018). Gene drives in our future: challenges of and opportunities for using a self-sustaining technology in pest and vector management. *BMC Proc* 12, 9 [DOI: 10.1186/s12919-018-0110-4].

Collins, C. R.; Das, Sujaan; Wong, Eleanor H.; Andenmatten, Nicole; Stallmach, Robert; Hackett, Fiona *et al.* (2013a). Robust inducible Cre recombinase activity in the human malaria parasite Plasmodium falciparum enables efficient gene deletion within a single asexual erythrocytic growth cycle. *Mol Microbiol* 88, 687–701 [DOI: 10.1111/mmi.12206].

Collins, C. R.; Hackett, Fiona; Strath, Malcolm; Penzo, Maria; Withers-Martinez, Chrislaine; Baker, David A. *et al.* (2013b). Malaria parasite cGMP-dependent protein kinase regulates blood stage merozoite secretory organelle discharge and egress. *PLoS Pathog* 9, e1003344 [DOI: 10.1371/journal.ppat.1003344].

Collins, W. E.; Jeffery, Geoffrey M. (2005). Plasmodium ovale: parasite and disease. *Clin Microbiol Rev* 18, 570–581 [DOI: 10.1128/CMR.18.3.570-581.2005].

Collins, W. E.; Jeffery, Geoffrey M. (2007). Plasmodium malariae: parasite and disease. *Clin Microbiol Rev* 20, 579–592 [DOI: 10.1128/CMR.00027-07].

Coppi, A.; Tewari, Rita; Bishop, Joseph R.; Bennett, Brandy L.; Lawrence, Roger; Esko, Jeffrey D. *et al.* (2007). Heparan sulfate proteoglycans provide a signal to Plasmodium sporozoites to stop migrating and productively invade host cells. *Cell Host Microbe* 2, 316–327 [DOI: 10.1016/j.chom.2007.10.002].

Counihan, N. A.; Chisholm, Scott A.; Bullen, Hayley E.; Srivastava, Anubhav; Sanders, Paul R.; Jonsdottir, Thorey K. *et al.* (2017). Plasmodium falciparum parasites deploy RhopH2 into the host erythrocyte to obtain nutrients, grow and replicate. *eLife* 6 [DOI: 10.7554/eLife.23217].

Counihan, N. A.; Kalanon, Ming; Coppel, Ross L.; Koning-Ward, Tania F. de (2013). Plasmodium rhoptry proteins: why order is important. *Trends Parasitol* 29, 228–236. https://pubmed.ncbi.nlm.nih.gov/23570755/ [DOI: 10.1016/j.pt.2013.03.003].

Cowman, A. F.; Berry, Drew; Baum, Jake (2012). The cellular and molecular basis for malaria parasite invasion of the human red blood cell. *J Cell Biol* 198, 961–971 [DOI: 10.1083/jcb.201206112].

Cowman, A. F.; Healer, Julie; Marapana, Danushka; Marsh, Kevin (2016). Malaria: Biology and Disease. *Cell* 167, 610–624 [DOI: 10.1016/j.cell.2016.07.055].

Cowman, A. F.; Tonkin, Christopher J.; Tham, Wai-Hong; Duraisingh, Manoj T. (2017). The Molecular Basis of Erythrocyte Invasion by Malaria Parasites. *Cell Host Microbe* 22, 232–245 [DOI: 10.1016/j.chom.2017.07.003].

Cox, F. E. (2010). History of the discovery of the malaria parasites and their vectors. *Parasit Vectors* 3, 5 [DOI: 10.1186/1756-3305-3-5].

Crosnier, C.; Bustamante, Leyla Y.; Bartholdson, S. Josefin; Bei, Amy K.; Theron, Michel; Uchikawa, Makoto *et al.* (2011). Basigin is a receptor essential for erythrocyte invasion by Plasmodium falciparum. *Nature* 480, 534–537 [DOI: 10.1038/nature10606].

Croucher, D. R.; Iconomou, Mary; Hastings, Jordan F.; Kennedy, Sean P.; Han, Jeremy Z. R.; Shearer, Robert F. *et al.* (2016). Bimolecular complementation affinity purification (BiCAP) reveals dimer-specific protein interactions for ERBB2 dimers. *Sci Signal* 9, ra69 [DOI: 10.1126/scisignal.aaf0793].

Dale, N. C.; Johnstone, Elizabeth K. M.; White, Carl W.; Pfleger, Kevin D. G. (2019). NanoBRET: The Bright Future of Proximity-Based Assays. *Front Bioeng Biotechnol* 7, 56 [DOI: 10.3389/fbioe.2019.00056].

Daneshvar, C.; Davis, Timothy M. E.; Cox-Singh, Janet; Rafa'ee, Mohammad Zakri; Zakaria, Siti Khatijah; Divis, Paul C. S. *et al.* (2009). Clinical and laboratory features of human Plasmodium knowlesi infection. *Clin Infect Dis* 49, 852–860 [DOI: 10.1086/605439].

Das, S.; Hertrich, Nadine; Perrin, Abigail J.; Withers-Martinez, Chrislaine; Collins, Christine R.; Jones, Matthew L. *et al.* (2015). Processing of Plasmodium falciparum Merozoite Surface Protein MSP1 Activates a Spectrin-Binding Function Enabling Parasite Egress from RBCs. *Cell Host Microbe* 18, 433–444 [DOI: 10.1016/j.chom.2015.09.007].

De Niz, M. de; Stanway, Rebecca R.; Wacker, Rahel; Keller, Derya; Heussler, Volker T. (2016). An ultrasensitive NanoLuc-based luminescence system for monitoring Plasmodium berghei throughout its life cycle. *Malar J* 15, 232 [DOI: 10.1186/s12936-016-1291-9].

Deiana, A.; Forcelloni, Sergio; Porrello, Alessandro; Giansanti, Andrea (2019). Intrinsically disordered proteins and structured proteins with intrinsically disordered regions have different functional roles in the cell. *PLoS ONE* 14, e0217889 [DOI: 10.1371/journal.pone.0217889].

Deponte, M.; Hoppe, Heinrich C.; Lee, Marcus C. S.; Maier, Alexander G.; Richard, Dave; Rug, Melanie *et al.* (2012). Wherever I may roam: protein and membrane trafficking in P. falciparum-infected red blood cells. *Mol Biochem Parasitol* 186, 95–116. https://pubmed.ncbi.nlm.nih.gov/23043991/ [DOI: 10.1016/j.molbiopara.2012.09.007].

Doerig, C.; Rayner, Julian C.; Scherf, Artur; Tobin, Andrew B. (2015). Post-translational protein modifications in malaria parasites. *Nat Rev Microbiol* 13, 160–172 [DOI: 10.1038/nrmicro3402].

Donald, R. G. K.; Zhong, Tanya; Wiersma, Helen; Nare, Bakela; Yao, Dan; Lee, Anita *et al.* (2006). Anticoccidial kinase inhibitors: identification of protein kinase targets secondary to cGMP-dependent protein kinase. *Mol Biochem Parasitol* 149, 86–98 [DOI: 10.1016/j.molbiopara.2006.05.003].

Draper, S. J.; Sack, Brandon K.; King, C. Richter; Nielsen, Carolyn M.; Rayner, Julian C.; Higgins, Matthew K. *et al.* (2018). Malaria Vaccines: Recent Advances and New Horizons. *Cell Host Microbe* 24, 43–56 [DOI: 10.1016/j.chom.2018.06.008].

Drazic, A.; Myklebust, Line M.; Ree, Rasmus; Arnesen, Thomas (2016). The world of protein acetylation. *Biochim Biophys Acta* 1864, 1372–1401 [DOI: 10.1016/j.bbapap.2016.06.007].

Dvorak, J. A.; Miller, L. H.; Whitehouse, W. C.; Shiroishi, T. (1975). Invasion of erythrocytes by malaria merozoites. *Science* 187, 748–750 [DOI: 10.1126/science.803712].

Dwane, S.; Kiely, Patrick A. (2011). Tools used to study how protein complexes are assembled in signaling cascades. *Bioeng Bugs* 2, 247–259 [DOI: 10.4161/bbug.2.5.17844].

El Khamlichi, C.; Reverchon-Assadi, Flora; Hervouet-Coste, Nadège; Blot, Lauren; Reiter, Eric; Morisset-Lopez, Séverine (2019). Bioluminescence Resonance Energy Transfer as a Method to Study Protein-Protein Interactions: Application to G Protein Coupled Receptor Biology. *Molecules* **24** [DOI: 10.3390/molecules24030537].

Enayati, A.; Hemingway, J. (2010). Malaria management: past, present, and future. *Annu Rev Entomol* **55**, 569–591 [DOI: 10.1146/annurev-ento-112408-085423].

England, C. G.; Ehlerding, Emily B.; Cai, Weibo (2016). NanoLuc: A Small Luciferase Is Brightening Up the Field of Bioluminescence. *Bioconjug Chem* **27**, 1175–1187 [DOI: 10.1021/acs.bioconjchem.6b00112].

Fairhurst, R. M.; Nayyar, Gaurvika M. L.; Breman, Joel G.; Hallett, Rachel; Vennerstrom, Jonathan L.; Duong, Socheat *et al.* (2012). Artemisinin-resistant malaria: research challenges, opportunities, and public health implications. *The American Journal of Tropical Medicine and Hygiene* **87**, 231–241 [DOI: 10.4269/ajtmh.2012.12-0025].

Filarsky, M.; Fraschka, Sabine A.; Niederwieser, Igor; Brancucci, Nicolas M. B.; Carrington, Eilidh; Carrió, Elvira *et al.* (2018). GDV1 induces sexual commitment of malaria parasites by antagonizing HP1-dependent gene silencing. *Science* **359**, 1259–1263 [DOI: 10.1126/science.aan6042].

Fillinger, U.; Lindsay, Steven W. (2011). Larval source management for malaria control in Africa: myths and reality. *Malar J* **10**, 353 [DOI: 10.1186/1475-2875-10-353].

Frénal, K.; Tay, Chwen L.; Mueller, Christina; Bushell, Ellen S.; Jia, Yonggen; Graindorge, Arnault *et al.* (2013). Global analysis of apicomplexan protein S-acyl transferases reveals an enzyme essential for invasion. *Traffic* **14**, 895–911 [DOI: 10.1111/tra.12081].

Frevert, U.; Sinnis, P.; Cerami, C.; Shreffler, W.; Takacs, B.; Nussenzweig, V. (1993). Malaria circumsporozoite protein binds to heparan sulfate proteoglycans associated with the surface membrane of hepatocytes. *J Exp Med* **177**, 1287–1298 [DOI: 10.1084/jem.177.5.1287].

Frimpong, A.; Kusi, Kwadwo Asamoah; Ofori, Michael Fokuo; Ndifon, Wilfred (2018). Novel Strategies for Malaria Vaccine Design. *Front Immunol* **9**, 2769 [DOI: 10.3389/fimmu.2018.02769].

Galbraith, C. G.; Galbraith, James A. (2011). Super-resolution microscopy at a glance. *J Cell Sci* **124**, 1607–1611 [DOI: 10.1242/jcs.080085].

Gao, X.; Gunalan, Karthigayan; Yap, Sally Shu Lin; Preiser, Peter R. (2013). Triggers of key calcium signals during erythrocyte invasion by Plasmodium falciparum. *Nat Commun* **4**, 2862 [DOI: 10.1038/ncomms3862].

Garcia, C. R.; Markus, R. P.; Madeira, L. (2001). Tertian and quartan fevers: temporal regulation in malarial infection. *J Biol Rhythms* **16**, 436–443 [DOI: 10.1177/074873001129002114].

Garcia, G. E.; Wirtz, R. A.; Barr, J. R.; Woolfitt, A.; Rosenberg, R. (1998). Xanthurenic acid induces gametogenesis in Plasmodium, the malaria parasite. *J Biol Chem* **273**, 12003–12005 [DOI: 10.1074/jbc.273.20.12003].

Garg, S.; Agarwal, Shalini; Dabral, Surbhi; Kumar, Naveen; Sehrawat, Seema; Singh, Shailja (2015). Visualization and quantification of Plasmodium falciparum intraerythrocytic merozoites. *Syst Synth Biol* **9**, 23–26 [DOI: 10.1007/s11693-015-9167-9].

Garten, M.; Nasamu, Armiyaw S.; Niles, Jacquin C.; Zimmerberg, Joshua; Goldberg, Daniel E.; Beck, Josh R. (2018). EXP2 is a nutrient-permeable channel in the vacuolar membrane of Plasmodium and is essential for protein export via PTEX. *Nat Microbiol* **3**, 1090–1098 [DOI: 10.1038/s41564-018-0222-7].

Gasteiger, E.; Hoogland, Christine; Gattiker, Alexandre; Duvaud, S'everine; Wilkins, Marc R.; Appel, Ron D. *et al.* (2005). Protein Identification and Analysis Tools on the ExPASy Server. In The Proteomics Protocols Handbook (Walker, J. M., ed), pp. 571–607, Humana Press Inc, Totowa, NJ. [https://link.springer.com/protocol/10.1385/1-59259-890-0:571]

Geda, P.; Patury, Srikanth; Ma, Jun; Bharucha, Nike; Dobry, Craig J.; Lawson, Sarah K. *et al.* (2008). A small molecule-directed approach to control protein localization and function. *Yeast* **25**, 577–594 [DOI: 10.1002/yea.1610].

Geiger, M.; Brown, Chris; Wichers, Jan Stephan; Strauss, Jan; Lill, Andrés; Thuenauer, Roland *et al.* (2020). Structural Insights Into PfARO and Characterization of its Interaction With PfAIP. *J Mol Biol* **432**, 878–896 [DOI: 10.1016/j.jmb.2019.12.024].

Gelly, J.-C.; Joseph, Agnel Praveen; Srinivasan, Narayanaswamy; Brevern, Alexandre G. de (2011). iPBA: a tool for protein structure comparison using sequence alignment strategies. *Nucleic Acids Res* 39, W18-23 [DOI: 10.1093/nar/gkr333].

Gerald, N.; Mahajan, Babita; Kumar, Sanjai (2011). Mitosis in the human malaria parasite Plasmodium falciparum. *Eukaryotic Cell* 10, 474–482 [DOI: 10.1128/EC.00314-10].

Gero, A. M.; Wood, A. M. (1991). New nucleoside transport pathways induced in the host erythrocyte membrane of malaria and Babesia infected cells. *Adv Exp Med Biol* 309A, 169–172 [DOI: 10.1007/978-1-4899-2638-8_38].

Ghorbal, M.; Gorman, Molly; Macpherson, Cameron Ross; Martins, Rafael Miyazawa; Scherf, Artur; Lopez-Rubio, Jose-Juan (2014). Genome editing in the human malaria parasite Plasmodium falciparum using the CRISPR-Cas9 system. *Nat Biotechnol* 32, 819–821 [DOI: 10.1038/nbt.2925].

Gilson, P. R.; Crabb, Brendan S. (2009). Morphology and kinetics of the three distinct phases of red blood cell invasion by Plasmodium falciparum merozoites. *Int J Parasitol* 39, 91–96. http://www.sciencedirect.com/science/article/pii/S0020751908003780 [DOI: 10.1016/j.ijpara.2008.09.007].

Goel, V. K.; Li, Xuerong; Chen, Huiqing; Liu, Shih-Chun; Chishti, Athar H.; Oh, Steven S. (2003). Band 3 is a host receptor binding merozoite surface protein 1 during the Plasmodium falciparum invasion of erythrocytes. *Proc Natl Acad Sci U S A* 100, 5164–5169 [DOI: 10.1073/pnas.0834959100].

Goldberg, D. E. (2005). Hemoglobin degradation. *Curr Top Microbiol Immunol* 295, 275–291 [DOI: 10.1007/3-540-29088-5_11].

Graumans, W.; Jacobs, Ella; Bousema, Teun; Sinnis, Photini (2020). When Is a Plasmodium-Infected Mosquito an Infectious Mosquito? *Trends Parasitol* 36, 705–716 [DOI: 10.1016/j.pt.2020.05.011].

Gray, E. M.; BRADLEY, TIMOTHY J. (2005). PHYSIOLOGY OF DESICCATION RESISTANCE IN ANOPHELES GAMBIAE AND ANOPHELES ARABIENSIS. The American Journal of Tropical Medicine and Hygiene, 73(3), 553-559. *The American Journal of Tropical Medicine and Hygiene* 73, 553–559 [DOI: 10.4269/AJTMH.2005.73.553].

Greenbaum, D. C.; Baruch, Amos; Grainger, Munira; Bozdech, Zbynek; Medzihradszky, Katlin F.; Engel, Juan *et al.* (2002). A role for the protease falcipain 1 in host cell invasion by the human malaria parasite. *Science* 298, 2002–2006 [DOI: 10.1126/science.1077426].

Greenwood, B. M.; Fidock, David A.; Kyle, Dennis E.; Kappe, Stefan H. I.; Alonso, Pedro L.; Collins, Frank H. *et al.* (2008). Malaria: progress, perils, and prospects for eradication. *J Clin Invest* 118, 1266–1276 [DOI: 10.1172/JCI33996].

Grüring, C.; Heiber, Arlett; Kruse, Florian; Ungefehr, Johanna; Gilberger, Tim-Wolf; Spielmann, Tobias (2011). Development and host cell modifications of Plasmodium falciparum blood stages in four dimensions. *Nat Commun* 2, 165 [DOI: 10.1038/ncomms1169].

Gu, W.; Müller, Günter; Schlein, Yosef; Novak, Robert J.; Beier, John C. (2011). Natural plant sugar sources of Anopheles mosquitoes strongly impact malaria transmission potential. *PLoS ONE* 6, e15996 [DOI: 10.1371/journal.pone.0015996].

Guerra, C. A.; Gikandi, Priscilla W.; Tatem, Andrew J.; Noor, Abdisalan M.; Smith, Dave L.; Hay, Simon I. *et al.* (2008). The limits and intensity of Plasmodium falciparum transmission: implications for malaria control and elimination worldwide. *PLoS Med* 5, e38 [DOI: 10.1371/journal.pmed.0050038].

Gupta, A.; Balabaskaran-Nina, Praveen; Nguitragool, Wang; Saggu, Gagandeep S.; Schureck, Marc A.; Desai, Sanjay A. (2018). CLAG3 Self-Associates in Malaria Parasites and Quantitatively Determines Nutrient Uptake Channels at the Host Membrane. *mBio* 9 [DOI: 10.1128/mBio.02293-17].

Gurnett, A. M.; Liberator, Paul A.; Dulski, Paula M.; Salowe, Scott P.; Donald, Robert G. K.; Anderson, Jennifer W. *et al.* (2002). Purification and molecular characterization of cGMP-dependent protein kinase from Apicomplexan parasites. A novel chemotherapeutic target. *J Biol Chem* 277, 15913–15922 [DOI: 10.1074/jbc.M108393200].

Guttery, D. S.; Roques, Magali; Holder, Anthony A.; Tewari, Rita (2015). Commit and Transmit: Molecular Players in Plasmodium Sexual Development and Zygote Differentiation. *Trends Parasitol* 31, 676–685 [DOI: 10.1016/j.pt.2015.08.002].

Haase, S.; Cabrera, Ana; Langer, Christine; Treeck, Moritz; Struck, Nicole; Herrmann, Susann *et al.* (2008). Characterization of a conserved rhoptry-associated leucine zipper-like protein in the malaria parasite Plasmodium falciparum. *Infect Immun* **76**, 879–887 [DOI: 10.1128/IAI.00144-07].

Hall, M. P.; Unch, James; Binkowski, Brock F.; Valley, Michael P.; Butler, Braeden L.; Wood, Monika G. *et al.* (2012). Engineered luciferase reporter from a deep sea shrimp utilizing a novel imidazopyrazinone substrate. *ACS Chem Biol* **7**, 1848–1857 [DOI: 10.1021/cb3002478].

Hammond, A.; Galizi, Roberto; Kyrou, Kyros; Simoni, Alekos; Siniscalchi, Carla; Katsanos, Dimitris *et al.* (2016). A CRISPR-Cas9 gene drive system targeting female reproduction in the malaria mosquito vector Anopheles gambiae. *Nat Biotechnol* **34**, 78–83 [DOI: 10.1038/nbt.3439].

Han, Y.; Branon, Tess Caroline; Martell, Jeffrey D.; Boassa, Daniela; Shechner, David; Ellisman, Mark H. *et al.* (2019). Directed Evolution of Split APEX2 Peroxidase. *ACS Chem Biol* **14**, 619–635 [DOI: 10.1021/acschembio.8b00919].

Hanahan, D. (1983). Studies on transformation of Escherichia coli with plasmids. *J Mol Biol* **166**, 557–580. https://pubmed.ncbi.nlm.nih.gov/6345791/ [DOI: 10.1016/s0022-2836(83)80284-8].

Hans, N.; Singh, Shailja; Pandey, Alok K.; Reddy, K. Sony; Gaur, Deepak; Chauhan, Virander S. (2013). Identification and characterization of a novel Plasmodium falciparum adhesin involved in erythrocyte invasion. *PLoS ONE* **8**, e74790 [DOI: 10.1371/journal.pone.0074790].

Hanssen, E.; Dekiwadia, Chaitali; Riglar, David T.; Rug, Melanie; Lemgruber, Leandro; Cowman, Alan F. *et al.* (2013). Electron tomography of Plasmodium falciparum merozoites reveals core cellular events that underpin erythrocyte invasion. *Cell Microbiol* **15**, 1457–1472 [DOI: 10.1111/cmi.12132].

Haruki, H.; Nishikawa, Junichi; Laemmli, Ulrich K. (2008). The anchor-away technique: rapid, conditional establishment of yeast mutant phenotypes. *Mol Cell* **31**, 925–932 [DOI: 10.1016/j.molcel.2008.07.020].

Hay, S. I.; Sinka, Marianne E.; Okara, Robi M.; Kabaria, Caroline W.; Mbithi, Philip M.; Tago, Carolynn C. *et al.* (2010). Developing global maps of the dominant anopheles vectors of human malaria. *PLoS Med* **7**, e1000209 [DOI: 10.1371/journal.pmed.1000209].

Healer, J.; Crawford, Simon; Ralph, Stuart; McFadden, Geoff; Cowman, Alan F. (2002). Independent translocation of two micronemal proteins in developing Plasmodium falciparum merozoites. *Infect Immun* **70**, 5751–5758 [DOI: 10.1128/iai.70.10.5751-5758.2002].

Heintzmann, R.; Ficz, Gabriella (2013). Breaking the resolution limit in light microscopy. *Methods Cell Biol* **114**, 525–544 [DOI: 10.1016/B978-0-12-407761-4.00022-1].

Hemingway, J.; Shretta, Rima; Wells, Timothy N. C.; Bell, David; Djimdé, Abdoulaye A.; Achee, Nicole *et al.* (2016). Tools and Strategies for Malaria Control and Elimination: What Do We Need to Achieve a Grand Convergence in Malaria? *PLoS Biol* **14**, e1002380 [DOI: 10.1371/journal.pbio.1002380].

Hempelmann, E.; Krafts, Kristine (2013). Bad air, amulets and mosquitoes: 2,000 years of changing perspectives on malaria. *Malar J* **12**, 232 [DOI: 10.1186/1475-2875-12-232].

Henry, N. B.; Sermé, Samuel Sindié; Siciliano, Giulia; Sombié, Salif; Diarra, Amidou; Sagnon, N'fale *et al.* (2019). Biology of Plasmodium falciparum gametocyte sex ratio and implications in malaria parasite transmission. *Malar J* **18**, 70 [DOI: 10.1186/s12936-019-2707-0].

Ho, S. N.; Hunt, Henry D.; Horton, Robert M.; Pullen, Jeffrey K.; Pease, Larry R. (1989). Site-directed mutagenesis by overlap extension using the polymerase chain reaction. *Gene* **77**, 51–59 [DOI: 10.1016/0378-1119(89)90358-2].

Hoffman, S. L.; Campbell, Carlos C.; White, Nicholas J. (2011). Malaria. In Tropical Infectious Diseases: Principles, Pathogens and Practice, pp. 646–675, Elsevier. [https://www.sciencedirect.com/book/9780702039355/tropical-infectious-diseases]

Holder, A. A. (1994). Proteins on the surface of the malaria parasite and cell invasion. *Parasitology* **108 Suppl**, S5-18 [DOI: 10.1017/s0031182000075673].

Holman, L.; Head, Megan L.; Lanfear, Robert; Jennions, Michael D. (2015). Evidence of Experimental Bias in the Life Sciences: Why We Need Blind Data Recording. *PLoS Biol* **13**, e1002190 [DOI: 10.1371/journal.pbio.1002190].

Howes, R. E.; Patil, Anand P.; Piel, Frédéric B.; Nyangiri, Oscar A.; Kabaria, Caroline W.; Gething, Peter W. *et al.* (2011). The global distribution of the Duffy blood group. *Nat Commun* **2**, 266 [DOI: 10.1038/ncomms1265].

Hu, G.; Cabrera, Ana; Kono, Maya; Mok, Sachel; Chaal, Balbir K.; Haase, Silvia *et al.* (2010). Transcriptional profiling of growth perturbations of the human malaria parasite Plasmodium falciparum. *Nat Biotechnol* **28**, 91–98 [DOI: 10.1038/nbt.1597].

Hu, C.-D.; Chinenov, Yurii; Kerppola, Tom K. (2002). Visualization of Interactions among bZIP and Rel Family Proteins in Living Cells Using Bimolecular Fluorescence Complementation. *Mol Cell* **9**, 789–798 [DOI: 10.1016/S1097-2765(02)00496-3].

Hung, V.; Zou, Peng; Rhee, Hyun-Woo; Udeshi, Namrata D.; Cracan, Valentin; Svinkina, Tanya *et al.* (2014). Proteomic mapping of the human mitochondrial intermembrane space in live cells via ratiometric APEX tagging. *Mol Cell* **55**, 332–341 [DOI: 10.1016/j.molcel.2014.06.003].

Ishino, T.; Yano, Kazuhiko; Chinzei, Yasuo; Yuda, Masao (2004). Cell-passage activity is required for the malarial parasite to cross the liver sinusoidal cell layer. *PLoS Biol* **2**, E4 [DOI: 10.1371/journal.pbio.0020004].

Istvan, E. S.; Das, Sudipta; Bhatnagar, Suyash; Beck, Josh R.; Owen, Edward; Llinas, Manuel *et al.* (2019). Plasmodium Niemann-Pick type C1-related protein is a druggable target required for parasite membrane homeostasis. *eLife* **8** [DOI: 10.7554/eLife.40529].

Ito, D.; Hasegawa, Tomoyuki; Miura, Kazutoyo; Yamasaki, Tsutomu; Arumugam, Thangavelu U.; Thongkukiatkul, Amporn *et al.* (2013). RALP1 is a rhoptry neck erythrocyte-binding protein of Plasmodium falciparum merozoites and a potential blood-stage vaccine candidate antigen. *Infect Immun* **81**, 4290–4298 [DOI: 10.1128/IAI.00690-13].

Janouškovec, J.; Tikhonenkov, Denis V.; Burki, Fabien; Howe, Alexis T.; Kolísko, Martin; Mylnikov, Alexander P. *et al.* (2015). Factors mediating plastid dependency and the origins of parasitism in apicomplexans and their close relatives. *Proc Natl Acad Sci U S A* **112**, 10200–10207 [DOI: 10.1073/pnas.1423790112].

Jones, M. L.; Das, Sujaan; Belda, Hugo; Collins, Christine R.; Blackman, Michael J.; Treeck, Moritz (2016). A versatile strategy for rapid conditional genome engineering using loxP sites in a small synthetic intron in Plasmodium falciparum. *Sci Rep* **6**, 21800 [DOI: 10.1038/srep21800].

Josling, G. A.; Llinás, Manuel (2015). Sexual development in Plasmodium parasites: knowing when it's time to commit. *Nat Rev Microbiol* **13**, 573–587 [DOI: 10.1038/nrmicro3519].

Josling, G. A.; Williamson, Kim C.; Llinás, Manuel (2018). Regulation of Sexual Commitment and Gametocytogenesis in Malaria Parasites. *Annu Rev Microbiol* **72**, 501–519 [DOI: 10.1146/annurev-micro-090817-062712].

Kaderi Kibria, K. M.; Rawat, Khushboo; Klinger, Christen M.; Datta, Gaurav; Panchal, Manoj; Singh, Shailja *et al.* (2015). A role for adaptor protein complex 1 in protein targeting to rhoptry organelles in Plasmodium falciparum. *Biochim Biophys Acta* **1853**, 699–710. https://pubmed.ncbi.nlm.nih.gov/25573429/ [DOI: 10.1016/j.bbamcr.2014.12.030].

Kafsack, B. F. C.; Rovira-Graells, Núria; Clark, Taane G.; Bancells, Cristina; Crowley, Valerie M.; Campino, Susana G. *et al.* (2014). A transcriptional switch underlies commitment to sexual development in malaria parasites. *Nature* **507**, 248–252 [DOI: 10.1038/nature12920].

Kalderon, D.; Roberts, Bruce L.; Richardson, William D.; Smith, Alan E. (1984). A short amino acid sequence able to specify nuclear location. *Cell* **39**, 499–509 [DOI: 10.1016/0092-8674(84)90457-4].

Kalocsay, M. (2019). APEX Peroxidase-Catalyzed Proximity Labeling and Multiplexed Quantitative Proteomics. *Methods Mol Biol* **2008**, 41–55 [DOI: 10.1007/978-1-4939-9537-0_4].

Kappe, S. H. I.; Buscaglia, Carlos A.; Nussenzweig, Victor (2004). Plasmodium sporozoite molecular cell biology. *Annu Rev Cell Dev Biol* **20**, 29–59 [DOI: 10.1146/annurev.cellbio.20.011603.150935].

Kats, L. M.; Black, Casilda G.; Proellocks, Nicholas I.; Coppel, Ross L. (2006). Plasmodium rhoptries: how things went pear-shaped. *Trends Parasitol* **22**, 269–276. https://pubmed.ncbi.nlm.nih.gov/16635585/ [DOI: 10.1016/j.pt.2006.04.001].

Kats, L. M.; Cooke, Brian M.; Coppel, Ross L.; Black, Casilda G. (2008). Protein trafficking to apical organelles of malaria parasites - building an invasion machine. *Traffic* **9**, 176–186. https://pubmed.ncbi.nlm.nih.gov/18047549/ [DOI: 10.1111/j.1600-0854.2007.00681.x].

Kelley, L. A.; Mezulis, Stefans; Yates, Christopher M.; Wass, Mark N.; Sternberg, Michael J. E. (2015). The Phyre2 web portal for protein modeling, prediction and analysis. *Nat Protoc* 10, 845–858 [DOI: 10.1038/nprot.2015.053].

Keskin, O.; Nussinov, Ruth (2005). Favorable scaffolds: proteins with different sequence, structure and function may associate in similar ways. *Protein Eng Des Sel* 18, 11–24 [DOI: 10.1093/protein/gzh095].

Kim, T.-W.; Park, Chan Ho; Hsu, Chuan-Chih; Zhu, Jia-Ying; Hsiao, Yuchun; Branon, Tess *et al.* (2019). Application of TurboID-mediated proximity labeling for mapping a GSK3 kinase signaling network in Arabidopsis. [https://www.biorxiv.org/content/10.1101/636324v1]

Kinjo, A. R.; Nishikawa, Ken (2004). Eigenvalue analysis of amino acid substitution matrices reveals a sharp transition of the mode of sequence conservation in proteins. *Bioinformatics* 20, 2504–2508 [DOI: 10.1093/bioinformatics/bth297].

Knuepfer, E.; Napiorkowska, Marta; van Ooij, Christiaan; Holder, Anthony A. (2017). Generating conditional gene knockouts in Plasmodium - a toolkit to produce stable DiCre recombinase-expressing parasite lines using CRISPR/Cas9. *Sci Rep* 7, 3881 [DOI: 10.1038/s41598-017-03984-3].

Kobayashi, K.; Kato, Kentaro (2016). Evaluating the use of heparin for synchronization of in vitro culture of Plasmodium falciparum. *Parasitol Int* 65, 549–551 [DOI: 10.1016/j.parint.2016.09.002].

Koch, M.; Baum, Jake (2016). The mechanics of malaria parasite invasion of the human erythrocyte - towards a reassessment of the host cell contribution. *Cell Microbiol* 18, 319–329 [DOI: 10.1111/cmi.12557].

Kodama, Y.; Hu, Chang-Deng (2012). Bimolecular fluorescence complementation (BiFC): a 5-year update and future perspectives. *BioTechniques* 53, 285–298 [DOI: 10.2144/000113943].

Koldsø, H.; Reddy, Tyler; Fowler, Philip W.; Duncan, Anna L.; Sansom, Mark S. P. (2016). Membrane Compartmentalization Reducing the Mobility of Lipids and Proteins within a Model Plasma Membrane. *The journal of physical chemistry. B* 120, 8873–8881 [DOI: 10.1021/acs.jpcb.6b05846].

Kono, M.; Heincke, Dorothee; Wilcke, Louisa; Wong, Tatianna Wai Ying; Bruns, Caroline; Herrmann, Susann *et al.* (2016). Pellicle formation in the malaria parasite. *J Cell Sci* 129, 673–680 [DOI: 10.1242/jcs.181230].

Kono, M.; Prusty, Dhaneswar; Parkinson, John; Gilberger, Tim W. (2013). The apicomplexan inner membrane complex. *Front Biosci (Landmark Ed)* 18, 982–992 [DOI: 10.2741/4157].

Kori, L. D.; Valecha, Neena; Anvikar, Anupkumar R. (2018). Insights into the early liver stage biology of Plasmodium. *J Vector Borne Dis* 55, 9–13 [DOI: 10.4103/0972-9062.234631].

Kremer, K.; Kamin, Dirk; Rittweger, Eva; Wilkes, Jonathan; Flammer, Halley; Mahler, Sabine *et al.* (2013). An overexpression screen of Toxoplasma gondii Rab-GTPases reveals distinct transport routes to the micronemes. *PLoS Pathog* 9, e1003213 [DOI: 10.1371/journal.ppat.1003213].

Krissinel, E. (2007). On the relationship between sequence and structure similarities in proteomics. *Bioinformatics* 23, 717–723 [DOI: 10.1093/bioinformatics/btm006].

Kublin, J. G.; Mikolajczak, Sebastian A.; Sack, Brandon K.; Fishbaugher, Matt E.; Seilie, Annette; Shelton, Lisa *et al.* (2017). Complete attenuation of genetically engineered Plasmodium falciparum sporozoites in human subjects. *Sci Transl Med* 9 [DOI: 10.1126/scitranslmed.aad9099].

Külzer, S.; Petersen, Wiebke; Baser, Avni; Mandel, Katharina; Przyborski, Jude M. (2013). Use of self-assembling GFP to determine protein topology and compartmentalisation in the Plasmodium falciparum-infected erythrocyte. *Mol Biochem Parasitol* 187, 87–90 [DOI: 10.1016/j.molbiopara.2012.11.004].

Kumar, R.; Adams, Brian; Musiyenko, Alla; Shulyayeva, Olena; Barik, Sailen (2005). The FK506-binding protein of the malaria parasite, Plasmodium falciparum, is a FK506-sensitive chaperone with FK506-independent calcineurin-inhibitory activity. *Mol Biochem Parasitol* 141, 163–173 [DOI: 10.1016/j.molbiopara.2005.02.007].

Kwong, W. K.; Campo, Javier del; Mathur, Varsha; Vermeij, Mark J. A.; Keeling, Patrick J. (2018). A widespread coral-infecting apicomplexan contains a plastid encoding chlorophyll biosynthesis, bioRxiv. [https://www.biorxiv.org/content/10.1101/391565v1]

Kyrou, K.; Hammond, Andrew M.; Galizi, Roberto; Kranjc, Nace; Burt, Austin; Beaghton, Andrea K. *et al.* (2018). A CRISPR-Cas9 gene drive targeting doublesex causes complete population suppression in caged Anopheles gambiae mosquitoes. *Nat Biotechnol* 36, 1062–1066 [DOI: 10.1038/nbt.4245].

Lal, K.; Prieto, Judith Helena; Bromley, Elizabeth; Sanderson, Sanya J.; Yates, John R.; Wastling, Jonathan M. *et al.* (2009). Characterisation of Plasmodium invasive organelles; an ookinete microneme proteome. *Proteomics* **9**, 1142–1151 [DOI: 10.1002/pmic.200800404].

Lambros, C.; Vanderberg, J. P. (1979). Synchronization of Plasmodium falciparum erythrocytic stages in culture. *J Parasitol* **65**, 418–420. [DOI: 10.2307/3280287]

Laurens, M. B. (2018). The Promise of a Malaria Vaccine-Are We Closer? *Annu Rev Microbiol* **72**, 273–292 [DOI: 10.1146/annurev-micro-090817-062427].

Leach, A.; Vekemans, Johan; Lievens, Marc; Ofori-Anyinam, Opokua; Cahill, Conor; Owusu-Agyei, Seth *et al.* (2011). Design of a phase III multicenter trial to evaluate the efficacy of the RTS,S/AS01 malaria vaccine in children across diverse transmission settings in Africa. *Malar J* **10**, 224 [DOI: 10.1186/1475-2875-10-224].

Lear, S.; Cobb, Steven L. (2016). Pep-Calc.com: a set of web utilities for the calculation of peptide and peptoid properties and automatic mass spectral peak assignment. *J Comput Aided Mol Des* **30**, 271–277 [DOI: 10.1007/s10822-016-9902-7].

Lee, A. H.; Symington, Lorraine S.; Fidock, David A. (2014). DNA repair mechanisms and their biological roles in the malaria parasite Plasmodium falciparum. *Microbiol Mol Biol Rev* **78**, 469–486 [DOI: 10.1128/MMBR.00059-13].

Lehmann, C.; Tan, Michele Ser Ying; Vries, Laura E. de; Russo, Ilaria; Sanchez, Mateo I.; Goldberg, Daniel E. *et al.* (2018). Plasmodium falciparum dipeptidyl aminopeptidase 3 activity is important for efficient erythrocyte invasion by the malaria parasite. *PLoS Pathog* **14**, e1007031 [DOI: 10.1371/journal.ppat.1007031].

Lemgruber, L.; Lupetti, Pietro; Souza, Wanderley de; Vommaro, Rossiane C. (2011). New details on the fine structure of the rhoptry of Toxoplasma gondii. *Microsc Res Tech* **74**, 812–818 [DOI: 10.1002/jemt.20960].

Liffner, B.; Frölich, Sonja; Heinemann, Gary K.; Liu, Boyin; Ralph, Stuart A.; Dixon, Matthew W. A. *et al.* (2020). PfCERLI1 is a conserved rhoptry associated protein essential for Plasmodium falciparum merozoite invasion of erythrocytes. *Nat Commun* **11**, 1411 [DOI: 10.1038/s41467-020-15127-w].

Lin, C. S.; Uboldi, Alessandro D.; Epp, Christian; Bujard, Hermann; Tsuboi, Takafumi; Czabotar, Peter E. *et al.* (2016). Multiple Plasmodium falciparum Merozoite Surface Protein 1 Complexes Mediate Merozoite Binding to Human Erythrocytes. *J Biol Chem* **291**, 7703–7715 [DOI: 10.1074/jbc.M115.698282].

Llinás, M.; Bozdech, Zbynek; Wong, Edith D.; Adai, Alex T.; DeRisi, Joseph L. (2006). Comparative whole genome transcriptome analysis of three Plasmodium falciparum strains. *Nucleic Acids Res* **34**, 1166–1173 [DOI: 10.1093/nar/gkj517].

Lobingier, B. T.; Hüttenhain, Ruth; Eichel, Kelsie; Miller, Kenneth B.; Ting, Alice Y.; Zastrow, Mark von *et al.* (2017). An Approach to Spatiotemporally Resolve Protein Interaction Networks in Living Cells. *Cell* **169**, 350-360.e12 [DOI: 10.1016/j.cell.2017.03.022].

López-Barragán, M. J.; Lemieux, Jacob; Quiñones, Mariam; Williamson, Kim C.; Molina-Cruz, Alvaro; Cui, Kairong *et al.* (2011). Directional gene expression and antisense transcripts in sexual and asexual stages of Plasmodium falciparum. *BMC Genomics* **12**, 587 [DOI: 10.1186/1471-2164-12-587].

Machleidt, T.; Woodroofe, Carolyn C.; Schwinn, Marie K.; Méndez, Jacqui; Robers, Matthew B.; Zimmerman, Kris *et al.* (2015). NanoBRET--A Novel BRET Platform for the Analysis of Protein-Protein Interactions. *ACS Chem Biol* **10**, 1797–1804 [DOI: 10.1021/acschembio.5b00143].

Madeira, F.; Park, Young Mi; Lee, Joon; Buso, Nicola; Gur, Tamer; Madhusoodanan, Nandana *et al.* (2019). The EMBL-EBI search and sequence analysis tools APIs in 2019. *Nucleic Acids Res* **47**, W636-W641 [DOI: 10.1093/nar/gkz268].

Maier, A. G.; Cooke, Brian M.; Cowman, Alan F.; Tilley, Leann (2009). Malaria parasite proteins that remodel the host erythrocyte. *Nat Rev Microbiol* **7**, 341–354 [DOI: 10.1038/nrmicro2110].

Malleret, B.; Claser, Carla; Ong, Alice Soh Meoy; Suwanarusk, Rossarin; Sriprawat, Kanlaya; Howland, Shanshan Wu *et al.* (2011). A rapid and robust tri-color flow cytometry assay for monitoring malaria parasite development. *Sci Rep* **1**, 118 [DOI: 10.1038/srep00118].

Manoukis, N. C.; Diabate, Abdoulaye; Abdoulaye, Adamou; Diallo, Moussa; Dao, Adama; Yaro, Alpha S. *et al.* (2009). Structure and dynamics of male swarms of Anopheles gambiae. *J Med Entomol* **46**, 227–235 [DOI: 10.1603/033.046.0207].

Marchler-Bauer, A.; Bryant, Stephen H. (2004). CD-Search: protein domain annotations on the fly. *Nucleic Acids Res* 32, W327-31 [DOI: 10.1093/nar/gkh454].

Margineanu, A.; Chan, Jia Jia; Kelly, Douglas J.; Warren, Sean C.; Flatters, Delphine; Kumar, Sunil *et al.* (2016). Screening for protein-protein interactions using Förster resonance energy transfer (FRET) and fluorescence lifetime imaging microscopy (FLIM). *Sci Rep* 6, 28186 [DOI: 10.1038/srep28186].

Marin-Mogollon, C.; van de Vegte-Bolmer, Marga; van Gemert, Geert-Jan; van Pul, Fiona J. A.; Ramesar, Jai; Othman, Ahmad Syibli *et al.* (2018). The Plasmodium falciparum male gametocyte protein P230p, a paralog of P230, is vital for ookinete formation and mosquito transmission. *Sci Rep* 8, 14902 [DOI: 10.1038/s41598-018-33236-x].

Marin-Mogollon, C. M.; van Pul, Fiona J. A.; Imai, Takashi; Ramesar, Jai; Chevalley-Maurel, Séverine; Roo, Guido M. de *et al.* (2016). Rapid Generation of Marker-Free P. falciparum Fluorescent Reporter Lines Using Modified CRISPR/Cas9 Constructs and Selection Protocol. *PLoS ONE* 11, e0168362 [DOI: 10.1371/journal.pone.0168362].

Martell, J. D.; Deerinck, Thomas J.; Sancak, Yasemin; Poulos, Thomas L.; Mootha, Vamsi K.; Sosinsky, Gina E. *et al.* (2012). Engineered ascorbate peroxidase as a genetically encoded reporter for electron microscopy. *Nat Biotechnol* 30, 1143–1148 [DOI: 10.1038/nbt.2375].

Mata-Cantero, L.; Lafuente, Maria J.; Sanz, Laura; Rodriguez, Manuel S. (2014). Magnetic isolation of Plasmodium falciparum schizonts iRBCs to generate a high parasitaemia and synchronized in vitro culture. *Malar J* 13, 112 [DOI: 10.1186/1475-2875-13-112].

Matz, J. M.; Beck, Josh R.; Blackman, Michael J. (2020). The parasitophorous vacuole of the blood-stage malaria parasite. *Nat Rev Microbiol* 18, 379–391 [DOI: 10.1038/s41579-019-0321-3].

May, D. G.; Scott, Kelsey L.; Campos, Alexandre R.; Roux, Kyle J. (2020). Comparative Application of BioID and TurboID for Protein-Proximity Biotinylation. *Cells* 9 [DOI: 10.3390/cells9051070].

Mehnert, A.-K.; Simon, Caroline Sophie; Guizetti, Julien (2019). Immunofluorescence staining protocol for STED nanoscopy of Plasmodium-infected red blood cells. *Mol Biochem Parasitol* 229, 47–52 [DOI: 10.1016/j.molbiopara.2019.02.007].

Meis, J. F.; Verhave, J. P.; Jap, P. H.; Meuwissen, J. H. (1983). An ultrastructural study on the role of Kupffer cells in the process of infection by Plasmodium berghei sporozoites in rats. *Parasitology* 86 (Pt 2), 231–242 [DOI: 10.1017/s003118200005040x].

Ménard, D.; Barnadas, Céline; Bouchier, Christiane; Henry-Halldin, Cara; Gray, Laurie R.; Ratsimbasoa, Arsène *et al.* (2010). Plasmodium vivax clinical malaria is commonly observed in Duffy-negative Malagasy people. *Proc Natl Acad Sci U S A* 107, 5967–5971 [DOI: 10.1073/pnas.0912496107].

Ménard, D.; Khim, Nimol; Beghain, Johann; Adegnika, Ayola A.; Shafiul-Alam, Mohammad; Amodu, Olukemi *et al.* (2016). A Worldwide Map of Plasmodium falciparum K13-Propeller Polymorphisms. *N Engl J Med* 374, 2453–2464 [DOI: 10.1056/NEJMoa1513137].

Mesén-Ramírez, P.; Reinsch, Ferdinand; Blancke Soares, Alexandra; Bergmann, Bärbel; Ullrich, Ann-Katrin; Tenzer, Stefan *et al.* (2016). Stable Translocation Intermediates Jam Global Protein Export in Plasmodium falciparum Parasites and Link the PTEX Component EXP2 with Translocation Activity. *PLoS Pathog* 12, e1005618 [DOI: 10.1371/journal.ppat.1005618].

Mikolajczak, S. A.; Lakshmanan, Viswanathan; Fishbaugher, Matthew; Camargo, Nelly; Harupa, Anke; Kaushansky, Alexis *et al.* (2014). A next-generation genetically attenuated Plasmodium falciparum parasite created by triple gene deletion. *Mol Ther* 22, 1707–1715 [DOI: 10.1038/mt.2014.85].

Miller, L. H.; Ackerman, Hans C.; Su, Xin-zhuan; Wellems, Thomas E. (2013). Malaria biology and disease pathogenesis: insights for new treatments. *Nat Med* 19, 156–167 [DOI: 10.1038/nm.3073].

Miller, K. E.; Kim, Yeonsoo; Huh, Won-Ki; Park, Hay-Oak (2015). Bimolecular Fluorescence Complementation (BiFC) Analysis: Advances and Recent Applications for Genome-Wide Interaction Studies. *J Mol Biol* 427, 2039–2055 [DOI: 10.1016/j.jmb.2015.03.005].

Miller, L. H.; Mason, S. J.; Clyde, D. F.; McGinniss, M. H. (1976). The resistance factor to Plasmodium vivax in blacks. The Duffy-blood-group genotype, FyFy. *N Engl J Med* 295, 302–304 [DOI: 10.1056/NEJM197608052950602].

Milner, D. A. (2018). Malaria Pathogenesis. *Cold Spring Harb Perspect Med* 8 [DOI: 10.1101/cshperspect.a025569].

Mishra, N.; Bharti, Ram Suresh; Mallick, Prashant; Singh, Om Prakash; Srivastava, Bina; Rana, Roma *et al.* (2016). Emerging polymorphisms in falciparum Kelch 13 gene in Northeastern region of India. *Malar J* **15**, 583 [DOI: 10.1186/s12936-016-1636-4].

Mitra, P.; Gupta, Enna Dogra; Sahar, Tajali; Pandey, Alok K.; Dangi, Poonam; Reddy, K. Sony *et al.* (2016). Evidence for the Nucleo-Apical Shuttling of a Beta-Catenin Like Plasmodium falciparum Armadillo Repeat Containing Protein. *PLoS ONE* **11**, e0148446 [DOI: 10.1371/journal.pone.0148446].

Mitzmain, M. B. (1917). The Malaria Parasite in the Mosquito: The Effects of Low Temperature and Other Factors on Its Development. *Public Health Reports (1896-1970)* **32**, 1400 [DOI: 10.2307/4574614].

Moore, R. B.; Oborník, Miroslav; Janouskovec, Jan; Chrudimský, Tomás; Vancová, Marie; Green, David H. *et al.* (2008). A photosynthetic alveolate closely related to apicomplexan parasites. *Nature* **451**, 959–963 [DOI: 10.1038/nature06635].

Mordmüller, B.; Surat, Güzin; Lagler, Heimo; Chakravarty, Sumana; Ishizuka, Andrew S.; Lalremruata, Albert *et al.* (2017). Sterile protection against human malaria by chemoattenuated PfSPZ vaccine. *Nature* **542**, 445–449 [DOI: 10.1038/nature21060].

Moreno-Pérez, D. A.; Ruíz, Jhenniffer A.; Patarroyo, Manuel A. (2013). Reticulocytes: Plasmodium vivax target cells. *Biol Cell* **105**, 251–260 [DOI: 10.1111/boc.201200093].

Morlon-Guyot, J.; Pastore, Sandra; Berry, Laurence; Lebrun, Maryse; Daher, Wassim (2015). Toxoplasma gondii Vps11, a subunit of HOPS and CORVET tethering complexes, is essential for the biogenesis of secretory organelles. *Cell Microbiol* **17**, 1157–1178 [DOI: 10.1111/cmi.12426].

Mu, J.; Joy, Deirdre A.; Duan, Junhui; Huang, Yaming; Carlton, Jane; Walker, John *et al.* (2005). Host switch leads to emergence of Plasmodium vivax malaria in humans. *Mol Biol Evol* **22**, 1686–1693 [DOI: 10.1093/molbev/msi160].

Mueller, C.; Klages, Natacha; Jacot, Damien; Santos, Joana M.; Cabrera, Ana; Gilberger, Tim W. *et al.* (2013). The Toxoplasma protein ARO mediates the apical positioning of rhoptry organelles, a prerequisite for host cell invasion. *Cell Host Microbe* **13**, 289–301 [DOI: 10.1016/j.chom.2013.02.001].

Mueller, C.; Samoo, Atta; Hammoudi, Pierre-Mehdi; Klages, Natacha; Kallio, Juha Pekka; Kursula, Inari *et al.* (2016). Structural and functional dissection of Toxoplasma gondii armadillo repeats only protein. *J Cell Sci* **129**, 1031–1045 [DOI: 10.1242/jcs.177386].

Müller, G. C.; Beier, John C.; Traore, Sekou F.; Toure, Mahamadou B.; Traore, Mohamed M.; Bah, Sekou *et al.* (2010). Successful field trial of attractive toxic sugar bait (ATSB) plant-spraying methods against malaria vectors in the Anopheles gambiae complex in Mali, West Africa. *Malar J* **9**, 210 [DOI: 10.1186/1475-2875-9-210].

NCBI, R. C. (2018). Database resources of the National Center for Biotechnology Information. *Nucleic Acids Res* **46**, D8-D13 [DOI: 10.1093/nar/gkx1095].

Nebl, T.; Prieto, Judith Helena; Kapp, Eugene; Smith, Brian J.; Williams, Melanie J.; Yates, John R. *et al.* (2011). Quantitative in vivo analyses reveal calcium-dependent phosphorylation sites and identifies a novel component of the Toxoplasma invasion motor complex. *PLoS Pathog* **7**, e1002222 [DOI: 10.1371/journal.ppat.1002222].

Nishi, H.; Shaytan, Alexey; Panchenko, Anna R. (2014). Physicochemical mechanisms of protein regulation by phosphorylation. *Front Genet* **5**, 270 [DOI: 10.3389/fgene.2014.00270].

Noden, B. H.; Kent, M. D.; Beier, J. C. (1995). The impact of variations in temperature on early Plasmodium falciparum development in Anopheles stephensi. *Parasitology* **111 (Pt 5)**, 539–545 [DOI: 10.1017/s0031182000077003].

Nussenzweig, R. S.; Vanderberg, J.; Most, H.; Orton, C. (1967). Protective immunity produced by the injection of x-irradiated sporozoites of plasmodium berghei. *Nature* **216**, 160–162 [DOI: 10.1038/216160a0].

Oakley, M. S.; Gerald, Noel; McCutchan, Thomas F.; Aravind, L.; Kumar, Sanjai (2011). Clinical and molecular aspects of malaria fever. *Trends Parasitol* **27**, 442–449 [DOI: 10.1016/j.pt.2011.06.004].

Oborník, M.; Modrý, David; Lukeš, Martin; Cernotíková-Stříbrná, Eva; Cihlář, Jaromír; Tesařová, Martina *et al.* (2012). Morphology, ultrastructure and life cycle of Vitrella brassicaformis n. sp., n. gen., a novel chromerid from the Great Barrier Reef. *Protist* **163**, 306–323 [DOI: 10.1016/j.protis.2011.09.001].

Olotu, A.; Fegan, Gregory; Wambua, Juliana; Nyangweso, George; Leach, Amanda; Lievens, Marc *et al.* (2016). Seven-Year Efficacy of RTS,S/AS01 Malaria Vaccine among Young African Children. *N Engl J Med* 374, 2519–2529 [DOI: 10.1056/NEJMoa1515257].

O'Reilly, F. J.; Rappsilber, Juri (2018). Cross-linking mass spectrometry: methods and applications in structural, molecular and systems biology. *Nat Struct Mol Biol* 25, 1000–1008 [DOI: 10.1038/s41594-018-0147-0].

Paaijmans, K. P.; Cator, Lauren J.; Thomas, Matthew B. (2013). Temperature-dependent pre-bloodmeal period and temperature-driven asynchrony between parasite development and mosquito biting rate reduce malaria transmission intensity. *PLoS ONE* 8, e55777 [DOI: 10.1371/journal.pone.0055777].

Pagola, S.; Stephens, P. W.; Bohle, D. S.; Kosar, A. D.; Madsen, S. K. (2000). The structure of malaria pigment beta-haematin. *Nature* 404, 307–310 [DOI: 10.1038/35005132].

Papanikou, E.; Day, Kasey J.; Austin, Jotham; Glick, Benjamin S. (2015). COPI selectively drives maturation of the early Golgi. *eLife* 4 [DOI: 10.7554/eLife.13232].

Patel, A.; Perrin, Abigail J.; Flynn, Helen R.; Bisson, Claudine; Withers-Martinez, Chrislaine; Treeck, Moritz *et al.* (2019). Cyclic AMP signalling controls key components of malaria parasite host cell invasion machinery. *PLoS Biol* 17, e3000264 [DOI: 10.1371/journal.pbio.3000264].

Patury, S.; Geda, Prasanthi; Dobry, Craig J.; Kumar, Anuj; Gestwicki, Jason E. (2009). Conditional nuclear import and export of yeast proteins using a chemical inducer of dimerization. *Cell Biochem Biophys* 53, 127–134 [DOI: 10.1007/s12013-009-9044-9].

Pazicky, S.; Dhamotharan, Karthikeyan; Kaszuba, Karol; Mertens, Haydyn; Gilberger, Tim; Svergun, Dmitri *et al.* (2019). Structural role of essential light chains in the apicomplexan glideosome, bioRxiv. [https://www.biorxiv.org/content/10.1101/867499v1]

Perrin, A. J.; Collins, Christine R.; Russell, Matthew R. G.; Collinson, Lucy M.; Baker, David A.; Blackman, Michael J. (2018). The Actinomyosin Motor Drives Malaria Parasite Red Blood Cell Invasion but Not Egress. *mBio* 9 [DOI: 10.1128/mBio.00905-18].

Pfleger, K. D. G.; Eidne, Karin A. (2006). Illuminating insights into protein-protein interactions using bioluminescence resonance energy transfer (BRET). *Nat Methods* 3, 165–174 [DOI: 10.1038/nmeth841].

Phillips, M. A.; Burrows, Jeremy N.; Manyando, Christine; van Huijsduijnen, Rob Hooft; van Voorhis, Wesley C.; Wells, Timothy N. C. (2017). Malaria. *Nature reviews. Disease primers* 3, 17050 [DOI: 10.1038/nrdp.2017.50].

Piovesan, D.; Tabaro, Francesco; Paladin, Lisanna; Necci, Marco; Micetic, Ivan; Camilloni, Carlo *et al.* (2018). MobiDB 3.0: more annotations for intrinsic disorder, conformational diversity and interactions in proteins. *Nucleic Acids Res* 46, D471-D476 [DOI: 10.1093/nar/gkx1071].

Poostchi, M.; Silamut, Kamolrat; Maude, Richard J.; Jaeger, Stefan; Thoma, George (2018). Image analysis and machine learning for detecting malaria. *Transl Res* 194, 36–55 [DOI: 10.1016/j.trsl.2017.12.004].

Pradel, G.; Frevert, U. (2001). Malaria sporozoites actively enter and pass through rat Kupffer cells prior to hepatocyte invasion. *Hepatology* 33, 1154–1165 [DOI: 10.1053/jhep.2001.24237].

Prapanthadara, L.-a.; Hemingway, Janet; Ketterman, Albert J. (1995). DDT-resistance in Anopheles gambiae (Diptera: Culicidae) from Zanzibar, Tanzania, based on increased DDT-dehydrochlorinase activity of glutathione S-transferases. *Bull. Entomol. Res.* 85, 267–274 [DOI: 10.1017/S0007485300034350].

Premji, Z. G. (2009). Coartem: the journey to the clinic. *Malar J* 8 Suppl 1, S3 [DOI: 10.1186/1475-2875-8-S1-S3].

Prinz, B.; Harvey, Katherine L.; Wilcke, Louisa; Ruch, Ulrike; Engelberg, Klemens; Biller, Laura *et al.* (2016). Hierarchical phosphorylation of apical membrane antigen 1 is required for efficient red blood cell invasion by malaria parasites. *Sci Rep* 6, 34479 [DOI: 10.1038/srep34479].

Prommana, P.; Uthaipibull, Chairat; Wongsombat, Chayaphat; Kamchonwongpaisan, Sumalee; Yuthavong, Yongyuth; Knuepfer, Ellen *et al.* (2013). Inducible knockdown of Plasmodium gene expression using the glmS ribozyme. *PLoS ONE* 8, e73783 [DOI: 10.1371/journal.pone.0073783].

Prugnolle, F.; Durand, Patrick; Neel, Cécile; Ollomo, Benjamin; Ayala, Francisco J.; Arnathau, Céline *et al.* (2010). African great apes are natural hosts of multiple related malaria species, including Plasmodium falciparum. *Proc Natl Acad Sci U S A* 107, 1458–1463 [DOI: 10.1073/pnas.0914440107].

Putyrski, M.; Schultz, Carsten (2012). Protein translocation as a tool: The current rapamycin story. *FEBS Lett* 586, 2097–2105 [DOI: 10.1016/j.febslet.2012.04.061].

Ramadurai, S.; Holt, Andrea; Krasnikov, Victor; van den Bogaart, Geert; Killian, J. Antoinette; Poolman, Bert (2009). Lateral diffusion of membrane proteins. *J Am Chem Soc* 131, 12650–12656 [DOI: 10.1021/ja902853g].

Raman, S.; Vernon, Robert; Thompson, James; Tyka, Michael; Sadreyev, Ruslan; Pei, Jimin *et al.* (2009). Structure prediction for CASP8 with all-atom refinement using Rosetta. *Proteins* 77 Suppl 9, 89–99 [DOI: 10.1002/prot.22540].

Ramasamy, R. (2014). Zoonotic malaria - global overview and research and policy needs. *Front Public Health* 2, 123 [DOI: 10.3389/fpubh.2014.00123].

Ranford-Cartwright, L. C.; Sinha, Abhinav; Humphreys, Georgina S.; Mwangi, Jonathan M. (2010). New synchronization method for Plasmodium falciparum. *Malar J* 9, 170 [DOI: 10.1186/1475-2875-9-170].

Rhee, H.-W.; Zou, Peng; Udeshi, Namrata D.; Martell, Jeffrey D.; Mootha, Vamsi K.; Carr, Steven A. *et al.* (2013). Proteomic mapping of mitochondria in living cells via spatially restricted enzymatic tagging. *Science* 339, 1328–1331 [DOI: 10.1126/science.1230593].

Richie, T. L.; Billingsley, Peter F.; Sim, B. Kim Lee; James, Eric R.; Chakravarty, Sumana; Epstein, Judith E. *et al.* (2015). Progress with Plasmodium falciparum sporozoite (PfSPZ)-based malaria vaccines. *Vaccine* 33, 7452–7461 [DOI: 10.1016/j.vaccine.2015.09.096].

Riglar, D. T.; Richard, Dave; Wilson, Danny W.; Boyle, Michelle J.; Dekiwadia, Chaitali; Turnbull, Lynne *et al.* (2011). Super-resolution dissection of coordinated events during malaria parasite invasion of the human erythrocyte. *Cell Host Microbe* 9, 9–20 [DOI: 10.1016/j.chom.2010.12.003].

Robinson, M. S.; Sahlender, Daniela A.; Foster, Samuel D. (2010). Rapid inactivation of proteins by rapamycin-induced rerouting to mitochondria. *Dev Cell* 18, 324–331 [DOI: 10.1016/j.devcel.2009.12.015].

Rodrigues, C. D.; Hannus, Michael; Prudêncio, Miguel; Martin, Cécilie; Gonçalves, Lígia A.; Portugal, Sílvia *et al.* (2008). Host scavenger receptor SR-BI plays a dual role in the establishment of malaria parasite liver infection. *Cell Host Microbe* 4, 271–282 [DOI: 10.1016/j.chom.2008.07.012].

Roller, N. R.; Desser, S. S. (1973). The effect of temperature, age and density of gametocytes, and changes in gas composition on exflagellation of Leucocytozoon simondi. *Can J Zool* 51, 577–587 [DOI: 10.1139/z73-084].

Rossati, A.; Bargiacchi, Olivia; Kroumova, Vesselina; Zaramella, Marco; Caputo, Annamaria; Garavelli, Pietro Luigi (2016). Climate, environment and transmission of malaria. *Infez Med* 24, 93–104. [PMID: 27367318]

Rost, B. (1999). Twilight zone of protein sequence alignments. *Protein Eng* 12, 85–94 [DOI: 10.1093/protein/12.2.85].

Roux, K. J.; Kim, Dae in; Raida, Manfred; Burke, Brian (2012). A promiscuous biotin ligase fusion protein identifies proximal and interacting proteins in mammalian cells. *J Cell Biol* 196, 801–810 [DOI: 10.1083/jcb.201112098].

Rowe, J. A.; Claessens, Antoine; Corrigan, Ruth A.; Arman, Mònica (2009). Adhesion of Plasmodium falciparum-infected erythrocytes to human cells: molecular mechanisms and therapeutic implications. *Expert Rev Mol Med* 11, e16 [DOI: 10.1017/S1462399409001082].

Roy, A.; Yang, Jianyi; Zhang, Yang (2012). COFACTOR: an accurate comparative algorithm for structure-based protein function annotation. *Nucleic Acids Res* 40, W471-7 [DOI: 10.1093/nar/gks372].

RTS, S. C. T. P. (2015). Efficacy and safety of RTS,S/AS01 malaria vaccine with or without a booster dose in infants and children in Africa: final results of a phase 3, individually randomised, controlled trial. *The Lancet* 386, 31–45 [DOI: 10.1016/S0140-6736(15)60721-8].

Rudlaff, R. M.; Kraemer, Stephan; Marshman, Jeffrey; Dvorin, Jeffrey D. (2020). Three-dimensional ultrastructure of Plasmodium falciparum throughout cytokinesis. *PLoS Pathog* 16, e1008587 [DOI: 10.1371/journal.ppat.1008587].

Sachs, J.; Malaney, Pia (2002). The economic and social burden of malaria. *Nature* 415, 680–685 [DOI: 10.1038/415680a].

Salazar, E.; Bank, Erin M.; Ramsey, Nicole; Hess, Kenneth C.; Deitsch, Kirk W.; Levin, Lonny R. *et al.* (2012). Characterization of Plasmodium falciparum adenylyl cyclase-β and its role in erythrocytic stage parasites. *PLoS ONE* 7, e39769 [DOI: 10.1371/journal.pone.0039769].

Salcedo, E.; Cortese, Joseph F.; Plowe, Christopher V.; Sims, Paul F.G.; Hyde, John E. (2001). A bifunctional dihydrofolate synthetase–folylpolyglutamate synthetase in Plasmodium falciparum identified by functional complementation in yeast and bacteria. *Mol Biochem Parasitol* 112, 239–252 [DOI: 10.1016/S0166-6851(00)00370-4].

Salcedo-Sora, J. E.; Caamano-Gutierrez, Eva; Ward, Stephen A.; Biagini, Giancarlo A. (2014). The proliferating cell hypothesis: a metabolic framework for Plasmodium growth and development. *Trends Parasitol* 30, 170–175 [DOI: 10.1016/j.pt.2014.02.001].

Salomaki, E. D.; Kolisko, Martin (2019). There Is Treasure Everywhere: Reductive Plastid Evolution in Apicomplexa in Light of Their Close Relatives. *Biomolecules* 9 [DOI: 10.3390/biom9080378].

Sanderson, T.; Rayner, Julian C. (2017). PhenoPlasm: a database of disruption phenotypes for malaria parasite genes. *Wellcome Open Res* 2, 45 [DOI: 10.12688/wellcomeopenres.11896.2].

Sawadogo, S. P.; Niang, Abdoulaye; Bilgo, Etienne; Millogo, Azize; Maïga, Hamidou; Dabire, Roch K. *et al.* (2017). Targeting male mosquito swarms to control malaria vector density. *PLoS ONE* 12, e0173273 [DOI: 10.1371/journal.pone.0173273].

Scheffzek, K.; Welti, Stefan (2012). Pleckstrin homology (PH) like domains - versatile modules in protein-protein interaction platforms. *FEBS Lett* 586, 2662–2673 [DOI: 10.1016/j.febslet.2012.06.006].

Scherf, A.; Lopez-Rubio, Jose Juan; Riviere, Loïc (2008). Antigenic variation in Plasmodium falciparum. *Annu Rev Microbiol* 62, 445–470 [DOI: 10.1146/annurev.micro.61.080706.093134].

Schofield, L.; Grau, Georges E. (2005). Immunological processes in malaria pathogenesis. *Nat Rev Immunol* 5, 722–735 [DOI: 10.1038/nri1686].

Seder, R. A.; Chang, Lee-Jah; Enama, Mary E.; Zephir, Kathryn L.; Sarwar, Uzma N.; Gordon, Ingelise J. *et al.* (2013). Protection against malaria by intravenous immunization with a nonreplicating sporozoite vaccine. *Science* 341, 1359–1365 [DOI: 10.1126/science.1241800].

Sen, A.; Madhivanan, Kayalvizhi; Mukherjee, Debarati; Aguilar, R. Claudio (2012). The epsin protein family: coordinators of endocytosis and signaling. *Biomol Concepts* 3, 117–126 [DOI: 10.1515/bmc-2011-0060].

Seydel, K. B.; Kampondeni, Samuel D.; Valim, Clarissa; Potchen, Michael J.; Milner, Danny A.; Muwalo, Francis W. *et al.* (2015). Brain swelling and death in children with cerebral malaria. *N Engl J Med* 372, 1126–1137 [DOI: 10.1056/NEJMoa1400116].

Shanks, G. D.; White, Nicholas J. (2013). The activation of vivax malaria hypnozoites by infectious diseases. *The Lancet Infectious Diseases* 13, 900–906 [DOI: 10.1016/S1473-3099(13)70095-1].

Sharp, P. M.; Plenderleith, Lindsey J.; Hahn, Beatrice H. (2020). Ape Origins of Human Malaria. *Annu Rev Microbiol* 74, 39–63 [DOI: 10.1146/annurev-micro-020518-115628].

Shivapurkar, R.; Hingamire, Tejashri; Kulkarni, Akshay S.; Rajamohanan, P. R.; Reddy, D. Srinivasa; Shanmugam, Dhanasekaran (2018). Evaluating antimalarial efficacy by tracking glycolysis in Plasmodium falciparum using NMR spectroscopy. *Sci Rep* 8, 18076 [DOI: 10.1038/s41598-018-36197-3].

Shu, X.; Lev-Ram, Varda; Deerinck, Thomas J.; Qi, Yingchuan; Ramko, Ericka B.; Davidson, Michael W. *et al.* (2011). A genetically encoded tag for correlated light and electron microscopy of intact cells, tissues, and organisms. *PLoS Biol* 9, e1001041 [DOI: 10.1371/journal.pbio.1001041].

Sidik, S. M.; Huet, Diego; Ganesan, Suresh M.; Huynh, My-Hang; Wang, Tim; Nasamu, Armiyaw S. *et al.* (2016). A Genome-wide CRISPR Screen in Toxoplasma Identifies Essential Apicomplexan Genes. *Cell* 166, 1423-1435.e12 [DOI: 10.1016/j.cell.2016.08.019].

Simossis, V. A.; Heringa, J. (2005). PRALINE: a multiple sequence alignment toolbox that integrates homology-extended and secondary structure information. *Nucleic Acids Res* 33, W289-94 [DOI: 10.1093/nar/gki390].

Sinden, R. E. (1982). Gametocytogenesis of Plasmodium falciparum in vitro: an electron microscopic study. *Parasitology* 84, 1–11 [DOI: 10.1017/s003118200005160x].

Sinden, R. E. (1983). Sexual Development of Malarial Parasites. In Advances in parasitology, pp. 153–216, Academic P, London. [DOI: 10.1016/s0065-308x(08)60462-5]

Sinden, R. E. (2015). The cell biology of malaria infection of mosquito: advances and opportunities. *Cell Microbiol* 17, 451–466 [DOI: 10.1111/cmi.12413].

Sinden, R. E.; Croll, N. A. (1975). Cytology and kinetics of microgametogenesis and fertilization in Plasmodium yoelii nigeriensis. *Parasitology* 70, 53–65. https://pubmed.ncbi.nlm.nih.gov/1118188/ [DOI: 10.1017/s0031182000048861].

Singh, P.; Alaganan, Aditi; More, Kunal R.; Lorthiois, Audrey; Thiberge, Sabine; Gorgette, Olivier *et al.* (2019). Role of a patatin-like phospholipase in Plasmodium falciparum gametogenesis and malaria transmission. *Proc Natl Acad Sci U S A* 116, 17498–17508 [DOI: 10.1073/pnas.1900266116].

Singh, S.; Chitnis, Chetan E. (2012). Signalling mechanisms involved in apical organelle discharge during host cell invasion by apicomplexan parasites. *Microbes and infection* 14, 820–824. https://pubmed.ncbi.nlm.nih.gov/22634343/ [DOI: 10.1016/j.micinf.2012.05.007].

Singh, B.; Daneshvar, Cyrus (2013). Human infections and detection of Plasmodium knowlesi. *Clin Microbiol Rev* 26, 165–184 [DOI: 10.1128/CMR.00079-12].

Singh, B.; Sung, Lee Kim; Matusop, Asmad; Radhakrishnan, Anand; Shamsul, Sunita S. G.; Cox-Singh, Janet *et al.* (2004). A large focus of naturally acquired Plasmodium knowlesi infections in human beings. *The Lancet* 363, 1017–1024 [DOI: 10.1016/S0140-6736(04)15836-4].

Sinha, A.; Hughes, Katie R.; Modrzynska, Katarzyna K.; Otto, Thomas D.; Pfander, Claudia; Dickens, Nicholas J. *et al.* (2014). A cascade of DNA-binding proteins for sexual commitment and development in Plasmodium. *Nature* 507, 253–257 [DOI: 10.1038/nature12970].

Sinka, M. E.; Bangs, Michael J.; Manguin, Sylvie; Coetzee, Maureen; Mbogo, Charles M.; Hemingway, Janet *et al.* (2010). The dominant Anopheles vectors of human malaria in Africa, Europe and the Middle East: occurrence data, distribution maps and bionomic précis. *Parasit Vectors* 3, 117 [DOI: 10.1186/1756-3305-3-117].

Sinka, M. E.; Bangs, Michael J.; Manguin, Sylvie; Rubio-Palis, Yasmin; Chareonviriyaphap, Theeraphap; Coetzee, Maureen *et al.* (2012). A global map of dominant malaria vectors. *Parasit Vectors* 5, 69 [DOI: 10.1186/1756-3305-5-69].

Sinnis, P.; Coppi, Alida (2007). A long and winding road: the Plasmodium sporozoite's journey in the mammalian host. *Parasitol Int* 56, 171–178 [DOI: 10.1016/j.parint.2007.04.002].

Sirima, S. B.; Cousens, Simon; Druilhe, Pierre (2011). Protection against malaria by MSP3 candidate vaccine. *N Engl J Med* 365, 1062–1064 [DOI: 10.1056/NEJMc1100670].

Smith Gueye, C.; Newby, Gretchen; Gosling, Roland D.; Whittaker, Maxine A.; Chandramohan, Daniel; Slutsker, Laurence *et al.* (2016). Strategies and approaches to vector control in nine malaria-eliminating countries: a cross-case study analysis. *Malar J* 15, 2 [DOI: 10.1186/s12936-015-1054-z].

Smith, R. C.; Vega-Rodríguez, Joel; Jacobs-Lorena, Marcelo (2014). The Plasmodium bottleneck: malaria parasite losses in the mosquito vector. *Mem. Inst. Oswaldo Cruz* 109, 644–661 [DOI: 10.1590/0074-0276130597].

Song, Y.; DiMaio, Frank; Wang, Ray Yu-Ruei; Kim, David; Miles, Chris; Brunette, Tj *et al.* (2013). High-resolution comparative modeling with RosettaCM. *Structure* 21, 1735–1742 [DOI: 10.1016/j.str.2013.08.005].

Sorber, K.; Dimon, Michelle T.; DeRisi, Joseph L. (2011). RNA-Seq analysis of splicing in Plasmodium falciparum uncovers new splice junctions, alternative splicing and splicing of antisense transcripts. *Nucleic Acids Res* 39, 3820–3835 [DOI: 10.1093/nar/gkq1223].

Souza, W. de (2006). Secretory organelles of pathogenic protozoa. *An Acad Bras Cienc* 78, 271–291 [DOI: 10.1590/s0001-37652006000200008].

Staines, H. M.; Rae, Caroline; Kirk, Kiaran (2000). Increased permeability of the malaria-infected erythrocyte to organic cations. *Biochimica et Biophysica Acta (BBA) - Biomembranes* 1463, 88–98 [DOI: 10.1016/S0005-2736(99)00187-X].

Straimer, J.; Lee, Marcus C. S.; Lee, Andrew H.; Zeitler, Bryan; Williams, April E.; Pearl, Jocelynn R. *et al.* (2012). Site-specific genome editing in Plasmodium falciparum using engineered zinc-finger nucleases. *Nat Methods* 9, 993–998 [DOI: 10.1038/nmeth.2143].

Strode, C.; Donegan, Sarah; Garner, Paul; Enayati, Ahmad Ali; Hemingway, Janet (2014). The impact of pyrethroid resistance on the efficacy of insecticide-treated bed nets against African anopheline mosquitoes: systematic review and meta-analysis. *PLoS Med* 11, e1001619 [DOI: 10.1371/journal.pmed.1001619].

Sturm, A.; Amino, Rogerio; van de Sand, Claudia; Regen, Tommy; Retzlaff, Silke; Rennenberg, Annika *et al.* (2006). Manipulation of host hepatocytes by the malaria parasite for delivery into liver sinusoids. *Science* **313**, 1287–1290 [DOI: 10.1126/science.1129720].

Suarez, C.; Lentini, Gaëlle; Ramaswamy, Raghavendran; Maynadier, Marjorie; Aquilini, Eleonora; Berry-Sterkers, Laurence *et al.* (2019). A lipid-binding protein mediates rhoptry discharge and invasion in Plasmodium falciparum and Toxoplasma gondii parasites. *Nat Commun* **10**, 4041 [DOI: 10.1038/s41467-019-11979-z].

Sutherland, C. J.; Tanomsing, Naowarat; Nolder, Debbie; Oguike, Mary; Jennison, Charlie; Pukrittayakamee, Sasithon *et al.* (2010). Two nonrecombining sympatric forms of the human malaria parasite Plasmodium ovale occur globally. *J Infect Dis* **201**, 1544–1550 [DOI: 10.1086/652240].

Szymczak, A. L.; Workman, Creg J.; Wang, Yao; Vignali, Kate M.; Dilioglou, Smaroula; Vanin, Elio F. *et al.* (2004). Erratum: Corrigendum: Correction of multi-gene deficiency in vivo using a single 'self-cleaving' 2A peptide–based retroviral vector. *Nat Biotechnol* **22**, 760 [DOI: 10.1038/nbt0604-760b].

Tabb, D. L. (2012). Evaluating protein interactions through cross-linking mass spectrometry. *Nat Methods* **9**, 879–881 [DOI: 10.1038/nmeth.2139].

Tan, K. P.; Nguyen, Thanh Binh; Patel, Siddharth; Varadarajan, Raghavan; Madhusudhan, M. S. (2013). Depth: a web server to compute depth, cavity sizes, detect potential small-molecule ligand-binding cavities and predict the pKa of ionizable residues in proteins. *Nucleic Acids Res* **41**, W314-21 [DOI: 10.1093/nar/gkt503].

Tan, K. P.; Varadarajan, Raghavan; Madhusudhan, M. S. (2011). DEPTH: a web server to compute depth and predict small-molecule binding cavities in proteins. *Nucleic Acids Res* **39**, W242-8 [DOI: 10.1093/nar/gkr356].

Tarr, S. J.; Osborne, Andrew R. (2015). Experimental determination of the membrane topology of the Plasmodium protease Plasmepsin V. *PLoS ONE* **10**, e0121786 [DOI: 10.1371/journal.pone.0121786].

Templeton, T. J.; Pain, Arnab (2016). Diversity of extracellular proteins during the transition from the 'proto-apicomplexan' alveolates to the apicomplexan obligate parasites. *Parasitology* **143**, 1–17 [DOI: 10.1017/S0031182015001213].

Tham, W.-H.; Healer, Julie; Cowman, Alan F. (2012). Erythrocyte and reticulocyte binding-like proteins of Plasmodium falciparum. *Trends Parasitol* **28**, 23–30 [DOI: 10.1016/j.pt.2011.10.002].

Tham, W.-H.; Lim, Nicholas T. Y.; Weiss, Greta E.; Lopaticki, Sash; Ansell, Brendan R. E.; Bird, Megan *et al.* (2015). Plasmodium falciparum Adhesins Play an Essential Role in Signalling and Activation of Invasion into Human Erythrocytes. *PLoS Pathog* **11**, e1005343 [DOI: 10.1371/journal.ppat.1005343].

Thornton, J. M.; Todd, A. E.; Milburn, D.; Borkakoti, N.; Orengo, C. A. (2000). From structure to function: approaches and limitations. *Nat Struct Biol* **7 Suppl**, 991–994 [DOI: 10.1038/80784].

Tibúrcio, M.; Sauerwein, Robert; Lavazec, Catherine; Alano, Pietro (2015). Erythrocyte remodeling by Plasmodium falciparum gametocytes in the human host interplay. *Trends Parasitol* **31**, 270–278 [DOI: 10.1016/j.pt.2015.02.006].

Tibúrcio, M.; Yang, Annie S. P.; Yahata, Kazuhide; Suárez-Cortés, Pablo; Belda, Hugo; Baumgarten, Sebastian *et al.* (2019). A Novel Tool for the Generation of Conditional Knockouts To Study Gene Function across the Plasmodium falciparum Life Cycle. *mBio* **10** [DOI: 10.1128/mBio.01170-19].

Tilley, L.; Dixon, Matthew W. A.; Kirk, Kiaran (2011). The Plasmodium falciparum-infected red blood cell. *Int J Biochem Cell Biol* **43**, 839–842 [DOI: 10.1016/j.biocel.2011.03.012].

Tirados, I.; Costantini, C.; Gibson, G.; Torr, S. J. (2006). Blood-feeding behaviour of the malarial mosquito Anopheles arabiensis: implications for vector control. *Med Vet Entomol* **20**, 425–437 [DOI: 10.1111/j.1365-2915.2006.652.x].

Tizifa, T. A.; Kabaghe, Alinune N.; McCann, Robert S.; van den Berg, Henk; van Vugt, Michele; Phiri, Kamija S. (2018). Prevention Efforts for Malaria. *Curr Trop Med Rep* **5**, 41–50 [DOI: 10.1007/s40475-018-0133-y].

Tokunaga, N.; Nozaki, Mamoru; Tachibana, Mayumi; Baba, Minami; Matsuoka, Kazuhiro; Tsuboi, Takafumi *et al.* (2019). Expression and Localization Profiles of Rhoptry Proteins in Plasmodium berghei Sporozoites. *Front Cell Infect Microbiol* **9**, 316 [DOI: 10.3389/fcimb.2019.00316].

Tonkin, M. L.; Roques, Magali; Lamarque, Mauld H.; Pugnière, Martine; Douguet, Dominique; Crawford, Joanna *et al.* (2011). Host cell invasion by apicomplexan parasites: insights from the co-structure of AMA1 with a RON2 peptide. *Science* 333, 463–467 [DOI: 10.1126/science.1204988].

Topolska, A. E.; Lidgett, Angela; Truman, Dirk; Fujioka, Hisashi; Coppel, Ross L. (2004). Characterization of a membrane-associated rhoptry protein of Plasmodium falciparum. *J Biol Chem* 279, 4648–4656 [DOI: 10.1074/jbc.M307859200].

Trampuz, A.; Jereb, Matjaz; Muzlovic, Igor; Prabhu, Rajesh M. (2003). Clinical review: Severe malaria. *Crit Care* 7, 315–323 [DOI: 10.1186/cc2183].

Treeck, M.; Zacherl, Sonja; Herrmann, Susann; Cabrera, Ana; Kono, Maya; Struck, Nicole S. *et al.* (2009). Functional analysis of the leading malaria vaccine candidate AMA-1 reveals an essential role for the cytoplasmic domain in the invasion process. *PLoS Pathog* 5, e1000322 [DOI: 10.1371/journal.ppat.1000322].

Trinkle-Mulcahy, L. (2019). Recent advances in proximity-based labeling methods for interactome mapping. *F1000Res* 8 [DOI: 10.12688/f1000research.16903.1].

Tropical Infectious Diseases: Principles, Pathogens and Practice, Elsevier. (2011). [https://www.sciencedirect.com/book/9780702039355/tropical-infectious-diseases]

Uwimana, A.; Legrand, Eric; Stokes, Barbara H.; Ndikumana, Jean-Louis Mangala; Warsame, Marian; Umulisa, Noella *et al.* (2020). Emergence and clonal expansion of in vitro artemisinin-resistant Plasmodium falciparum kelch13 R561H mutant parasites in Rwanda. *Nat Med* [DOI: 10.1038/s41591-020-1005-2].

Uzureau, P.; Barale, Jean-Christophe; Janse, Chris J.; Waters, Andrew P.; Breton, Catherine Braun (2004). Gene targeting demonstrates that the Plasmodium berghei subtilisin PbSUB2 is essential for red cell invasion and reveals spontaneous genetic recombination events. *Cell Microbiol* 6, 65–78 [DOI: 10.1046/j.1462-5822.2003.00343.x].

Vaughan, A. M.; Kappe, Stefan H. I. (2017a). Genetically attenuated malaria parasites as vaccines. *Expert Rev Vaccines* 16, 765–767 [DOI: 10.1080/14760584.2017.1341835].

Vaughan, A. M.; Kappe, Stefan H. I. (2017b). Malaria Parasite Liver Infection and Exoerythrocytic Biology. *Cold Spring Harb Perspect Med* 7 [DOI: 10.1101/cshperspect.a025486].

Vaughan, A. M.; Mikolajczak, Sebastian A.; Wilson, Elizabeth M.; Grompe, Markus; Kaushansky, Alexis; Camargo, Nelly *et al.* (2012). Complete Plasmodium falciparum liver-stage development in liver-chimeric mice. *J Clin Invest* 122, 3618–3628 [DOI: 10.1172/JCI62684].

Venugopal, K.; Werkmeister, Elisabeth; Barois, Nicolas; Saliou, Jean-Michel; Poncet, Anais; Huot, Ludovic *et al.* (2017). Dual role of the Toxoplasma gondii clathrin adaptor AP1 in the sorting of rhoptry and microneme proteins and in parasite division. *PLoS Pathog* 13, e1006331 [DOI: 10.1371/journal.ppat.1006331].

Verra, F.; Angheben, Andrea; Martello, Elisa; Giorli, Giovanni; Perandin, Francesca; Bisoffi, Zeno (2018). A systematic review of transfusion-transmitted malaria in non-endemic areas. *Malar J* 17, 36 [DOI: 10.1186/s12936-018-2181-0].

Vicidomini, G.; Bianchini, Paolo; Diaspro, Alberto (2018). STED super-resolved microscopy. *Nat Methods* 15, 173–182 [DOI: 10.1038/nmeth.4593].

Volz, J. C.; Yap, Alan; Sisquella, Xavier; Thompson, Jenn K.; Lim, Nicholas T. Y.; Whitehead, Lachlan W. *et al.* (2016). Essential Role of the PfRh5/PfRipr/CyRPA Complex during Plasmodium falciparum Invasion of Erythrocytes. *Cell Host Microbe* 20, 60–71 [DOI: 10.1016/j.chom.2016.06.004].

Votýpka, J.; Modrý, David; Oborník, Miroslav; Šlapeta, Jan; Lukeš, Julius (2017). Apicomplexa. In Handbook of the protists, 2nd ed. (Archibald, J. M., Simpson, A. G. B. & Slamovits, C. H., eds), pp. 567–624, Springer, Cham. [https://link.springer.com/referenceworkentry/10.1007%2F978-3-319-28149-0_20]

Wadi, I.; Nath, Mahendra; Anvikar, Anupkumar R.; Singh, Pargat; Sinha, Abhinav (2019). Recent advances in transmission-blocking drugs for malaria elimination. *Future Med Chem* 11, 3047–3088 [DOI: 10.4155/fmc-2019-0225].

Waite, J. L.; Suh, Eunho; Lynch, Penelope A.; Thomas, Matthew B. (2019). Exploring the lower thermal limits for development of the human malaria parasite, Plasmodium falciparum. *Biol Lett* 15, 20190275 [DOI: 10.1098/rsbl.2019.0275].

Walker, J. M., ed (**2005**). The Proteomics Protocols Handbook, Humana Press Inc, Totowa, NJ. [https://www.springer.com/gp/book/9781588293435]

Walliker, D.; Quakyi, I. A.; Wellems, T. E.; McCutchan, T. F.; Szarfman, A.; London, W. T. *et al.* (**1987**). Genetic analysis of the human malaria parasite Plasmodium falciparum. *Science* **236**, 1661–1666 [DOI: 10.1126/science.3299700].

Wang, P.; Wang, Qi; Yang, Yonghong; Coward, James K.; Nzila, Alexis; Sims, Paul F. G. *et al.* (**2010**). Characterisation of the bifunctional dihydrofolate synthase-folylpolyglutamate synthase from Plasmodium falciparum; a potential novel target for antimalarial antifolate inhibition. *Mol Biochem Parasitol* **172**, 41–51 [DOI: 10.1016/j.molbiopara.2010.03.012].

Wassmer, S. C.; Taylor, Terrie E.; Rathod, Pradipsinh K.; Mishra, Saroj K.; Mohanty, Sanjib; Arevalo-Herrera, Myriam *et al.* (**2015**). Investigating the Pathogenesis of Severe Malaria: A Multidisciplinary and Cross-Geographical Approach. *The American Journal of Tropical Medicine and Hygiene* **93**, 42–56 [DOI: 10.4269/ajtmh.14-0841].

Weedall, G. D.; Mugenzi, Leon M. J.; Menze, Benjamin D.; Tchouakui, Magellan; Ibrahim, Sulaiman S.; Amvongo-Adjia, Nathalie *et al.* (**2019**). A cytochrome P450 allele confers pyrethroid resistance on a major African malaria vector, reducing insecticide-treated bednet efficacy. *Sci Transl Med* **11** [DOI: 10.1126/scitranslmed.aat7386].

Weiss, G. E.; Gilson, Paul R.; Taechalertpaisarn, Tana; Tham, Wai-Hong; Jong, Nienke W. M. de; Harvey, Katherine L. *et al.* (**2015**). Revealing the sequence and resulting cellular morphology of receptor-ligand interactions during Plasmodium falciparum invasion of erythrocytes. *PLoS Pathog* **11**, e1004670 [DOI: 10.1371/journal.ppat.1004670].

White, N. J. (**2011**). Determinants of relapse periodicity in Plasmodium vivax malaria. *Malar J* **10**, 297 [DOI: 10.1186/1475-2875-10-297].

White, N. J.; Pukrittayakamee, Sasithon; Hien, Tran Tinh; Faiz, M. Abul; Mokuolu, Olugbenga A.; Dondorp, Arjen M. (**2014**). Malaria. The Lancet, 383(9918), 723-735. *The Lancet* **383**, 723–735 [DOI: 10.1016/S0140-6736(13)60024-0].

WHO (**2019**). World Malaria Report 2019, WHO, [https://www.who.int/publications/i/item/world-malaria-report-2019].

Wicht, K. J.; Mok, Sachel; Fidock, David A. (**2020**). Molecular Mechanisms of Drug Resistance in Plasmodium falciparum Malaria. *Annu Rev Microbiol* **74**, 431–454 [DOI: 10.1146/annurev-micro-020518-115546].

Wickramarachchi, T.; Devi, Yengkhom S.; Mohmmed, Asif; Chauhan, Virander S. (**2008**). Identification and characterization of a novel Plasmodium falciparum merozoite apical protein involved in erythrocyte binding and invasion. *PLoS ONE* **3**, e1732 [DOI: 10.1371/journal.pone.0001732].

Woo, Y. H.; Ansari, Hifzur; Otto, Thomas D.; Klinger, Christen M.; Kolisko, Martin; Michálek, Jan *et al.* (**2015**). Chromerid genomes reveal the evolutionary path from photosynthetic algae to obligate intracellular parasites. *eLife* **4**, e06974 [DOI: 10.7554/eLife.06974].

Xiong, X.; Wu, Geng; Wei, Yue; Liu, Liqiong; Zhang, Yubing; Su, Rui *et al.* (**2020**). SspABCD-SspE is a phosphorothioation-sensing bacterial defence system with broad anti-phage activities. *Nat Microbiol* [DOI: 10.1038/s41564-020-0700-6].

Xu, T.; Johnson, Cole A.; Gestwicki, Jason E.; Kumar, Anuj (**2010**). Conditionally controlling nuclear trafficking in yeast by chemical-induced protein dimerization. *Nat Protoc* **5**, 1831–1843 [DOI: 10.1038/nprot.2010.141].

Xu, D.; Zhang, Yang (**2012**). Ab initio protein structure assembly using continuous structure fragments and optimized knowledge-based force field. *Proteins* **80**, 1715–1735 [DOI: 10.1002/prot.24065].

Xu, D.; Zhang, Yang (**2013**). Toward optimal fragment generations for ab initio protein structure assembly. *Proteins* **81**, 229–239 [DOI: 10.1002/prot.24179].

Yahata, K.; Treeck, Moritz; Culleton, Richard; Gilberger, Tim-Wolf; Kaneko, Osamu (**2012**). Time-lapse imaging of red blood cell invasion by the rodent malaria parasite Plasmodium yoelii. *PLoS ONE* **7**, e50780 [DOI: 10.1371/journal.pone.0050780].

Yang, X.; Coulombe-Huntington, Jasmin; Kang, Shuli; Sheynkman, Gloria M.; Hao, Tong; Richardson, Aaron *et al.* (**2016**). Widespread Expansion of Protein Interaction Capabilities by Alternative Splicing. *Cell* **164**, 805–817 [DOI: 10.1016/j.cell.2016.01.029].

Yang, J.; Roy, Ambrish; Zhang, Yang (2013a). BioLiP: a semi-manually curated database for biologically relevant ligand-protein interactions. *Nucleic Acids Res* 41, D1096-103 [DOI: 10.1093/nar/gks966].

Yang, J.; Roy, Ambrish; Zhang, Yang (2013b). Protein-ligand binding site recognition using complementary binding-specific substructure comparison and sequence profile alignment. *Bioinformatics* 29, 2588–2595 [DOI: 10.1093/bioinformatics/btt447].

Yang, J.; Zhang, Yang (2015). I-TASSER server: new development for protein structure and function predictions. *Nucleic Acids Res* 43, W174-81 [DOI: 10.1093/nar/gkv342].

Yeoh, L. M.; Goodman, Christopher D.; Mollard, Vanessa; McHugh, Emma; Lee, V. Vern; Sturm, Angelika *et al.* (2019a). Alternative splicing is required for stage differentiation in malaria parasites. *Genome Biol* 20, 151 [DOI: 10.1186/s13059-019-1756-6].

Yeoh, L. M.; Lee, V. Vern; McFadden, Geoffrey I.; Ralph, Stuart A. (2019b). Alternative Splicing in Apicomplexan Parasites. *mBio* 10 [DOI: 10.1128/mBio.02866-18].

Yeoh, S.; O'Donnell, Rebecca A.; Koussis, Konstantinos; Dluzewski, Anton R.; Ansell, Keith H.; Osborne, Simon A. *et al.* (2007). Subcellular discharge of a serine protease mediates release of invasive malaria parasites from host erythrocytes. *Cell* 131, 1072–1083 [DOI: 10.1016/j.cell.2007.10.049].

Yuan, L.; Hao, Mingming; Wu, Lanou; Zhao, Zhen; Rosenthal, Benjamin M.; Li, Xiaomei *et al.* (2014). Refrigeration provides a simple means to synchronize in vitro cultures of Plasmodium falciparum. *Exp Parasitol* 140, 18–23 [DOI: 10.1016/j.exppara.2014.03.010].

Zanghì, G.; Vembar, Shruthi S.; Baumgarten, Sebastian; Ding, Shuai; Guizetti, Julien; Bryant, Jessica M. *et al.* (2018). A Specific PfEMP1 Is Expressed in P. falciparum Sporozoites and Plays a Role in Hepatocyte Infection. *Cell Rep* 22, 2951–2963 [DOI: 10.1016/j.celrep.2018.02.075].

Zeng, L.; Wang, Wen-Horng; Arrington, Justine; Shao, Gengbao; Geahlen, Robert L.; Hu, Chang-Deng *et al.* (2017). Identification of Upstream Kinases by Fluorescence Complementation Mass Spectrometry. *ACS Cent Sci* 3, 1078–1085 [DOI: 10.1021/acscentsci.7b00261].

Zhang, Y. (2009). I-TASSER: fully automated protein structure prediction in CASP8. *Proteins* 77 Suppl 9, 100–113 [DOI: 10.1002/prot.22588].

Zhang, C.; Gao, Han; Yang, Zhenke; Jiang, Yuanyuan; Li, Zhenkui; Wang, Xu *et al.* (2017). CRISPR/Cas9 mediated sequential editing of genes critical for ookinete motility in Plasmodium yoelii. *Mol Biochem Parasitol* 212, 1–8 [DOI: 10.1016/j.molbiopara.2016.12.010].

Zhang, M.; Wang, Chengqi; Otto, Thomas D.; Oberstaller, Jenna; Liao, Xiangyun; Adapa, Swamy R. *et al.* (2018). Uncovering the essential genes of the human malaria parasite Plasmodium falciparum by saturation mutagenesis. *Science* 360 [DOI: 10.1126/science.aap7847].

Zhou, H.-X.; Pang, Xiaodong (2018). Electrostatic Interactions in Protein Structure, Folding, Binding, and Condensation. *Chem Rev* 118, 1691–1741 [DOI: 10.1021/acs.chemrev.7b00305].

Zuccala, E. S.; Gout, Alexander M.; Dekiwadia, Chaitali; Marapana, Danushka S.; Angrisano, Fiona; Turnbull, Lynne *et al.* (2012). Subcompartmentalisation of proteins in the rhoptries correlates with ordered events of erythrocyte invasion by the blood stage malaria parasite. *PLoS ONE* 7, e46160 [DOI: 10.1371/journal.pone.0046160].

PUBLICATIONS

Structural Insights Into PfARO and Characterization of its Interaction With PfAIP

Michael **Geiger**, Chris **Brown**, Jan Stephan Wichers, Jan Strauss, Andrés Lill, Roland Thuenauer, Benjamin Liffner, Louisa Wilcke, Sarah Lemcke, Dorothee Heincke, Samuel Pazicky, Anna Bachmann, Christian Löw, Danny William Wilson, Michael Filarsky, Paul-Christian Burda, Kun Zhang, Murray Junop, Tim Wolf Gilberger

J Mol Biol. 2020 Feb 14;432(4):878-896. doi: 10.1016/j.jmb.2019.12.024. Epub 2019 Dec 23.

DANKSAGUNG

Zuallererst möchte ich mich bei meinem Doktorvater Prof. Dr. Tim Gilberger dafür bedanken, dass er mir die Gelegenheit gegeben hat meine Promotion, und das vorangegangene Praktikum, in seiner Arbeitsgruppe durchzuführen. Danke auch für die Möglichkeit, eigene Ideen umzusetzen und diese selbstständig zu verfolgen, sowie die Erreichbarkeit, wenn einmal etwas nicht klar war. Und besonders vielen Dank für die konstruktive Kritik, die Korrekturen an meiner Dissertation und das Auge für die wirklich wichtigen Dinge.

Prof. Dr. Egbert Tannich und Dr. Tobias Spielmann danke ich für die Übernahme der Co-Betreuung, und insbesondere Tobias, der jederzeit für Fragen erreichbar war und das Zweitgutachten der Dissertation übernahm. Dank geht auch an Prof. Dr. Murray Junop und dessen Labor für die Auflösung der *Pf*ARO-Kistallstruktur und an die Proteomics Core Facility (EMBL, Heidelberg) für die Massenspektrometrie.

Vielen Dank an Dr. Louisa Wilcke für die Einarbeitung in die Methoden während meines Praktikums und die Anmerkungen und Korrekturvorschläge zu meiner Dissertation. Alex Arnold danke ich für die gründliche Korrektur meiner Dissertation und das Austellen des Sprachzertifikats.

Ganz besonders möchte ich mich bei den Spielbergern bedanken. Allen voran Sarah Lemcke und Dr. Paolo Mesén-Ramírez, mit denen die Zeit in Hamburg viel Spaß gemacht hat. Danke auch an Bärbel Bergmann und an alle nicht namentlich genannten Spielberger für das sympathische Arbeitsumfeld, sowie die gemeinsame Zeit auch außerhalb des Labors.

Zu guter Letzt möchte ich allen meinen Freunden und ganz besonders meinem Partner Roger Hoffmann danken. Deine großartige Unterstützung während der letzten Jahre hat mir sehr dabei geholfen dieses Projekt erfolgreich abzuschließen.

APPENDIX

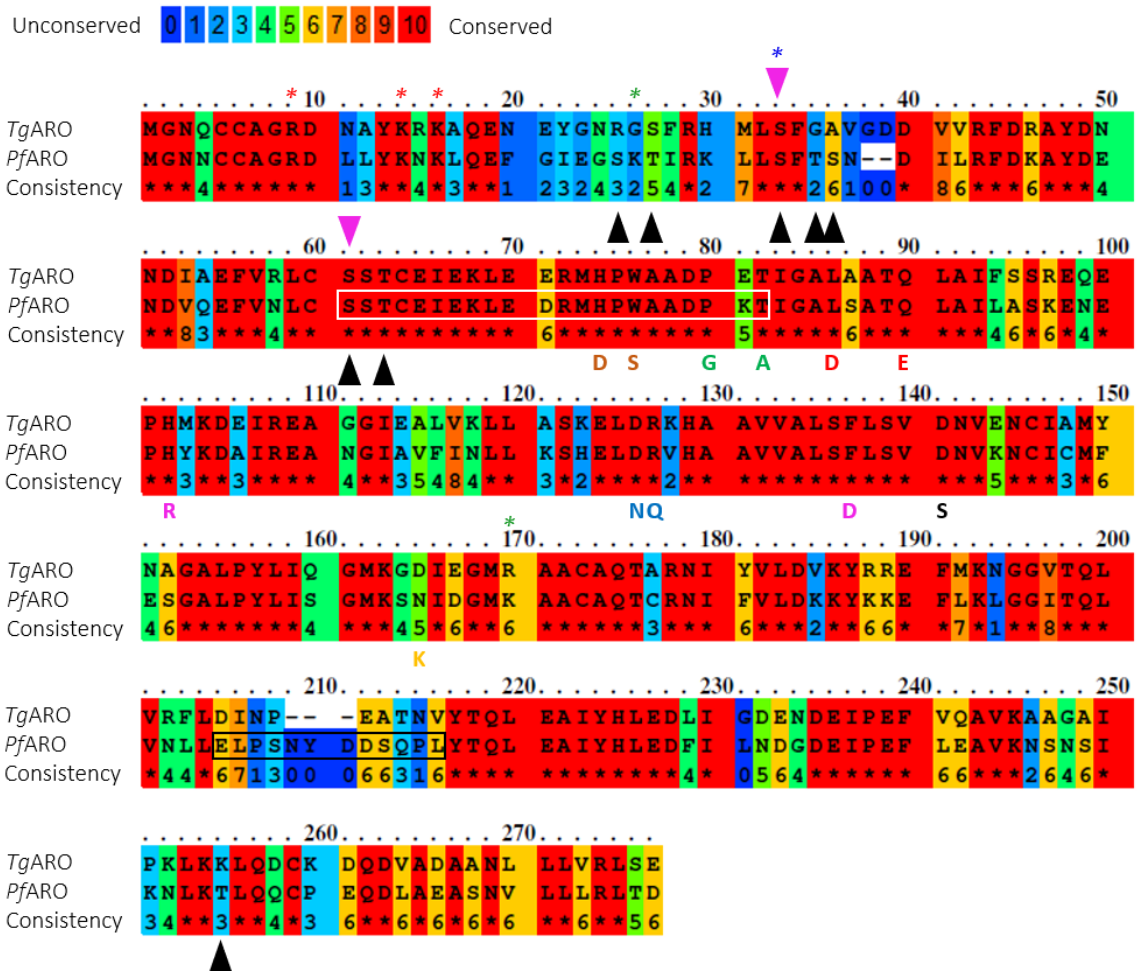

S1 | Sequence homology of *Tg*ARO and *Pf*ARO. PRALINE sequence alignment of *Tg*ARO (TGME49_261440) and *Pf*ARO (PF3D7_0414900). Phosphorylation-sites (displayed at ToxoDB and PlasmoDB) of *Tg*ARO and *Pf*ARO are indicated by magenta and black arrowheads, respectively. *Pf*ARO phosphorylations are: S_{25}, T_{27}, S_{33}, T_{35}, S_{36}, S_{59}, T_{61} and T_{253}. *Pf*ARO loop1 (S_{60} to T_{80}) and loop2 (E_{203} to L_{214}) are indicated by white and black box, respectively. Mutations inserted in *Pf*ARO (see Fig. 3.6A) are indicated by coloured letters beneath the alignment. Mutation 1 (H72D/W74S, brown); mutation 2 (L84D/Q88E, red); mutation 3 (P78G/T80A, green); mutation 4 (D124N/R125Q, blue); mutation 5 (deletion of loop1 by removal of residues I64-K79); mutation 6 (F135D, magenta). The positively charged residues R_9, K_{14} and K_{16} which are important for rhoptry membrane attachment of *Pf*ARO [Cabrera *et al.*, 2012] are indicated by red asterisks. Calcium-dependent phosphorylation of *Tg*ARO at S_{33} [Nebl *et al.*, 2011] is indicated by blue asterisk. Acetylation of K_{26} and K_{168} [Cobbold *et al.*, 2016] is indicated by green asterisks.

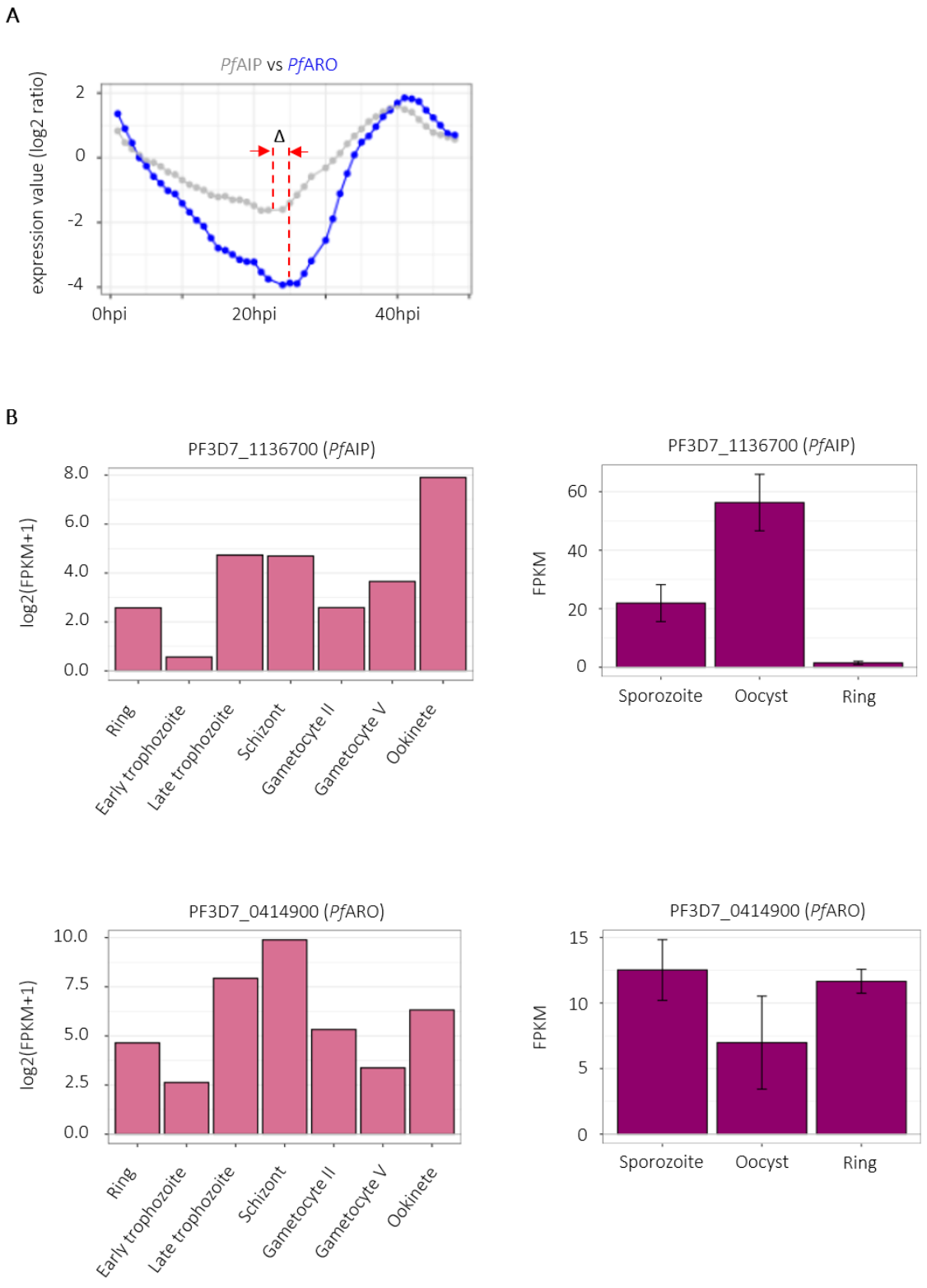

S2 | *Pf*AIP and *Pf*ARO RNA expression profiles. (**A**) Microarray expression data of *P. falciparum* 3D7 wild-type strain was used to overlay and compare *Pf*AIP and *Pf*ARO expression profiles during the erythrocytic stage. Hpi, hours post infection; Δ, difference in onset of transcription. (**B**) Transcriptional data of *Pfaip* and *Pfaro* genes from 3D7 wild-type sexual and asexual life stages. FPKM, transcript levels of fragments per kilobase of exon model per million reads mapped. (A-B) Transcriptional data was retrieved from PlasmoDB.

A

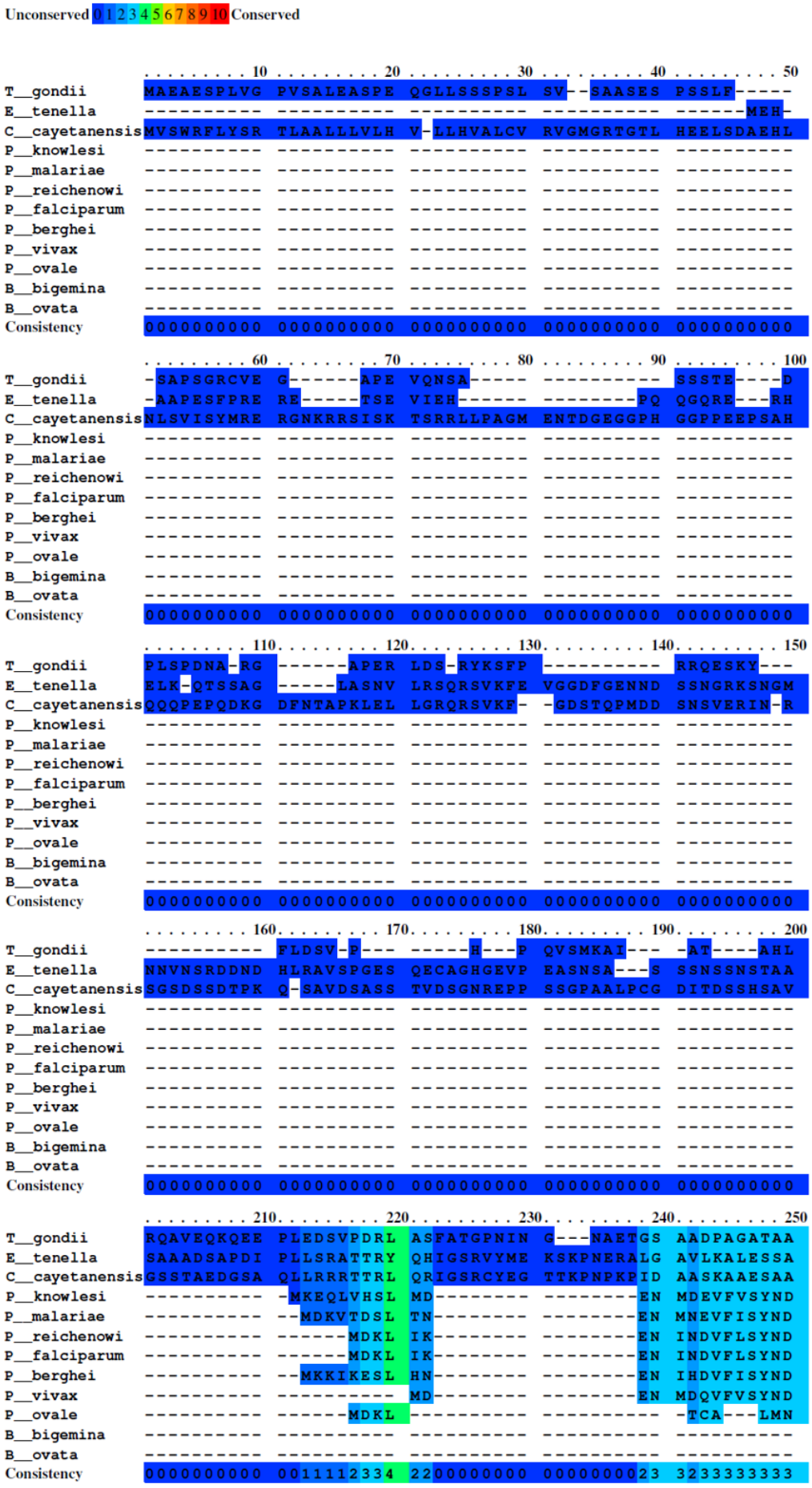
Unconserved 0 1 2 3 4 5 6 7 8 9 10 Conserved
T__gondii
E__tenella
C__cayetanensis
P__knowlesi
P__malariae
P__reichenowi
P__falciparum
P__berghei
P__vivax
P__ovale
B__bigemina
B__ovata
Consistency

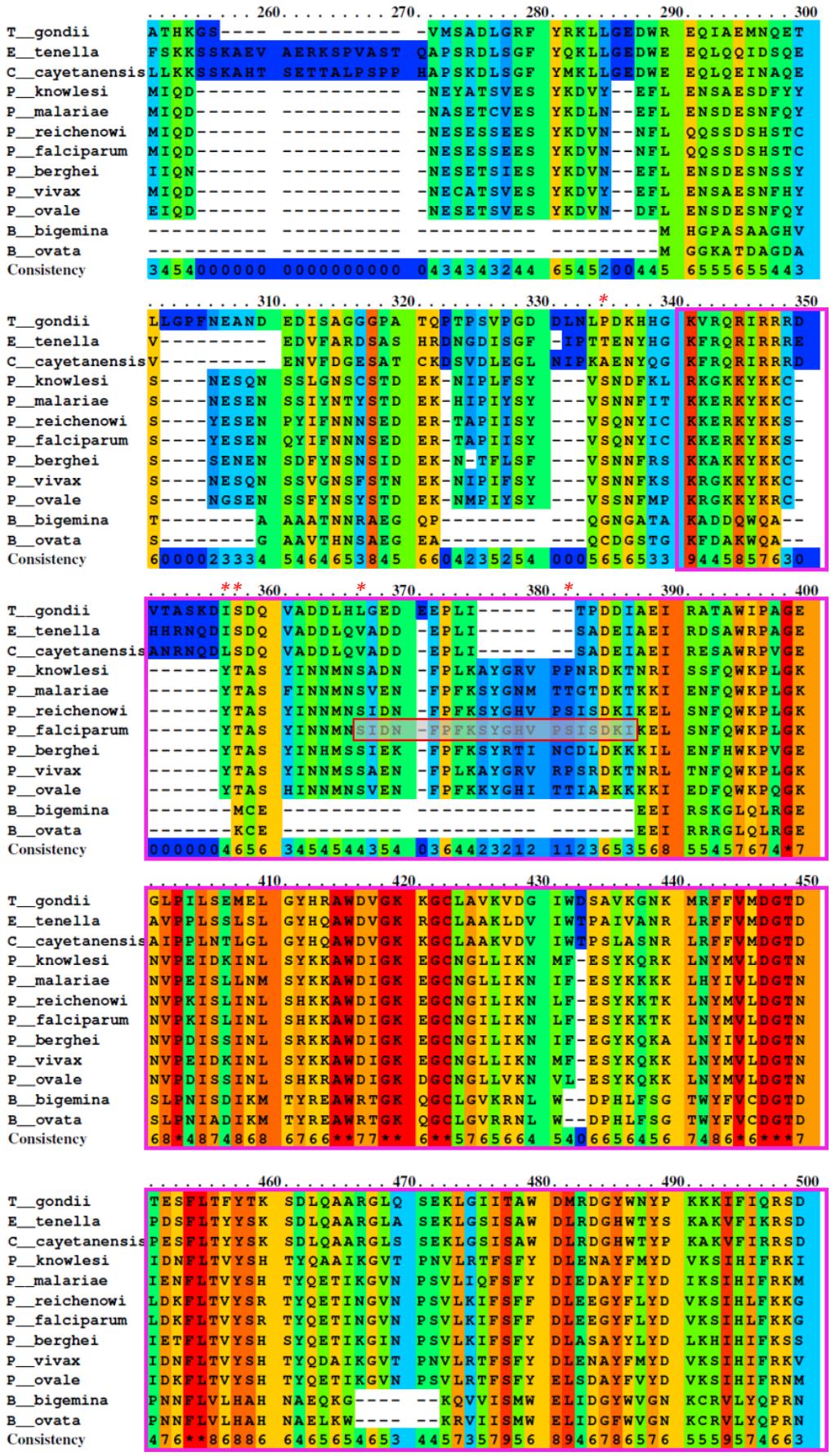
260 270 280 290 300
T__gondii ATHKGS---- ---------- -VMSADLGRF YRKLLGEDWR EQIAEMNQET
E__tenella FSKKSSKAEV AERKSPVAST QAPSRDLSGF YQKLLGEDWE EQLQQIDSQE
C__cayetanensis LLKKSSKAHT SETTALPSPP HAPSKDLSGF YMKLLGEDWE EQLQEINAQE
P__knowlesi MIQD------ ---------- -NEYATSVES YKDVY--EFL ENSAESDFYY
P__malariae MIQD------ ---------- -NASETCVES YKDLN--EFL ENSDESNFQY
P__reichenowi MIQD------ ---------- -NESESSEES YKDVN--NFL QQSSDSHSTC
P__falciparum MIQD------ ---------- -NESESSEES YKDVN--NFL QQSSDSHSTC
P__berghei IIQN------ ---------- -NESETSIES YKDVN--EFL ENSDESNSSY
P__vivax MIQD------ ---------- -NECATSVES YKDVY--EFL ENSAESNFHY
P__ovale EIQD------ ---------- -NESETSVES YKDVN--DFL ENSDESNFQY
B__bigemina ---------- ---------- ---------- ---------M HGPASAAGHV
B__ovata ---------- ---------- ---------- ---------M GGKATDAGDA
Consistency 3454000000 0000000000 0434343244 6545200445 6555655443
310 320 330 340 350
T__gondii LLGPFNEAND EDISAGGGPA TQFTPSVPGD DLNLPDKHHG KVRQRIRRRD
E__tenella V---------- EDVFARDSAS HRDNGDISGF -IPTTENYHG KFRQRIRRRE
C__cayetanensis V---------- ENVFDGESAT CKDSVDLEGL NIPKAENYQG KFRQRIRRRD
P__knowlesi S----NESQN SSLGNSCSTD EK-NIPLFSY ---VSNDFKL RKGKKYKKC-
P__malariae S----NESEN SSIYNTYSTD EK-HIPIYSY ---VSNNFIT KKERKYKKC-
P__reichenowi S----YESEN PYIFNNNSED ER-TAPIISY ---VSQNYIC KKERKYKKS-
P__falciparum S----YESEN QYIFNNNSED ER-TAPIISY ---VSQNYIC KKERKYKKS-
P__berghei S----SENEN SDFYNSNSID EK-N-TFLSF ---VSNNFRS KKAKKYKKC-
P__vivax S----NESQN SSVGNSFSTN EK-NIPIFSY ---VSNNFKS KRGKKYKKC-
P__ovale S----NGSEN SSFYNSYSTD EK-NMPIYSY ---VSSNFMP KRGKKYKRC-
B__bigemina T--------A AAATNNRAEG QP-------- ---QGNGATA KADDQWQA--
B__ovata S---------G AAVTHNSAEG EA-------- ---QCDGSTG KFDAKWQA--
Consistency 6000023334 5464653845 6604235254 0005656533 9445857630
360 370 380 390 400
T__gondii VTASKDISDQ VADDLHLGED EEPLI----- --TPDDIAEI RATAWIPAGE
E__tenella HHRNQDISDQ VADDLQVADD -EPLI----- --SADEIAEI RDSAWRPAGE
C__cayetanensis ANRNQDLSDQ VADDLQVADD -EPLI----- --SADEIAEI RESAWRPVGE
P__knowlesi ------YTAS YINNMNSADN -FPLKAYGRV PPNRDKTNRI SSFQWKPLGK
P__malariae ------YTAS FINNMNSVEN -FPFKSYGNM TTGTDKTKKI ENFQWKPLGK
P__reichenowi ------YTAS YINNMNSIDN -FPFKSYGHV PSISDKIKEL SNFQWKPLGK
P__falciparum ------YTAS YINNMNSIDN -FPFKSYGHV PSISDKIKEL SNFQWKPLGK
P__berghei ------YTAS YINHMSSIEK -FPFKSYRTI NCDLDKKKIL ENFHWKPVGE
P__vivax ------YTAS YINNMSSAEN -FPLKAYGRV RPSRDKTNRL TNFQWKPLGK
P__ovale ------YTAS HINNMNSVEN -FPFKKYGHI TTIAEKKKKI EDFQWKPQGK
B__bigemina -------MCE ---------- ---------- -------EEI RSKGLQLRGE
B__ovata -------KCE ---------- ---------- -------EEI RRRGLQLRGE
Consistency 0000004656 3454544354 0364423212 1123653568 5545767474*7
410 420 430 440 450
T__gondii GLPILSEMEL GYHRAWDVGK KGCLAVKVDG IWDSAVKGNK MRFFVMDGTD
E__tenella AVPPLSSLSL GYHQAWDVGK RGCLAAKLDV IWTPAIVANR LRFFVMDGTD
C__cayetanensis AIPPLNTLGL GYHQAWDVGK KGCLAAKVDV IWTPSLASNR LRFFVMDGTD
P__knowlesi NVPEIDKINL SYKKAWDIGK EGCNGLLIKN MF-ESYKQRK LNYMVLDGTN
P__malariae NVPEISLLNM SYKKAWDIGK EGCNGLLIKN IF-ESYKKKK LHYIVLDGTN
P__reichenowi NVPKISLINL SHKKAWDIGK EGCNGILIKN LF-ESYKKTK LNYMVLDGTN
P__falciparum NVPKISLINL SHKKAWDIGK EGCNGILIKN LF-ESYKKTK LNYMVLDGTN
P__berghei NVPDISSINL SRKKAWDIGK EGCNGILIKN IF-EGYKQKA LNYIVLDGTN
P__vivax NVPEIDKINL SYKKAWDIGK EGCNGLLIKN MF-ESYKQKK LNYMVLDGTN
P__ovale NVPDISSINL SHKRAWDIGK DGCNGLLVKN VL-ESYKQKK LNYMVLDGTN
B__bigemina SLPNISDIKM TYREAWRTGK QGCLGVKRNL W--DPHLFSG TWYFVCDGTD
B__ovata SLPNIADIKM TYREAWRTGK QGCLGVRRNL W--DPHLFSG TWYFVCDGTD
Consistency 68*4874868 6766**77** 6**5765664 5406656456 7486*6***7
460 470 480 490 500
T__gondii TESFLTFYTK SDLQAARGLQ SEKLGIITAW DMRDGYWNYP KKKIFIQRSD
E__tenella PDSFLTYYSK SDLQAARGLA SEKLGSISAW DLRDGHWTYS KAKVFIKRSD
C__cayetanensis PESFLTYYSK SDLQAARGLS SEKLGSISAW DLRDGHWTYP KAKVFIRRSD
P__knowlesi IDNFLTVYSH TYQAAIKGVT PNVLRTFSFY DLENAYFMYD VKSIHIFRKI
P__malariae IENFLTVYSH TYQETIKGVN PSVLIQFSFY DIEDAYFIYD IKSIHIFRKM
P__reichenowi LDKFLTVYSR TYQETINGVN PSVLKIFSFF DLEEGYFLYD VKSIHLFKKG
P__falciparum LDKFLTVYSR TYQETINGVN PSVLKIFSFF DLEEGYFLYD VKSIHLFKKG
P__berghei IETFLTVYSH SYQETIKGIN PSVLKIFSFY DLASAYYLYD LKHIHIFKSS
P__vivax IDNFLTVYSH TYQDAIKGVT PNVLRTFSFY DLENAYFMYD VKSIHIFRKV
P__ovale IDKFLTVYSH TYQETIKGVN PSVLRTFSFY ELSDAYFVYD VKSIHIFRNM
B__bigemina PNNFLVLHAH NAEQKG---- --KQVVISMW ELIDGYWVGN KCRVLYQPRN
B__ovata PNNFLVLHAH NAELKW---- --KRVIISMW ELIDGFWVGN KCRVLYQPRN
Consistency 476**86886 6465654653 4457357956 8946786576 5559574663

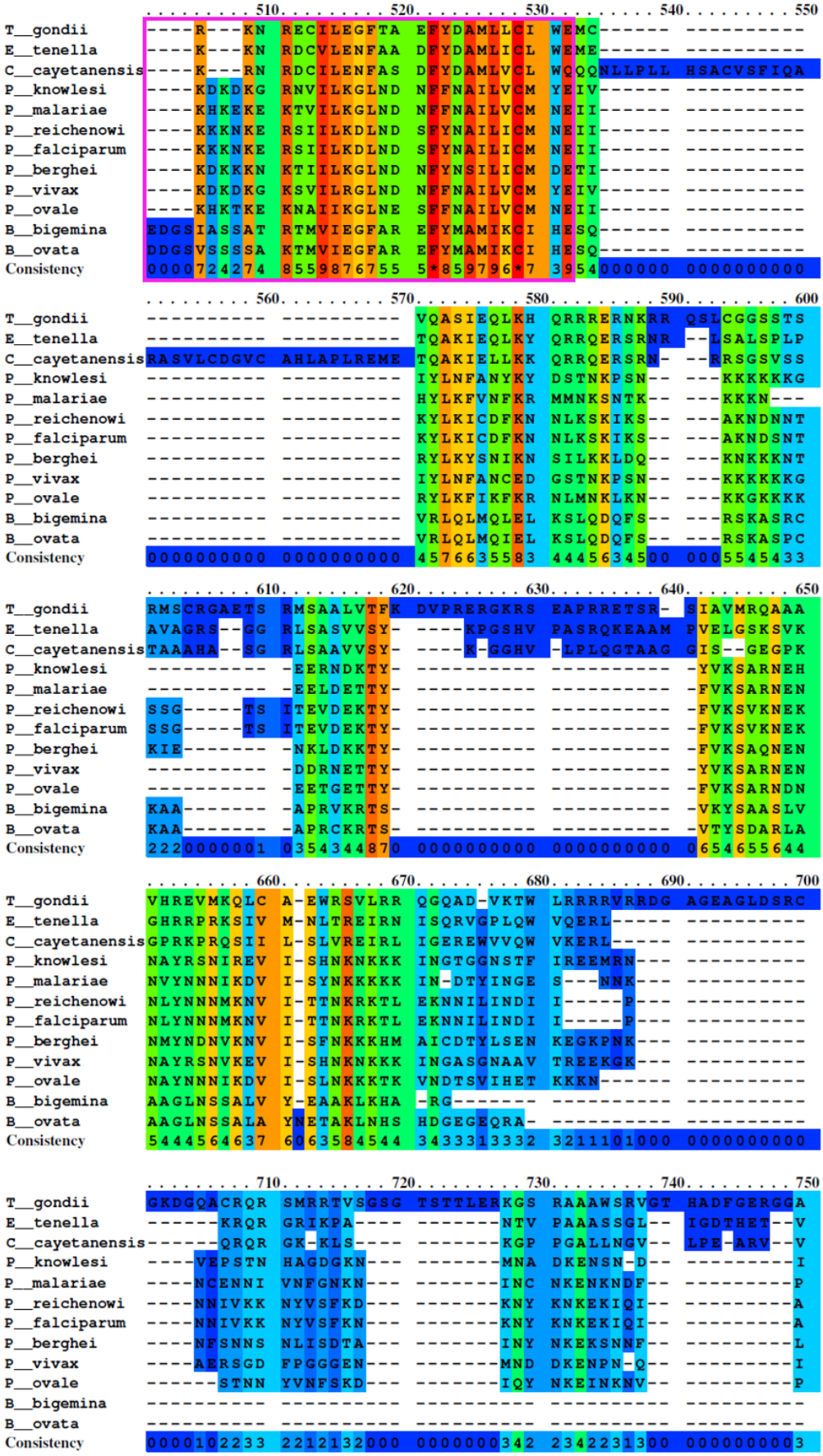
510 520 530 540 550
T__gondii ----R---KN RECILEGFTA EFYDAMLLCI WEMC------ ----------
E__tenella ----K---KN RDCVLENFAA DFYDAMLICL WEME------ ----------
C__cayetanensis ----K---RN RDCILENFAS DFYDAMLVCL WQQQNLLPLL HSACVSFIQA
P__knowlesi ----KDKDKG RNVILKGLND NFFNAILVCM YEIV------ ----------
P__malariae ----KHKEKE KTVILKGLND NFFNAILVCM NEII------ ----------
P__reichenowi ----KKKNKE RSIILKDLND SFYNAILICM NEII------ ----------
P__falciparum ----KKKNKE RSIILKDLND SFYNAILICM NEII------ ----------
P__berghei ----KDKKKN KTIILKGLND NFYNSILICM DETI------ ----------
P__vivax ----KDKDKG KSVILRGLND NFFNAILVCM YEIV------ ----------
P__ovale ----KHKTKE KNAIIKGLNE SFFNAILVCM NEII------ ----------
B__bigemina EDGSIASSAT RTMVIEGFAR EFYMAMIKCI HESQ------ ----------
B__ovata DDGSVSSSSA KTMVIEGFAR EFYMAMIKCI HESQ------ ----------
Consistency 0000724274 8559876755 5*85979 6*7 3954000000 0000000000
560 570 580 590 600
T__gondii ---------- ---------- VQASIEQLKH QRRRERNKRR QSLCGGSSTS
E__tenella ---------- ---------- TQAKIEQLKY QRRQERSRNR --LSALSPLP
C__cayetanensis RASVLCDGVC AHLAPLREME TQAKIELLKK QRRQERSRN- --RRSGSVSS
P__knowlesi ---------- ---------- IYLNFANYKY DSTNKPSN-- ---KKKKKKG
P__malariae ---------- ---------- HYLKFVNFKR MMNKSNTK-- ---KKKN---
P__reichenowi ---------- ---------- KYLKICDFKN NLKSKIKS-- ---AKNDNNT
P__falciparum ---------- ---------- KYLKICDFKN NLKSKIKS-- ---AKNDSNT
P__berghei ---------- ---------- RYLKYSNIKN SILKKLDQ-- ---KNKKKNT
P__vivax ---------- ---------- IYLNFANCED GSTNKPSN-- ---KKKKKKG
P__ovale ---------- ---------- RYLKFIKFKR NLMNKLKN-- ---KKGKKKK
B__bigemina ---------- ---------- VRLQLMQLEL KSLQDQFS-- ---RSKASRC
B__ovata ---------- ---------- VRLQLMQIEL KSLQDQFS-- ---RSKASPC
Consistency 0000000000 0000000000 4576635583 4445634500 0005545433
610 620 630 640 650
T__gondii RMSCRGAETS RMSAALVTFK DVPRERGKRS EAPRRETSR- SIAVMRQAAA
E__tenella AVAGRS--GG RLSASVVSY- ----KPGSHV PASRQKEAAM PVELGSKSVK
C__cayetanensis TAAAHA--SG RLSAAVVSY- ----K-GGHV -LPLQGTAAG GIS--GEGPK
P__knowlesi ---------- -EERNDKTY- ---------- ---------- -YVKSARNEH
P__malariae ---------- -EELDETTY- ---------- ---------- -FVKSARNEN
P__reichenowi SSG-----TS ITEVDEKTY- ---------- ---------- -FVKSVKNEK
P__falciparum SSG-----TS ITEVDEKTY- ---------- ---------- -FVKSVKNEK
P__berghei KIE------- -NKLDKKTY- ---------- ---------- -FVKSAQNEN
P__vivax ---------- -DDRNETTY- ---------- ---------- -YVKSARNEN
P__ovale ---------- -EETGETTY- ---------- ---------- -FVKSARNDN
B__bigemina KAA------- -APRVKRTS- ---------- ---------- -VKYSAASLV
B__ovata KAA------- -APRCKRTS- ---------- ---------- -VTYSDARLA
Consistency 2220000001 0354344870 0000000000 0000000000 0654655644
660 670 680 690 700
T__gondii VHREVMKQLC A-EWRSVLRR QGQAD-VKTW LRRRRVRRDG AGEAGLDSRC
E__tenella GHRRPRKSIV M-NLTREIRN ISQRVGPLQW VQERL----- ----------
C__cayetanensis GPRKPRQSII L-SLVREIRL IGEREWVVQW VKERL----- ----------
P__knowlesi NAYRSNIREV I-SHNKNKKK INGTGGNSTF IREEMRN--- ----------
P__malariae NVYNNNIKDV I-SYNKKKKK IN-DTYINGE S---NNK--- ----------
P__reichenowi NLYNNNMKNV I-TTNKRKTL EKNNILINDI I-----P--- ----------
P__falciparum NLYNNNMKNV I-TTNKRKTL EKNNILINDI I-----P--- ----------
P__berghei NMYNDNVKNV I-SFNKKKHM AICDTYLSEN KEGKPNK--- ----------
P__vivax NAYRSNVKEV I-SHNKNKKK INGASGNAAV TREEKGK--- ----------
P__ovale NAYNNNIKDV I-SLNKKKTK VNDTSVIHET KKKN------ ----------
B__bigemina AAGLNSSALV Y-EAAKLKHA -RG------- ---------- ----------
B__ovata AAGLNSSALA YNETAKLNHS HDGEGEQRA- ---------- ----------
Consistency 5444564637 6063584544 3433313332 3211101000 0000000000
710 720 730 740 750
T__gondii GKDGQACRQR SMRRTVSGSG TSTTLERKGS RAAAWSRVGT HADFGERGGA
E__tenella ------KRQR GRIKPA---- -------NTV PAAASSGL-- IGDTHET--V
C__cayetanensis ------QRQR GK-KLS---- -------KGP PGALLNGV-- LPE-ARV--V
P__knowlesi ----VEPSTN HAGDGKN--- -------MNA DKENSN-D-- ---------I
P__malariae ----NCENNI VNFGNKN--- -------INC NKENKNDF-- ---------P
P__reichenowi ----NNIVKK NYVSFKD--- -------KNY KNKEKIQI-- ---------A
P__falciparum ----NNIVKK NYVSFKN--- -------KNY KNKEKIQI-- ---------A
P__berghei ----NFSNNS NLISDTA--- -------INY NKEKSNNF-- ---------L
P__vivax ----AERSGD FPGGGEN--- -------MND DKENPN-Q-- ---------I
P__ovale ------STNN YVNFSKD--- -------IQY NKEINKNV-- ---------P
B__bigemina ---------- ---------- ---------- ---------- ----------
B__ovata ---------- ---------- ---------- ---------- ----------
Consistency 0000102233 2212132000 0000000342 2342231300 0000000003

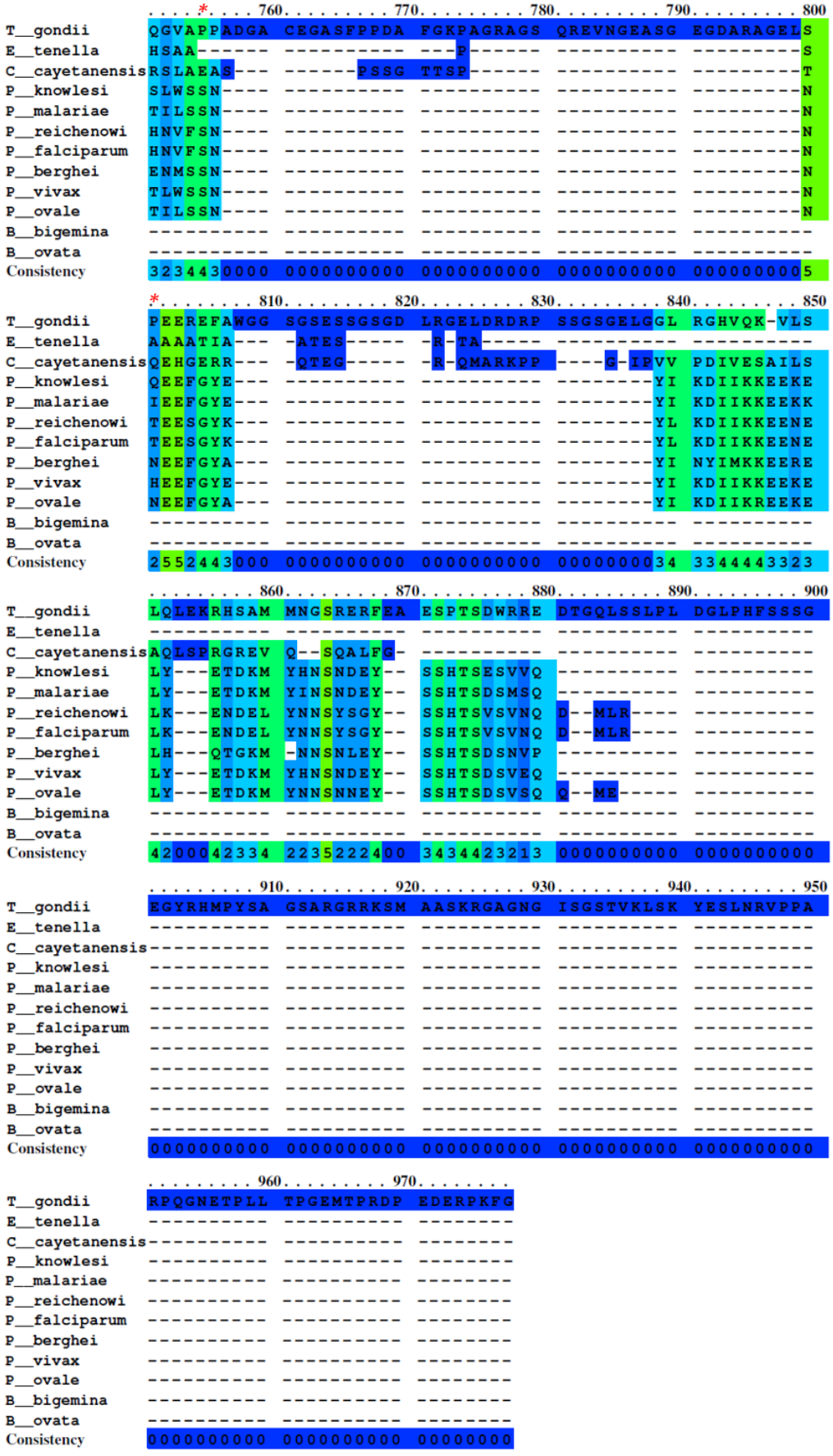
760 770 780 790 800
T__gondii QGVAPPADGA CEGASFPPDA FGKPAGRAGS QREVNGEASG EGDARAGELS
E__tenella HSAA------ ---------- ---P------ ---------- ---------S
C__cayetanensis RSLAEAS--- ------PSSG TTSP------ ---------- ---------T
P__knowlesi SLWSSN---- ---------- ---------- ---------- ---------N
P__malariae TILSSN---- ---------- ---------- ---------- ---------N
P__reichenowi HNVFSN---- ---------- ---------- ---------- ---------N
P__falciparum HNVFSN---- ---------- ---------- ---------- ---------N
P__berghei ENMSSN---- ---------- ---------- ---------- ---------N
P__vivax TLWSSN---- ---------- ---------- ---------- ---------N
P__ovale TILSSN---- ---------- ---------- ---------- ---------N
B__bigemina ---------- ---------- ---------- ---------- ----------
B__ovata ---------- ---------- ---------- ---------- ----------
Consistency 3234430000 0000000000 0000000000 0000000000 0000000005
810 820 830 840 850
T__gondii PEEREFAWGG SGSESSGSGD LRGELDRDRP SSGSGELGGL RGHVQK-VLS
E__tenella AAAATIA--- -ATES----- -R-TA----- ---------- ----------
C__cayetanensis QEHGERR--- -QTEG----- -R-QMARKPP ----G-IPVV PDIVESAILS
P__knowlesi QEEFGYE--- ---------- ---------- --------YI KDIIKKEEKE
P__malariae IEEFGYE--- ---------- ---------- --------YI KDIIKKEEKK
P__reichenowi TEESGYK--- ---------- ---------- --------YL KDIIKKEENE
P__falciparum TEESGYK--- ---------- ---------- --------YL KDIIKKEENE
P__berghei NEEFGYA--- ---------- ---------- --------YI NYIMKKEERE
P__vivax HEEFGYE--- ---------- ---------- --------YI KDIIKKEEKE
P__ovale NEEFGYA--- ---------- ---------- --------YI KDIIKREEKE
B__bigemina ---------- ---------- ---------- ---------- ----------
B__ovata ---------- ---------- ---------- ---------- ----------
Consistency 2552443000 0000000000 0000000000 0000000034 3344443323
860 870 880 890 900
T__gondii LQLEKRHSAM MNGSRERFEA ESPTSDWRRE DTGQLSSLPL DGLPHFSSSG
E__tenella ---------- ---------- ---------- ---------- ----------
C__cayetanensis AQLSPRGREV Q--SQALFG- ---------- ---------- ----------
P__knowlesi LY---ETDKM YHNSNDEY-- SSHTSESVVQ ---------- ----------
P__malariae LY---ETDKM YINSNDEY-- SSHTSDSMSQ ---------- ----------
P__reichenowi LK---ENDEL YNNSYSGY-- SSHTSVSVNQ D--MLR---- ----------
P__falciparum LK---ENDEL YNNSYSGY-- SSHTSVSVNQ D--MLR---- ----------
P__berghei LH---QTGKM -NNSNLEY-- SSHTSDSNVP ---------- ----------
P__vivax LY---ETDKM YHNSNDEY-- SSHTSDSVEQ ---------- ----------
P__ovale LY---ETDKM YNNSNNEY-- SSHTSDSVSQ Q--ME----- ----------
B__bigemina ---------- ---------- ---------- ---------- ----------
B__ovata ---------- ---------- ---------- ---------- ----------
Consistency 4200042334 2235222400 3434423213 0000000000 0000000000
910 920 930 940 950
T__gondii EGYRHMPYSA GSARGRRKSM AASKRGAGNG ISGSTVKLSK YESLNRVPPA
E__tenella ---------- ---------- ---------- ---------- ----------
C__cayetanensis ---------- ---------- ---------- ---------- ----------
P__knowlesi ---------- ---------- ---------- ---------- ----------
P__malariae ---------- ---------- ---------- ---------- ----------
P__reichenowi ---------- ---------- ---------- ---------- ----------
P__falciparum ---------- ---------- ---------- ---------- ----------
P__berghei ---------- ---------- ---------- ---------- ----------
P__vivax ---------- ---------- ---------- ---------- ----------
P__ovale ---------- ---------- ---------- ---------- ----------
B__bigemina ---------- ---------- ---------- ---------- ----------
B__ovata ---------- ---------- ---------- ---------- ----------
Consistency 0000000000 0000000000 0000000000 0000000000 0000000000
960 970
T__gondii RPQGNETPLL TPGEMTPRDP EDERPKFG
E__tenella ---------- ---------- --------
C__cayetanensis ---------- ---------- --------
P__knowlesi ---------- ---------- --------
P__malariae ---------- ---------- --------
P__reichenowi ---------- ---------- --------
P__falciparum ---------- ---------- --------
P__berghei ---------- ---------- --------
P__vivax ---------- ---------- --------
P__ovale ---------- ---------- --------
B__bigemina ---------- ---------- --------
B__ovata ---------- ---------- --------
Consistency 0000000000 0000000000 00000000

B

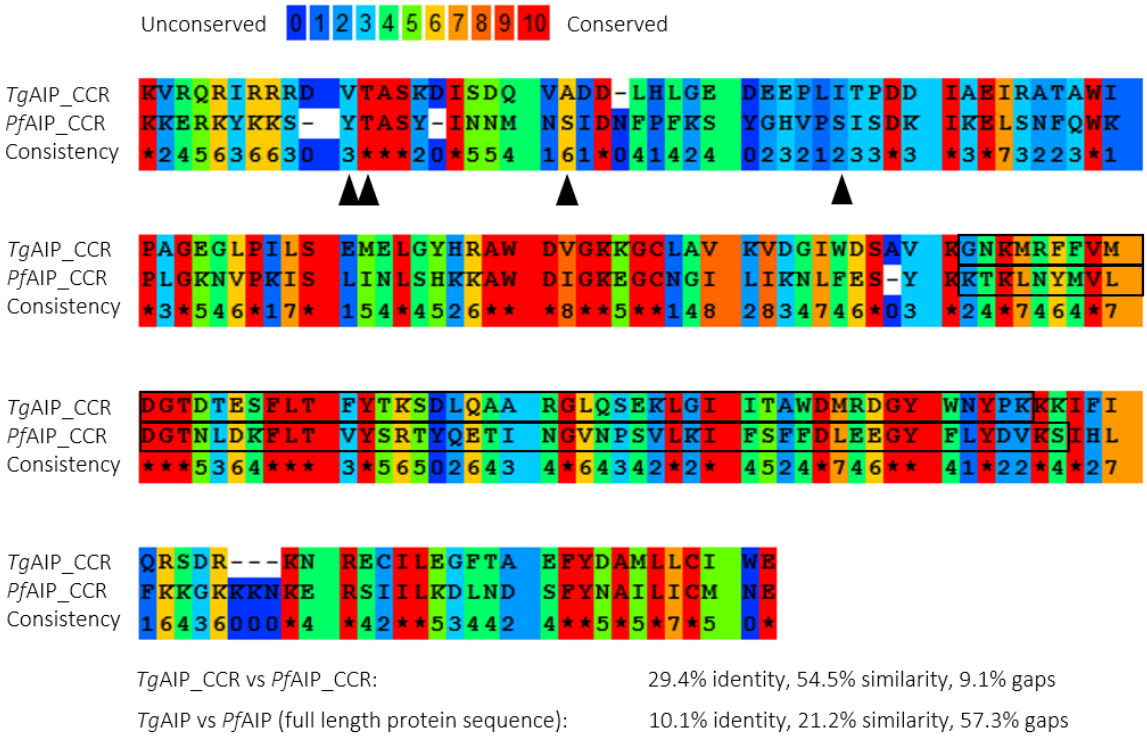

C

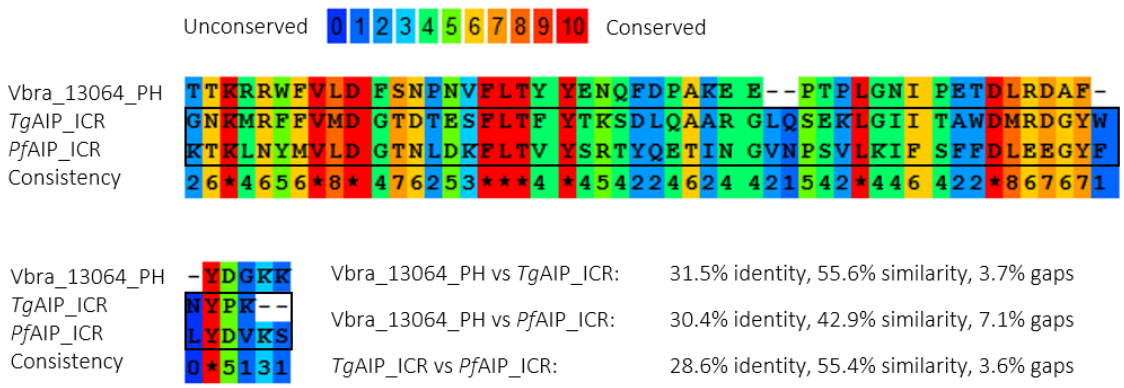

S3 | Sequence alignment of apicomplexan AIP homologues identified a conserved core region. (**A**) Protein sequences of various putative AIP homologues (see Fig. 3.1A) were aligned using PRALINE multiple sequence alignment. Amino acid consensus between *Tg*AIP and homologues is shown. A conserved core region (CCR) was identified (magenta box). Exon 3 that is spliced out in splice variant PF3D7_1136700.2 is indicated by a red box. Red asterisks indicate phosphorylation of *Pf*AIP residues S_{76}, Y_{91}, T_{92}, S_{101}, S_{115}, S_{371} and T_{374} (www.PlasmoDB.org) (**B**) *Tg*AIP and *Pf*AIP CCRs were aligned using PRALINE. Black box indicates inner core region (ICR) explained in (C). Needle alignment was performed to calculate identity and similarity of CCRs and full-length protein sequences. (**C**) Vbra_13064 was retrieved by BLASTp search (see Fig. 3.1A). CD-search was performed for Vbra_13064 and identified a predicted PH domain spanning residues T_{1605} to K_{1656}. EMBOSS Needle alignment of *Tg*AIP and *Pf*AIP CCRs was performed to identify an inner core region (ICR, black box) that is similar to predicted Vbra_13064 PH domain (residue T_{1605} to K_{1656}). Needle alignment was performed to calculate identity and similarity of ICRs to Vbra_13064 PH domain. *Pf*AIP phosphorylations at residues Y_{91}, T_{92}, S_{101} and S_{115} of *Pf*AIP CCR are indicated by black arrowheads. (A-C) PRALINE multiple sequence alignment was performed using BLOSUM62 matrix and default settings. Level of conservation is indicated by colour code and scaled from blue to red indicating low to full conservation, respectively. Black asterisks indicate identical residues. (B-C) EMBOSS Needle alignment was performed using BLOSUM62 matrix and default settings.

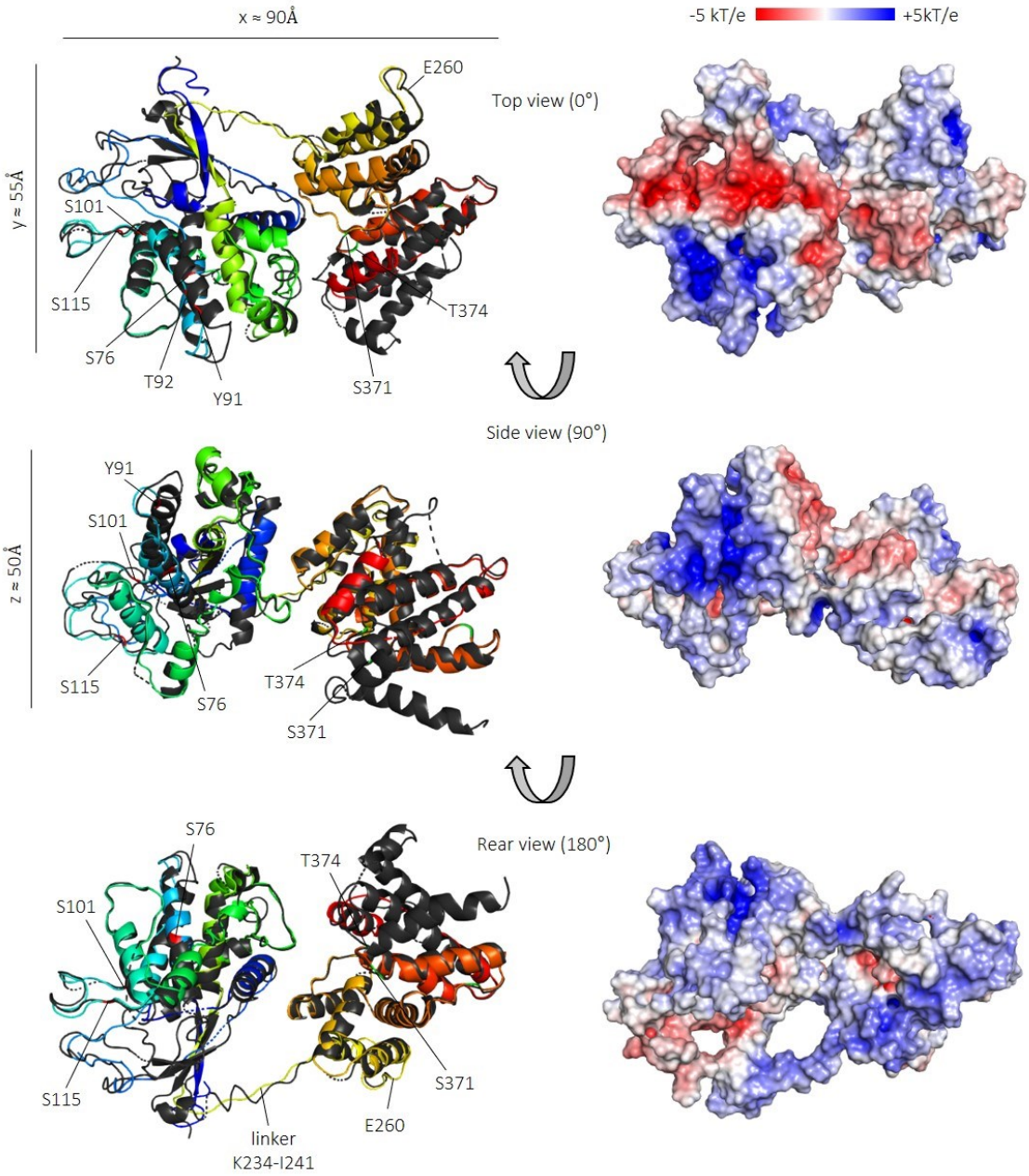

S4 | Structure prediction of the *Pf*AIP protein. Three-dimensional structural model of *Pf*AIP predicted by I-TASSER server. The *Pf*AIP protein sequence was submitted to I-TASSER using default settings. The model with the highest C-score is shown from three different angles (top, side and rear view). Views in 90° increments are indicated by rotation arrows. C-score of the model: -2.15; estimated TM-score: 0.46 ± 0.15; Estimated RMSD: 12.1 ± 4.4 Å. The *Pf*AIP model dimensions are indicated by x, y and z. Peptides in chain are colored in a spectrum from blue to red (residues from the N-terminus to the C-terminus). Closest structural similarity to the predicted *Pf*AIP model was determined by I-TASSER for the crystal structure of an SspE monomer (PDB accession number: 6JIV) with a TM-score of 0.958. The crystal structure of SspE is shown in dark grey and is superimposed on the predicted *Pf*AIP model. *Pf*AIP phosphorylation-sites (S_{76}, Y_{91}, T_{92}, S_{101}, S_{115}, S_{371} and T_{374}) are marked in red and green. According to DEPTH analysis, residue S_{76} is buried appr. 10 Å inside the structure, whereas all other phosphorylation-sites are predicted to be surface exposed. Residue E_{260} marks the end of the determined conserved core region (CCR). The electrostatic surface potential of the corresponding *Pf*AIP model is shown on the right. The scale is from -5 kT/e (red) to +5 kT/e (blue). Light grey indicates neutral electrostatic potential. Model visualization and dimension measurements were performed using Pymol. Electrostatic surface potential was calculated by Pymol APBS plugin.

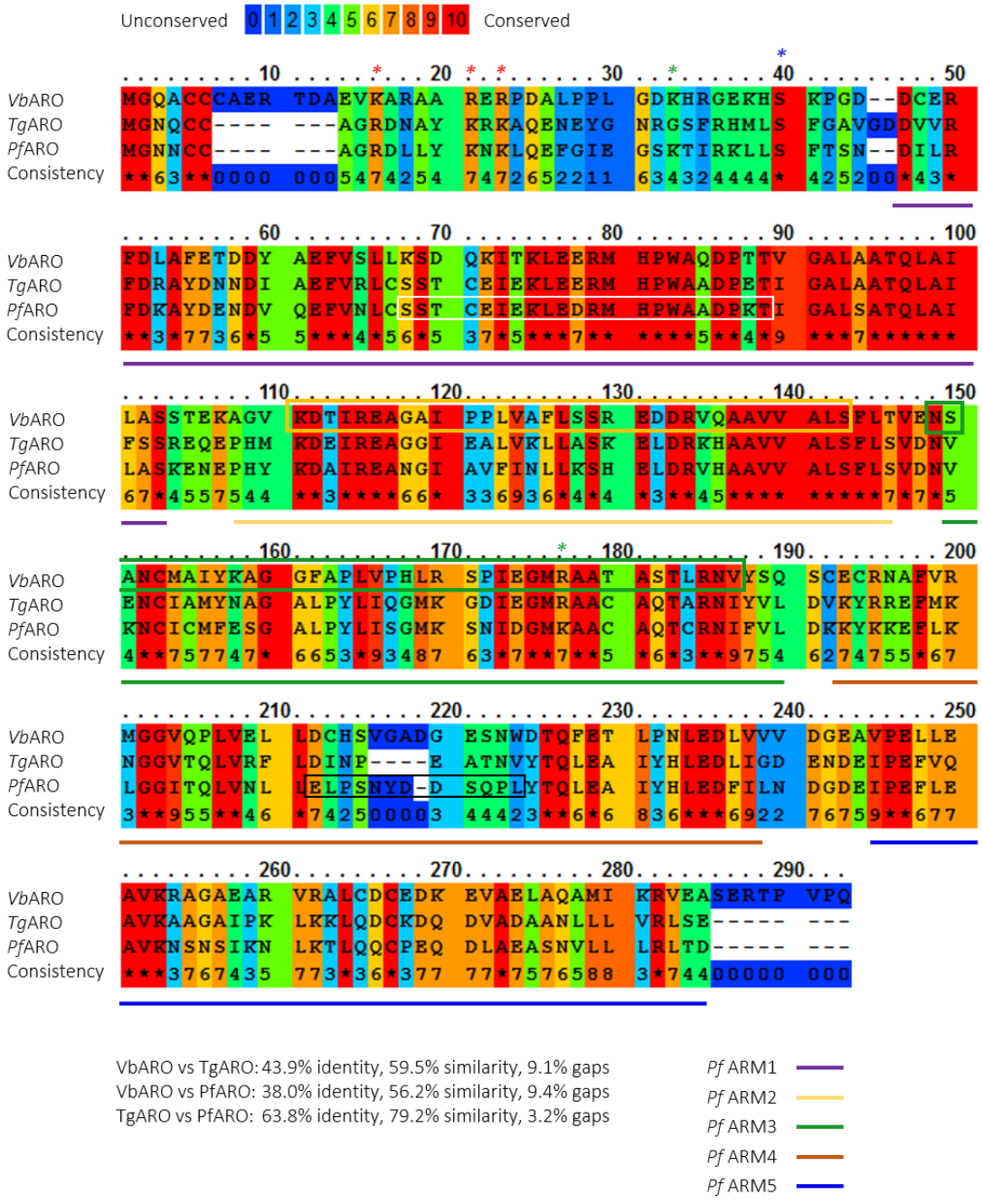

S5 | A homologue of ARO is present in *V. brassicaformis*. BLASTp search analysis using *Tg*ARO (Gene ID: TGME49_261440) protein sequence as query against nr database retrieved *Vb*ARO (Gene ID: Vbra_4126) as *Tg*ARO homologue in *Vitrella brassicaformis* (*Vb*). PRALINE multiple sequence alignment was performed for *Vb*ARO, *Tg*ARO and *Pf*ARO (Gene ID: PF3D7_0414900). The level of conservation is indicated by colour code and scaled from blue to red indicating low to full conservation, respectively. Black asterisks indicate identical residues. CD-search analysis predicted two Armadillo (ARM) repeats for *Vb*ARO spanning residue K_{109} to S_{141} (orange box) and N_{147} to V_{185} (green box). *Pf*ARO ARM repeats 1 to 5 [Geiger & Brown *et al.*, 2020] are shown as color-coded lines beneath the sequence alignment. ARM1, purple; ARM2, orange; ARM3, green; ARM4, brown; ARM5, blue. *Pf*ARO loop1 and loop2 are indicated by white and black box, respectively. The positively charged residues R_9, K_{14} and K_{16} which are important for rhoptry membrane attachment of *Pf*ARO [Cabrera *et al.*, 2012], are indicated by red asterisks. Calcium-dependent phosphorylation of *Tg*ARO at S_{33} [Nebl *et al.*, 2011] is indicated by blue asterisk. Acetylation of *Pf*ARO K_{26} and K_{168} [Cobbold *et al.*, 2016] is indicated by green asterisks. Identity and similarity of *Vb*ARO, *Tg*ARO and *Pf*ARO was determined using EMBOSS Needle alignment. EMBOSS Needle and PRALINE multiple sequence alignments were performed using BLOSUM62 matrix and default settings.